# EXOPLANETARY SYSTEMS IN TECHNICOLOR

by

David Berardo

M.Sc., McGill University (2017)
B.S., McGill University (2015)

Submitted to the Department of Physics
in partial fulfillment of the requirements for the degree of

Doctor of Philosophy

at the

MASSACHUSETTS INSTITUTE OF TECHNOLOGY

June 2023



Author .....
Department of Physics
May 18, 2023

Certified by .....
Julien de Wit
Assistant Professor
Thesis Supervisor

Accepted by .....
Lindley Winslow
Associate Department Head of Physics

# EXOPLANETARY SYSTEMS IN TECHNICOLOR

by

David Berardo

Submitted to the Department of Physics
on May 18, 2023, in partial fulfillment of the
requirements for the degree of
Doctor of Philosophy

## Abstract

As the number of confirmed extra-solar planets surpasses 5000, our ability to characterize exoplanets has equally advanced in the era of high precision photometry afforded by instruments such as the James Webb Space Telescope. With increased precision, longer baselines of observation, and access to multi-instrument data sets, the study of exoplanets has reached a level of detail never before possible. In this thesis, I focus on the analysis of several multi-planet transiting exoplanet systems observed with the *KEPLER, K2, Spitzer, TESS* and *Hubble* instruments. Using data from these instruments, I present a detailed study of the bright HIP41378 five-planet system, extracting the orbital periods of two long-period planets, refining transit center measurements, and detecting Transit Timing Variations (TTVs) of one of the innermost planets in the system, which hints at the presence of an undetected $6^{th}$ planet.

Beyond individual systems, I also consider two observable properties of exoplanets at a population-level scale, in the context of treating planets as 3D objects. Measuring the shape of a planet provides us with insight towards their internal structure, formation, and atmosphere, and allows us to disentangle observational degeneracies between surface features and their orbital parameters. First, I expand the study of rotation-induced oblateness to a sample of almost 400 planets, quantifying the detectability of oblateness for these planets in the context of future high-precision observations with the James Webb Space Telescope and other observatories. Next, I examine the observational effects of tidal deformation by the host star of nearly 200 exoplanets, and how current and future uncertainties in the measurement of a planets density allow for such an effect to be detectable. Additionally, I report on the analysis of a large data-set of the TRAPPIST-1 system obtained using the *STIS* instrument on the Hubble Space Telescope. In keeping with the theme of planets in 3-D, this analysis aims to search for extended neutral Hydrogen exospheres around the TRAPPIST-1 planets, which would appear as transit-like signals in the Lyman-$\alpha$ emission of the host star.

Finally, I turn to the stars themselves around which exoplanet orbit, considering the effects of non-homogeneous stellar surfaces on exoplanet observations. I investi-

gate how spatially and time varying surface features of a star contribute to baseline trends that must be removed when analyzing exoplanet transits, and assess the feasibility of empirically extracting precise stellar spectra due to star spots, which directly impact the precision of measuring planetary emission spectra. Through these studies, I aim to disentangle higher-order effects and biases which will become prevalent as the quality of observations improves, and to contribute to a more complete understanding of exoplanetary systems.

Thesis Supervisor: Julien de Wit
Title: Assistant Professor

# Acknowledgments

I wouldn't be where I am today if were not for the people that have been a part of my life. I first and foremost would like to thank my parents, Peter & Rita, for always having been there for me, offering support, encouragement, and pushing me to always be a better person. I'd also like to thank my brother Alexander who, despite us having as different interests as could be, has always been someone I could count on and who I will always care for. I am also thankful for Amanda Sitren, my loving partner who has stuck by throughout these many years, and has always had nothing but support and encouragement, through good times and bad.

I owe an immense debt of gratitude to my grandparents; Luigi, Rosina, Antonio, and Rossana. They left behind all they knew in order to find a better life for their families, and it is only because of their sacrifices and tenacity that I even had the opportunity in the first place to pursue the path that has led me to completing a PhD at one of the best institutions in the world. Furthermore, I have always been lucky to have the love and support of my extended family, and would like to thank Tony, Carmela, Josie, Jean-Francois, Daniel, Vanessa, Felix, and Laurent for always being supportive and loving.

I'd like to thank Julien de Wit, my academic advisor, who took me in under his wing when my journey as a graduate student hit a bump in the road. He has always been kind, thoughtful, insightful, and an endless source of inspiration and encouragement. I'd also like to thank the the members of the disruptive planets research group, including Prajwal Niraula, Benjamin Rackham, Artem Burdanov, and Zoe de Boeurs. A thank you as well to the administrators of the group, Roberta Allard & Kayla Bauer.

I am also ever thankful for the astro pals, my fellow classmates in the astro division that have made grad school a truly wonderful experience. Thanks to Nicholas Mehrle, Michael Calzadilla, Chris Whittle, Kaley Brauer, Halston Lim, Benjamin Lane, and the rest of the astro division. Thank you as well to the ever helpful administrators Cathy Modica, Debbie Meinbresse, Thea Paneth, and Sydney Miller.

In addition to my academic cohort, I've had the great luck to have met some of my closest friends very early on in my life, and I'm grateful that many of them are still in my life to this day. Thanks to Jesse Jurkowski & Adriano Chiello, for making sure so many years passed by without ever a dull moment.

Finally, it would be foolish to think that I would not have made it to where I am today without having met and interacted with a series of wonderful educators throughout the years. They provided me with guidance, inspiration, and continuously fanned the flame of my curiosity that kept me on the path that has ultimately led to this moment. Thank you to Enrico Uva, Rhys Adams, and Andrew Cumming.

# Contents

# List of Figures

# List of Tables

# Part I

# Overview of Thesis

# Chapter 1

# Introduction

## 1.1 The Growth of Exoplanet Observations

For thousands of years up until the last decade of the $20^{th}$ century, as far as humanity was concerned there were roughly nine planets in the known universe (plus or minus a few as discoveries were confirmed, debunked, and demoted over time). With a solar system sample of one, it was impossible to answer questions pertaining to the multitude and variability of planets that might possibly exist. Questions such as the formation and evolution of the solar system, of the individual planets themselves, of the interactions that might have led to what we call home today, while each having their own theories and possible explanations, were locked away behind the inability to observe alternate outcomes. While there was no reason to believe that planets shouldn't exist elsewhere in the solar system, for a long time we did not possess the technical capability and instrumental precision required to detect them.

Amid various tentative discoveries, it finally came to pass in 1995 that the first extra-solar planet orbiting a solar-like star was confirmed to exist [Mayor and Queloz, 1995]. In the nearly 30 years that have since passed, the field of exoplanet astronomy has exploded from the study of a handful of ideal candidates to a current sample of over 5000 confirmed extra-solar planets along with over 6000 candidate exoplanets[1]. An early example of one such surprise that came about this growth in sample size

[1] https://exoplanetarchive.ipac.caltech.edu/exoplanetplots/

was the discovery of so-called 'hot jupiters' [Mayor and Queloz, 1995], planets with sizes and masses similar to that of Jupiter in our solar system, but which orbited significantly closer to their host stars. Where our Jupiter has an orbital period of 12 years, hot Jupiters often orbit on timescales of days to even hours [Howard et al., 2010]. Another example of discoveries of planets unlike anything in our solar system are "super-Earths" and "mini-Neptunes". As their names imply, they share some features in common with the Earth and Neptune, be it their interior composition or atmospheric characters, but in the case of super-Earths they can be as much as 8x as massive (such as 55 Cancri e [McArthur et al., 2004]).

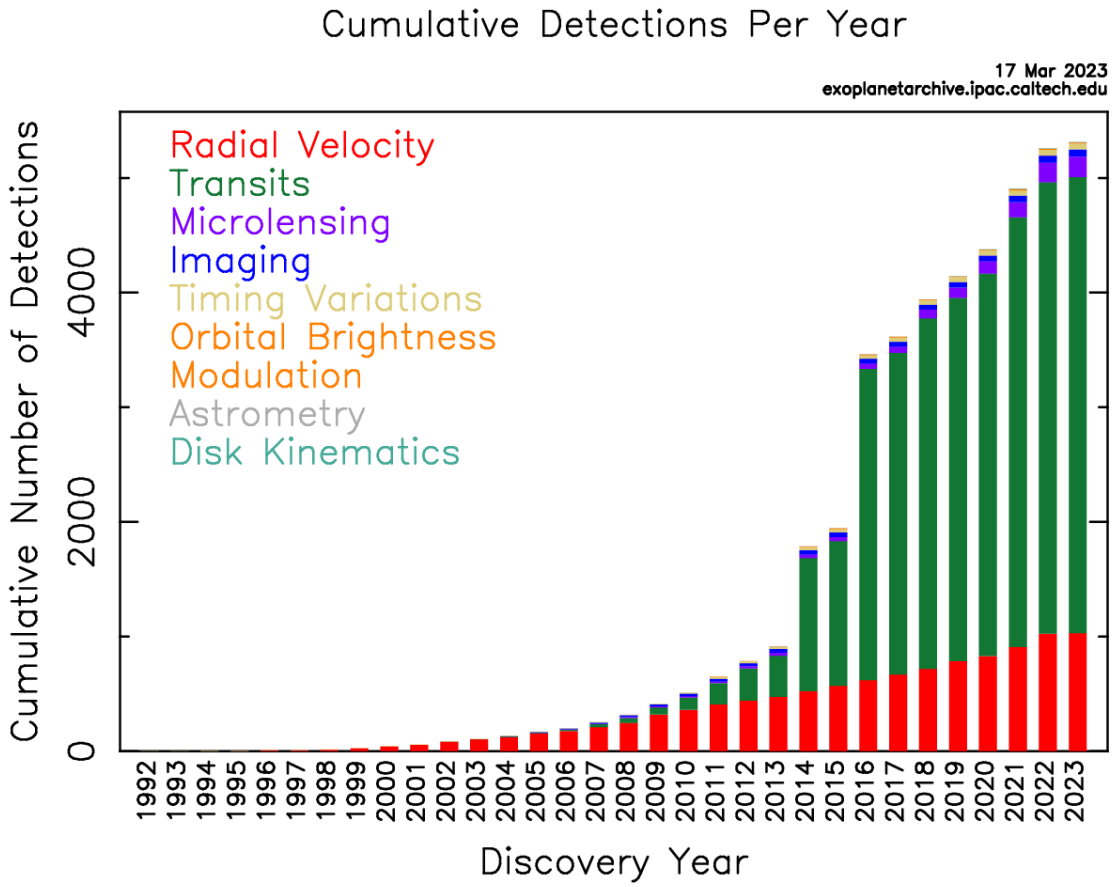


Figure 1-1: The total number of known exoplanets over time, broken down by detection method. Figure courtesy of the Exoplanet Archive.

In addition to these entire outlier classes of planets, we've learned a great deal about planet populations, such as the dichotomy in planetary radii [Fulton et al.,

2017] or the Neptunian desert [Szabó and Kiss, 2011, Mazeh, T. et al., 2016]. These discoveries provide insight towards the kinds of planets that are capable of existing, and help us to place our own solar system on a scale of remarkable outlier to average member.

Figure 1-1 shows the growth of known planets over time, broken down by discovery methods. This explosive growth over the past few decades can be attributed to the development of exoplanet-centric missions such as *Kepler* [Koch et al., 2010, Borucki et al., 2010], (and later *K2* [Howell et al., 2014]), *TESS* [Ricker et al., 2014], as well as the steadily improving precision and quality of observations. Along with this growth in sample size has been the growth of multi-disciplinary science, with researchers from biology, seismology, geology, chemistry, orbital dynamics, stellar physics, and many more fields finding a home amongst the data sets of exoplanets

## 1.2 Exoplanet Detection Methods

### 1.2.1 Radial Velocity

In the early days of exoplanet observations, as can be seen in figure 1-1, the radial velocity (RV) method of planet detection provided the largest source of exoplanet discoveries. In this case, the measurement being made is the Doppler shift in the spectrum of a host star due to the perturbation of a massive planet. The key equation behind radial velocities is:

$$K = \sqrt{\frac{G}{1-e^2}} m_2 \sin i \left(m_1 + m_2\right)^{-1/2} a^{-1/2} \tag{1.1}$$

where K is the semi-amplitude of the radial velocity oscillations, $e$ is the eccentricity of the planet's orbit, $m_2$ is the mass of the perturbing planet, $\sin i$ is the inclination of the orbital plane relative to the observer, $m_1$ is the mass of the host star, and $a$ is the semi-major axis of the binary orbit.

RVs provide a direct measurement of the mass of an exoplanet, which is one of the two main measurements required to characterise an exoplanet's composition

and potential atmospheric properties [Seager et al., 2007]. In the modern era of Extreme Precision Radial Velocity (EPRV) instruments such as ESPRESSO [Pepe et al., 2021], the sensitivity of these measurements is approaching the scale of 1cm/s deviations in the reflex motion of the star, which corresponds to a detectable planet mass approaching that of the Earth.

### 1.2.2 Transits

While RV measurements are critical to the study of exoplanets, as time went on transits became the primary method of detecting exoplanets. Of the over 5000 known exoplanets, the transit methods accounts for just over 4000 of them[2]. The primary reason for this has been the launch of dedicated transit-finding missions, such as *Kepler* (and later k2) and *TESS*, which could observe large sections of the sky at once and simultaneously detect multiple planets.

In figure 1-2 we show a diagram of the different components of a transiting exoplanet. The most commonly observed piece of this is the primary transit, when the planet passes between the star and the observer. This produces a drop in flux anywhere from 10s of parts per million (ppm) up to several thousand ppm, in the case of larger planets and/or smaller host stars.

The precise shape of an exoplanet transit is capable of providing us with the inclination, semi-major axis, eccentricity, argument of periastron, and critically the size of the exoplanet, which is measured through the depth of the transit [Winn, 2010]. This allows only for a measurement relative to the stellar radius, however this is often measured to sufficient accuracy as to not be a limiting factor in the uncertainty of the planetary radius. In particular, if we have for the planet radius $r_p$

$$r_p = \delta * R_\star \tag{1.2}$$

where $\delta$ is the transit depth, often measured in parts per million (ppt) or parts per thousand (ppt) for larger gas giants, and $R_\star$ is the stellar radius, we can write

[2]https://exoplanetarchive.ipac.caltech.edu

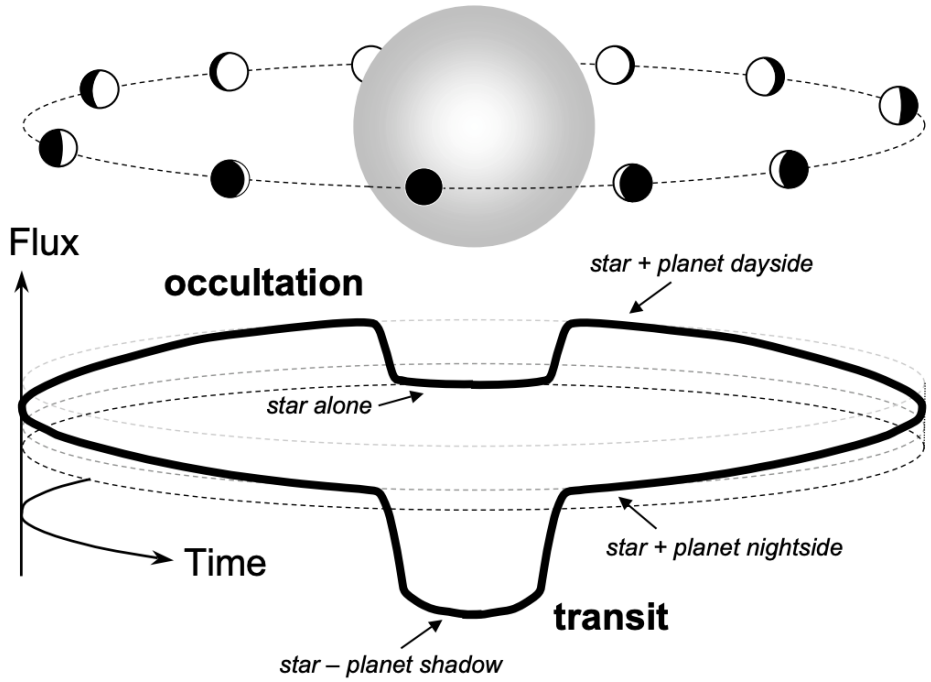


Figure 1-2: A schematic of the observable flux of a star-planet system, indicating the possibilities of transit, phase curve, and occultation measurements. Figure taken from Winn [2010]

the uncertainty on the radius of the planet ($\sigma_{r_p}$) as

$$\frac{\sigma_{r_p}}{r_p} = \sqrt{\left(\frac{\sigma_\delta}{\delta}\right)^2 + \left(\frac{\sigma_{R_\star}}{R_\star}\right)^2} \tag{1.3}$$

We can thus directly quantify the contribution of each component, a technique which we explore further in chapter 6 in the context of planet density measurements.

In addition to measurements described so far, if a planet is observed to transit multiple times during a continuous observation, then its orbital period can also be determined. Using Kepler's 3rd law of orbital dynamics:

$$P^2 = \frac{4\pi^2 a^3}{G M_\star} \tag{1.4}$$

allows one to directly measure the density of the host star by scaling by the volume of the star:

$$P^2 = \frac{4\pi^2 a^3}{GM_\star} \frac{\frac{4}{3}\pi R_\star^3}{\frac{4}{3}\pi R_\star^3} \tag{1.5a}$$

$$P^2 = \frac{3\pi (a/R_\star)^3}{G\rho_\star} \tag{1.5b}$$

$$\rho_{star} = \frac{3\pi (a/R_\star)^3}{GP^2} \tag{1.5c}$$

where we have combined the mass and radius of the star into $\rho_\star$ [Seager and Mallén-Ornelas, 2003], and we note that $a/R_\star$ is the variable that is provided by fitting exoplanet lightcurves (since flux values are always normalized, thus allowing only relative measures of scales).

Alternatively, one can use the expression for the duration of a transit ($T_{\rm dur}$)

$$T_{\rm dur} = \frac{P}{\pi (a/R_\star)} \tag{1.6}$$

to eliminate the semi-major axis parameter and re-write the stellar density in terms of variables which are entirely model-independant (i.e. the time between transits and the duration of a transit, which can be read off directly from an observation):

$$\rho_\star = \frac{3P}{\pi^2 G T_{\rm dur}^3} \tag{1.7}$$

This relation however only holds true in the case of a perfectly circular orbit. If the density of the host star is well known from previous observations, this can then be used as a test of orbital eccentricity. One can compare the value obtained in equation 1.7 with the known stellar density, and using the framework of Dawson and Johnson [2012], discrepancies between the two can be used to measure the eccentricity and argument of periastron of the planets orbit.

### 1.2.3 Transit Timing Variations

The previous two measurement methods rely on the interaction between a planet and its host star. Another way in which exoplanets can be detected is through their impacts on other planets in a multi-planet system. If two planets are in near resonance

with regards to their orbital periods (i.e. if their periods are near to a ratio of p/q where p and q are whole numbers) then gravitational interactions will cause their orbits to alter slightly, resulting in an oscillating transit center from the point of view of an observer, as was first seen the three planet Kepler-9 system [Torres et al., 2010]. These transit timing variations (TTVs), can be used to infer the presence of a non-transiting planet, providing an estimate of its orbital period and mass.

In particular, for two planets in a co-planar orbit that lie near a j:j-1 orbital resonance, we can analytically calculate the super-period of the TTV [Lithwick et al., 2012], i.e. the period of the sinusoidal variation of the transit center of a perturbed planet, as:

$$P^j = \frac{P'}{j|\Delta|} \tag{1.8}$$

where $\Delta$, which characterises how close to resonance the two orbits are, is defined as:

$$\Delta = \frac{P'}{P}\frac{j-1}{j} - 1 \tag{1.9}$$

where $P$ and $P'$ are the orbital periods of the two planets. This model represents a simplified case of two planets resulting in perfectly sinusoidal variations, but dynamical simulations of multi-planet systems reveal the potential for more complicated behaviour for systems with more than two planets Deck et al. [2014].

### 1.2.4 Additional Detection Methods

In addition to the methods mentioned here, there exist additional techniques for discovering and characterising exoplanets. One such method is known as direct imaging, and allows for a direct detection of exoplanets, rather than through inferred effects on their host star [Marois et al., 2008]. By comparing the brightness of the observed planet and its age (inferred through the age of the system) with theoretical models, this allows one to infer the mass of the observed planet [Baraffe et al., 2003, Bowler, 2016, Berardo et al., 2017]. Additionally, observing gaps and other structure in the

dust disk surrounding the star allows for an analysis of the formation of the system. Instruments such as the Gemini Planet Imager [Macintosh et al., 2014] have allowed us to directly image massive, Jupiter-sized planets far out from their host star, and new instruments such as the Roman Space Telescope [Spergel et al., 2015] will continue to push the envelope, allowing the detection of lower mass planets orbiting closer in to their host star [Li et al., 2021].

A non-exhaustive list of further detection methods includes

1. **Microlensing** : The inferred presence of a planet due to due gravitational magnification of a background object as a planet-hosting system passes between it and an observer [Alcock et al., 1993, Udalski et al., 1993].

2. **Astrometry** : The visual detection of orbital motion of a star around an offset center of mass, due to planetary bodies [Perryman et al., 2014].

3. **Pulsar Timing Variations** : Variations in the timing of a pulsar beam, which is again due to gravitational interactions with a planetary body [Wolszczan and Frail, 1992].

## 1.3 Characterising Exoplanets: Shapes & Surfaces

The methods described in the previous section allow us to characterise exoplanets in a variety of different ways. Knowing the mass and radius of a planet allows us to measure its density, which in turn allows us to estimate what its interior composition may be [Rogers and Seager, 2010]. Spectral observations allow us to gain insight as to whether or not a planet has a significant atmosphere, and what it may be comprised of. All of these measurements however rely on a series of assumptions, which must be continuously re-evaluated as the quality and quantity of observations continue to improve, with instruments such as the James Webb Telescope (JWST) [Gardner et al., 2006] and other future missions such as the proposed ELTs/TMTs, the Vera C. Rubin observatory [Ivezić et al., 2019], and the LUVOIR mission [The LUVOIR Team, 2019].

### 1.3.1 The Shape of an Exoplanet

To first order, an exoplanet is often assumed to be perfectly spherical. This is the assumption that is used in some of the most popular transit light-curve simulation codes such as BATMAN [Kreidberg et al., 2014], which follows the analytic framework of Mandel and Agol [2002] to calculate the effect of a spherical planet transiting in front of a spherical star under the influence of various limb-darkening laws. However, we know from our own solar system that planets need not be perfectly spherical, in the case of of Saturn whose radius has been found to be $\sim 10\%$ larger at its equator relative to its poles. In most cases, the variations imparted on a lightcurve due to a non-spherical planet are typically too small to be observed [Seager and Hui, 2002, Barnes and Fortney, 2003, Carter and Winn, 2010a]. However, it was shown in de Wit et al. [2012] that for planets observed at a high enough Signal to Noise Ratio (SNR), degeneracies between orbital parameters, planetary surface features, and the shape of a planet are degenerate with one another with regards to their observational effect on light curves, particularly during ingress and egress. Thus if we ever hope to be able to one day map the surface of an exoplanet, we must be certain that we understand the effects due every aspect that may alter a lightcurve.

A brief derivation of the surface of a planet provides us insight to the forces at play. The total surface potential of a planet is comprised of two components. Firstly, a gravitational term

$$V_{grav}(r,\psi) = -\frac{GM_p}{r}\left[1 - \sum_{n=2}^{\infty} J_n \left(\frac{R_{eq}}{r}\right)^n P_2(cos\psi)\right] \tag{1.10}$$

where $J_n$ are the spherical mass moment associated with rotation[3] , $\psi$ is the latitudinal angle along the planet's surface, $R_{eq}$ is the equatorial radius of the planet, and $P_n$ is the Legendre polynomial of degree n. The other piece of the potential is the rotational component:

$$V_c(r,\psi) = \frac{1}{3}\Omega^2 r^2 \left[P_2(cos\psi) - 1\right)] \tag{1.11}$$

[3] $\mathrm{J}_n = \frac{1}{M_p R_{eq}^n} \int_0^{R_{eq}} \int_{-1}^{+1} r^n P_n(\mu)\rho(r,\mu) 2\pi r^2 d\mu dr$

where $\Omega = 2\pi/P$ is the rotational angular frequency of the planet. A common assumption is that the $J_2$ term dominates the potential, which allows us to write the total potential as

$$V_{tot} = -\frac{GM_p}{r} + \left(\frac{GM_p R_{eq}^2}{r^3} J_2 + \frac{1}{3}\Omega^2 r^2\right) P_2(cos\psi) - \frac{1}{3}\Omega^2 r^2 \tag{1.12}$$

Finally, we can use the fact that the surface of an exoplanet must lie on a surface of equipotential in order to be stable, which can be expressed as $V_{tot}(R_{eq}, \pi/2) = V_{tot}(R_{pol}, 0)$, which can be solved to leading order to arrive at a final expression relating the polar ($R_{pol}$ and equatorial radii ($R_{eq}$):

$$\frac{R_{eq} - R_{pol}}{R_{eq}} = \frac{3}{2} J_2 + \frac{1}{2}\frac{\Omega^2 R_{eq}^3}{GM_p} \tag{1.13}$$

A derivation of the previous equations can be found in Murray and Dermott [1999], Hubbard [1984]. This relationship allow us to tie directly observable properties of an exoplanet (namely its equatorial and polar radii) to it's mass, size, and of greater interest the distribution of mass throughout its interior, based on the value of the $J_2$ parameter. While it has been possible for many years to determine bulk properties of a planet like its mass and radius, describing a planet with higher order features such as its internal structure remains an important goal in characterising the multitude of planets which exist in the universe.

### 1.3.2 Non-Homogeneity of Stars

A guiding tenet in the field of exoplanet astronomy is "know thy star, know thy planet". In most cases, in a planet-star system it is the star which will contribute a significant portion of any observed signal. The first step in almost any analysis of an exoplanet is the removal of this dominating signal, be it normalizing a lightcurve in order to quantify relative changes in flux due to a planet, or subtracting a stellar spectrum in order to study the emission from an exoplanet atmosphere [Seager and Sasselov, 2000].

A first example of the complexity of stellar surfaces which must be considered

when analysing in particular the lightcurve of a transiting planet is the limb-darkening effect, in which the surface of a star appears dimmer towards its edges. A typical limb darkening law can be written as a polynomial equation of the form

$$\frac{I(\mu)}{I_0} = 1 - u1\,(1-\mu) - u2\,(1-\mu)^2 \tag{1.14}$$

where here we have stopped after a quadratic term [Kopal, 1950]. In this expression, $\mu$ is the cosine of the angle between the normal to the stellar surface and the observers line of sight, and $I_0$ is the intensity at the center of the star. Many more limb darkening laws exist, including higher order polynomials as well as logarithmic expressions. The effect of limb darkening is to alter the shape of ingress and egress of a transit. Given that many features, such as variation in shape, also express themselves through ingress and egress of a transit, it is imperative to have proper grasp of limb darkening profiles, which vary with temperature and stellar type.

Limb darkening represents but the simplest form of stellar non-homogeneity, and one which is very well understood [Claret, 2000]. More complicated variations include features such as star spots and stellar flares, which can vary on a range of timescales and introduce a host of degeneracies and biases into an analysis of an exoplanet [Ioannidis, P. et al., 2016, Rackham et al., 2018], or even mimic the signal of a transiting exoplanet [Dittmann et al., 2009]. Furthermore, in the era of high precision stellar spectra provided by current and upcoming space based instruments such as JWST, it has been found that discrepancies between physical models used to simulate stellar spectra pose as a potential bottleneck when attempting to reach the photon-noise limited regime. [Rackham and de Wit, 2023]

## 1.4 Outline of Thesis

This thesis is organized into three main parts (following this introduction). Part 2 (chapters 2-4) focuses on the detailed analysis and characterisation of multi-planet systems, focusing on the bright star HIP41378 which has five known transiting planets, with tentative evidence for a sixth planet. I analyse the system using archival *Kepler*,

*K2*, and *Spitzer* data, as well as observations from a *Spitzer* proposal for which I was the Principle Investigator. I additionally highlight work I contributed towards the analysis of the multi-planet systems GJ 9827 and HIP 106315.

In part 3, comprising chapters 5-7, I focus on the methodology of analysing planets in the context of them being three-dimensional objects which are potentially not perfectly spherical. I analyse the observable outcomes of two effects, rotation-induced oblateness and tidal distortion, and the biases that may be introduced if standard spherical planet models are used to model their transit lightcurves. I also consider these effects in the context of planet populations, where past studies have focused on only the most likely candidates to present such effects. Additionally, I present a study of the TRAPPIST-1 System conducted with the Space Telescope Imaging Spectrograph (STIS) instrument on the Hubble Space Telescope, with the focus to search for extended Hydrogen exospheres around its seven transiting planets.

Finally, in part 4 (chapters 8 & 9) I shift gears and focus on the stars themselves around which exoplanets live. I consider the non-homogeneity of their surfaces, and how features such as temporally and spatially varying spots and opaque disks may interact to produce complex lightcurve signals. In the last chapter, I extend this further by attempting to empirically recover the spectrum of a star and any surface inhomogeneities, using a framework which considers stellar spectra as a linear combination of 'basis curves' generated by spot features. This is done without relying on physical models which may not be accurate enough to extract the maximal amount of information out of high-precision observations, allowing the empirical retrieval of spectral libraries which can be used to accurately measure exoplanet emission spectra.

# Part II

# Architecture and Stability of Multiplanetary Systems

# Chapter 2

# Multi-Instrument Observations of the Five Planet System HIP41378

*The work presented in this chapter originally appeared in the literature as*

David Berardo, Ian J. M. Crossfield, Michael Werner, Erik Petigura, Jessie Christiansen, David R. Ciardi, Courtney Dressing, Benjamin J. Fulton, Varoujan Gorjian, Thomas P. Greene, Kevin Hardegree-Ullman, Stephen R. Kane, John Livingston, Farisa Morales and Joshua E. Schlieder, *The Astronomical Journal, 157, 185, (2019).*

## 2.1 Abstract

We present new observations of the multi-planet system HIP 41378, a bright star (V = 8.9, Ks = 7.7) with five known transiting planets. Previous K2 observations showed multiple transits of two Neptune-sized bodies and single transits of three larger planets (RP = 0.33RJ , 0.47RJ , 0.88RJ ). K2 recently observed the system again in Campaign 18 (C18). We observe one new transit each of two of the larger planets d/f, giving maximal orbital periods of 1114/1084 days, as well as integer divisions of these values down to a lower limit of about 50 days. We use all available photometry to determine the eccentricity distributions of HIP41378 d f, finding that periods $\lesssim$ 300 days require non-zero eccentricity. We check for overlapping orbits of

planets d and f to constrain their mutual periods, finding that short periods (P $<$ 300 days) for planet f are disfavoured. We also observe transits of planets b and c with Spitzer/IRAC, which we combine with the K2 observations to search for transit timing variations (TTVs). We find a linear ephemeris for planet b, but see a significant TTV signal for planet c. The ability to recover the two smaller planets with Spitzer shows that this fascinating system will continue to be detectable with Spitzer, CHEOPS, TESS, and other observatories, allowing us to precisely determine the periods of d and f, characterize the TTVs of planet c, recover the transits of planet e, and further enhance our view of this remarkable dynamical laboratory.

## 2.2 Introduction

Multi-planetary systems are just one of the many exciting discoveries that NASA's *Kepler* and *K2* missions have produced since the spacecraft's launch in 2009. These systems allow us to probe details regarding the formation, stability, and general structure of exoplanets, providing crucial data to motivate theories of exoplanet dynamics e.g. [Becker et al., 2015, Weiss et al., 2018]. Although the *K2* mission is winding down, as we enter the next generation of exoplanet missions (*TESS*, *CHEOPS*, and eventually *JWST* and *ARIEL*), *K2* has proven its usefulness yet again with new observations of the multiplanet 41378 system[1], which it previously observed during Campaign 5 (C5) [Vanderburg et al., 2016].

The initial observation revealed a rich system of two shorter-period planets and three single transit events, which were statistically significant as planets. As is often the case with such systems, additional data were needed to refine the orbital and physical properties of these outer planets and this was recently provided by *K2* during Campaign 18 (C18), which took both long and short cadence observations of HIP 41378. This system is not only one of a handful of known stars hosting five planets, but is also the second brightest such system, with the host star having a V band magnitude of 8.9 and K magnitude of 7.7 - beaten only by the 55 Cancri system

[1]RA: 08h26m27.85s, DEC: +10d04m49.4s

[Fischer et al., 2008] - making it a compelling target for future characterization if the periods of the larger planets can be precisely determined.

In Sec. 2.3 we discuss the various observations and analysis methods we use to further characterize the system. In Sec. 2.4 we provide updated stellar parameters for the host star based on *Gaia* data. Sec. 2.5 discusses the techniques and results of our dynamical study of the system, including eccentricity estimates. Finally in Sec. 2.6 we summarize our results and discuss the potential for future observations.

## 2.3 Photometric Observations and Analysis

Below we describe our time-series photometry analysis of HIP 41378, which includes photometry from *K2* (Sec. 2.3.1), from *Spitzer* (Sec. 4), and a joint analysis of data sets from both telescopes (Sec. 2.3.3).

### 2.3.1 K2

HIP 41378 was originally observed by the *Kepler* space telescope during Campaign 5 of the *K2* mission for approximately 75 days. The system was then observed again during Campaign 18 for approximately 50 days[2,3]. Additionally, since the system was known to host planets, short cadence (1 minute) photometry was collected during C18[4]. The C5 data spans from $\mathrm{BJD}_{TDB} = 2457140.5$ to 2457214.4 and is composed of 3378 frames, corresponding to observations every 30 minutes (with frames removed for thruster firing and other data quality flags). The C18 data spans $\mathrm{BJD}_{TDB} = 2458251.5$ to 2458302.4 and consists of 2195 frames for the long cadence data and 60000 frames for the short cadence data, again with frames removed due to quality issues. Thus there is a gap of approximately 1037 days between the end of C5 and the beginning of C18.

In the analysis that follows we use the fully detrended C5 lightcurve provided by

[2]While there was also partial overlap between the fields of Campaigns 5, 16 and 18, HIP 41378 was not observed in C16.

[3]Long cadence observations proposed for in C18 GO programs 3, 6, 27, 36, 47, 49, 65, 67, 901

[4]Short cadence observations proposed for in C18 GO programs 6,27,36,47

A. Vanderburg [Vanderburg et al., 2016]. The calibrated C18 short and long cadence data are downloaded from MAST as target pixel files. These are then converted into lightcurves by performing simple aperture photometry, using a circular aperture centered on the 'center of light' of each image to measure the stellar flux. The center of light is determined by taking the weighted mean of the flux of each pixel in the image. We then detrend both the long and short cadence lightcurves following the methods outlined in Vanderburg and Johnson [2014]. Low frequency variations in each lightcurve are removed by first masking out points associated with transits, and then fitting a basis spline and dividing out the best fit to produce flattened light curves. Additionally, we trimmed the data to include only points within two transit durations from an expected transit center, to reduce analysis run times (Figure 2-1 shows the full short cadence lightcurve). This is done in order to fit for individual planets without interference from the transit signals of the other planets in the system. This process produces 15 lightcurves, corresponding to three observations times five planets. Before trimming, we also check the lightcurves for signs of planet e, and while there additional transit-like signals in the lightcurve, none of them agree with the depth or duration of the known planets in the system and are likely due to detrending issues.

We derive a best fit lightcurve model by fitting for each planet individually, using the `batman`[5] [Kreidberg, 2015] and `emcee`[6] [Foreman-Mackey et al., 2012] Python packages to perform an MCMC analysis. When calculating lightcurves with `batman`, we divide the lightcurve into 30 minute intervals and then average over 10 points within each interval. This is done to simulate the 30 minute cadence of the K2 data. For 1 minute cadence, it was found that averaging over 1 minute intervals changed the lightcurve at a level well below the scatter of the data, so averaging was not done. We evolve 150 walkers for 20,000 burn-in steps, followed by an additional 20,000 steps which are used to estimate the posterior values of the fitted parameters. These parameters are the center of transit $t_0$, orbital period $p$, scaled planet radius

[5]https://github.com/lkreidberg/batman
[6]http://dfm.io/emcee/current/

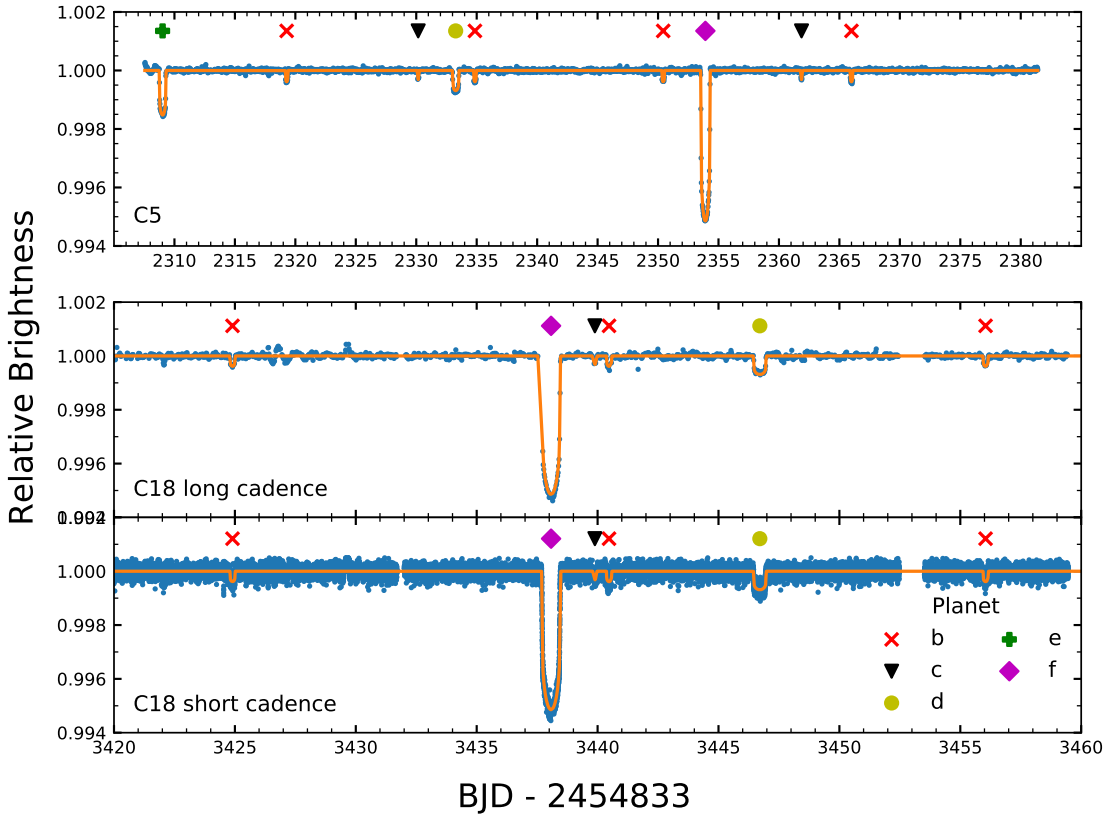


Figure 2-1: Light curves of HIP 41378across all three observation (in blue) with transits of each planet highlighted. The orange line represents the best fit model.

$r_p/r_s$ (where $r_s$ is the radius of the host star), scaled semi-major axis $a/r_s$, orbital inclination $i$, and two limb darkening parameters for a quadratic limb darkening model $q_1, q_2$ [Kipping, 2013]. Additionally, the scatter $\sigma$ of each lightcurve is left as a free parameter during the fit, producing three additional parameters (one for each observation). Thus the likelihood being maximized has the form:

$$\mathrm{Ln}\mathcal{L} = -\frac{1}{2}\sum_i \frac{(\mathrm{flux_i} - \mathrm{model_i})^2}{\sigma_i^2} - 2\mathrm{Ln}(\sigma_i) \tag{2.1}$$

where the index i runs over the three observations, flux is the observed lightcurve, and the model is the calculated lightcurve given a set of orbital parameters [Carter and Winn, 2009]. For all parameters except the limb darkening coefficients, we use

flat priors. We also use a flat prior for the limb darkening coefficients when fitting for planet f. The high signal to noise of planet f produces the tightest constraints on these parameters. For planets b through e, we then use the values of q1 and q2 found for planet f as gaussian priors when running the MCMC. The resulting parameters are given in Table 2.4, where we quote the median value of the MCMC posterior distribution with 68% confidence intervals. The best fit models are shown in Figure 2-1[7], and in Figure 2-2 we show the individual lightcurves for each planet, phase folded on their respective periods. In each case, the posterior value for the scatter is consistent with the out of transit standard deviation of the lightcurves.

### 2.3.2 Spitzer

We also observed HIP 41378 using the $4.5\mu m$ channel on Spitzer's IRAC camera as part of observing programs 11026 centered on BJD_UTC 2457606.932 and 13052 centered on BJD_UTC 2457790.680 (PI Werner). The first observation coincides with an expected transit of HIP41378 c while the second corresponds to an expected transit of HIP41378 b.

We downloaded data from the *Spitzer* Heritage Archive[8] and processed it into lightcurves as follows. First, we used a median filter with a span of 10 frames to remove anomalous pixels (flux values $> 4\sigma$ from the median) due to cosmic rays and other effects. The centroid of each frame is then calculated in two ways, once by fitting a two dimensional Gaussian brightness profile, and again by calculating the center of light:

$$x_c = \frac{\sum_i f_i x_i}{\sum f_i}, y_c = \frac{\sum_i f_i y_i}{\sum f_i} \tag{2.2}$$

where $f_i$ is the flux of the i$^{th}$ column and $x_i$ is the x-position for of the i$^{th}$ column (similarly for $y$ and the rows). For each frame, we also calculated the background level by taking the flux in a 10×10 square in each corner of the image, fitting a Gaussian to the distribution of flux values, and taking the mean of the Gaussian to be the

[7]For planets d and f we show the fit results assuming the maximal period, although other periods are possible as discussed in Sec. 2.5

[8]http://sha.ipac.caltech.edu/applications/Spitzer/SHA/

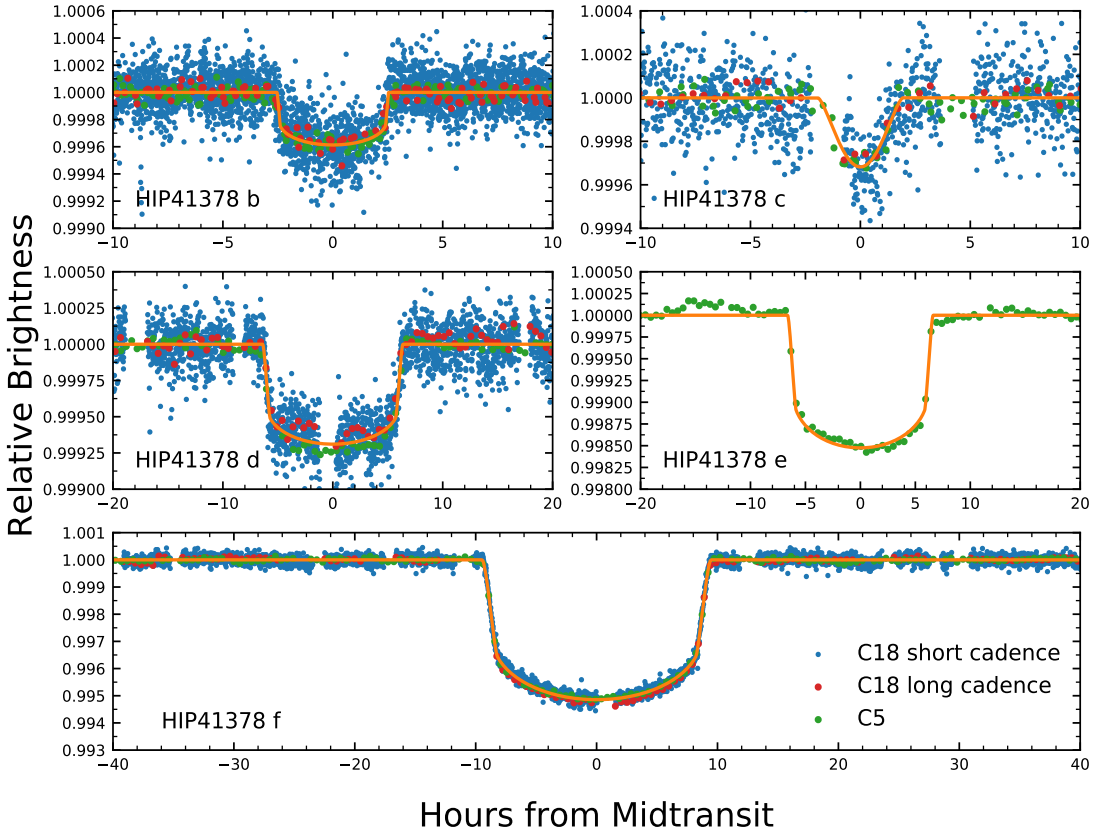


Figure 2-2: Transits of all five planets of HIP 41378, showing *K2* data from C5 (green points) and C18 short and long cadence (blue and red points), along with our best-fit transit models (solid orange line). Planet e was not observed to transit during C18, and so we only show C5 data for it.

background level.

Light curves are then computed by summing up the flux in a circular aperture around the centroid and subtracting the appropriate amount of background flux, using the `photutils` [Bradley et al., 2018] python package to account for partial pixels. We do this for apertures whose radii span from 1.8 to 3.4 pixels in 0.2 pixel increments, producing lightcurves for each combination of centroid method and aperture radius. For each of these, we determine a best fit systematics model using the Pixel Level Decorrelation (PLD) technique [Deming et al., 2015]. This method attempts to correct

for the varying response of the pixels as the centroid moves around the CCD. Despite centroid motions of only about a tenth of a pixel, the magnitude of the intrapixel sensitivity, combined with the shallow depths of the transits (100's of ppm) requires detrending of this effect in order to recover the transits.

We model the total flux as

$$S = \sum_i c_i f_i + DE(t) + ht + gt^2 \tag{2.3}$$

where D is the transit depth, E(t) is the transit model, $f_i$ is the flux of the i'th pixel, $c_i$ are coefficients correcting for the varying response of the pixels, and h and g are parameters used to model a quadratic time ramp. We perform a $\chi^2$ minimization for each lightcurve to determine the best fit parameters, and use the quality of the fits to determine which lightcurve to ultimately use. This is done by binning the residuals of the fit, plotting the standard deviation versus bin factor, and choosing the one which has the closest slope to -0.5 (in log space), indicating the lowest amount of correlated noise. In addition to choosing the best lightcurve, we also bin down the data and see what effect this has on the results as well. This procedure ends up selecting a 2D-Gaussian fit for centroiding, an aperture radius of 2.4 pixels, and a bin size of 200 points per bin.

Once we have chosen the best lightcurve for each observation, as for the *K2* data we run an MCMC chain in order to obtain posterior probability distributions and determine the errors for each parameter. The values being fit during the MCMC are the PLD pixel coefficients, the two time ramp parameters, the center of transit, the transit depth, as well as the orbital inclination and semi-major axis. The best fit transit signals are shown in Figure 2-3 and the values are listed in Table 2.5.

We also performed analyses with two independent implementations of PLD, fitting the *Spitzer* data by itself (Hardegree-Ullman et al., in preparation) and also simultaneously with the *K2* data (Livingston et al., in review), and the resulting parameter estimates were consistent. We find that for both planets, the values of semi-major axis and depth are consistent within the quoted errors between the *Spitzer* and *K2*

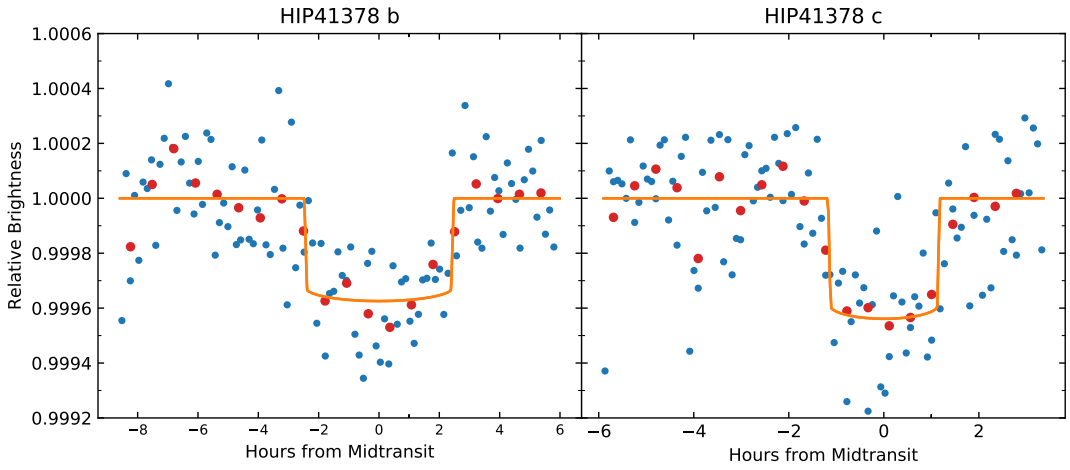


Figure 2-3: *Spitzer* photometry of HIP 41378b (left) and c (right). Blue dots show the (binned) photometry after removing systematic effects, red dots show the photometry binned by an additional factor of five, and the solid orange line shows the best fit transit models.

values.

### 2.3.3 Joint K2+Spitzer Analysis

Combining the *K2* and *Spitzer* observations provides a total of 8 transits of HIP41378 b and 4 transit of HIP41378 c, which allows us to check for transit timing variations (TTVs) that could indicate the presence of other non-transiting bodies and/or constrain the planets' masses. For both planets b and c, we keep fixed all of the best-fit parameters described in Sec. 2.3.1 and re-fit each transit individually across the C5, C18 short cadence, and *Spitzer* data, allowing only the transit center to vary. For each planet we then fit a linear ephemeris to their epochs and observed transit times (taking into account their relative uncertainties), and plot the difference between the observed and calculated values in Figure 2-4 (these values are also listed in Tables 2.6 and 2.7). For planet b we discard the last observation, where we find a large offset in the transit center which we attribute to our detrending of the short cadence C18 data. We feel comfortable discarding this point since we have two other transits of planet b during C18 to establish a long baseline with previous observations.

For HIP41378 b we find results consistent with a linear ephemeris. For HIP41378 c, we find that the the transit times are inconsistent with a linear ephemeris. While the systematic effects of the *Spitzer* observation make it difficult to obtain precise orbital parameters, as mentioned in Sec. 4 we have two external independent analyses of the observations which both produce similar TTV signals. We note while the C5 and *Spitzer* observations are broadly consistent with a linear ephemeris, although they predict that the transit of HIP41378 c in C18 should be $\sim 3$ hours from where it is currently measured. Despite larger scatter in the C18 data than the C5 data, we do not believe that the transit center would shift by that amount. Additional transits are required to confirm the TTV signal seen here (see Figure 2-4 and Sec. 2.6.1).

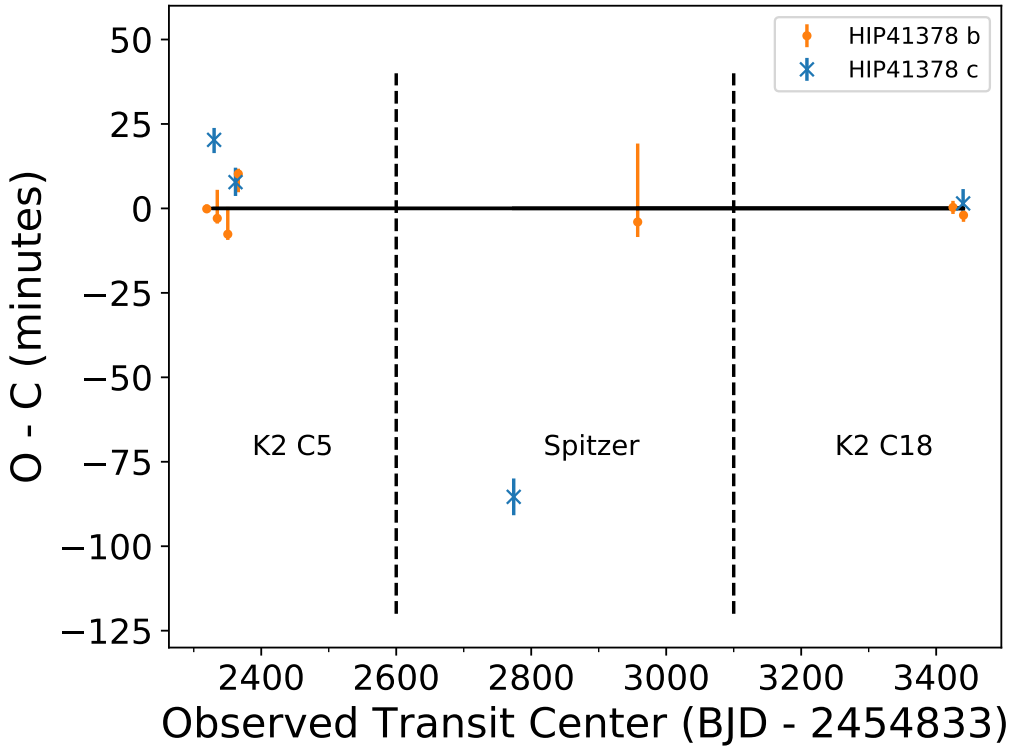


Figure 2-4: Transit timing variations plot for HIP41378 b and c. Here we show the deviation from a linear ephemeris as a function of measured transit center for the two inner short period planets of the system. The dashed lines separate the three observations.

## 2.4 Stellar Parameters

We derive an updated set of stellar parameters for HIP 41378 for use in our subsequent analysis. Vanderburg et al. [2016] report $T_{\rm eff} = 6199 \pm 50$ K using spectroscopic techniques. We infer $T_{\rm eff} = 6283 \pm 43$ by comparing the $B-V$, $V-K_s$, and $J-H$ colors to Table 5 of Pecaut and Mamajek [2013] and taking a weighted mean of the individual values from each color. We use the weighted mean of these two independent temperatures, along with the Gaia DR2 parallax [Gaia Collaboration et al., 2016, 2018] and the apparent stellar magnitudes in $Ks$ and $W1$, as input parameters for the `isochrones` package [Morton, 2015] with the MIST tracks [Choi et al., 2016]. The computed parameters are $T_{\rm eff} = 6226 \pm 43$ K, $R_* = 1.375 \pm 0.021$ $R_\odot$, $M_* = 1.168 \pm 0.072$ $M_\odot$, and $d = 106.58 \pm 0.65$ pc. None of these (except $R_*$) change by more than $1.5\sigma$ if we instead use the parallax with the magnitudes in $V$, $B$, $J$, $H$, $K_s$, $W1$, and $W2$. In this second analysis we find $R_* = 1.310 \pm 0.016$ $R_\odot$, so we take the mean and report an uncertainty that covers both values. Thus our final stellar radius is $1.343 \pm 0.032$ $R_\odot$. Our updated stellar parameters are listed in Table 2.1; all are consistent with (but more precise than) those of Vanderburg et al. [2016].

We also derive stellar parameters using a high-resolution optical spectrum taken from Keck/HIRES, following the approach of Fulton and Petigura [2018] . This spectrum implies $T_{\rm eff} = 6266 \pm 100$, $R_* = 1.33 \pm 0.013$ $R_\odot$, $M_* = 1.17 \pm 0.030$ $M_\odot$, consistent with our analysis above.

Finally, we observe solar-like oscillations in the C18 short cadence data. These could further refine the stellar parameters, but we defer that analysis for a subsequent paper.

## 2.5 Dynamics

We used the transits of HIP 41378 f and HIP 41378 d to constrain each planet's orbital eccentricity by applying the "photoeccentric" formalism of Dawson and Johnson [2012], using the same software and approach as described by Schlieder et al. [2016].

Table 2.1: Updated HIP 41378 Parameters

| Parameter | Units | Value | Comment |
|---|---|---|---|
| $\varpi$ | mas | $9.3799 \pm 0.059$ | Gaia Collaboration et al. |
| $R_*$ | $R_\odot$ | $1.343 \pm 0.032$ | This work, Sec. 2.4 |
| $M_*$ | $M_\odot$ | $1.168 \pm 0.072$ | This work, Sec. 2.4 |
| $\rho_*$ | g cm$^{-3}$ | $0.680 \pm 0.064$ | This work, Sec. 2.4 |
| $T_{eff}$ | K | $6226 \pm 43$ | This work, Sec. 2.4 |

This technique uses knowledge of the true stellar density $\rho_\star$ (calculated using our parameters in Sec 2.4), combined with the derived stellar density from a fit assuming zero eccentricity $\rho_{\star,circ}$,

$$\rho_{\star,circ} = \frac{3\pi(a/r_s)^3}{GP^2} \tag{2.4}$$

in order to estimate the eccentricity of the orbit, where $a/r_s$ is the scaled semi-major axis and $P$ is the orbital period.

Since the two transits of HIP41378 d/f have a gap of $\sim$ 1000 days between them, there is a range of allowed periods that would produce the observed signals. The maximal possible period for the two planets, given by the delay between the observed transits, is 1114 days for planet d and 1084 days for planet f. The minimum possible periods are 48 days for planet d and 46 for planet f (shorter periods would have produced additional transits in either C5 or C18). Any fractional value of the longest period is also valid, and so this gives a range of 23 possible periods for both planets, for each of which we perform a photoeccentric analysis[9]. We show the results of the five longest (and most plausible, as described below) periods for each planet in Tables 2.3 & 2.2, listing the maximum-likelihood values and 15.8% and 84.2% confidence intervals for all parameters. In addition to $e$ and $\omega$, we include the photoeccentric parameter $g$,

$$g(e,\omega) = \frac{1 + e\sin\omega}{\sqrt{1-e^2}} = \left(\frac{\rho_{*,circ}}{\rho_*}\right)^{1/3} \tag{2.5}$$

See Fig. 2 of Dawson et al. [2016] for the allowed relationships between $e$ and $\omega$ for

[9]None of the allowed periods predict transits of planet d or f during our *Spitzer* observations.

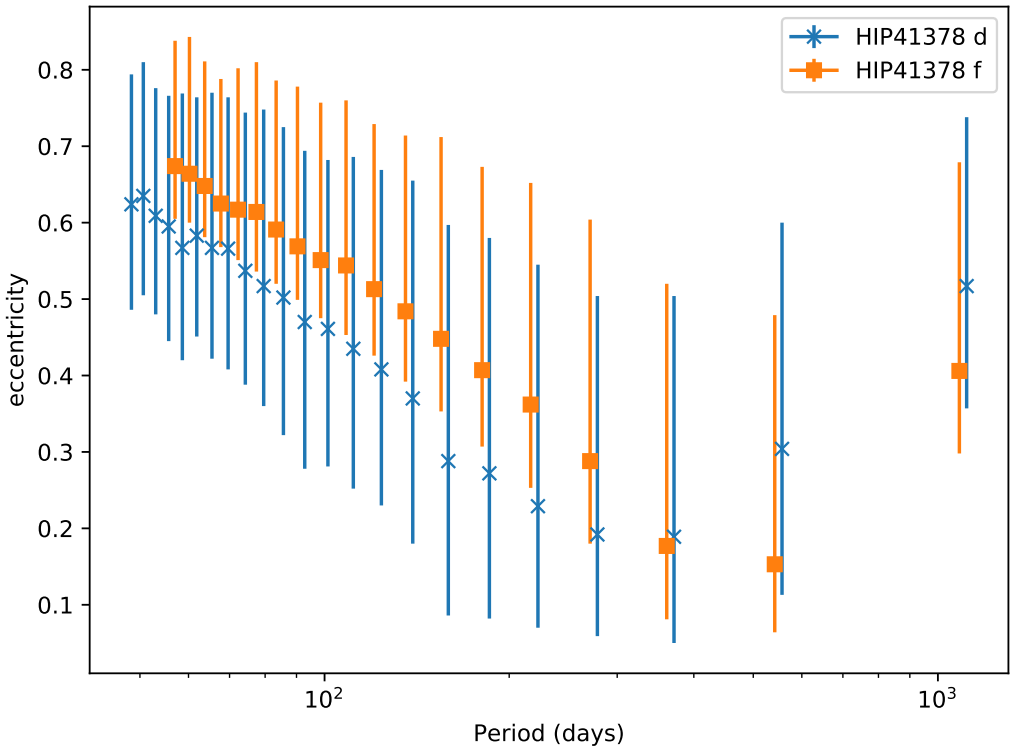


Figure 2-5: Possible eccentricities of HIP 41378d (blue) and f (orange) from our photoeccentric analyses. We see a similar decreasing trend in eccentricity for both planets, indicating that lower eccentricities are consistent with longer periods.

various values of $g$. For $\rho_*$, the stellar density, we use the value in Table 2.1. For $\rho_{*,circ}$, the density inferred solely from the transit light curve assuming a circular orbit [Seager and Mallén-Ornelas, 2003], we take the posteriors computed directly from our MCMC analyses.

For both HIP 41378f and HIP 41378d, we find that $g$, $e$, and $e\sin\omega$ have fairly well-determined values. In contrast, the parameter $\omega$ and combination $e\cos\omega$ are only poorly constrained and so are not listed. Notable is that most possible periods are consistent with non-zero eccentricity at the $> 2\sigma$, and even the lowest possible eccentricity is $1\sigma$ $>$ than e $= 0$, indicating that both planets are most likely on eccentric orbits (see Figure 2-5) .

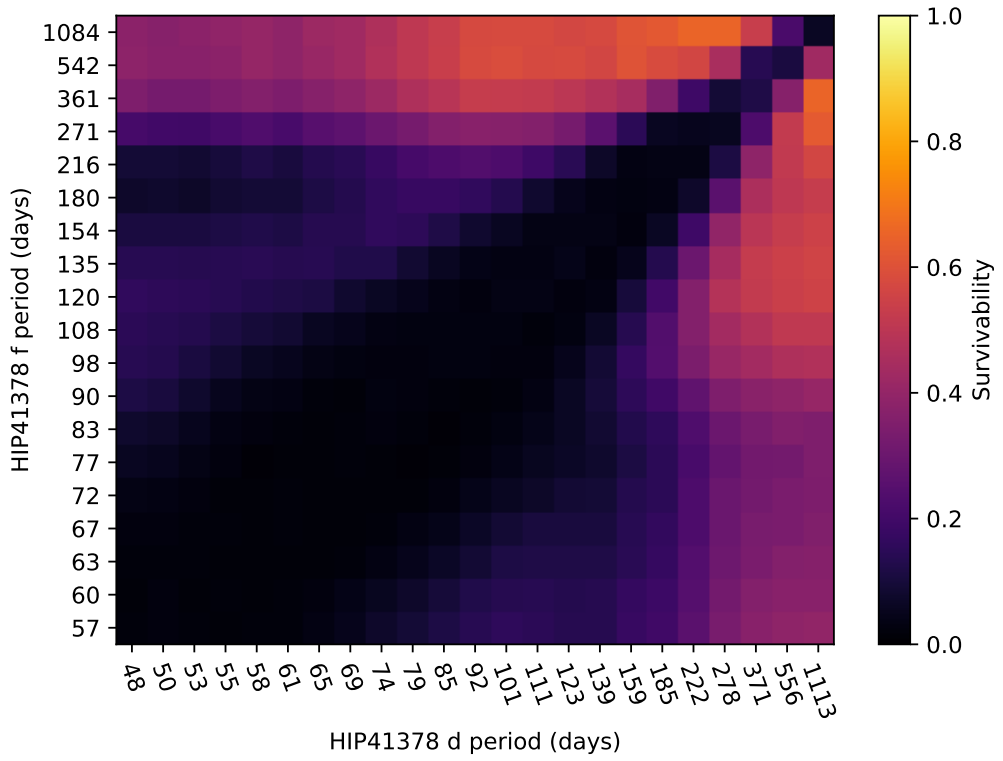


Figure 2-6: System stability of the HIP 41378 system for all possible periods of planets d and f (see Sec. 2.5.1). It is unlikely that both planets have short periods ( $P \lesssim 300$ days), because then their orbits must be highly eccentric and they would interact with planet c. Similarly, these two outer planets will be unstable if they both have similar periods. We therefore find that one planet having a long period and the other having a shorter period is the most likely scenario.

Table 2.2: Photoeccentric Analysis for HIP41378 d

| Period | $g(e,\omega)$ | $e$ | $e\sin\omega$ |
|---|---|---|---|
| 1114 | $1.47^{+0.229}_{-0.138}$ | $0.517^{+0.221}_{-0.16}$ | $0.262^{+0.136}_{-0.242}$ |
| 557 | $1.154^{+0.171}_{-0.113}$ | $0.304^{+0.296}_{-0.191}$ | $0.07^{+0.135}_{-0.139}$ |
| 371 | $1.022^{+0.135}_{-0.072}$ | $0.189^{+0.315}_{-0.139}$ | $-0.008^{+0.102}_{-0.128}$ |
| 278 | $0.974^{+0.095}_{-0.096}$ | $0.192^{+0.312}_{-0.133}$ | $-0.066^{+0.099}_{-0.149}$ |
| 222 | $0.936^{+0.106}_{-0.111}$ | $0.229^{+0.316}_{-0.159}$ | $-0.115^{+0.128}_{-0.171}$ |

### 2.5.1 Orbital Overlap

By using the results of the photoeccentric analysis, we perform a first-order stability analysis by calculating the possible orbits of planets d and f and excluding combi-

Table 2.3: Photoeccentric Analysis for HIP41378 f

| Period | $g(e,\omega)$ | $e$ | $e\sin\omega$ |
|---|---|---|---|
| 1084 | $1.337^{+0.031}_{-0.03}$ | $0.406^{+0.273}_{-0.108}$ | $0.217^{+0.061}_{-0.236}$ |
| 542 | $1.059^{+0.026}_{-0.024}$ | $0.153^{+0.326}_{-0.089}$ | $0.035^{+0.031}_{-0.104}$ |
| 361 | $0.931^{+0.023}_{-0.022}$ | $0.177^{+0.343}_{-0.096}$ | $-0.095^{+0.036}_{-0.11}$ |
| 271 | $0.844^{+0.02}_{-0.019}$ | $0.288^{+0.316}_{-0.108}$ | $-0.2^{+0.039}_{-0.126}$ |
| 216 | $0.784^{+0.019}_{-0.017}$ | $0.362^{+0.29}_{-0.109}$ | $-0.274^{+0.04}_{-0.13}$ |

nations of parameters where the planets' come within 3.5 mutual Hill radii of one another [Kane et al., 2016], with the mutual Hill radius of two objects given by

$$r_H = 0.5(a_1 + a_2)[(m_1 + m_2)/M]^{1/3} \tag{2.6}$$

where we take $M$ to be the mass of the host star (Table 2.1) and $m_1$ / $a_1$ and $m_2$ / $a_2$ are the masses / semi-major axes of planets d and f. Since the masses of planets d and f are unknown, we conservatively choose the smallest reasonable masses. We use the publicly available `Forecaster` code [Chen and Kipping, 2017] to estimate the probabilistic masses of the two planets given their radii ($r = 0.33R_J, 0.88R_J$ for planets d and f respectively). We then take the values one sigma below the median masses as our conservative mass estimate for the planets. We find masses of 0.02 $M_J$ & 0.2 $M_J$ for planets d and f, which results in a value of $r_H/(a_1 + a_2)$ of $\sim 3\%$.

Since the eccentricity and semi-major axis span a wide range of values, we draw samples from the posterior distributions obtained from the MCMC fits discussed in Sec 2.3.1 and in our photoeccentric analysis. Since there are 20 possible periods for planet f and 23 for d, we run an MCMC analysis for each possible period, and perform a stability check for each pair of $20 * 23$ periods. In this way, we calculate the likelihood for the two planets to have orbits with overlapping Hill spheres. In addition to checking for Hill sphere crossings, we also demand that any given orbit of HIP41378 f and d does not overlap with the orbit of HIP 41378 c, which has a well-defined period and semi-major axis.

An important point is that in the analysis above we do not consider the effects of the fifth planet HIP41378 e. Due to only observing a single transit, we are not able

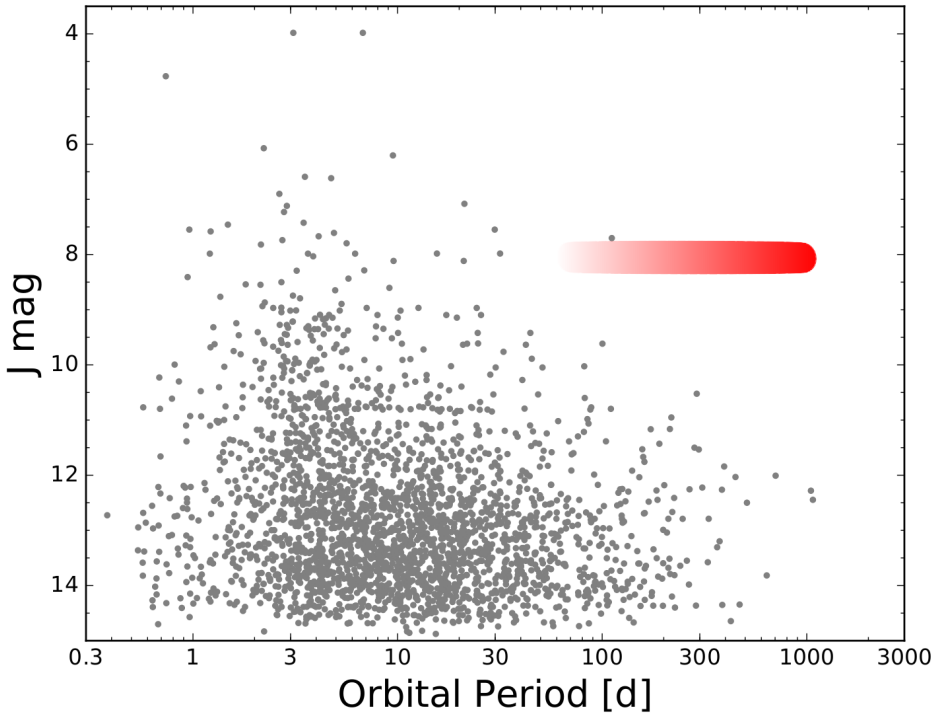


Figure 2-7: HIP 41378d and f in context: orbital period vs. $J$ mag for all known transiting planets. The shaded red lozenge approximately indicates HIP 41378d and f — whatever the orbital periods of these planets, this system is several magnitudes brighter than any comparable systems.

to constrain its period or semi-major axis and so elect to disregard any effects it may have on the system.

We show the results of this analysis in Figure 2-6, with darker colors indicating higher probability of overlap. At low periods (p $\lesssim$ 300 days) there is a higher chance of overlap than long periods. This is likely due to the fact that at low periods, the photoeccentric analysis predicts increasing eccentricities, shown in Figure 2-5, making it much more likely that the orbits will overlap with either each other or with planet c. Additionally, the dark diagonal indicates that similar periods for f and d are highly disfavored.

In the most favored scenario (i.e. the one with the highest relative survivability), HIP41378 d has $p = 1114$ days and HIP41378 f has $p = 361$ or 542 days; Fig. 2-5

shows that this scenario also corresponds to the lowest eccentricities for these two planets.

## 2.6 Discussion

We analyze new transits of four out of the five planets in the HIP41378 system using *K2* data, two of which previously only had a single observed transit. We study the possible periods of the two planets, and also employ a photoeccentric analysis to study their eccentricity distributions. We find that the eccentricity of the planets increases with decreasing period, however this implies that their orbits will overlap and so disfavors short periods.

We also observe one additional transit each of planets b and c using *Spitzer* IRAC, providing a sufficient baseline to check for TTVs. For HIP41378 b we find all observations consistent with a linear ephemeris ($t_0 = 2457152.281 \pm 0.015$ BJD & p = $15.572119 \pm 0.000022$ days). For HIP41378 c the *Spitzer* photometry, which occurs roughly at the midpoint between the *K2* campaigns, implies a transit deviation on the order of 50 - 100 minutes. Our *Spitzer* analysis is consistent with two independent, external analyses performed on the same data set.

### 2.6.1 Follow-up Opportunities

For HIP41378 f, it might seem that such a long-period planet around such a bright star would be an attractive target for high-contrast characterization. Unfortunately, the system lies 106 pc away and so even a 1084 d (2.2 AU) orbit places HIP 41378f just 20 mas from its host star. Assuming a Jupiter-like geometric albedo of 0.35 and a Lambertian phase function, the most favorable planet/star contrasts define a locus from $6 \times 10^{-8}$ at 6 mas (for a 217 d period), to $7 \times 10^{-9}$ at 18 mas (for $P = 1084$ d). These values appear to lie just beyond the regime accessible to proposed high-contrast instruments on the next generation of ground-based telescopes [Macintosh et al., 2006, Beuzit et al., 2006, Crossfield, 2016]. Nonetheless, that the planets could come so close to detection bodes well for high-contrast characterization of long-period planets

around nearby stars discovered via single transits in *TESS* photometry [Villanueva et al., 2018]. Additionally, we find that JWST transmission spectroscopy of the planets is possible at a S/N of $8-10$ for a cloud-free H2-dominated atmospheres if the systematic noise can be kept extremely low ($\sim$ 5 ppm). While this seems like a strict requirement, it is nonetheless interesting to note that such measurements may be feasible for any or all of the larger planets in the system, if their periods can be properly constrained.

The two outer planets d and f also fall into a less-widely appreciated class of planets, transiting giants on ultra-long periods (T-GULPs). T-GULPs are those planets with the longest orbital periods, orbiting at the widest separations, and consequently having the lowest known equilibrium temperatures of any known transiting planet. Figure 2-7 lists the known T-GULPs (see also table 7 of Beichman et al. [2018] for a list of the properties of their properties). Interestingly, few other T-GULPs are known to be in multi-planet systems, and no others orbit stars as bright as HIP 41378 ($V = 9$ mag). Whatever their true periods, HIP 41378d and f (together with their sibling planets) form an exceptional system that will be studied for many years to come.

The sample of T-GULPs will likely grow only slowly in the years to come, since *TESS* and other future transit missions will not observe any single field of view nearly as long as *Kepler*. Only through the extraordinary endurance of *K2* was this observatory able to redetect the transits of HIP 41378d and f. *TESS* will find a few longer-period planets in its continuous viewing zones [e.g., Sullivan et al., 2015], but only through an extended mission can the population of truly long-period T-GULPS be substantially expanded.

Because the typical T-GULP has only a few transits observed, the effects of additional perturbing bodies or simple ephemeris drift could eventually result in many of these rare specimens being lost. The situation is even more complicated for HIP 41378d and f, since only a finite range of possible periods are known. Such long-duration transits (13 hours for planet d and 19 hours for planet f) are challenging to observe from the ground (though it can be done e.g., Shporer et al. [2010]). In

Table 2.4: K2 Fit Parameters

| Planet name | $T_0^1$ | Period[2] | $a/r_s$ | Inc.[3] | $r_p/r_s$ | q1 | q2 |
|---|---|---|---|---|---|---|---|
| HIP41378 b | $2319.2818^{+0.0012}_{-0.0012}$ | $15.572098^{+0.000018}_{-0.000019}$ | $21^{+2}_{-5}$ | $88.8^{+0.8}_{-1.4}$ | $0.01843^{+0.0011}_{-0.00037}$ | $0.463^{+0.015}_{-0.016}$ | $0.064^{+0.028}_{-0.028}$ |
| HIP41378 c | $2330.1609^{+0.0023}_{-0.0027}$ | $31.70648^{+0.00024}_{-0.00019}$ | $22^{+57}_{-7}$ | $87.5^{+2.2}_{-1.4}$ | $0.0200^{+0.018}_{-0.0037}$ | $0.456^{+0.017}_{-0.016}$ | $0.050^{+0.030}_{-0.027}$ |
| HIP41378 d | $2333.2604^{+0.0017}_{-0.0017}$ | $1113.4491^{+0.0018}_{-0.0018}$ | $533^{+81}_{-56}$ | $89.930^{+0.025}_{-0.018}$ | $0.02560^{+0.0005}_{-0.0007}$ | $0.444^{+0.015}_{-0.014}$ | $0.028^{+0.022}_{-0.018}$ |
| HIP41378 e | $2309.0194^{+0.001}_{-0.001}$ | - | $283^{+172}_{-177}$ | $89.910^{+0.22}_{-0.045}$ | $0.03686^{+0.0011}_{-0.0008}$ | $0.451^{+0.015}_{-0.015}$ | $0.041^{+0.026}_{-0.024}$ |
| HIP41378 f | $2353.91423^{+0.00039}_{-0.00038}$ | $1084.16156^{+0.00040}_{-0.00042}$ | $460^{+5}_{-4}$ | $89.98^{+0.009}_{-0.006}$ | $0.06602^{+0.00017}_{-0.00016}$ | $0.455^{+0.015}_{-0.014}$ | $0.044^{+0.029}_{-0.026}$ |

[1] $BJD_{\mathrm{TDB}} - 2454833$
[2] Period in days
[3] Inclination in degrees

Note. - The limb darkening parameters for planets b-e use the posterior values from the fit for planet f as gaussian priors.

contrast, space-based transit photometry is a proven technique for producing high-quality system parameters. We have shown here that *Spitzer* is capable of retrieving transits of the two smaller planets in the system, measuring their transit times to within a few minutes. This implies that it will be easy to observe planets d and f, larger planets with longer transit durations.

By employing a strategic observing strategy (i.e. observing during the fourth longest period to simultaneously check for the eighth and sixteenth longest periods), and using the mutual likelihood plot of the planet periods (figure 2-6, it may be possible to pin down the periods of both HIP41378-d and f with only a few additional measurements.

HIP41378 will also be in the field of view of *TESS* camera 1 in sector 7 (calculated using the Web Tess Viewing tool[10]), from 01-07-2019 to 02-04-2019. This time frame lines up with transits of 6 of the possible periods of planet d (53, 55, 58, 74, 111, and 222 days) and 4 of the possible periods of planet f (57, 60, 77, 120 days). This viewing window also coincides with an expected transit of planet c, allowing us to add an additional point to the TTV analysis separated by $\sim$ 200 days from the previous measurement.

[10] https://heasarc.gsfc.nasa.gov/cgi-bin/tess/webtess/wtv.py

Table 2.5: Spitzer Fit Parameters

| Planet name | $T_0$ [$BJD_{TDB}$] | Transit Depth (ppm) | $r_p/r_s$ | $a/r_s$ | Inclination (deg.) |
|---|---|---|---|---|---|
| HIP41378 b | $2457790.734^{+0.016}_{-0.0035}$ | $374^{+60}_{-65}$ | $0.0194^{+0.0015}_{-0.0016}$ | $22^{+3}_{-7}$ | $89.05^{+0.6}_{-1.3}$ |
| HIP41378 c | $2457606.985^{+0.0036}_{-0.0036}$ | $444^{+92}_{-95}$ | $0.0211^{+0.0022}_{-0.0022}$ | $85^{+14}_{-31}$ | $89.6^{+0.2}_{-0.6}$ |

Table 2.6: Individual Transit Center for HIP41378 b

| Epoch | Observed [$BJD_{TDB} - 2454833$] | Calculated [$BJD_{TDB} - 2454833$] | O - C (min.) | Data Set |
|---|---|---|---|---|
| 0 | $2319.2797^{+0.0008}_{-0.0006}$ | 2319.2798 | $-0.1^{+1.2}_{0.9}$ | *K2* C5 |
| 1 | $2334.8499^{+0.0061}_{-0.001}$ | 2334.8519 | $-2.9^{+8.7}_{1.5}$ | *K2* C5 |
| 2 | $2350.4187^{+0.0055}_{-0.0011}$ | 2350.424 | $-7.7^{+8.0}_{1.6}$ | *K2* C5 |
| 3 | $2366.0033^{+0.001}_{-0.0039}$ | 2365.9962 | $10.3^{+1.5}_{5.6}$ | *K2* C5 |
| 41 | $2957.734^{+0.016}_{-0.003}$ | 2957.737 | $-4.0^{+23.2}_{4.3}$ | *Spitzer* |
| 71 | $3424.90086^{+0.00021}_{-0.00021}$ | 3424.9007 | $0.2^{+0.3}_{0.3}$ | *K2* C18 |
| 72 | $3440.47139^{+0.00021}_{-0.00021}$ | 3440.47282 | $-2.1^{+0.3}_{0.3}$ | *K2* C18 |

Note. - The calculated ephemeris is given by t = 2319.27979 + (15.57213)×E, where E is the epoch of the transit. Errors on the calculated ephemeris are included in the errors of O-C listed above.

Table 2.7: Individual Transit Center for HIP41378 c

| Epoch | Observed [$BJD_{TDB} - 2454833$] | Calculated [$BJD_{TDB} - 2454833$] | O - C (min.) | Data Set |
|---|---|---|---|---|
| 0 | $2330.16576^{+0.00245}_{-0.00272}$ | 2330.15167 | $20.3^{+3.5}_{3.9}$ | *K2* C5 |
| 1 | $2361.86375^{+0.00297}_{-0.00284}$ | 2361.85836 | $7.8^{+4.3}_{4.1}$ | *K2* C5 |
| 14 | $2773.986^{+0.0036}_{-0.0036}$ | 2774.04529 | $-85.4^{+5.2}_{5.2}$ | *Spitzer* |
| 35 | $3439.88676^{+0.0008}_{-0.00074}$ | 3439.8857 | $1.5^{+1.2}_{1.1}$ | *K2* C18 |

Note. - The calculated ephemeris is given by t = 2330.15160 + (31.70669)×E, where E is the epoch of the transit. Errors on the calculated ephemeris are included in the errors of O-C listed above.

# Chapter 3

# Spitzer Follow up to Confirm Transit Timing Variations

*This chapter refers to observations taken with the Spitzer Space Telescope, arising from a proposal for Director's Discretionary Time (DDT) on which I was the Principle Investigator (program 14215 DDT)*

In light of the new insights provided by the joint analysis of observations from *Kepler*, *K2*, and *Spitzer*, it was determined that additional follow up with *Spitzer* would be an ideal opportunity to further characterise the dynamics of this multi-planet system orbiting one of the brightest stars hosting long period planets. The goal of the observations was twofold: (1) obtain additional transits of planet c, in order to refine its transit timing measurement, and (2) search for an additional transit of planet d to either rule out or confirm possible values of its orbital period.

## 3.1 The TTV Signal of planet HIP41378 c

Based on the work described in the previous chapter, it was found that HIP41378 c displayed transit variations (TTVS) in the range of 20-100 minutes, the strongest evidence for which was provided by a previous observation made of the system with the IRAC instrument on *Spitzer*. TTVS are commonly modelled as sinusoidal variations

[Lithwick et al., 2012], which allows the extraction of further constraints on planetary properties (mass, orbital elements, etc.) than can be obtained from transits alone; however, the HIP41378 system did not at the time have enough data to robustly identify any individual TTV model. In figure 3-1 we show the range of possible sinusoids which could fit the current TTV data for planet c, extrapolated out to the two Spitzer windows requested in our proposal, as well as a 27 day window during which TESS would observe the system. We note however that a single measurement based on a TESS observation would still be degenerate with several potential TTV signals. While just the first Spitzer visit alone offered the chance to characterize the TTV signal, there was still opportunity for strong degeneracy between different models, and so it was determined that two visits would be ideal to help uniquely constrain the TTV characteristics of HIP41378 c.

In the case that the TTV signal turned out to be nearly sinusoidal, which would occur if the perturbation was due to a single other planet, we could then extract the "superperiod" of planet c (the period on which the TTV amplitude varies), which would in turn uniquely determine the period of the perturbing planet [Lithwick et al., 2012]. From the previous data sets there is enough information to determine that the period of planet b, the nearest planet in the system, is incompatible with the TTV variations already seen for planet c. With these new measurements, we hoped to gain enough insight in order to determine which of the known planets is causing the perturbations to transit of planet c, or if indeed they are due to a sixth planet which does not transit and thus hasn't been observed.

## 3.2 Constraining the Period of HIP41378 d

In addition to the TTV signal of planet c, two of the single transiting planets in the system (d and f), were seen to transit again during the campaign 18 K2 observations. The spacing between these two observations ($\sim$ 1000 days) provides an upper limit on their orbital periods, as well as narrowing them down to integer divisions of these maximal periods. Furthermore, the length of the longest observation ($\sim$ 80 days from

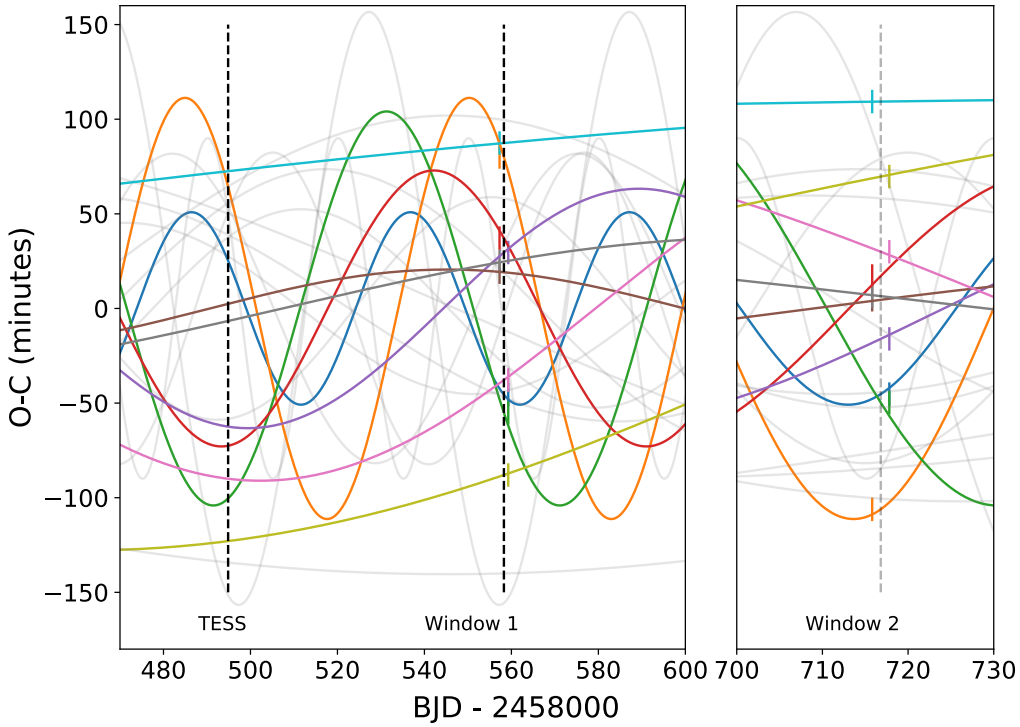


Figure 3-1: The different sinusoids that fit the TTV data for planet c from previous observations. Here we show them projected forward into the TESS viewing window as well as the two requested Spitzer DDT windows. The coloured curves show a representative sample of all possible sinusoids, while the gray curves show the remaining ones. Errorbars during the Spitzer transits indicate the uncertainty on the transit center previously measured for Spitzer observations of planet c.

the original campaign 5 observation) provides a lower bound on their orbital periods. The depth of planet f is large enough that ground follow-up was a feasible opportunity to determine its orbital period. However planet d with a transit depth of ∼750 ppm is too small to be detectable from the ground with current instruments.

It was determined that there was a unique window of opportunity during which both planet c and d would transit, if planet d were to have an orbital period of 56, 70, 92, 140, or 142 days. This allowed the opportunity to either confirm a quarter of the possible orbital periods of d, or rule out 75% of them. Given the duration of the transit of planet d (∼ 12 hours), a full observation of both transits, allowing for TTV variations for planet c, would have been well over 24 hours for just the first visit. However, since the transit center of planet d is known with minute precision,

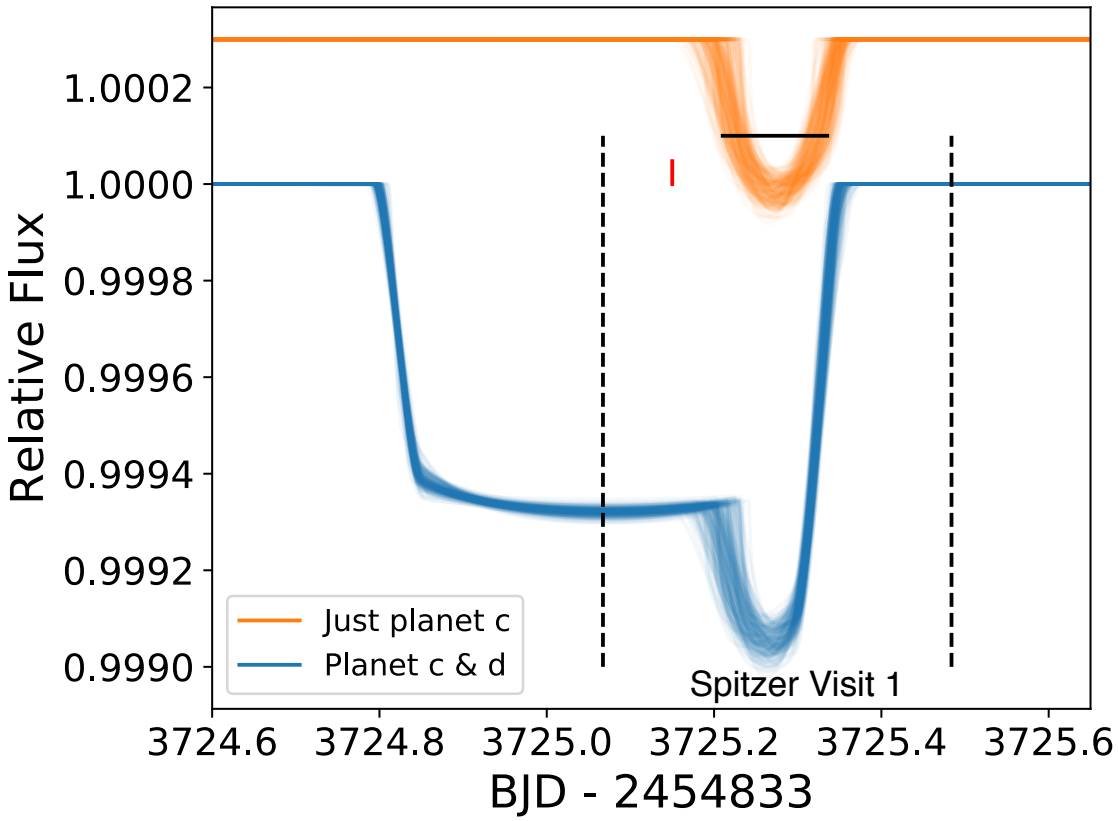


Figure 3-2: The observing window chosen to coincide with a transit of HIP41378 c, accounting for possible TTVs, as well as potential transits of HIP41378 d. The scatter in the lightcurves comes from drawing samples from the previous best fit posteriors for the orbital parameters of planets c & d.

and the goal is only to detect the presence or lack of a transit, we elected for a transit window in which only the egress of the transit of planet d is visible.

We show in figure 3-2 the requested window during with both planets would transit. Our observing strategy involved ensuring the there was sufficient baseline on either side of the expected transit of planet c, such that a robust transit center could be measured in the case of up to a 1.5 hour transit variation in either direction. We illustrate potential signals that might be detected in the case of only a single transit of planet c, or in the case of a double transit with planet d.

Table 3.1: Spitzer DDT Observing Parameters

| Observation | Number of 0.4s Frames | AOR Duration [hr] |
|---|---|---|
| Peak-up and Settle - Visit 1 (4.5m) | 1 × 64 | 0.50 |
| HIP41378 c/d transit - Visit 1 (4.5m) | 1366 × 64 | 10.5 |
| Warm pixel check - Visit 1 (4.5m) | 1 × 64 | 0.17 |
| Peak-up and Settle - Visit 1 (4.5m) | 1 × 64 | 0.5 |
| HIP41378 c transit - Visit 2 (4.5m) | 1366 × 64 | 10.5 |
| Warm pixel check - Visit 2 (4.5m) | 1 × 64 | 0.17 |

## 3.3 Collected Data & Analysis

As a result of our proposal, we were awarded 22.3 hours of observation across both requested observing windows. In table 3.1 we show the parameters of the observing schedule. The data was downloaded from the Spitzer Heritage Archive [1] and pre-processed using similar methods described in Chapter 2. As before we first flag bad or bright pixels using a sigma-clipping filter to remove high variance pixels, flagging pixels $> 5\sigma$ away from the median along the time axis for each pixel. We then calculate the background in two ways, either an annulus centered on the center of light (COL) as well as by counting the flux in the corners of an image. We then extract the centroid of the image by fitting a two-dimensional gaussian profile to the brightness map of each individual 64x64 pixel frame. We additionally trim the first and last 5% of each data set, in order to avoid biases near the beginning and end of the observation.

Once the data has been processed, we simultaneously fit the data for both transit signals, as well as variations due the differing response of the pixels. The details of this Pixel Level Decorrelation are similar to those describe in chapter 2, and we again focus on a 3×3 grid of pixels focused on the peak of the fitted gaussian profile.

[1] https://sha.ipac.caltech.edu/applications/Spitzer/SHA/

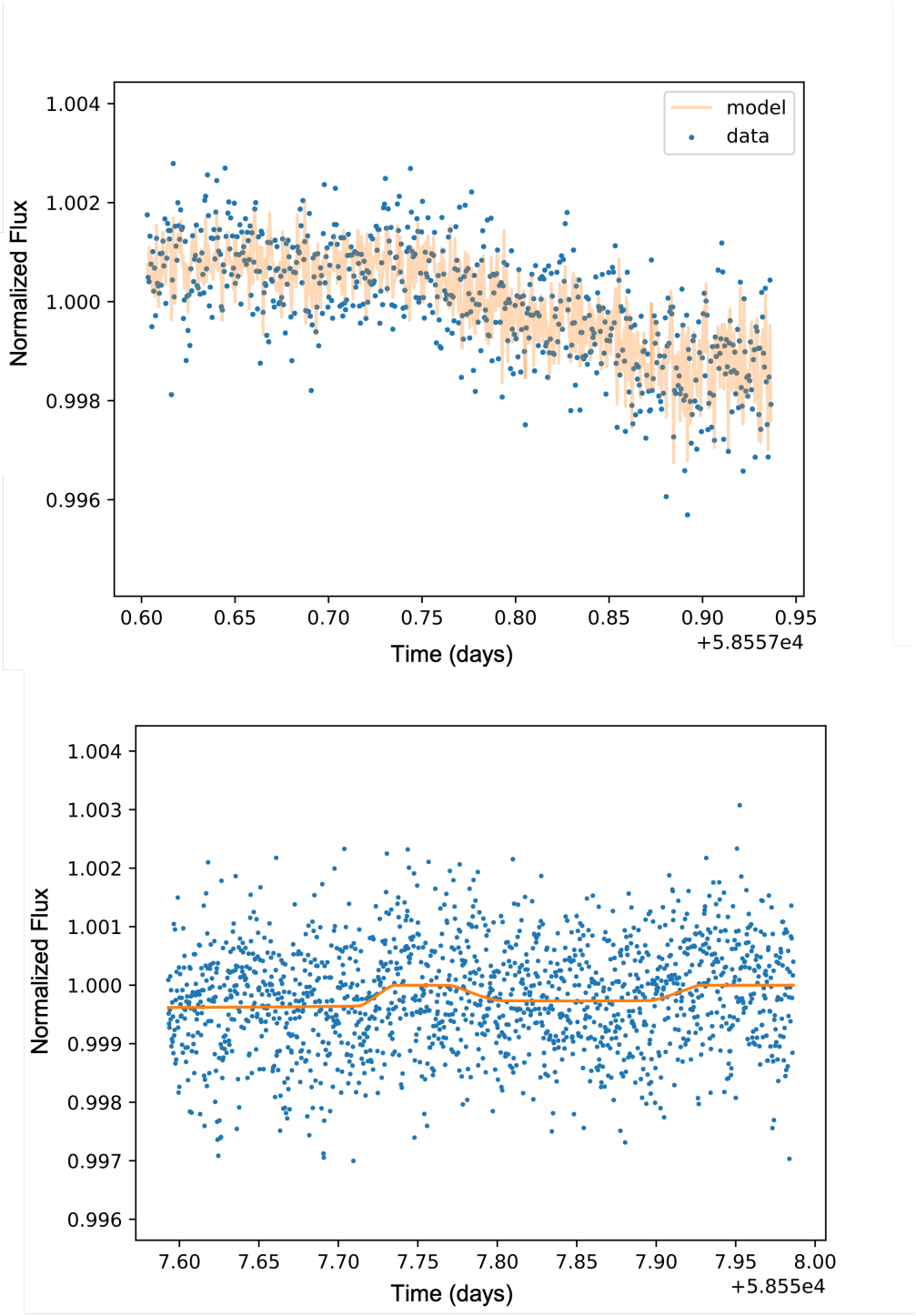


Figure 3-3: The top panel shows the raw data, binned by a factor of 200 in blue. In orange we show the best fit model, which includes two transiting planets with as well as a noise model representing the pixel variation effect. In the bottom panel, we show again the data and model (orange line), this time having subtracted the detector noise model from both, leaving just the baseline flux and two transit signals.

### 3.3.1 Analysis of First Observing Window

The first observing window was the one in which planet d was expected to potentially transit. When fitting the data, we considered models both with and without planet d, in order to robustly assess the transit center of planet c. Given that the focus was solely on the transit center of planet c, and additionally since the ability of *Spitzer* to characterise the shape of a transit is worse than instruments such as *Kepler* due to higher scatter, we fit only for the period and depth of the transit signal. For all other orbital parameters, including period, inclination, and semi-major axis, we use the best values from previous observations. In addition, we include a quadratic ramp, as well as nine pixel coefficients, to account for the flux variation in the PLD model.

We first run an MCMC analysis with the described noise model and a transit template of planet c only. We recover a transit depth of 350 ppm, which is consistent with previously values measured with *Spitzer*. We then run an MCMC fit with the same model, this time including a transit model of planet d as well. We show an example fit for the two transit model in figure 3-3, including both the global fit, illustrating the strength of the model in capturing the noise signal, as well a lightcurve with the noise model removed, showing the two transit fits.

In the case of a two planet fit, we find that the measured depth and transit center of planet c match the case when planet d is excluded. Additionally, we find that the residuals for the fit which exclude planet d are higher in the location where planet d is expected to transit, indicating that the model struggles to match the data in that part of the lightcurve. Regarding the fit for planet d, we find a depth of 520 ppm, which is consistent with previous measurements (within 1 $\sigma$).

### 3.3.2 Analysis of Second Observing Window

The second observing window was chosen to coincide with only a single transit of HIP41378 c, and thus we run an MCMC analysis with only a single light curve model. As for the first visit, we allow only the transit depth and center to vary, and hold all other orbit parameters fixed to their best fit values. We again find a consistent

Table 3.2: Best Fit Transit Parameters for Both Observations

| Parameter | Value | Lower Err. | Upper Err. | Comments |
|---|---|---|---|---|
| Transit Center c (BJD) | 58716.372 | 0.001 | 0.001 | Visit 2, planet c only |
| Transit Depth c (ppm) | 350 | 75 | 75 | Visit 2, planet c only |
| Transit Center c (BJD) | 58557.848 | 0.003 | 0.004 | Visit 1, planet c only |
| Transit Depth c (ppm) | 300 | 72 | 71 | Visit 1, planet c only |
| Transit Center c (BJD) | 58557.844 | 0.013 | 0.007 | Visit 1, planet c & d |
| Transit Depth c (ppm) | 289 | 80 | 100 | Visit 1, planet c & d |
| Transit Center d (BJD) | 58557.47 | 0.0042 | 0.0074 | Visit 1, planet c & d |
| Transit Depth d (ppm) | 520 | 156 | 167 | Visit 1, planet c & d |

transit depth, and we record the outputs of all MCMC fits in table 3.2.

## 3.4 Transit Timing Analysis

Having estimated the best fit transit centers for the two transits of HIP41378 c, we now focus on a transit timing variation analysis, including all previous timing measurements of the transits of planet c. As mentioned, two planets perturbing one another will produce a sinusoidal TTV signal, however we would like to allow for more exotic behaviours and so we model the TTV measurements using the `TTVFaster` package Deck et al. [2014]. Standard methods of simulating timing variations require the a significant number of orbital integrations in order to recreate the dynamics of a perturbed system. `TTVFaster` employs the use of simplectic integrators in order to rapidly calculate the transit centers. The gain in speed with comes with a trade-off of a loss of accuracy, however this is a tunable parameter within the model.

The benefit of a code like `TTVFaster` is that it allows an MCMC analysis of the observed TTVs in the system, during which the TTV model may be called millions of times. The forward model takes as input a list of planets, and for each planet in the system it requires a mass, period, eccentricity, argument of periastron ($\omega$), and transit center. In order to avoid boundary issues favoring non-zero eccentricities, the eccentricity and $\omega$ parameters are re-parameterized as $ecos\omega$ and $esin\omega$.

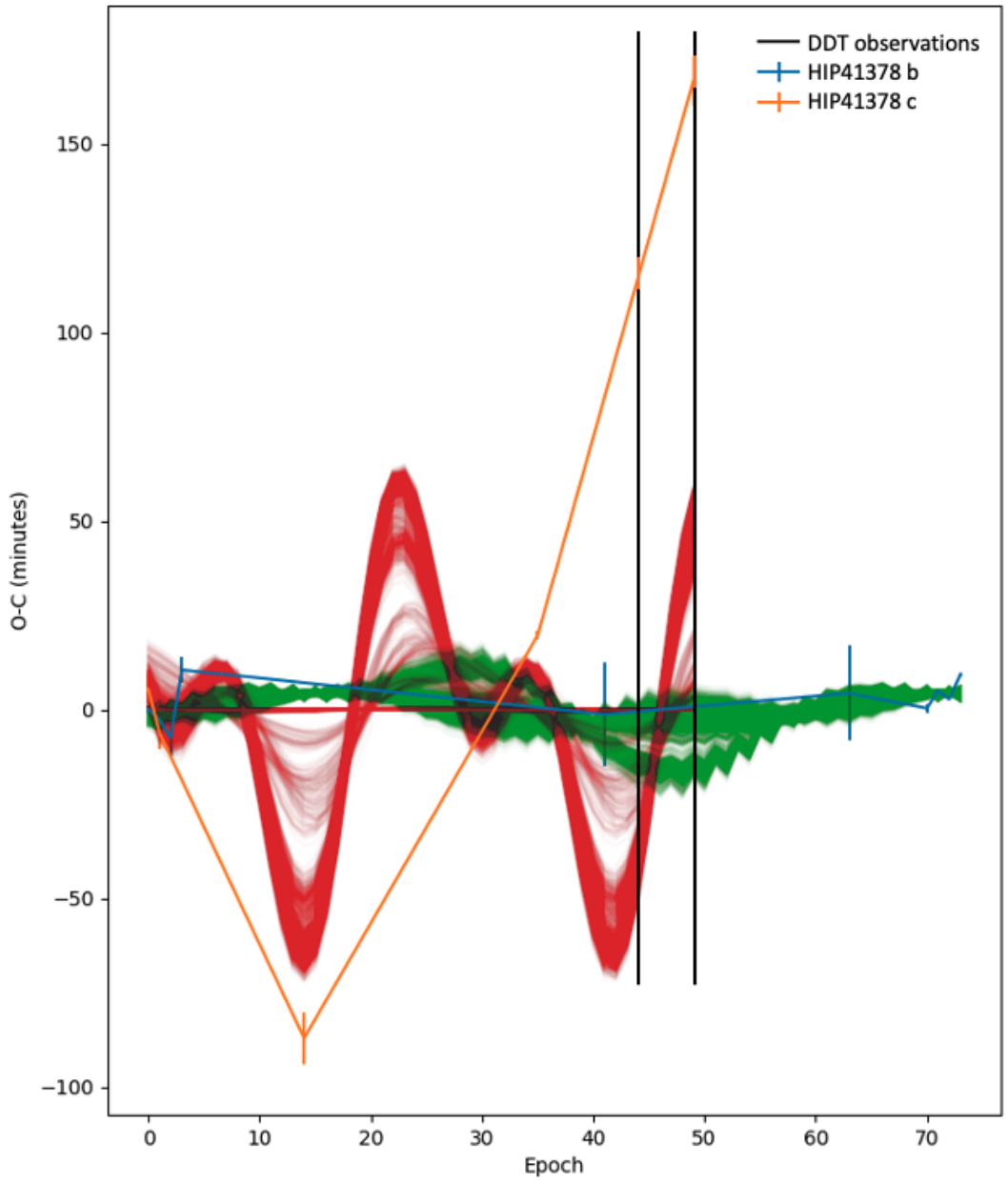


Figure 3-4: A distribution of posterior models (red curves) to the TTV signal of planet c (orange line), along with a distribution of posterior models (green curves) to the TTV signal of planet b (blue line). In this figure, posterior distributions come from a TTV model which includes the five known planets in the HIP41378 system. The black lines represent the location of the two new transit centers obtained from the our observations.

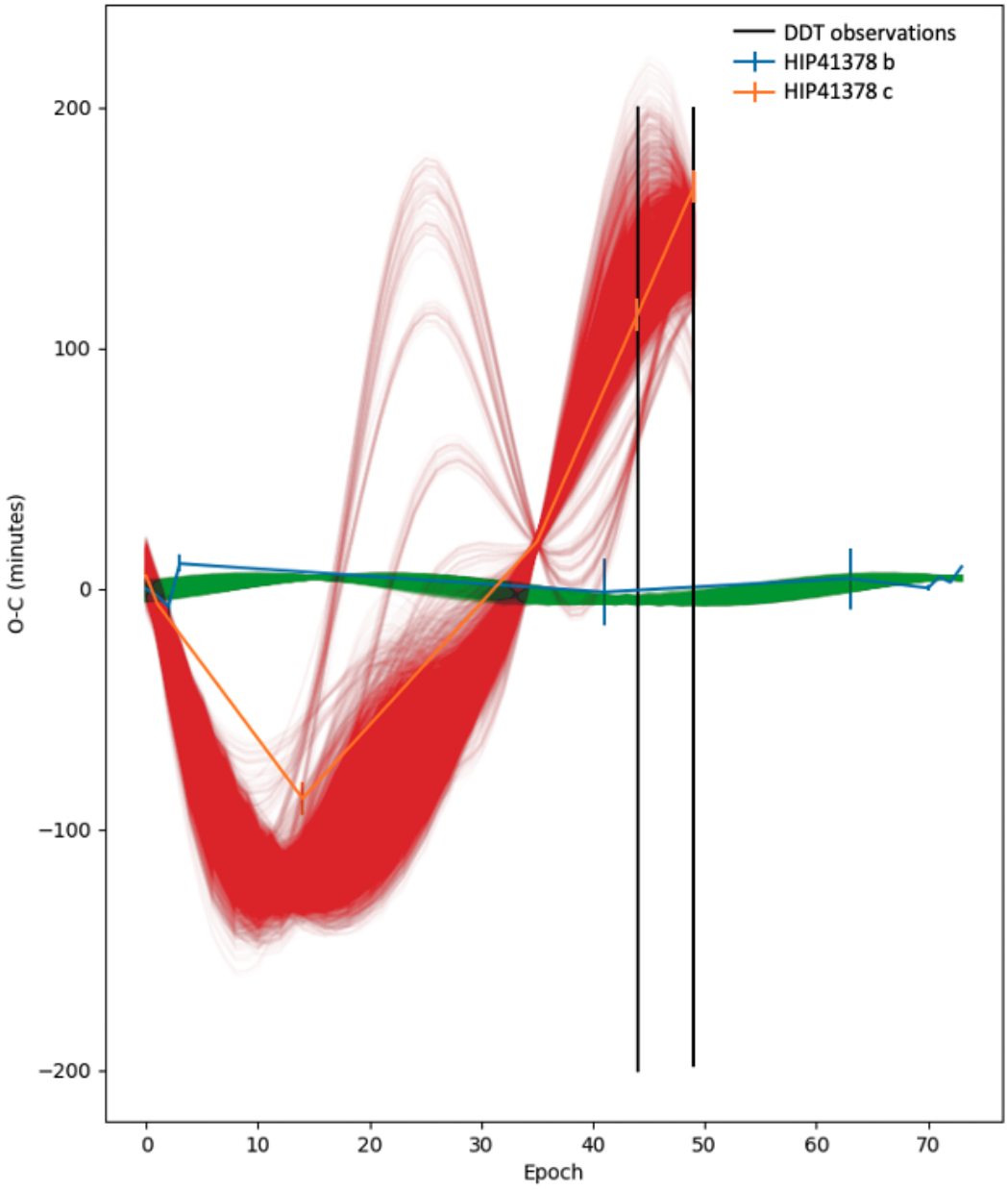


Figure 3-5: A distribution of posterior models (red curves) to the TTV signal of planet c (orange line), along with a distribution of posterior models (green curves) to the TTV signal of planet b (blue line). In this figure, posterior distributions come from a TTV model which includes the five known planets in the HIP41378 system, along with a sixth planet with a freelying varying orbital period and mass. The black lines represent the location of the two new transit centers obtained from the our observations.

In our first set of fits, we include the parameters for the five known planets in the system. For the masses of the planets, we use priors based on the results of extensive radial velocity measurements of the system Santerne et al. [2019]. For planets d and f, we chose the values 278.3618 days and 542.08 days respectively for the orbital periods, from their list of possible values. These represent the highest likelihood periods based on the analysis in Section 2.5.1. During the MCMC fit, for each set of parameters we calculate the expected transit centers for planets b and c, and compare them to measured values. We show the best fit posterior TTV signal in figure 3-4. We find in this case that the model is incapable of fitting the TTV signal observed for planet c, being unable in particular to explain the transit times of the two new measurements based on our new observations.

In addition to fitting the TTV signal with the five known planets in the HIP41378 system, we run a similar fit where include a sixth planet. In this case, we find that the model is able to properly fit the observed transit centers of planet c, and we show the best fit posteriors in figure 3-5. We show the best fit values for the parameters of the potential sixth planet in table 3.3.

Previous observations, particularly campaign 5 of the *Kepler* mission, have continuously observed the system for longer than 62 days, indicating that a planet on a 62 day orbital period would have had at least one observable transit thus far. Given the mass of the host star ($M_\star = 1.26 M_\odot$ Stassun et al. [2019]), we can estimate the semi-major axis of this hypothetical planet g from Kepler's law, which we find to be 55 times the stellar radius ($R_\star = 1.31 R_\odot$). This in turn allows us to calculate the maximum inclination value which would cause the planet to not transit, which we find to be 88.95 degrees. Thus the fit value of 88.46 degrees quoted in table 3.3 would be consistent with the planet being non-transiting.

Table 3.3: MCMC Posterior Values When Fitting With a 6th Planet (HIP41378 g)

| Parameter | Value | Lower Err. | Upper Err. |
|---|---|---|---|
| $M_g$ ($M_J$) | 8.602 | 2.4 | 3.9 |
| $Per_g$ (days) | 62.415 | 0.062 | 0.038 |
| ecos$\omega$ | -0.003 | 0.042 | 0.053 |
| esin$\omega$ | 0.004 | 0.047 | 0.044 |
| Inclination (deg) | 88.46 | 0.25 | 0.25 |

## 3.5 Discussion & Recent Observations of the HIP41378 System

We have analysed two new observations of the HIP4378 system made using the IRAC instrument on *Spitzer*, observing at 4.5$\mu m$. We add two new transit center measurements for HIP41378 c, bringing the total up to nine, as well as expanding the baseline of observations to just over four years. We find that the five known planets in the HIP41378 system are unable to explain the observed transit centers, however with the inclusion of an as yet undetected sixth planet orbiting on a 62 day period we are able to robustly fit the transit centers. Additionally, we marginally detect the presence of a transit with a depth of ∼550ppm during the second observation window, which would correspond with HIP41378 d having only four out of its 23 allowed periods.

Following the analysis performed in this and the previous chapter, several other observations have been made of the HIP41378 system which support our findings. The first study we wish to highlight is an extensive radial velocity campaign to characterise the system and measure the masses of its planets. This work is summarized in Santerne et al. [2019]. In particular, they find tentative RV evidence of a sixth planet, which they dub HIP41378 g, with an orbital period of 62.06 ± 0.32 days, which is consistent with the value obtained from our TTV fitting. They additionally measure a mass of 7.5 ± 1.5 $M_J$ (under the assumption of an 88 degree inclination), which is similarly consistent with both the mass and inclination retrieved by our fit.

Regarding the orbital period of planet d, the recent work of Grouffal et al. [2022] reported on measurements of the Rossiter-McLaughin (RM) effect [Holt, 1893, Rossiter, 1924, McLaughlin, 1924] for HIP41378 d using the HARPS-N/TNG and

ESPRESSO/ESO-VLT spectrographs. These measurement allow them to confirm that the orbital period is $\sim$ 278 days, which is consistent with the orbital period required for planet d to transit during our second observation window. Thus we find supporting evidence not only that we observed a transit of planet d, but additionally that the measured TTVs of planet c are accurate and consistent with fitting for two transit signals during the second observing window.

# Chapter 4

# Spitzer Follow-Up and Ephemerides Refinement of Two Multi-Planet Systems

*The work presented in this chapter originally appeared as a contributed section in the literature as*

Molly R. Kosiarek, David A. Berardo, Ian J. M. Crossfield, et. al., *The Astronomical Journal, 161, 47, (2020).*

*The focus of this manuscript was a detailed characterisation of two multi-planet systems, for which I contributed an analysis of Spitzer observations, resulting in additional transit depth measurements as well as refined ephemerides to ensure the observability of future transits.*

## 4.1 Introduction

Bright stars hosting earth-sized planets provide exciting opportunities to characterize exoplanet atmospheres, due to their high signal-to-noise observations and associated transmission spectroscopy metrics of their orbiting planets (TSM, Kempton et al.

[2018]). Mass and radius alone are often degenerate with a range of interior planet compositions, which atmospheric characterisation provides the opportunity to differentiate [Figueira et al., 2009, Rogers and Seager, 2010]. We report here the results of following up two multi-planet systems orbiting bright stars, GJ 9827 and HD 106315, with the *Spitzer* space telescope. In addition to obtaining planet radii in a new waveband, which can help to constrain atomspheric models, we also obtained refined ephemerides on the planets, ensuring the ability to observe their transits in the future.

## 4.2 HD106315

HD 106315 (K2-109) is a bright (V=8.97 mag, K=7.85 mag) F5 dwarf star hosting two planets discovered in K2 Campaign 10 [Crossfield et al., 2017, Rodriguez et al., 2017]. Planet b is a small ($R_b$=2.40 $\pm$ 0.20 $R_\oplus$) planet with an orbital period of 9.55 days; planet c is a warm Neptune-sized ($R_c$=4.379 $\pm$ 0.086 $R_\oplus$) planet with an orbital period of 21.06 days.

## 4.3 GJ 9827

GJ 9827 (K2-135) is a bright (V=10.3 mag, K=7.2 mag), nearby (distance=30 pc) K6 dwarf star hosting three planets discovered in K2 Campaign 12 [Niraula et al., 2017, Rodriguez et al., 2018]. Planets b and c orbit near a 3:1 resonance at 1.2 days and 3.6 days, with planet d at 6.2 days. These three planets span the gap seen in the radius distribution of small planets [Fulton et al., 2017] sized at 1.529$\pm$0.058 $R_\oplus$, 1.201$\pm$0.046 $R_\oplus$, and 1.955$\pm$0.075 $R_\oplus$ respectively. Niraula et al. [2017] additionally collected 7 radial velocity observations with the FIbrefed Echelle Spectrograph (FIES) [Frandsen and Lindberg, 1999, Telting et al., 2014] to vet the system and to derive stellar parameters.

## 4.4 Observations and Data Analysis

Predicting precise future transit times becomes harder as more time elapses from previous transit observations and the uncertainty from the orbital period compounds Dragomir et al. [2020]. These systems contain promising targets for future atmospheric follow-up which require small uncertainties on the predicted transit time. Therefore, we collected additional transit observations on the Spitzer Space Telescope to refine the ephemerides for each planet as well as to provide a depth measurement at $4.5\mu m$. These observations were taken as part of the K2 follow-up program 13052 (PI: Werner), using the $4.5\mu$m channel of IRAC [Fazio et al., 2004]. A single transit of each planet was observed, except for HD 106315 bwhich was observed twice. All of the observations were collected with 0.4 second exposures and the target placed on the 'sweet spot' of the detector.

Table 4.1: Spitzer Transit Results

| Planet | Date(UT) | Time of Conjunction (BJD) | Rp/R$_*$ (4.5) | Semimajor Axis (R$_*$) | Inc. (°) |
|---|---|---|---|---|---|
| GJ 9827 b | 2018-03-10 | $2457738.82384^{+0.00081}_{-0.00080}$ | $0.0225^{+0.0018}_{-0.0017}$ | $7.19^{+0.56}_{-0.40}$ | $87.7^{+1.8}_{-1.6}$ |
| GJ 9827 c | 2018-03-06 | $2457742.1993^{+0.0025}_{-0.0028}$ | $0.0201^{+0.0023}_{-0.0020}$ | $13.0^{+1.7}_{-1.3}$ | $88.5^{+1.4}_{-1.1}$ |
| GJ 9827 d | 2018-03-28 | $2457740.98800^{+0.00064}_{-0.00055}$ | $0.0348^{+0.0014}_{-0.0013}$ | $21.8^{+2.5}_{-1.6}$ | $87.72^{+0.37}_{-0.21}$ |
| HD 106315 b | 2017-4-19 | $2457586.5394^{+0.0056}_{-0.0109}$ | $0.0201^{+0.0026}_{-0.0024}$ | $16.4^{+5.1}_{-3.1}$ | $88.4^{+2.3}_{-1.1}$ |
| HD 106315 b | 2017-9-10 | $2457586.5826^{+0.0121}_{-0.0043}$ | $0.0219^{+0.0034}_{-0.0026}$ | $10.4^{+2.2}_{-1.3}$ | $87.6^{+3.0}_{-1.7}$ |
| HD 106315 c | 2017-4-20 | $2457569.0103^{+0.0012}_{-0.0012}$ | $0.0329^{+0.0013}_{-0.0012}$ | $29.5^{+5.7}_{-4.2}$ | $88.89^{+0.69}_{-0.51}$ |

We follow a similar analysis approach to that described in Berardo et al. [2019], which detrends the data using the Pixel Level Decorrelation method outlined in Deming et al. [2015]. In brief, we first applied a median filter to each pixel in the image and calculated a background level for each frame by taking the median of the flux in an annulus centered on the point spread function. We estimated the centroid of each frame by fitting a two dimensional Gaussian to the image, and obtained a light curve using a fixed radius aperture. We varied the aperture size and performed a linear regression to determine the optimal radius; we found 2.4 pixels minimized the root mean square (RMS) of the residuals for all observations.

We modeled systematics in the light curve by weighting the nine brightest pixels individually as well as fitting for a quadratic time ramp. We then chose the combination of pixel coefficients, aperture size, and time-series binning that resulted in the

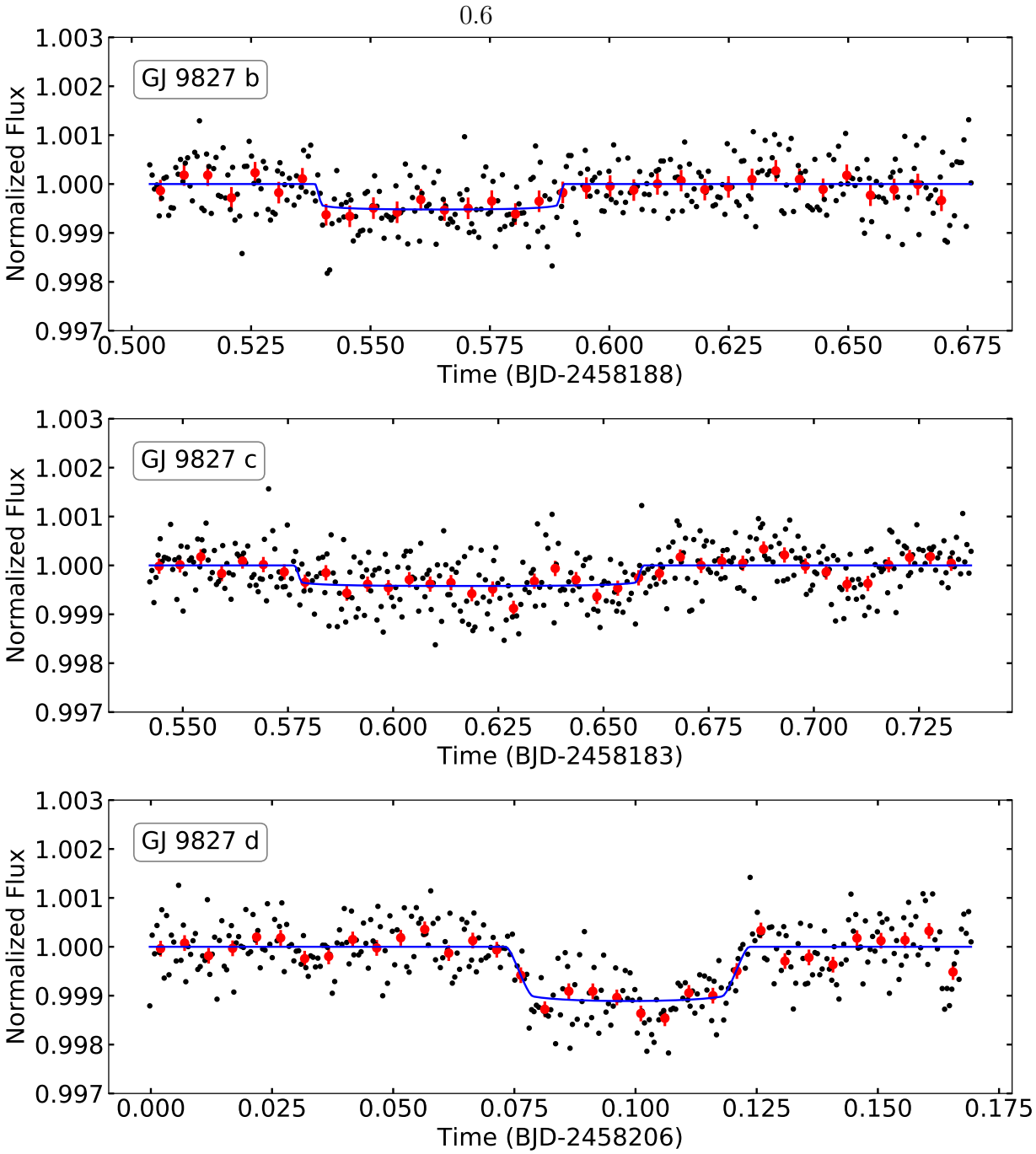


Figure 4-1: Spitzer transits of GJ9827 b, c & d. Data (black points), binned data (red circles), and model fit (blue line) are shown.

smallest RMS deviation. We ran a Markov-Chain Monte Carlo (MCMC) analysis to estimate parameter uncertainties, using the systematic model in addition to a transit signal which we modeled using `batman` [Kreidberg et al., 2015]. We fixed the period

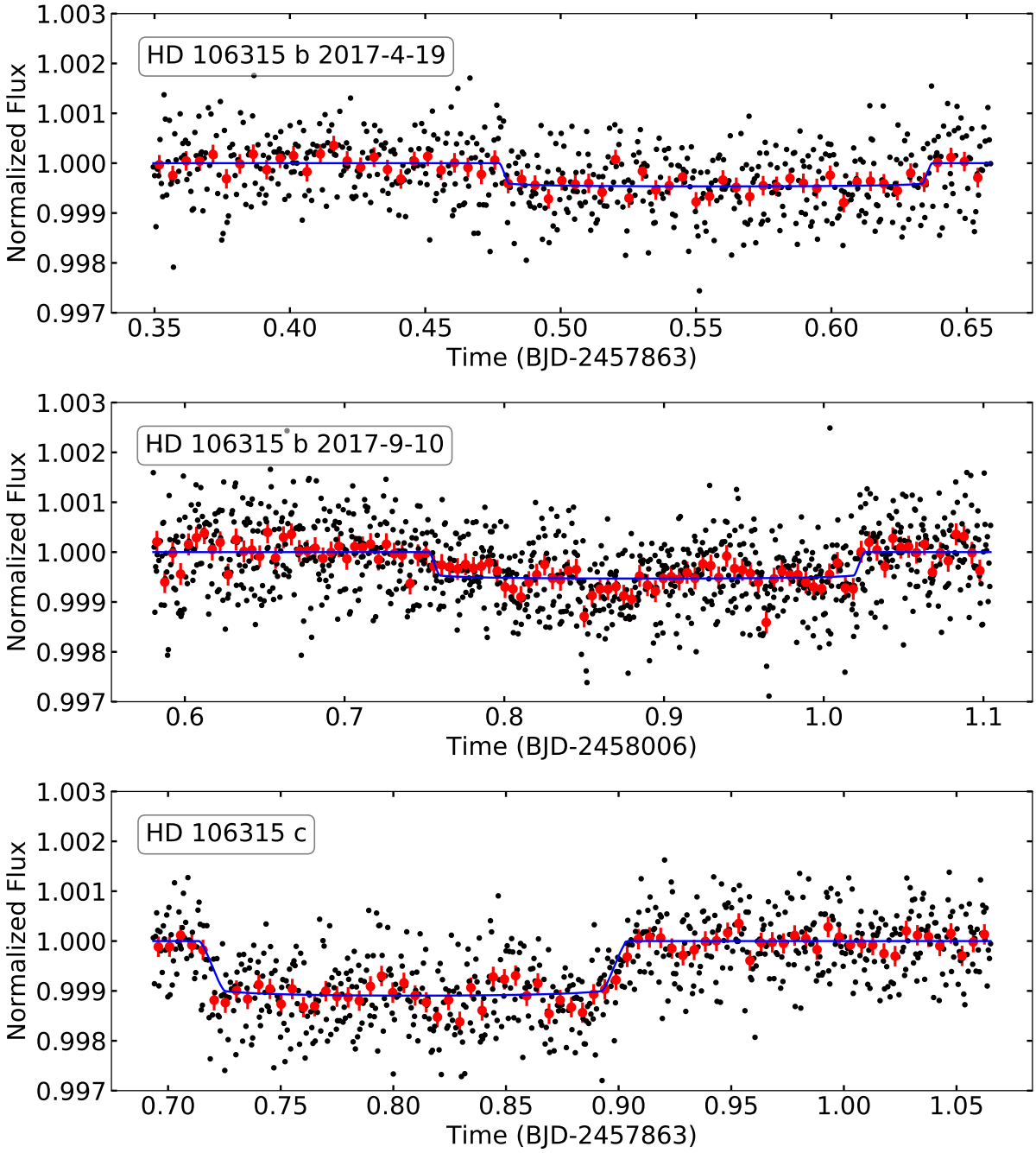


Figure 4-2: Spitzer transits HD 106315 b & c. Data (black points), binned data (red circles), and model fit (blue line) are shown.

of each planet to the most recent measurements [Barros et al., 2017, Rice et al., 2019] and allowed the transit depth, center, orbital inclination, and semi major axis to vary. We also left the uncertainty of the data points as a free parameter, which we found

Table 4.2: Ephemerides Update

| Planet | Time of Conjunction (BJD) | Period (days) |
|---|---|---|
| GJ 9827 b | 2457738.82586±0.00026 | 1.2089765±2.3e-06 |
| GJ 9827 c | 2457742.19931±0.00071 | 3.648096±2.4e-05 |
| GJ 9827 d | 2457740.96114±0.00044 | 6.20183±1.0e-05 |
| HD 106315 b | 2457586.5476±0.0025 | 9.55287±0.00021 |
| HD 106315 c | 2457569.01767±0.00097 | 21.05652±0.00012 |

converged to the RMS scatter of the raw light curve. We held fixed the quadratic limb darkening parameters, which were determined using the tables of Claret and Bloemen [2011]. The fit results are shown in Table 4.1 and Figures 4-1 and 4-2.

We calculated updated ephemerides (Table 4.2) to further refine the time of conjunction and orbital period for future atmospheric follow-up and to better constrain these values for radial velocity fits. We fit a straight line to the transit centers obtained from each individual observation, incorporating all ground-based published transits thus far [Lendl et al., 2017, Barros et al., 2017]. These planets will be accessible for future transmission spectroscopy observations throughout the JWST era. As an example, the transit time uncertainty in 2025 is under two hours for all five planets (GJ 9827 b: 0.1hr, GJ 9827 c: 0.5hr, GJ 9827 d: 0.1hr, HD 106315 b: 1.7hr, HD 106315 c: 0.4hr).

# Part III

# Planets in 3D

# Chapter 5

# On the Effects of Planetary Oblateness on Exoplanet Studies

*The work presented in this chapter originally appeared in the literature as*

David Berardo and Julien de Wit, *The Astrophysical Journal, 935, 178, (2022).*

## 5.1 Abstract

When studying transiting exoplanets it is common to assume a spherical planet shape. However short rotational periods can cause a planet to bulge at its equator, as is the case with Saturn whose equatorial radius is almost 10% larger than its polar radius. As a new generation of instruments comes online, it is important to continually assess the underlying assumptions of models to ensure robust and accurate inferences. We analyze bulk samples of known transiting planets and calculate their expected signal strength if they were to be oblate. We find that for noise levels below 100ppm, as many as 100 planets could have detectable oblateness. We also investigate the effects of fitting spherical planet models to synthetic oblate lightcurves. We find that this biases the retrieved parameters by several standard deviations for oblateness values $> 0.1$-$0.2$. When attempting to fit an oblateness model to both spherical and oblate lightcurves, we find that the sensitivity of such fits is correlated with both the SNR

as well as the time sampling of the data, which can mask the oblateness signal. For typical values of these quantities for Kepler observations, it is difficult to rule out oblateness values less than $\sim$0.25. This results in an accuracy wall of 10-15% for the density of planets which may be oblate. Finally, we find that a precessing oblate planet has the ability to mimic the signature of a long-period companion via transit timing variations, inducing offsets at the level of 10s of seconds.

## 5.2 Introduction

Young planets which have yet to come into tidal equilibrium with their host star may be rotating at speeds sufficient to cause their equators to bulge and thus deviate substantially from a sphere. When analyzing the lightcurves of transiting exoplanets it is typical to assume that a planet is perfectly spherical, as is the case of the many fitting routines which implement the transit models of Mandel and Agol [2002]. Within our own solar system however, we observe that the equatorial radii of Saturn and Jupiter are 9.8% and 6.5% larger than their polar radii. Planets can become distorted due to tidal forces from their host star or, as is the case with Jupiter and Saturn, due to rapid rotation, causing them to bulge uniformly about their rotation axis. The amount by which a planet is oblate is tied to its rotation rate as well as its internal structure, which determines its deformability. The ability to measure the oblateness of a planet would thus allow us to better understand its current rotational properties and internal dynamics, as well as its formation and evolution (which determine its current rotation) [Lissauer, 1995].

The effect of oblateness on the lightcurve of a transiting planet has previously described in the works of Seager and Hui [2002], Barnes and Fortney [2003], Carter and Winn [2010a], and Carter and Winn [2010b]. These works highlight the features of an oblate lightcurve, which is primarily a variation in the ingress and egress of their transits on the order of 10's to 100's of ppm for the most optimal of planets. These properties outline the difficulties in detecting oblateness through lightcurve variations, which has thus far proven to be a difficult task. In Zhu et al. [2014], short

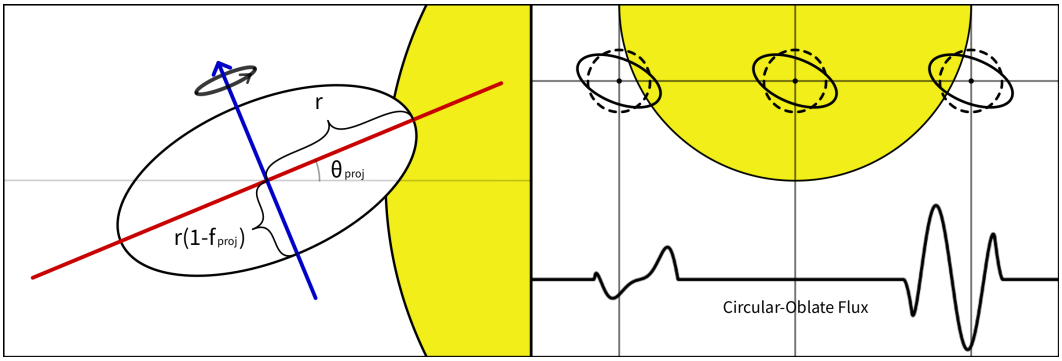


Figure 5-1: Left: A schematic showing the configuration of the planet and all relevant quantities. The blue (polar) minor axis is the planet's axis of rotation, which is scaled down by a factor of $(1 - f_{\rm proj})$ relative to the red (equatorial) major axis. The planet may also be tilted by an angle $\theta_{\rm proj}$ relative to its orbital plane. Note these quantities are the sky-plane projected values an observer would see. Right: The difference in the lightcurve of an oblate planet (solid) to a spherical planet (dashed) with the same projected area. For a uniformly bright star, there is no difference once the planets are fully inside the stellar disk. Note the asymmetry induced by the orbit having a non-zero impact parameter.

cadence planets in the *Kepler* survey were searched, yielding a tentative result of oblateness for the planet Kepler-39b (KOI432.01). A further search was conducted in Biersteker and Schlichting [2017], which attempted to detect oblateness using depth variations across multiple transits as an oblate planet precesses over time. This yielded yet another tentative result of oblateness for the warm Saturn Kepler-427b. Recently Akinsanmi et al. [2020] studied the potential of spectroscopic measurements to detect oblateness, finding that a combination of photometry and spectroscopy has the potential to provide more accurate and precise oblateness measurements.

In section 5.3 we outline the relevant quantities and processes that control planetary oblateness. We then analyze a bulk sample of planets to determine how many should have detectable oblateness for varying levels of sensitivity. In section 5.4 we fit spherical planet models to synthetic oblate lightcurves to study biases on the retrieved transit parameters. As shown in de Wit et al. [2012], orbital parameters can compensate for shape and brightness distribution effects on the shape of transit and eclipses, an effect which we seek to further understand. In section 5.5, we fit oblate models to synthetic and real planets in order to determine the regimes in which such models

can properly measure or rule out oblateness, as well as to determine if populations can be separated into oblate/non-oblate based on properties such as orbital period. Finally in section 5.6 we discuss the effects oblateness may have on the precision of measured planet densities, as well as the ability for time-varying oblateness to mimic transit timing variations due to precession of a planet's orbital axis.

## 5.3 Description and Physical Background of Oblateness

Oblateness refers to the amount by which the equatorial radius of a planet differs from its polar radius. A common cause of planet shape distortions are tidal forces which induce a bulge towards the host star [Love, 1911]. In our case we are interested in oblateness induced by a planets rotation, which causes its equator to bulge out perpendicular to its rotation axis. Standard notation uses the parameter $f$ for oblateness, which is defined as:

$$f = \frac{R_{eq} - R_{pol}}{R_{eq}} \tag{5.1}$$

where $R_{eq}$ and $R_{pol}$ are the equatorial and polar radii of a planet [Murray and Dermott, 1999]. Thus oblateness ranges from 0 (for a perfectly spherical planet) to 1 (for a planet completely flattened along the radial direction). In principle $f$ could also be negative for the case of a prolate planet, whose polar radius is larger than its equatorial radius. While we restrict the oblateness to be a positive value in this work, we do allow its rotational axis to be tilted up to 90 degrees relative to its orbital axis, which would cause an oblate planet to appear prolate. For the planets in our own solar system, $f$ ranges from near zero for the rocky planets such as mercury and earth, to approximately 0.065 and 0.1 for Jupiter ($P_{Rot} = 9.93$ hrs) and Saturn ($P_{Rot} = 10.65$ hrs) respectively[1]. The rotational period of a planet and its oblateness are related by [Hubbard, 1984]

[1]Values taken from https://nssdc.gsfc.nasa.gov/planetary/planetfact.html

$$P_{rot} = 2\pi\sqrt{\frac{R_{eq}^3}{GM_p\,(2f - 3J_2)}} \tag{5.2}$$

where $M_p$ is the planet's mass, and $J_2$ is its quadrupole moment, which is around 0.015 for Jupiter and Saturn, around 0.001 for Earth and Mars, and $< 0.00001$ for Mercury and Venus.

The planet may also be tilted relative to its orbital plane by two obliquity angles $\theta$ and $\phi$. When an ellipsoid is rotated in three dimensions and projected onto the sky plane we observe an ellipse which we can characterise by a *projected* oblateness $f_{\rm proj}$and a *projected* obliquity $\theta_{\rm proj}$, as shown in the left panel of figure 5-1. The projected values are related to the true values by

$$f_{\rm proj} = 1 - \sqrt{\sin^2\theta' + (1-f)^2\cos^2\theta'} \tag{5.3a}$$

$$\tan\theta_{\rm proj} = \tan\theta\sin\phi \tag{5.3b}$$

$$\cos^2\theta' = \sin^2\theta\sin^2\phi + \cos^2\theta \tag{5.3c}$$

This implies that for most planets what will be observed is an oblateness value that is smaller than their true oblateness, diminishing the deviations from a spherical planet. If one assumes that the orbital axis is randomly oriented (i.e. uniformly distributed on the unit sphere), then the median projected oblateness would be between 75% to 70% of the true oblateness (see appendix A). Constraints on the amount by which a planet's rotation can be tilted away from the normal vector of its orbital plane would allow us to put limits on the effect of projection. However in our own solar system we observe Uranus to have its rotational axis oriented by 97.77° relative to its orbital plane, providing us with the two extremes of perfect alignment (as is the case for Mercury) as well as perfect misalignment, along with several intermediate values.

The observable effect of an oblate planet is illustrated in the right panel of figure 5-1. During ingress and egress of a transit, two planets with differing shapes will block differing amounts of light from their host star. More specifically, the time-dependence

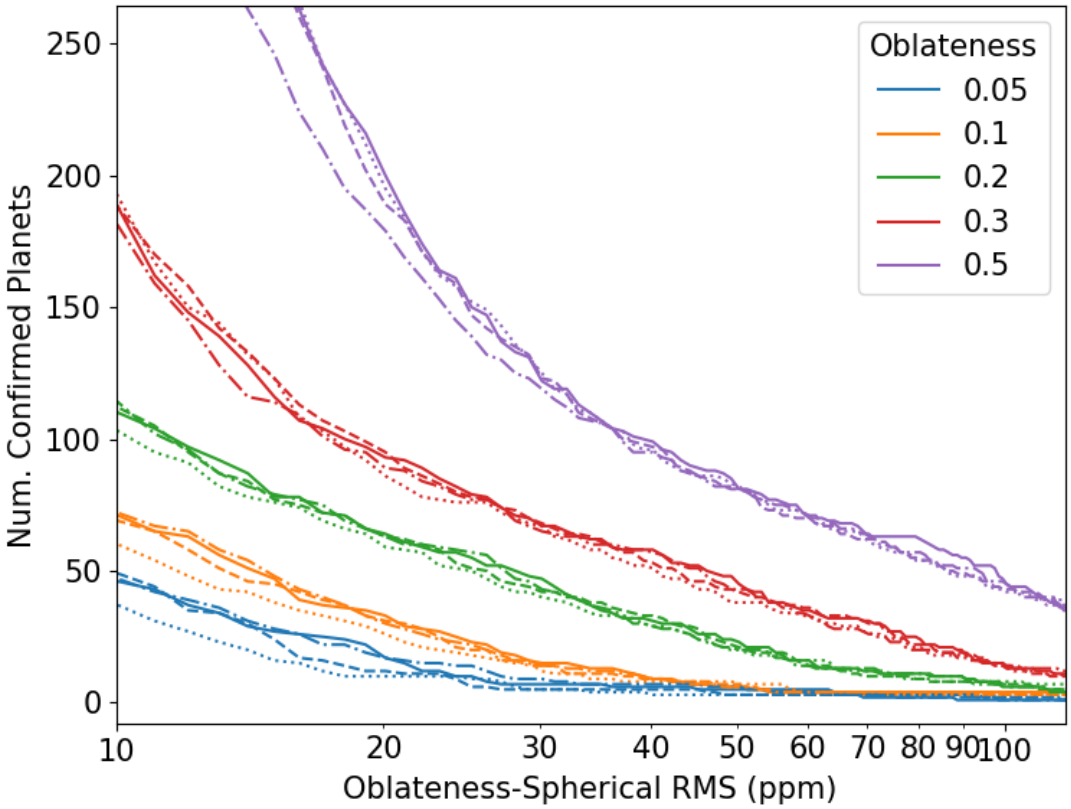


Figure 5-2: The number of confirmed transiting planets whose lightcurve would vary by a given amount if they had a certain level of oblateness, with a one minute integration time. The x-axis represents the Root-Mean-Square (RMS) deviations during ingress. The solid, dashed, dotted, and dash-dot lines represent obliquities of 0, 45, 60, and 90 degrees respectively.

of the amount of light they block will vary, which affects the shape of the lightcurve as the planet enters and exists the limb of the stellar disk. Once the planet is fully inside the disk of the star, the dominating factor in the amount of light blocked is the total projected area of the planet. Stellar heterogeneities such as limb darkening and star spots would still produce differing signals for spherical and non-spherical planets, however the effect is much weaker when compared to the differences during ingress and egress, which may be be upwards of several 100's of parts per million (ppm). It is thus critical when searching for oblateness to ensure that the limbs of the transit are sufficiently sampled in time.

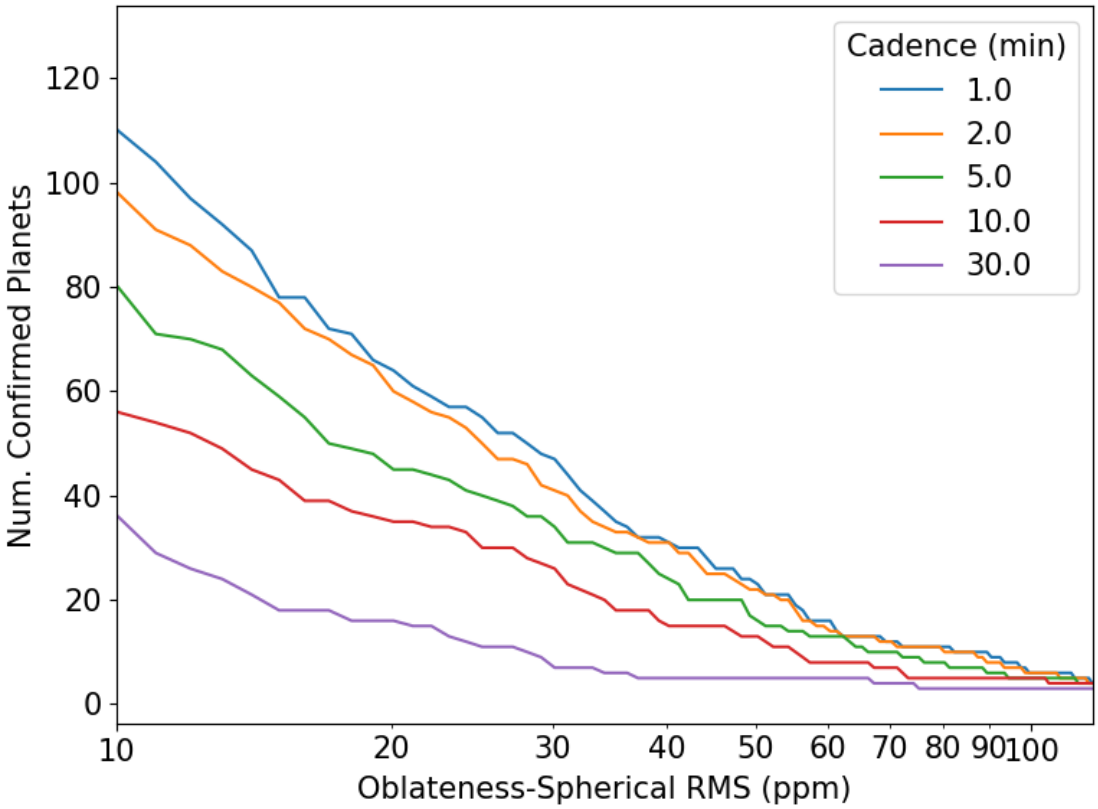


Figure 5-3: For the same sample of planets as in a), we keep the oblateness fixed to 0.2 in all cases. The curves correspond to different observing cadences which smooth out the oblateness signal.

Figure 5-4: The expected oblateness of confirmed transiting planets

### 5.3.1 The observability of oblateness for known planets

Currently, the detection of oblateness is limited to a handful of tentative measurements among the most suitable planet candidates. Previous studies such as Zhu et al. [2014] and Biersteker and Schlichting [2017] have used the *Kepler* survey as their pool of observations, which have provided us with some of the highest quality, as well as longest baseline, transit observations to date.

The goal of this section is to quantify the average strength of an oblateness signal that one expects to see across all known planets. This allows us to determine both the number of expected planets whose oblateness may be measured with upcoming instruments, as well as the potential to place upper limits on the oblateness of planets

if no such signal is seen at increased signal to noise ratios (SNR). The amplitude of an oblateness signal depends on properties such as the planet-to-star area ratio, inclination, impact parameter etc. in non-linear ways, and so planets must be assessed on an individual basis. We compiled a list of all known transiting planets, taken from the exoplanet archive table of confirmed planets [NASA Exoplanet Archive, 2019]. As will be discussed in section 5.6.3, it is expected that planets with short orbital periods ($\lesssim$ 15 days) will be rotating too slowly to be oblate. We thus cut out planets with a period of less than 10 days, in order to exclude planets which we confidently do not expect to exhibit oblateness so as to not inflate the number of potential candidates. We also exclude planets which do not have reported values for any of the transit parameters necessary to calculate a lightcurve model.

This leaves us with a sample of ∼900 planets. For each of these we then generate synthetic lightcurves for a spherical planet (using the Batman package of Kreidberg [2015]), as well for varying levels of oblateness. The oblateness is kept to be less than 0.5 ($r_{eq} \leq 2r_{pol}$) for stability considerations. Equating the centripetal and gravitational forces at the planets surface

$$\frac{GM}{r_{eq}^2} = \frac{v^2}{r} \tag{5.4}$$

and substituting equation 5.2 into $v = 2\pi r_{eq}/P_{rot}$ to relate the velocity at the surface to the oblateness parameter f, we find

$$f_{crit} = (1 + 3J_2)/2 \tag{5.5}$$

which is approximately 0.5, for $3J_2 << 1$. To obtain values of f larger than 0.5, the necessary rotational velocity of the planet would overcome its gravitational attraction and become unstable.

We generate 1-minute cadence lightcurves of oblate planets using a Monte-Carlo integration routine, based off appendix A of Carter and Winn [2010a], which includes a quadratic limb darkening law[2]. The uncertainty in the model itself is at the level

[2]Using the corrected versions of equations (B5) and (B6) noted in Zhu et al. [2014], $r$ =

of 1-2 ppm (set by the number of points used in the integration).

When generating oblate lightcurves of a given planet, we fix the transit parameters to their measured values. The only parameter we vary is the equatorial radius of the planet, which we adjust so that the depth of the transit remains constant. The transit depth of a planet of oblateness f is given by

$$\delta_{ob} = r_{eq} r_{polar} = r_{eq} r_{eq} (1 - f) \tag{5.6}$$

and so if we were to keep the radius the same, the depth between an oblate and spherical planet would differ in proportion to f. Given that during the center of transit there is little to no information regarding the shape of the planet (depending on the degree of limb darkening) we set $\delta_{ob} = \delta_{circ}$, which gives the relation between the equatorial radius of an oblate and spherical planet as

$$r_{ob} = r_{circ} / \sqrt{1 - f} \tag{5.7}$$

We calculate the difference between the spherical and oblate lightcurves, and then calculate the root mean square of the difference during ingress and egress, which we show in figure 5-2. Alternatively, we could have chosen the amplitude or maximum difference between the lightcurves. However for many planets which have low time-sampling during ingress / egress, it would be misleading to report what is usually a single high point as the overall strength of the oblateness signal.

We find that between 10ppm - 100ppm is when most planets begin to exhibit oblateness. For nearly maximal value of f$\sim$0.5 we find as many as 50 planets with RMS deviations above 100ppm. However this is an extreme case, and as mentioned due to projection effects it is unlikely many planets would display such a high level of oblateness. At a signal amplitude of approximately 50ppm, there are on the order of 30 planets which would exhibit variations at this level if they were to have an oblateness factor of 0.2, and almost double this number of planets if they had an oblateness of 0.3. Going down to 10ppm, we see these numbers roughly double again.

$\sqrt{u + (1-u)(a_1/a_2)^2}$ and $\theta = (1-v)\theta_1 + v\theta_2$

In addition to oblateness, we also vary the obliquity angle of the planets. We find that when considering a bulk population the obliquity does not significantly change the number of observable planets at a given signal level. As shown in the right panel of figure 5-1, it is possible for the signal to vary significantly between ingress and egress, indicating that transit asymmetry may be a potential sign of oblateness. If we calculate the RMS separately for ingress and egress and compare them, we find that the ratio of their values is on average between 0.8 and 0.9, depending on the oblateness value. For planets with sufficiently sampled limbs this effect would be an additional marker of oblateness.

We also study the effect of observing cadence (i.e. the integration time between data points), which is shown in figure 5-3. Given that oblateness primarily causes variations during ingress and egress, the number of observations during these parts of the transit directly impacts the ability to detect oblateness. We hold the oblateness level fixed at 0.2 and alter the duration of the observing cadence, ranging from 1 minute to 30 minutes, as a reflection of the Kepler observing cadence modes. We see in this case that for a given signal level, the number of planets which exhibit oblateness decreases by more than half as the integration time increases. We note that for most of the planets in our sample, a one minute observing cadence corresponds to about 5 - 50 data points during the transit limbs, with a median of 16 data points. The effect of time sampling, which smooths and distorts the shape of a transit, is often not considered when discussing oblateness. The significance of this is analysed further in section 5.5.2.

### 5.3.2 Where are all the oblate planets?

We have shown that as many as several tens of exoplanets should have levels of oblateness in the 30-100ppm range at observing cadences of $< 10$ minutes. While a small signal, this is certainly within the capabilities of facilities such as *Kepler*, as shown in figure 5 of Koch et al. [2010]. To date, there is only a small handful of planets which have had tentative detections of oblateness, as mentioned in section 5.2. This begs the question of why there haven't been a larger number of conclusive

oblateness measurements. One explanation for this is that exoplanets are simply not oblate, which would make the case of Saturn's oblateness an extreme outlier, or that oblate planets happen to be found around dimmer stars with lower photometric precision. Another option which we will explore in the next section is that the transit parameters of associated with a spherical planet model are able to mimic the signature of oblateness and thus compensate for it.

## 5.4 Mapping the Degeneracies Between Oblateness and Transit Parameters

As shown in the previous section, the typical deviations induced by oblateness will be in the best case a few hundred ppm, and much more typically well below 100 ppm. The additional fact of the signal being confined solely to the limbs of a transit means that for many planets, depending on the duration of the transit and the cadence at which the observations are taken, only a handful of data points may be useful in detecting oblateness. It is thus not surprising that when analysing an exoplanet transit the standard practice is to assume a perfectly spherical planet. Nevertheless, we propose that even in cases of non-detection oblateness may have a significant effect on parameter retrieval.

### 5.4.1 Bias on retrieved parameters during a transit analysis

Parameters of a model are often degenerate with one another, and given the low signal strength of oblateness it's possible that other transit parameters may be able to compensate and mask an oblateness signal at current SNR. Assuming a planet to be perfectly spherical could then introduce a bias when fitting for parameters such as inclination or the semi-major axis of the planets orbit. The goal of this section is to quantify such an effect through a series of simulation-retrieval studies. We note that in Barnes and Fortney [2003] a similar analysis was done to study the biases of assuming an oblate planet to be spherical. However in that case the effect was

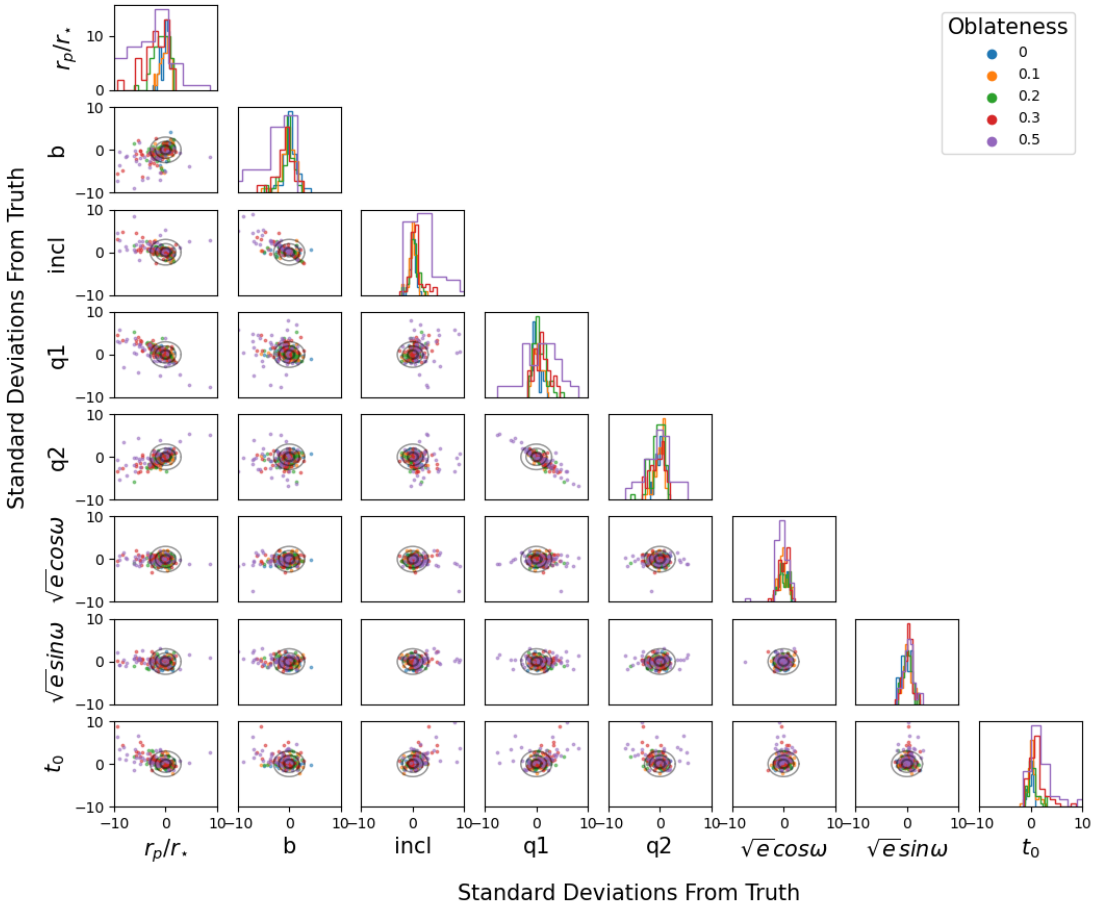


Figure 5-5: Corner plot showing the deviations for each parameter from their truth values, in units of standard deviations of the posterior. Colors represent different levels of oblateness. The black circles show boundaries of 1, 2, and 3 standard deviations.

only studied for a single planet, HD209458b [Charbonneau et al., 2000], whereas our aim is to expand this analysis to a wider set of planets to understand the effect more globally. We follow the methodology of de Wit et al. [2012] which looked at the degeneracies between the orbital properties of a planet and its potential to have non-uniform surface brightness, measured through minor variations during eclipse.

We first generate a set of lightcurves for a sample of oblate planets. The planet parameters we use come from the exoplanet archive list of confirmed transiting planets, as was done in the previous section. The parameter space of possible planet and

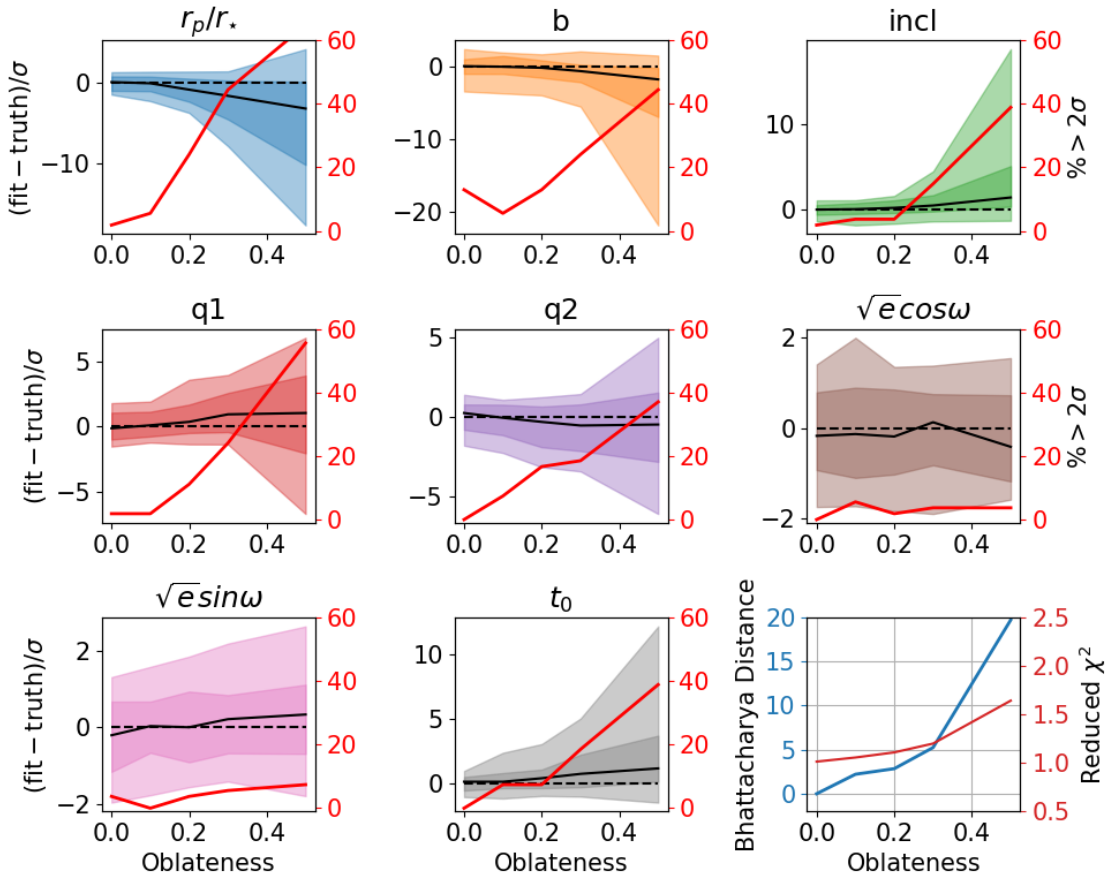


Figure 5-6: Results of fitting a spherical planet model to simulated data of an oblate planet, using orbital parameters for the 100 largest (in terms of planet to stellar radius) Kepler planets with periods greater than 10 days. The left vertical axis in each plot represents the number of standard deviations between the truth and fitted value for the planet to stellar radius, impact parameter, inclination, quadratic limb darkening parameters, eccentricity parameters, and transit center. Dark and light regions represent where 65% and 95% of the planets in the sample appear. The right vertical axis and solid red line show the percentage of planets for which the retrieved parameters deviate by >2 standard deviations. The bottom right panel shows the median values of the reduced $\chi^2$ in red, as well as the median Bhattacharyya distance in blue.

orbital configurations is large, and so we restrict our study to known planets, which at the time of writing is a sample of greater than 4000 objects, and from these we take the 100 planets with the largest planet to stellar radius ratios (since the oblateness signal scales proportionally with radius). For those planets, we generate 1 minute cadence lightcurves with oblateness value from the range of 0, 0.1, 0.2, 0.3, and 0.5. We

add Gaussian noise with a standard deviation of 50ppm for each data point. We then run a Monte-Carlo Markov-Chain (MCMC) fit to the synthetic data using the emcee package [Foreman-Mackey et al., 2012], assuming a spherical planet model during the fit.

### 5.4.2 Description of Fit

We choose to fit for planet-to-stellar radius ratio, transit impact parameter, inclination angle, eccentricity, argument of periastron, as well as two parameters of a quadratic limb darkening model, using the q1 & q2 parametrization of Kipping [2013] and finally center of transit. We hold the orbital period fixed. We note that some of these parameters, specifically the eccentricity, could be constrained by radial velocity observations which would be unaffected by planetary shape variations. Additionally, for the fits described in this section we hold the obliquity angle of the planet fixed at 45 degrees. We ran a similar analysis for a fixed obliquity of zero which we discuss further down.

Regarding the radius of the planet, we do not fit for it directly but rather scale it by the appropriate oblateness factor as previously mentioned. If we fit for the radius directly, we would see deviations on the order of 20% or more as oblateness increased (in order to match the transit depth), however this would be somewhat misleading. While it is true that the equatorial radius would differ by such an amount, the surface area (and thus total occulted stellar area) would remain relatively unchanged. This means that a 20% change in equatorial radius between a spherical and oblate planet does not represent the same magnitude of change between two spherical planets whose radii differ by 20%. By fitting for the scaled radius, any deviation we see is a more meaningful difference in quantities such as the total surface area or volume of the planet.

For a given planet we compare the posterior distributions of each fitted parameter to the known value that was used to generate the simulated data. We calculate the median value of the posterior distributions as well as the standard deviation. We then calculate by how many standard deviations the fitted parameter value is from the true

parameter used when generating the data. If one assumes Gaussian uncertainties for the fitted parameters, then for an appropriate model it would be expected that ∼68% of the time the true parameter should be within one standard deviation, ∼95% of the time within two standard deviations and ∼98% of the time within three standard deviations.

### 5.4.3 Results of injection-retrieval tests

The compiled outputs of our set of fits is shown in figures 5-5 & 5-6. As expected, for low oblateness values the fitted parameters cluster around the true value, with a spread of ∼ 2 standard deviations. This is the statistically expected result for a model which matches the data.

#### 5.4.3.1 Biases on radius, impact parameter, and inclination

We observe significant biases with clear trends for the equatorial radius $r_p/r_\star$, impact parameter (b), and inclination (incl). For oblateness values greater than 0.2, we see that the first two of these parameters become biased towards smaller values, while inclination is biased towards larger values (i.e. the orbits tend towards the observer line of sight). We also see the distribution of fit parameters widen, which could be an indication that the errors on these parameters are being underestimated.

For $(r_p/r_\star)$ we find that 20% of the fits deviate by $> 2\sigma$ at f = 0.2, with this number increasing to >60% as the oblateness increases. For the impact parameter we find that 10% of the fits deviate by $> 2\sigma$ increasing to 40% at f = 0.5, and for inclination we find that from f = 0.2 to f = 0.5 the percentage of fits $>2\sigma$ rises from ∼5% to 40%.

A potential explanation for this is the effect of oblateness at the very beginning and end of transits. Compared to a spherical planet, and based on its orientation, an oblate planet will begin transiting slightly earlier and end transiting slightly later. This leads to a change in the overall duration of transit, which we see here is being compensated for by the three parameters which directly affect the length of the transit

chord.

In figure 5-5 we note a significant correlation in particular between the impact parameter and inclination of the planet. We observe a similarly strong correlation between the inclination and radius ratio.

For the specific case of HD209458b, it was found in Barnes et al. [2007] that when fitting a spherical planet model to a simulated lightcurve of an oblate planet the impact parameter tended towards a critical value of $b = 0.707$ in order to account for the change in ingress/egress duration. We do not observe a similar trend for the larger sample of planets and parameters we have studied in this work. One important distinction between the two analyses is that we have included additional parameters in our fit, namely the inclination. The effect of this is that we have additional ways to account for the change in transit durations. Thus we find differing trends in the combination of impact parameter and inclination which can account for the variations between spherical and oblate lightcurve models.

#### 5.4.3.2 Biases on limb darkening coefficients

For both limb darkening parameters q1 and q2 there is no clear upwards or downwards trend, although we do see a widening of distributions (although with a smaller amplitude of deviations compared to the other parameters). If a change in transit duration is indeed the cause of any observed biases, this would make sense given that the limb darkening parameters are unable to alter the length of the transit chord and are less strongly biased. Despite a lack of a clear trend however, we still find that a significant number of fits deviate by more than 2 standard deviations, indicating that the limb darkening coefficients are still affected by the change in transit shape to some degree.

For q1 we find that 10% of the fits deviate by $> 2\sigma$ at f = 0.2, increasing to 60% as the oblateness increases towards 0.5. For q2 we see a larger initial value, with $\sim$20% of fits deviating by $> 2\sigma$ at f = 0.2, increasing to $\sim$40% at f = 0.5.

#### 5.4.3.3 Biases on transit center

In the case of non-zero obliquity, we observe a significant shift in transit center for large oblateness values. As will be discussed in section 5.6.2, this is an expected effect due to the asymmetry in ingress and egress for a tilted planet. As previously mentioned, we ran a similar analysis for a fixed obliquity of zero. In this case, the transit will always be perfectly symmetric about its center, and thus no shift in transit center is expected which is what was observed. We note here that the direction of the shift is always the same. This is due to the fact that the obliquity is the same for all planets, and we assign the impact parameter to positive values. Thus the asymmetry induced in the lightcurve will always be in the same direction with regards to ingress and egress. For f = 0.2 $\sim$ 10% of fits deviate by $>2\sigma$, increasing to 40% as f approaches 0.5.

#### 5.4.3.4 Biases on eccentricity

For eccentricity and the argument of periastron $\omega$ (parameterized as $\sqrt{e}cos\omega$ and $\sqrt{e}sin\omega$) we find that the retrieved values are statistically consistent with the values used to generate the data (i.e. all samples are $<3\sigma$). We note however that this is likely to be a limitation of the data sets being analysed, which are single transit observations. Eccentricity can be more tightly constrained when additional information such as stellar density [Dawson and Johnson, 2012] and planetary eclipses are used [Winn et al., 2007]. We thus would expect to obtain significant biases on these parameters from perturbed ingress/egress for the increased precision derived from joint fits of primary eclipses, secondary eclipses, and/or radial velocity measurements–similarly to the point made in Fig. 4 of de Wit et al. [2012].

#### 5.4.3.5 Goodness of Fit Metrics

In addition to having measured a clear bias for certain parameter when assuming a spherical planet model, we also check the goodness of fit statistic to asses if, given current precisions, there exists a range of oblateness leading to perturbations in the

transit shape which cannot be compensated for by the orbital parameters. We show in the bottom right panel of figure 5-6 the median value of the reduced $\chi^2$ across all planets in the sample for differing oblateness values. We note that this is measured only using data points during ingress and egress of transit, as the rest of the lightcurve is expected to be the same for both spherical and oblate planets. As shown, the value remains close to one, increasing only for values of oblateness approaching 0.5 (although still remaining below $\sim$1.5). In the same panel we also show the mean value of the Bhattacharyya distance ($D_B$), which is a metric for comparing the similarity of two distributions defined as

$$D_B(p,q) = -\ln\left(\Sigma_i \sqrt{p(\theta_i)q(\theta_i)}\right) \tag{5.8}$$

for two probability distribution p and q over a set of parameters $\theta$. The value shown for a given oblateness is a comparison between the multi-dimensional posterior distribution of that value and the posterior distribution for zero oblateness. We see a clear trend to higher values as the oblateness increases, indicating a statistically significant variation between the two distributions. Thus we find that assuming planets to be spherical can statistically bias results in a way that does not set off the most common alarm for improper models.

## 5.5 The sensitivity of oblateness retrieval & planet populations

Measuring the oblateness of an individual planet is difficult and requires very precise and well-sampled observations. The approach taken in this section is to study ensembles of planets in order to determine if planets can be separated into populations of oblate and non-oblate planets. For example, as given by equation 5.12, the tidal spin-down timescale varies strongly with orbital period (to the $4^{\text{th}}$ power). Planets below a period of 15 days are expected to have very short spin-down timescales, implying they will be tidally locked to their host star and will have slowed down enough

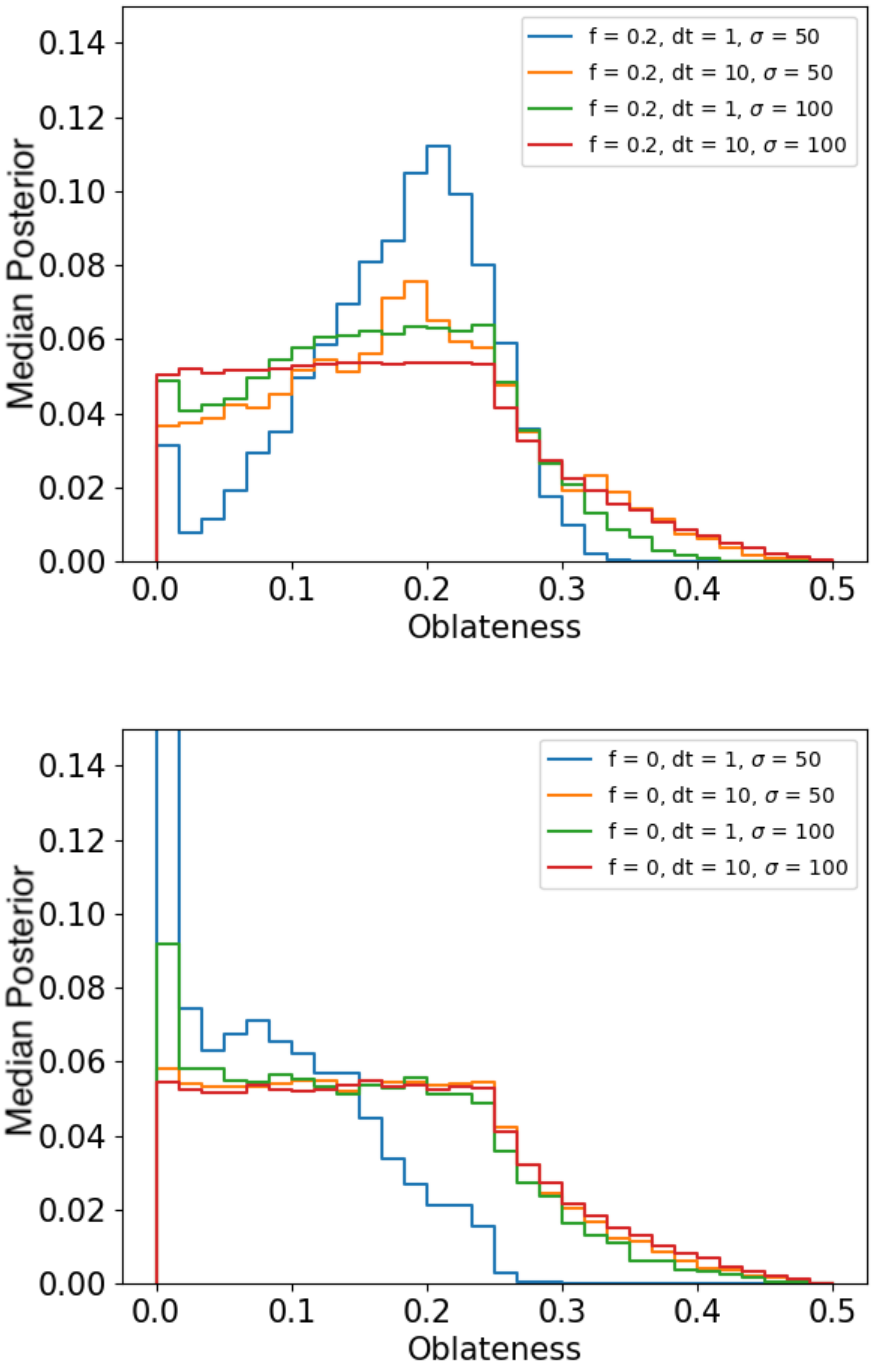


Figure 5-7: The results of MCMC retrievals to two populations of planets, using a model which accounts for oblateness and obliquity. On the top is a population where each planet has an oblateness value of 0.2, and the bottom plot is a population of planets with zero oblateness. For each group, we test difference levels of observing cadence (dt in minutes) and Gaussian noise level ($\sigma$ in ppm)

to have effectively zero oblateness. For planets with an orbital period above 15 days with much longer spin-down times, they are expected to have retained a high rate of rotation from their formation and thus have non-zero oblateness. In addition to searching for oblateness across a population, we also measure the sensitivity of oblateness fits to the quality of the data, which we characterise by SNR and time sampling of data points.

### 5.5.1 Synthetic populations

We generate 200 planets whose periods, radii, semi-major axis, and inclinations are drawn from the population of known transiting planets. For a given choice of observing cadence, oblateness factor, and noise level we simulate an oblate lightcurve as in previous sections. We do this process for two populations of planets with identical planet parameters, with one having zero oblateness and the other having an oblateness of 0.2 for all planets.

Once we have these lightcurves, we run an MCMC retrieval on them using the Allesfitter package [Günther and Daylan, 2021, 2019]. We include in Allesfitter our own oblateness model, which allows us to fit for the oblateness parameters f (oblateness) and $\theta$ (the obliquity of the planet).

We show in figure 5-7 the results of this analysis, in particular the posterior distributions retrieved for the oblateness. We note that in our analysis we reparametrize f and $\theta$ as $\sqrt{f}\cos\theta$ and $\sqrt{f}\sin\theta$, similar to the parametrization often used when fitting for eccentricities [Van Eylen and Albrecht, 2015]. These reparametrized versions of the shape parameters do not have hard boundaries at 0 and instead vary from -1 to 1, which removes the bias of forcing oblateness to be positive.

We first note that in the case of zero oblateness (the right panel), the general trend is a flat posterior below a certain value, in this case around $f = 0.25$, followed by a sharp decrease beyond that. The model is able to confidently rule out high oblateness values, which in turn can be used to rule out large rotational periods of planets. Below the cutoff point the model is less sensitive to oblateness. We see that for the most constraining set of parameters, namely a short observing cadence of dt

= 1 minute and a small noise level of 50 ppm, the model is able to exclude smaller oblateness values more confidently.

In the left panel of figure 5-7 we see two cases emerge, depending on the noise properties and time sampling. For the shortest time sampling and lowest noise level, the model is able to retrieve the population oblateness level of 0.2. As the noise level increase along the with the time sampling, the posterior gradually shifts to that of a zero oblateness population. Thus we see that between 50-100 ppm, and between 1min - 10 min observing cadence there is a cutoff point where oblateness shifts from being confidently detectable to completely undetectable.

### 5.5.2 Sensitivity of oblateness fits to data quality

In order to investigate the shift in retrieval seen, we sample a grid of data quality, which we characterise by two metrics. One metric is the signal-to-noise ratio, which in our case we take to be the transit depth divided by the amplitude of Gaussian noise. The other value we use to quantify the data quality is the number of data points observed during ingress, which is calculated as the duration of transit divided by the observing cadence. For each data point sampled, we run an MCMC retrieval as described above, and calculate the oblateness value which encompasses 95% of the posterior distribution (which is often asymmetric due to the boundary at f = 0).

The results of this are shown in figure 5-8. In this case the data being fit has an oblateness value of zero, i.e. spherical planets. Thus we are demonstrating the ability of the model to confidently rule out non-zero oblateness. We see that for low SNR values and a low number of transit data points, the model is unable to rule out values of oblateness below 0.3 at the one standard deviation level, and f = 0.4 at the $2\sigma$ level. It is only for very high SNR values > several hundred and more than at least 10 transit points that the model is even able to rule out oblateness values of 0.2 or greater. We note that the oblateness value within each cell varies to a certain degree amongst the different planets. This is due to the fact that properties such as the impact parameter also play a role in measuring oblateness, however here we focus on the bulk results marginalized across such parameters.

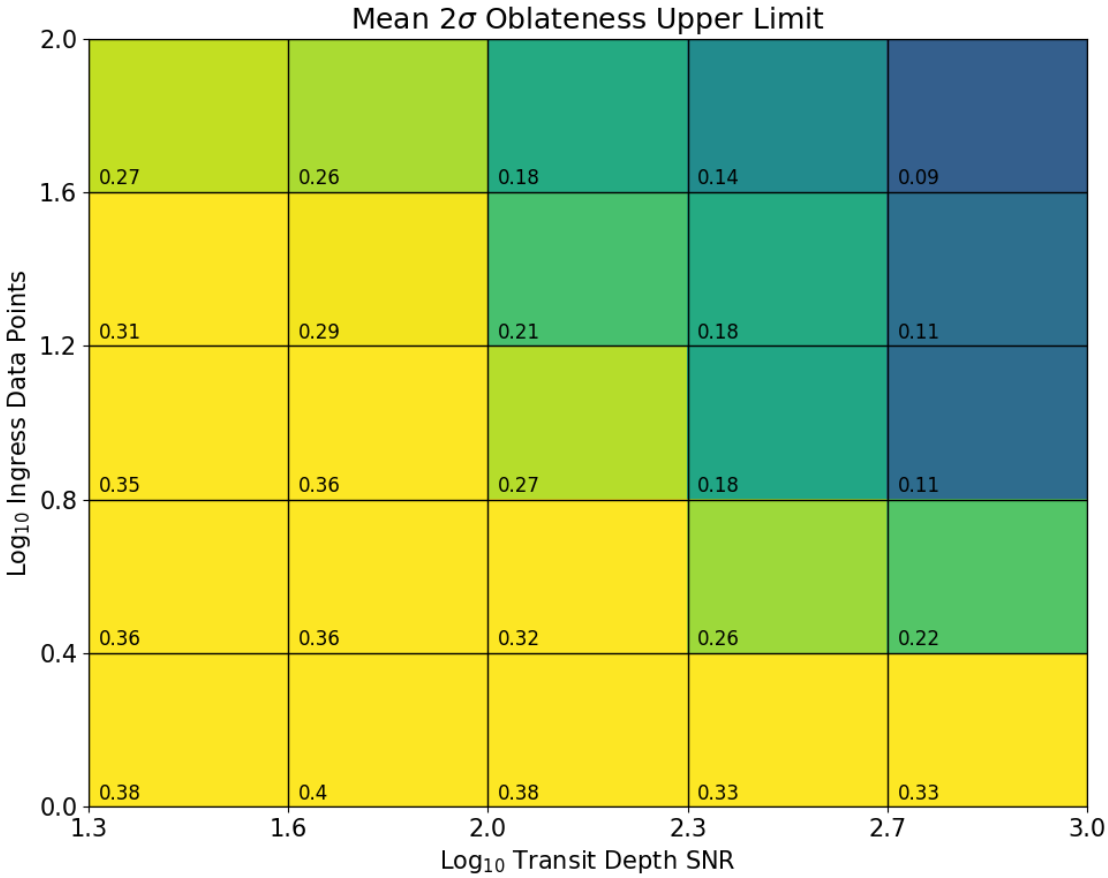


Figure 5-8: The median $2\sigma$ oblateness upper limit values across a sample of planets retrieved when fitting an oblate planet model to synthetic data sets with zero oblateness (values shown in grid cells). The x axis indicates the transit depth divided by the amplitude of Gaussian noise. The y axis shows the duration of transit ingress divided by the observing cadence.

The significance of this is that the majority of transiting planet observations are completely degenerate between a spherical planet and a planet having an oblateness of $\lesssim 0.25$. In the context of section 5.6.1 for example, this implies that analysis which rely on relative density errors below $\sim 15\%$ are over-confident, in the case of planets which have the potential to be oblate (i.e. planets which are unlikely to be tidally locked).

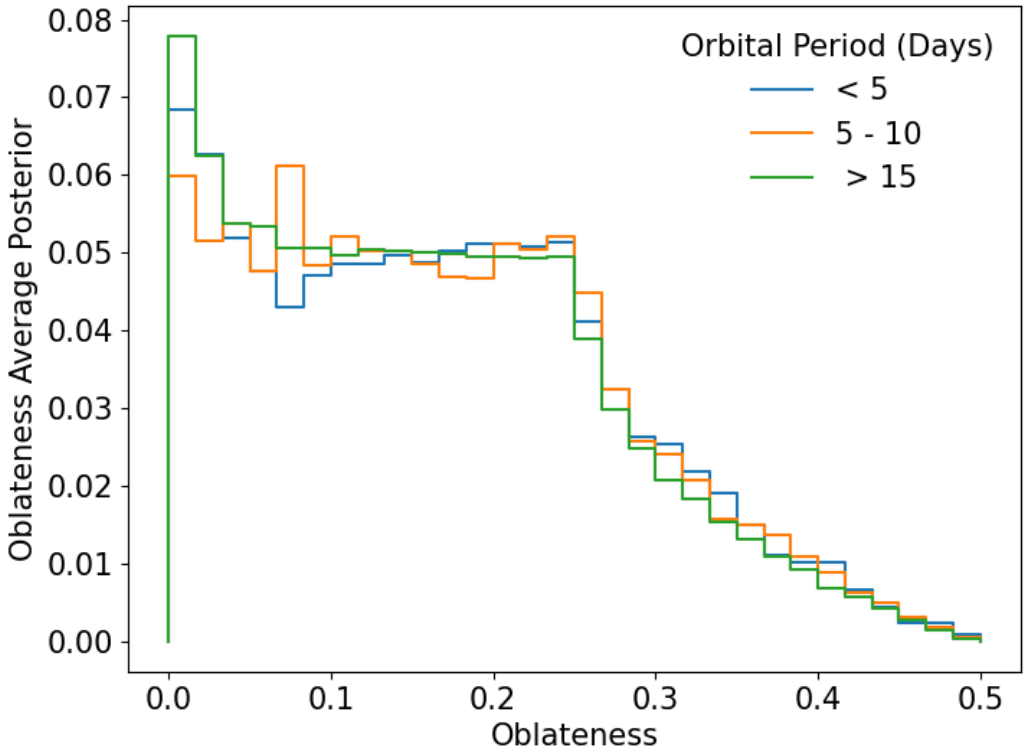


Figure 5-9: Oblateness posteriors when fitting confirmed Kepler planets, separated by orbital periods.

### 5.5.3 Oblateness fit of long and short period Kepler planets

We now turn to the potential oblateness of planets discovered by the Kepler survey. The reason for picking this as our sample is the large number of planets it contains, the fact that many of them were observed at a short (1 minute) cadence, the duration of the survey which provides a large number of transits for most planets, and finally the SNR it provides for most planets, which far surpasses ground based and many spaced-based transit observations.

In contrast to previous studies which have searched for oblateness in individual planets, our goal is to see if it is possible to highlight populations of planets which globally either do or do not exhibit oblateness. Given that planetary rotation is the root of the signal, we propose to separate planets into fast and slow rotators, which would then translate into populations of high and low oblateness planets.

We download the short cadence lightcurves of all planets with radii larger than a cutoff value of 6 $R_e$, to exclude rocky planets with low tidal dissipation factors (and thus extremely short circularization timescales). We do this using the lightkurve package [Lightkurve Collaboration et al., 2018], and extract the PDCSAP lightcurves. We then run them through a suite of post-processing and normalizing steps. We first remove points which have bad data quality labels. We next identify all transits of a system, including those with multiple planets. We chose not to exclude these systems, although we do remove observations where two transits come within a multiple of 3 transit durations of one another. We then apply a Savitzky-Golay filter to remove long term variations in the lightcurve. We mask the known transits while doing this in order to not have them bias the detrending. We next correct for systems which exhibit large TTVs, which in some cases can be on the order of tens of minutes. We do by this running an MCMC fit for each individual transit, holding fixed all known transit parameters and allowing only the transit center and depth to vary.

Once we have measured transit centers for all planets, we repeat the previous detrending steps, using the shifted transit centers to accurately mask out the transits when fitting for low frequency lightcurve trends. Once this is done we phase fold the data into a single lightcurve, which is what is finally used in the fitting routine. We run an MCMC fit to the data utilizing the Allesfitter package as we did in the previous sections.

We show in figure 5-9 the stacked posterior distributions for planets with periods either above or below 15 days. We find similar distributions as in the previous section for the cases in which the fit was unable to identify significant oblateness. The fact that both distributions look similar indicate that the sample of Kepler planets does not exhibit an oblateness bias or grouping based on their period. We analyzed different groups of periods, cutting below 10 days or above 20, and similarly found no biases or differences between any groups.

We also see the same cutoff at oblateness values above $\sim$0.25, again as in the previous section. This indicates that the MCMC disfavors such high levels of oblateness. High oblateness values in general are unlikely, due to the projection effects

described in section 5.3 and Appendix A. In section 5.3.1 we showed the oblateness signal induced among known planets, and show that very few planets produce a signal beyond 100ppm. However for many planets in the Kepler survey the noise level is on the order of 100s of ppm. Thus while we are able to exclude high values of oblateness in general, we find that the sensitivity factors described in the previous subsection limit the ability to detect or rule out more moderate values of oblateness.

We do note a slight increase in the posterior for oblateness values $< 0.05$ for planets with orbital period $> 15$ days. This is again most likely due to increased sensitivity discussed in the previous section, given that planets with larger orbital periods will have increased sampling during ingress / egress and also tend to be larger. Thus we do not attribute this as indicating that larger period planets have lower oblateness.

## 5.6 Discussion

So far we have studied the effects on standard transit analysis when allowing for an exoplanet to be oblate instead of spherical. If not properly taken into consideration, ignoring the potential of a planet to be oblate could introduce additional biases into more sophisticated exoplanet analysis. This highlights a main point of this work, which is that as the quality of data continues to improve, features such as oblateness which were once undetectable may begin to bias and effect a wider range of conclusions one may make about explanatory systems. In this section we consider the measurement of bulk densities of planets, as well as transit timing variations and the ways in which oblateness may impact any conclusions drawn. We also describe a metric for quantifying which planets are more or less likely to exhibit oblateness, based not only signal strength but also on their likelihood to be oblate in the first place.

### 5.6.1 The relative uncertainty of bulk densities

When discussing radii in section 5.4, care was taken when comparing a spherical planet described by just one radius to an elliptical planet with two radii. However for

a quantity such as the density of the planet, there is less of a distinction since the bulk density is typically the quantity of interest. We will illustrate that any analysis which utilizes precise density measurements may be subject to biases due to the shape of the planet.

Consider a planet which has an oblateness f, which induces oblateness at a level that is too low to be detectable or even to induce the biases previously mentioned. The depth - radius relation for an oblate planet is given by $\delta = r_{eq} r_{pol} = r_{eq}^2(1-f)$. This would translate to a measured planet volume of

$$Vol_{ob} = \frac{4\pi}{3} r_{eq}^2 r_{pol} = \frac{4\pi}{3} r_{eq}^3 (1-f) = \frac{4\pi}{3} \frac{\delta^{3/2}}{(1-f)^{1/2}} \tag{5.9}$$

Assuming mass measured by radial velocities to be independent of shape, we can compare the inferred volumes of a spherical and oblate planet, and thus their densities, as

$$\frac{\rho_{circ}}{\rho_{ob}} = \frac{4\pi}{3} \frac{\delta^{3/2}}{(1-f)^{1/2}} \frac{3}{4\pi} \frac{1}{\delta^{3/2}} = \frac{1}{(1-f)^{1/2}} \tag{5.10}$$

For an oblateness of even just $f = 0.1$, this would translate to a true density that is 5% smaller than the density inferred for a spherical planet. An oblateness of $f = 0.2$ would mean a discrepancy of almost 11%.

In figure 5-10 we compare this oblateness induced density variation to the relative uncertainty of the density of known planets. We take all planets from the exoplanet archive which have a reported value of both physical radius and mass, as well as reported uncertainty values. We calculate their relative density errors, and find for an oblateness of 0.2, up to 20 planets would have their density differ by more than their relative uncertainty. For an oblateness of 0.3, that number rises to almost 60. It was demonstrated in section 5.5.2 that at low data sampling and/or transit SNR it is impossible to rule out oblateness values less than 0.3 at the $2\sigma$ level. This in turn imposes an accuracy wall on relative uncertainty of a planet's bulk density at the level of 10$\sim$15%.

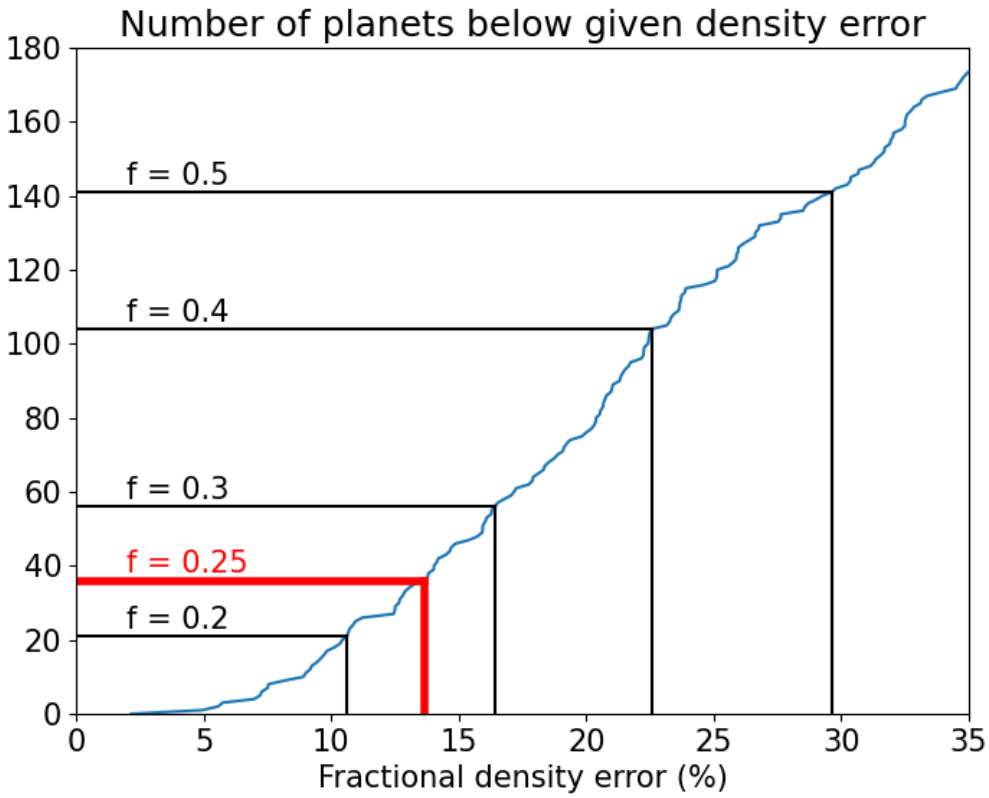


Figure 5-10: The cumulative number of planets with a fractional density error below a certain value (blue line). The black lines show the percentage by which the density would change if a previously assumed spherical planet were to be oblate to a certain degree, calculated using equation 5.10. The red line indicating a value of f = 0.25 is in reference the limits of current observations discussed in section 5.5.2.

### 5.6.2 TTV-like Signal induced by Oblateness

Thus far we have considered the oblateness of a planet to be constant, however it is possible that a planet with a non-zero obliquity angle will precess over time as it orbits its host star and exchanges angular momentum. For uniform precession in a fixed orbit, the precession period is given by [Ward, 1975]

$$P_{prec} = 13.3 \text{ years} \times \left(\frac{P_{orb}}{15 \text{ days}}\right)^2 \left(\frac{10\text{hr}}{P_{\text{rot}}}\right) \left(\frac{\lambda/J_2}{13.5}\right) \frac{1}{\cos\theta} \tag{5.11}$$

where the value of 13.5 comes from the estimate of $\lambda/J_2$ for Saturn [Ward and Hamilton, 2004]. In this equation $\theta$ is the obliquity angle of the planet, which we

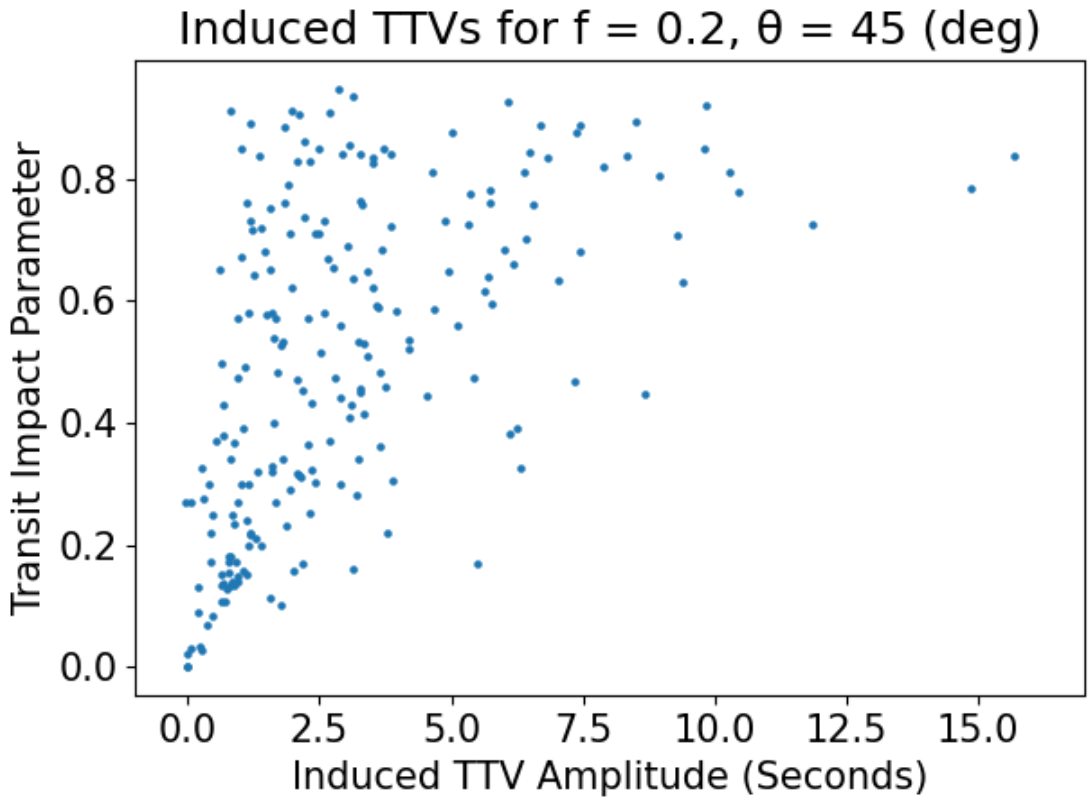


Figure 5-11: The distribution of retrieved TTV amplitudes induced by asymmetry stemming from oblate planets with f = 0.2 and $\theta = \pi/4$. The y axis shows the impact parameter of the transiting planets, which we expect to be correlated with the asymmetry signal.

recall is the angle between the polar axis of the planet and its orbital plane. As mentioned in section §5.3, as the orientation of an oblate planet changes in space, an observer will see different elliptical projections on the sky plane. This will lead to a time varying projected oblateness and obliquity, which will in turn lead to a time varying transit shape.

The focus of Biersteker and Schlichting [2017] was to try and detect oblateness due to do variations in the depth of a planets transit, caused by a time varying projected surface area (including a change in both the projected oblateness as well as equatorial radius). A secondary effect which was first mentioned in Carter and Winn [2010b] is that the duration of the transit may change as well, which could mimic the appearance of a transit timing variation (TTV) signal.

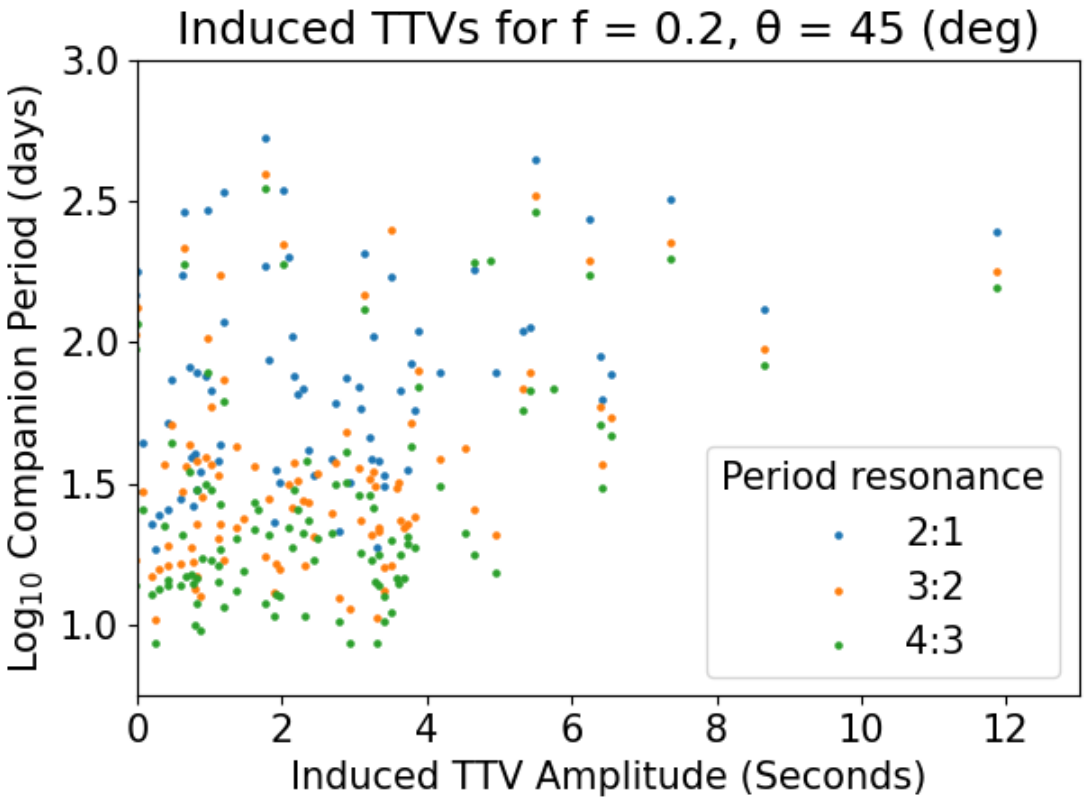


Figure 5-12: The orbital periods of a companion that would be needed to induce the TTV signals seen, based off the precession period and possible orbital resonance.

If an oblate planet has a non-zero impact parameter and obliquity, then it will exhibit asymmetry in ingress and egress (as in figure 5-1). Thus when attempting to fit a spherical transit model to the lightcurve of an oblate planet, the result could be a perceived shift in the center of the transit. This effect is typically attributed to another planet in the same system gravitationally perturbing the observed planets orbit [Agol and Fabrycky, 2018]. Thus attempting to fit a spherical planet model to a precessing oblate planet could potentially lead one to conclude the existence of an additional planet causing timing variations.

We perform a set of injection retrieval tests, attempting to measure a shift in the center of transit. We simulate a transit lightcurve of an oblate planet across multiple epochs while altering the obliquity over time according to its precession period. As the true obliquity of the planet changes over time, we also update the projected obliquity

and projected oblateness. We must additionally account for the change in projected equatorial radius of the planet, which we do using equation 4 of Carter and Winn [2010b]. The formula provides the relative transit depth as a function of oblateness and inclination parameters.

We use the same sample of planets as in previous sections in order to determine the degree to which the current population of planets may be affected. We note that the precession period given in equation 5.11 is only an estimate, and further effects such as interactions with other planets in the same system could disrupt or alter the precession in someway [Saillenfest et al., 2019]. We hold the parameter $\lambda/J_2$ fixed to the value of 13.5 for Saturn, and note that the precession period scales linearly with it. We sample the obliquity of the planet from three value spaced out between 0 and PI/2. In the case of of either zero or maximal (PI/2) obliquity, there would be no ingress/egress asymmetry and thus no induced TTV signal. For these values we find that most precession periods range from 10 - 100 years, although there are some planets with potential periods of only a couple years or less. For most planets such an effect will thus occur on too long of a timescale to be observable. As the field of exoplanetary science enters its $4^{th}$ decade however, it becomes more and more feasible to observe such a long baseline transit shift and falsely attribute it to a long period companion.

Many of the trials return a constant transit center as the best fit, indicating no detectable variation. For a significant number of cases however the best fit is a clear sinusoidal variation in the transit center, as one would expect from TTVs. For these cases we fit a sinusoid to the time varying signal and retrieve the amplitude of the variation. In figure 5-11 we show the distribution of these amplitudes, in units of seconds, as a function of the impact parameter of the transit. We note a correlation with the impact parameter, which is extremely tight for values less than 0.15, and then widens above that. We find that for an underlying oblateness of 0.2 and an obliquity of 45 degrees, the scale of the deviations is on the order of several seconds, with the peak value being upwards of 15 seconds (and thus 30 seconds peak to peak). While small, transit deviations have been measured at the level of seconds, for example

in WASP-12 b [Maciejewski et al., 2016].

In figure 5-12 we show the possible orbital periods of the companion planets that would be required to induce the observed TTV signal. This is calculated using equations 6 and 7 of Lithwick et al. [2012], where we substitute the precession period of the oblate planet for the super-period of the TTV signal. We calculate a companion period under the assumption of a 2:1, 3:2 and 4:3 period resonance. The periods we find span the range of 10 - 1000 days.

As mentioned we repeated the above analysis while varying the obliquity angle of the planet. This was done to ensure the results are consistent with the expectation that for obliquity angles further from 45 degrees the induced amplitudes should be smaller due to the reduced asymmetry between ingress and ingress. This is indeed what was found, and in particular for an obliquity of zero/90 degrees (in which the entire transit is perfectly symmetric about its midpoint) there were no statistically significant transit center variations.

### 5.6.3 A metric to identify prime oblateness candidates

In this section we define an oblateness observability metric to determine which planets are the most ideal for a targeted study of oblateness. It is built in such a way to favor planets which would not only have a large oblateness signal, but which are also likely to be oblate in the first place. The key factor we use to determine if a planet is likely to be oblate or not is the age of its host star. As a planets rotation slows down over time due to tidal de-spinning, its oblateness similarly decreases. The timescale for a planet to spin down and become tidally locked can be estimated by:

$$\begin{aligned}\tau_{spin} = 1.22 \text{ Gyr} \times \left(\frac{M_p}{M_J}\right)\left(\frac{Q_p}{10^{6.5}}\right)\left(\frac{\lambda}{0.25}\right) \\ \times \left(\frac{P_{\text{orb}}}{15 \text{ days}}\right)^4 \left(\frac{R_J}{R_e q}\right)^3 \left(\frac{10hr}{P_{\text{rot,i}}} - \frac{10hr}{P_{\text{rot}}}\right)\end{aligned} \tag{5.12}$$

which is derived by integrating the spin down rate of a planet as described in

Goldreich and Soter [1966]. The quantities $Q_p$ and $\lambda$ are the tidal dissipation factor and normalized moment of inertia $\lambda = I/(M_p R_p^2)$. If the mass of the planet is known, one can additionally directly calculated the rotational period required for various levels of oblateness.

Given the uncertainty and difficulty in calculating Q, we conservatively set it to $10^{6.5}$, which is above the estimate for the solar system values of Saturn and Jupiter, which are typically on the order of $10^4$ and $10^6$ respectively [Storch and Lai, 2014]. By over-estimating Q, we in turn will likely be over-estimating the tidal spin-down timescale. Thus, we can be confident that systems which are older still than this estimate will have already spun-down and are unlikely to be oblate. For the parameter $\lambda$ we adopt the commonly used value of 0.25 for gas giants. As a comparison, the Darwin-Radau equation[3] gives a value of $\lambda = 0.22$ for Saturn, and $\lambda = 0.27$ is calculated for Jupiter from Juno gravity measurements [Ni, 2018].

Conversely, planets whose associated star has an age that is well below 1 Gyr can be assumed to not have had enough time to spin down and may still have a high rotation gained during formation. We incorporate this information using a sigmoid function, defined as $\sigma(x) = 1/(1 + e^{-x})$ which is a smoothed out step function. We scale the step width by the uncertainty of the stellar age, to allow for flexibility for spin down estimates near the stellar age.

We multiply the factor for the timescale by both the RMS variation induced by oblateness (as described in section 5.3.1), and additionally by a term which is proportional to the expected SNR of a detection, for a given waveband. This takes the form

$$Metric = RMS_{ob} \times 10^{-M/5} \times \sigma((Age_\star - \tau_{spin}^{upper})/\sigma_{Age_\star}) \tag{5.13}$$

Where M is the magnitude of the host star in a given waveband, and the exponential term signifies the square-root SNR estimate of a given number of photons.

[3] $\frac{J_2}{f} = -3/10 + 5/2\lambda - 15/8\lambda^2$

| Planet | Period (days) | Radius (Rj) | K-Mag | Ob. Amp (ppm) |
|---|---|---|---|---|
| TOI-1899 b | 29.02 | 1.15 | 10.51 | 110.45 |
| TOI-1278 b | 14.48 | 1.09 | 9.74 | 57.67 |
| Kepler-699 b | 27.81 | 1.46 | 13.67 | 104.8 |
| CoRoT-10 b | 13.24 | 0.96 | 11.78 | 66.27 |
| TOI-837 b | 8.32 | 0.77 | 8.93 | 29.19 |

Table 5.1: Top ranked planets according to oblateness metric

The $RMS_{ob}$ term is the same ingress/egress deviation measured in the section 5.3.1.

## 5.7 Conclusions

In this work we have analyzed the effect of planetary oblateness on the analysis of transit lightcurves, primarily through the use of injection-retrieval studies of spherical / oblate planets using spherical / oblate transit lightcurve models. We first estimated the level of variation between the lightcurves of a spherical and oblate planet which otherwise have identical orbital and planetary parameters. We find that for most planets with periods greater than 10 days, this variation is at the 10-100ppm level. This result is obtained across a sample of planets which range in size, orbital period, impact parameter, and semi-major axis, which all affect the structure of an oblate planets lightcurve.

Given that this is a level at which instruments such as *Kepler* are capable of reaching, we then studied effects which may obscure oblateness signals, notably compensation by orbital parameters [Barnes and Fortney, 2003, de Wit et al., 2012]. In addition to SNR, we also analyzed the effects of time sampling on the ability to robustly measure or rule out oblateness. What is found is that ruling out Saturn like oblateness (f = 0.1) at the $2\sigma$ confidence level requires a sampling of $> 10$ data points during ingress/egress and a transit depth which is $\geq 100$ times the level of uncorrelated Gaussian noise. Combining both of these effects implies that for many planets there will be a sensitivity wall which limits the ability of a retrieval method such as MCMC to detect oblateness. When analyzing a sample of short cadence Kepler observations, we find this limiting factor to be in the range of f = 0.15 - 0.25. A

consequence of this result is a limit on the accuracy of the bulk density which can be measured for planets which are potentially oblate. We find that relative density uncertainties below 10% for planets with periods $>$ than 10 days are likely to be overestimated, given the difficulty in ruling out oblateness levels below f = 0.2. If we extend this statement to planets which have been distorted through other processes such as tidal bulging, then the effect may be prevalent for planets with shorter periods as well.

In addition to density, we also find that attempting to fit spherical transit models to data which come from oblate planets produces fits which are both statistically consistent with regards to the reduced $\chi^2$, but which also deviate significantly from the values used to generate the data. For an oblateness approaching 0.5, we do find that the reduced $\chi^2$ begins to approach 2, indicating that the model is insufficient for the data. However in the range of f = 0.1 - 0.3, we find that it remains close to 1, while the Bhattacharyya distance becomes $\gtrsim 3$ indicating deviation from the true parameter distributions.

The planet radius, inclination, impact parameter, and transit center all demonstrate biasing trends as oblateness increases, while the two parameters of a quadratic limb darkening law deviate symmetrically about the true value. The eccentricity and argument of perihelion however remain unbiased and consistent with the truth values, even for large values of oblateness. This is expected given that we do not consider additional information such as secondary eclipses or radial velocity observations, which would provide a much more accurate measurement of eccentricity (in which case we would expect biases to appear). Additionally, time variation of oblateness due to precession is capable of mimicking a transit timing variation signal. We note however that this variation would be over significant timescales ($>$ 1 year) and only at the level of 10's of seconds.

When considering the biases and degeneracies we have found for oblateness, we note that there is the potential to extend this to other sources of shape variation. The models of Barnes et al. [2009] describe the effect of winds on an exoplanets atmosphere, which would distort its outer shell into a myriad of potential shapes

which may each bias a lightcurve fit in different ways.

Furthermore, atmospheric studies of exoplanet surfaces, such as those which leverage the eclipsing of a planet by its host star, could benefit significantly by having the properties of the planets shape be pinned down precisely through an analysis of its transit, where the signal is often much stronger. Alternatively, if a planet which is potentially oblate is assumed to be spherical, this may further bias the results of any higher order analysis which is based off an understanding of the orbital and physical properties of a planet derived from transit observations.

## 5.8 Appendix A: The Degeneracy of Projecting an Ellipsoid Onto a Two-Dimensional Plane

When observing an oblate planet what is seen is a two-dimensional projection, which is itself still an ellipse which can be characterised by a projected oblateness and projected obliquity. We consider the amount by which the true oblateness is altered if we assume a planet to have any uniform orientation in space. Note that it is only possible for projection to decrease the oblateness factor. When considering reorientations of the planet, which has two long major axes A and a short major axis $B = A(1-f)$, the radii of the cross section of any rotation must be larger than B and smaller than A. Namely the projected short axis b must obey $B_{\rm proj} \geq B$ and the project long axis $A_{\rm proj} \leq A$. Recalling the definition of oblateness we find

$$f_{\rm proj} = 1 - \frac{B_{\rm proj}}{A_{\rm proj}} \leq 1 - \frac{B_{\rm proj}}{A} \leq 1 - \frac{B}{A} \leq f \tag{5.14}$$

When considering random rotations, in figure 5-13 we show the average transformation of a uniform distribution of oblateness values. As expected we see a noticeable shift towards shorter oblateness values. In this case we have chosen the two orientation angles of the planet to be uniformly distributed across the unit sphere. Analysing a large number of random projections, we find that any given oblateness value is on average decreased by a factor of about 20%.

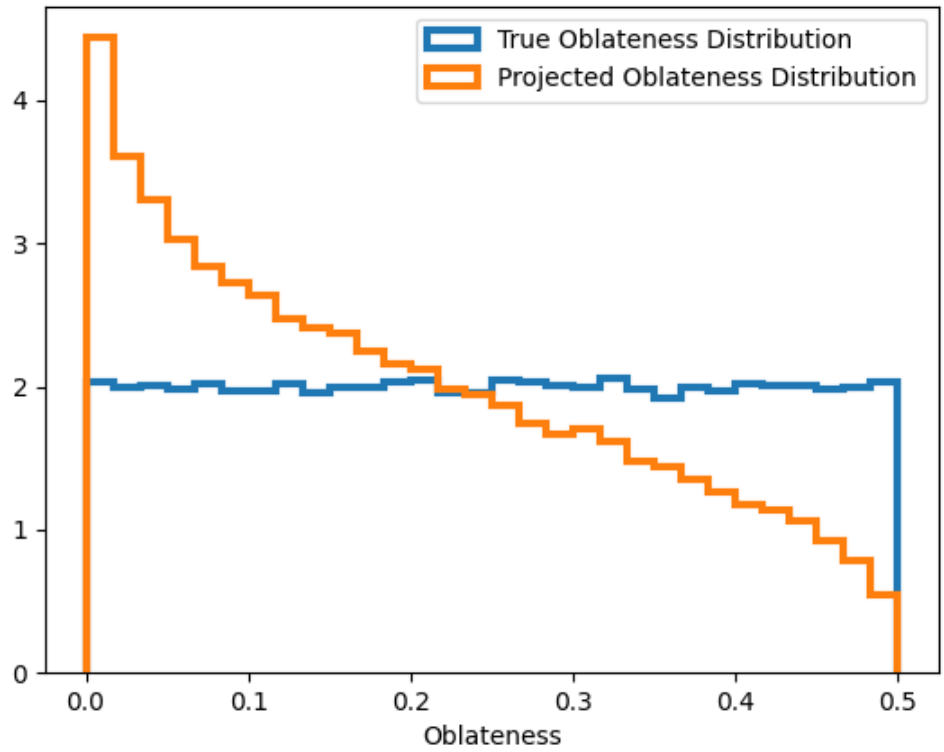


Figure 5-13: The effect of projecting a three-dimensional ellipsoid onto the sky plane, when its rotational axis is uniformly distributed across the unit sphere. As expected there is general shift towards lower oblateness values. This implies an additional level of difficulty when attempting to measure oblateness, since even if a planet were to have a high oblateness it would present itself as closer to spherical. Utilising a more informed model for the orientation of planets would provide a more accurate description of the transformation, however this would still be plagued by uncertainty about the true underlying oblateness distribution.

We may also ask, given a measurement from say an MCMC fit to a planet in which one retrieves a best fit value along with an uncertainty for the (projected) oblateness and obliquity, what possible underlying distribution of the true shape properties would match the observed values. For a choice of the azimuthal angle, there is a unique mapping between the projected and un-projected values, which can be obtained using equations 5.3a,5.3b,5.3c. The results of this are shown in figure 5-14. For an azimuthal angle of 90 degrees we find that the two distributions are the same. In this case the rotational axis of the planet is tipped towards the observer,

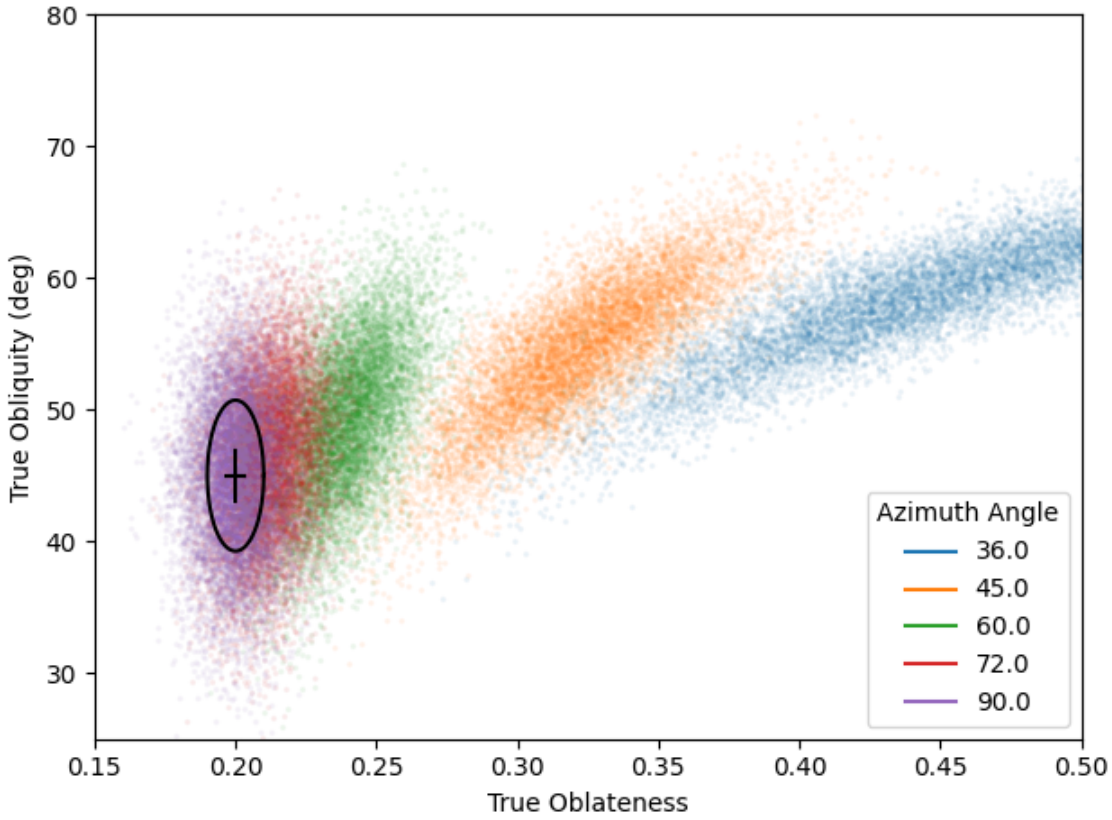


Figure 5-14: The solid black cross and oval represent the $1\sigma$ measurements of a potential planet's (projected) oblateness. The coloured patches represent various distributions for the true (i.e. un-projected) values of oblateness and obliquity which would match the projected observation, for different choices of the azimuthal angle.

thus the two semi-major axes seen are always the true long and short axis (implying $f_{\text{proj}} = f_{\text{true}}$) and the obliquity angle is similarly observed to be the same as the un-projected value.

# Chapter 6

# The Biasing Effect of Tidal Distortions

*The work presented in this chapter originally appeared in the literature as*

David Berardo and Julien de Wit, *The Astrophysical Journal, 941, 155, (2022).*

## 6.1 Abstract

Improvements in the number of confirmed planets and the precision of observations implies a need to better understand subtle effects which may bias interpretations of exoplanet observations. One such effect is the distortion of a short period planet by its host star, affecting its derived density. We extend the work of Burton et al. [2014], Correia [2014] and others, using a gravitational potential formulation to a sample of nearly 200 planets with periods less than three days. We find five planets exhibiting density variations of $> 10\%$, and as many as twenty planets with deviations $> 5\%$. We derive an analytic approximation for this deviation as a function of the orbital period, transit depth, and mass ratio between the planet and host star, allowing for rapid determination of such tidal effects. We find that current density error-bars are typically larger than tidal deviations, but that reducing the uncertainty on transit depth and RV amplitude by a factor of three causes tidal effects to dominate density

errors ($> 50\%$) in $>40\%$ of planets in our sample, implying that in the near future upgraded observational precision will cause shape deviations to become a bottleneck with regards to analysis of exoplanet compositions. These two parameters are found to dominate uncertainties compared to errors on stellar mass and radius. We identify a group of eight planets (including WASP-19 b, HAT-P-7 b, and WASP-12 b) for which current density uncertainties are as much as four times smaller than the potential shift due to tides, implying a possible $4\sigma$ bias on their density estimates.

## 6.2 Introduction

As the list of confirmed exoplanets grows we continuously expand the sampled space of known planetary parameters. Categories of planets such as those with ultra-short orbital periods have gone from containing a handful of planets to hundreds of planets thanks to missions such as *Kepler* [Borucki et al., 2010] and *TESS* [Ricker et al., 2014]. In addition to this increase in population, the precision of instruments has continued to reach new heights, reducing the uncertainty in quantities such as transit depth or planetary mass. This trend will accelerate further with the next generation of observatories and instruments such as JWST and PLATO [Heras et al., 2020], as well as high precision RV instruments such as CARMENES [Reiners et al., 2018] and ESPRESSO [Schmidt et al., 2021]. This increase in both the size and quality of our sample implies that subtle effects which in the past where either too small to be detectable or which affected a single digit number of planets may no longer be disregarded. An example of this behaviour is the 'Transit Light Source' effect [Rackham et al., 2018], in which variability of the stellar surface causes biases in atmospheric characterisation by mimicking or muting effects which produce similar results, acting a bottleneck towards properly understanding a planets atmosphere.

The focus of this work is on effects which alter the shape of an exoplanet, which is often considered to be a perfect sphere such as in the commonly used models of Mandel and Agol [2002], implemented in the widely used batman package [Kreidberg, 2015].

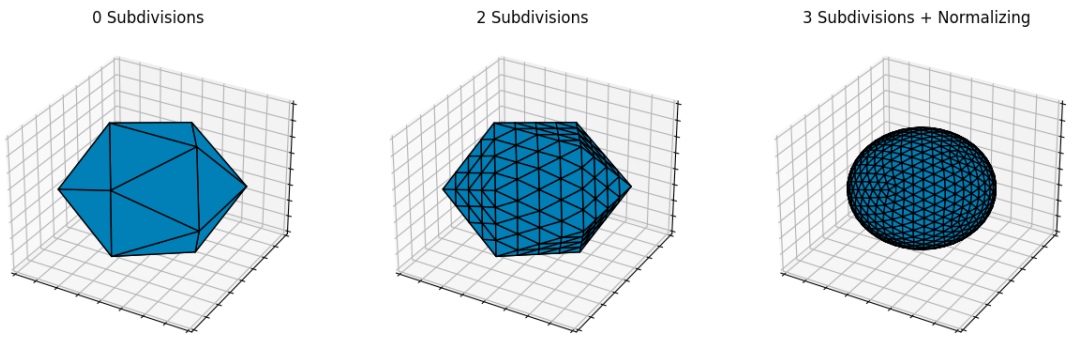


Figure 6-1: An illustration of the process by which the surface of the sphere is constructed. Starting from an icosahedron on the left, triangular faces are continually subdivided. Finally, the points are normalized to generate a uniformly sampled sphere.

For short period planets close to their host star, one such effect are tidal distortions which can cause a planet to bulge out towards its host star [Leconte et al., 2011]. This effect in particular has the potential to introduce a significant bias on the density of a planet since its sky projection remains close to a perfect circle. When considering for example a planet which is deformed due to rotation causing ts equator to bulge, its projection becomes elliptical [Seager and Hui, 2002, Barnes and Fortney, 2003]. In this case, subtle difference in the shape of ingress / egress of the transit lightcurve may be used to break the degeneracy between a spherical and oblate planet [Carter and Winn, 2010a, Berardo and de Wit, 2022]. For tidally deformed planets, phase curve observations which observe the planet from different directions could in principle determine these so called 'ellipsoidal variations' through lightcurve deviations [Correia, 2014, Kreidberg et al., 2018], however full phase curve observations require a significant amount of observing time to obtain, and at high precision there is likely to be a significant amount of degeneracy between the orbit, shape, and brightness distribution of a planet [de Wit et al., 2012].

Tidal distortions imply an underestimate of the volume of a planet, which in turn implies an overestimate of its bulk density. Theoretical considerations of the effect of this have previously been studied in Leconte et al. [2011] This effect has already been considered, primarily in the work of Burton et al. [2014], which calculated the magnitude of the distortion and the degree to which it altered the density measurement

for a sample of just over 30 planets. Additionally, Correia [2014] expanded on this work using a more detailed model to derive an analytic expression for the change in density as a function of distance to the host star.

In this work we aim to expand on these efforts in several ways. Our primary effort is to increase the sample of planets analysed using a gravitational potential model, which has been found to provide similar results to more complicated structural models. In the time since these previous studies were published, roughly 6x as many planets have now been found to be in the space of parameters which are susceptible to tidal distortion effects (i.e. planets with orbital periods below three days on circular orbits).

In section 6.3 we briefly outline the theory of tidal deformation and describe our method for calculating the effects of tidal interactions, and thus altered planetary densities. In section 6.4 we first highlight our sample of planets to be analysed, followed by the results of our analyses. We highlight trends as a function of various system parameters and derive an approximation which accurately describes the changes in density without the need for a full simulation. In section 6.5 we first highlight the biases that may be introduced when attempting to retrieve the interior composition of a planet using mass-radius relations under the assumption of being perfectly spherical. We then compare the changes in density to current density uncertainties, and we also analyse the relative contributions to these uncertainties from five parameters underlying parameters. This allows us to determine how upcoming improvements in quantities such as planet mass and stellar parameters will affect the ability to ignore such effects, for example through extreme precision radial velocity efforts [Crass et al., 2021].

## 6.3 Calculating the Density of a Tidally Deformed Planet

### 6.3.1 Physical description of scenario

To model the shape of the planet, we follow a similar methodology as that of Burton et al. [2014], where the surface of the planet is assumed to be on a gravitational equipotential. The value of the gravitational potential generated by a rotating planet and its host star is calculated using the Roche approximation [Chandrasekhar, 1987]:

$$\Phi_1 = -\frac{GM_1}{((x+a)^2+y^2+x^2)^{1/2}} \tag{6.1}$$

$$\Phi_2 = -\frac{GM_2}{(x^2+y^2+x^2)^{1/2}} \tag{6.2}$$

$$\Phi_3 = -\frac{1}{2}\Omega^2\left[(x+\mu_1 a)^2+y^2\right] \tag{6.3}$$

where $G$ is the gravitational constant, $M_1$ is the mass of the host star, $M_2$ is the mass of the planet, $a$ is the separation between the host star and planet (i.e. the semi-major axis of a circular orbit), $\mu_1 = M_1/(M_1+M_2)$ and $\Omega = 2\pi/P$ where $P$ is the orbital period of the planet. The coordinate system is such that the origin is placed at the center of the planet. The x coordinate points along the line connecting the center of masses of the two bodies, the z axis points along the orbital plane in the direction of motion of the planet, and the y axis points normal to the orbital plane.

In order to use such an approximation to model the distortion of a planets surface, we assume the planet is both tidally locked as well on a non-eccentric orbit. As we shall see in later sections, the effect of the distortion is strongest for low period planets (p $<$ 3 days) which are most likely to be tidally locked and be on circular orbits[Barnes, 2017].

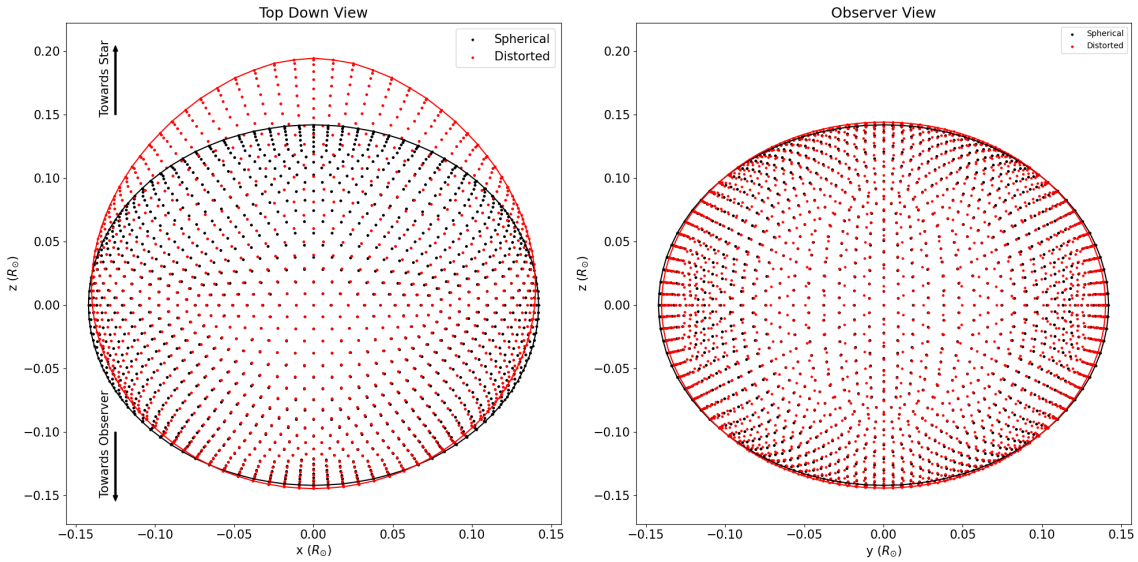


Figure 6-2: This figure shows two views of the surface of WASP-19 b. Points in black show the spherical planet which matches the observed transit depth, while points in red show the surface generated by fitting for an equipotential while also matching the observed transit depth. On the left we see a top down view of the orbital plane. On the right we see the view along the line of sight between the centers of mass of the planet and star.

### 6.3.2 Calculating the volume of a deformed planet

We first calculate the surface of a deformed planet and then 'measure' its volume in order to determine the amount by which its density is altered. In order to generate the surface of our planet, we first construct a geodesic icosahedron as an approximation of a sphere. This is an object commonly used in computer graphics and 3D rendering software which has the benefit of having its points uniformly spread out across its surface. We begin with the vertices of an icosahedron and then iteratively subdivide each of its faces into smaller triangles (as shown in figure 6-1). After the last round of subdivisions we normalize the length of each vertex from the origin to generate a tiled sphere.

This process leaves us with a collection of triangular faces which allows us to calculate two necessary quantities, the total projected surface area visible to an observer as well as the enclosed volume of each tetrahedron generated by the origin and any given triangular face. An additional benefit of this method is that we can adjust the

number of iterations in order to achieve any level of precision we desire. We find that after 5 subdivisions the calculated volume of our icosphere differs from that of a perfect sphere by only 0.05%, while the calculated projected area varies by only 0.03%. We use this as a benchmark for the accuracy of our method and fix all further calculations to 5 subdivisions, which gives us a surface of 10242 triangular tiles.

We next scale each vertex radially until all points have the same gravitational potential, which requires us to pick a value of the equipotential $\Phi$. We choose $\Phi$ such that the projected surface area matches the observed transit depth, similar to what is done in Burton et al. [2014]. We first evaluate the equipotential function for a range of radii centered on the spherical planet radius. For each value of $\Phi$ generated this way, we then calculate the radius of each vertex using a least squares regression in order to find the surface of constant potential. For this surface, we then calculate the projected planet area. This gives us a mapping between gravitational potential and transit depth, which we use to select the value of $\Phi$ which corresponds to any depth value of our choosing.

The result of this process is shown in figure 6-2, where we have calculated the deformation of WASP-19 b [Hebb et al., 2009] using the described process. This example highlights the potential for tidal deformation to alter a planets measured density. In the left panel we see a significant deviation from a pure sphere, as the planet is pulled towards its host star. However in the right panel we see that the observer-projected shape of the planet remains nearly perfectly circular.

## 6.4 Density Variations of Confirmed Planets

### 6.4.1 Planet Sample

We begin with the full list of confirmed planets found in the exoplanet archive [NASA Exoplanet Archive, 2019] which currently contains just over 5000 exoplanets. As mentioned in the previous section, as well as motivated by the results of Burton et al. [2014], we focus our efforts on short period planets, specifically planets with orbital

period of less than 3 days. We do also analyze planets with periods in the range of 3-5 days, but those were found to have negligible tidal distortion effects, consistent with expectations.

We additionally focus only on planets which have reported mass values. In principle, relative variations in density can be measured based on just changes in planet volume which is the focus of this work. However we also consider the magnitude of such a difference relative to the uncertainty in the measured density, for which a mass value (along with an error-bar) is required. We also cut for planets with eccentricity values below e = 0.05. This leaves us with a final sample of 196 planets, just over 6 times larger than the sample of planets used in Burton et al. [2014].

### 6.4.2 Density Variation Results

We apply the process described in section 6.3.2 to each of the planets in our sample. For each planet, we calculate its volume under tidal deformation that produces a depth value which matches the median reported value to within 0.1% in order to minimize differences caused by truncation or any other numerical effects. All analyses in this section use these values in order to compare the spherical and tidal planet densities.

#### 6.4.2.1 Absolute changes in density & trends

We first look at the percent difference in the density of each planet under the assumptions of being perfectly spherical or tidally deformed

$$\frac{\Delta\rho}{\rho_{sph}} = \frac{\rho_{sph} - \rho_{tide}}{\rho_{sph}} \tag{6.4}$$

where we calculate the value of $\rho_{sph}$ ourselves using the reported values of mass, depth, and stellar radius. This is done to ensure a fair comparison in order to accurately represent the amount by which density can shift due to changes in volume. As we will see in the next section, this quantity is often comparable to the density uncertainty, which is set by the underlying uncertainties from transit depth and RV semi-amplitude measurements used to calculate density. Using the reported value of

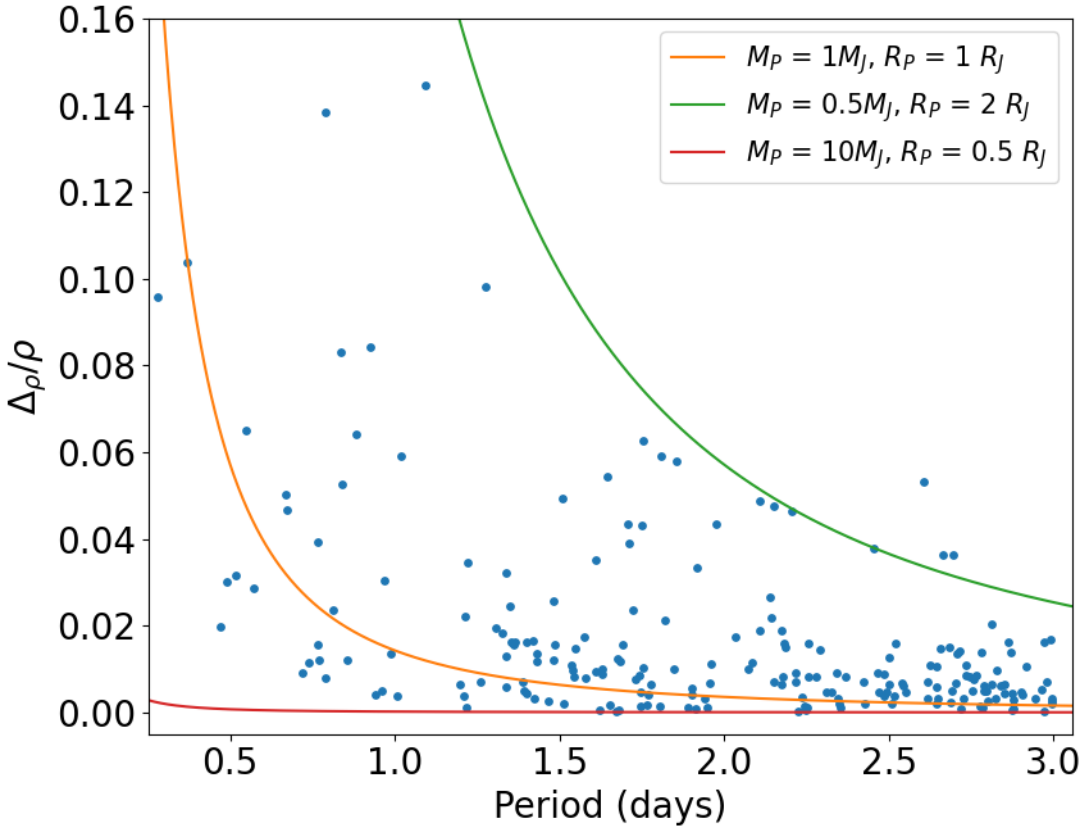


Figure 6-3: Relative change in the density of planets with orbital periods less than three days. The curves show the functional dependence of equation 6.8 for representative values of planet mass and radius.

planet density thus suffers the risk of including measurement uncertainty (depending on how density is reported which varies between analyses) when at this stage we only wish to determine intrinsic differences. Thus we ensure that both our measurements correspond to identical values of depth and planet mass.

The results of this are shown in figure 6-3. We show the variation as a function of orbital period, where we note that the variation decreases as period increases. This is not surprising given the factor of $1/p^2$ which appears in the potential equation, and acts as an additional confirmation that our code is accurately calculating planet deformations (a similar trend with fewer planets was also seen in Burton et al. [2014]).

We truncate the plot at an upper limit of $p = 3$ days, but note that we calculated the deformation out to a period of 5 days and found that the trend continued, in

particular the upper envelope which flattens out at a maximal deviation of $\sim 2\%$. We find that for planets with orbital periods below 1.5 days, the tidal density may deviate by as much as 15% compared to the density which comes from assuming a perfectly spherical planet.

#### 6.4.2.2 Functional Approximation of Density Variations

The scatter in figure 6-3 implies that orbital period is not the sole factor in determining density variations, which is also apparent from the additional terms in equation 6.1. We attempt to derive a functional form of the variation in density by comparing the full tidal potential to that of an isolated spherically symmetric body, given by $\Phi_{sph} = -GM_p/r$. We first assume that points along the surface of a tidally distorted planet are at a similar distance to the center of the planet as for a non-distorted planet, i.e. no part of the planet is distorted by a factor of say two or more. Thus in the Roche approximation we may replace quantities such as $x^2 + y^2 + z^2$ with $r_p^2$ or equivalently $\sqrt{\delta}R_s$ where $\delta$ is the observed transit depth and $R_s$ is the stellar radius. We also assume that $a >> R_p$ (in our sample we always have at least $a/R_p > 10$), and also that that solar mass is much larger than the planetary mass (for our sample we always have $M_s/M_p > 10^2$). Under these assumptions the three terms from equation 6.1 become:

$$\Phi_1 \sim -\frac{GM_s}{a},\ \Phi_2 \sim -\frac{GM_p}{r_p},\ \Phi_3 \sim -\frac{1}{2}\Omega^2 a^2 \tag{6.5}$$

which we then combine and scale by $\Phi_{sph}$ to get

$$\frac{\Phi_{sph} - \Phi_{tide}}{\Phi_{sph}} = \frac{3}{2}\frac{M_p}{M_s}\frac{r_p}{a} \tag{6.6}$$

where we've used Kepler's 3rd law to combine the orbital period and semi-major axis terms.

We now have an equation for the change in gravitational potential, which must be converted to a change in density. Given that the potential is treated as a radial 1D function, a reasonable assumption might be that the scaling term (rp/a) needs to be

cubed in order to obtain a relationship for density. To confirm this, we parameterize the change in density as

$$\frac{\Delta\rho}{\rho_{sph}} = \alpha \left(\frac{Mp}{Ms}\right)^{\beta} \left(\frac{r_p}{a}\right)^{\gamma} \tag{6.7}$$

and fit for $\alpha$, $\beta$, $\gamma$ against the calculated values for $\Delta_\rho/\rho$. We do indeed find that $\gamma \sim 3$, as well as $\alpha \sim 2$ and $\beta \sim 1$. We present the final effect on the change in density (having re-converted to orbital period) as

$$\frac{\Delta\rho}{\rho_{sph}} = 0.01428 \left(\frac{P}{\mathrm{day}}\right)^{-2} \left(\frac{R_p}{\mathrm{R_J}}\right)^{3} \left(\frac{M_p}{\mathrm{M_J}}\right)^{-1} \tag{6.8}$$

We plot this function for representative values of planet radius and planet mass in our sample in figure 6-3, where we find good agreement particularly in the upper envelope of the data points which closely follows an inverse square dependence on the period.

We additionally compare this analytic description of the change in density directly to the values calculated in section 6.4.2.1 and show the results in figure 6-4. We find that the bulk of the data points follow a linear relationship with a slope of ∼2, although we do still note a certain amount of scatter above the line. Planets which deviate significantly from the trend tend to have smaller masses (closer to being earth sized). This implies that one or more of the assumption we have made in deriving this relationship breaks down for sufficiently low mass planets. At the scales involved, our approximation deviates by at most a factor of ten from the true relative density change. This implies an underestimate of the true volume change by at most 10%, which in turn corresponds to an error on the linear scale of the planet by $1.1^{1/3} \sim 3\%$. The true deviation is almost always larger than our functional approximation. Thus equation 6.8 represents a fairly robust metric to determine if a planet may be susceptible to tidal deformations, without needing to run a full gravitational potential calculation.

A similar metric was derived in Correia [2014] (eq. 27), using a different approach considering the Love number and fluid displacement of an exoplanet [Love, 1911]. The

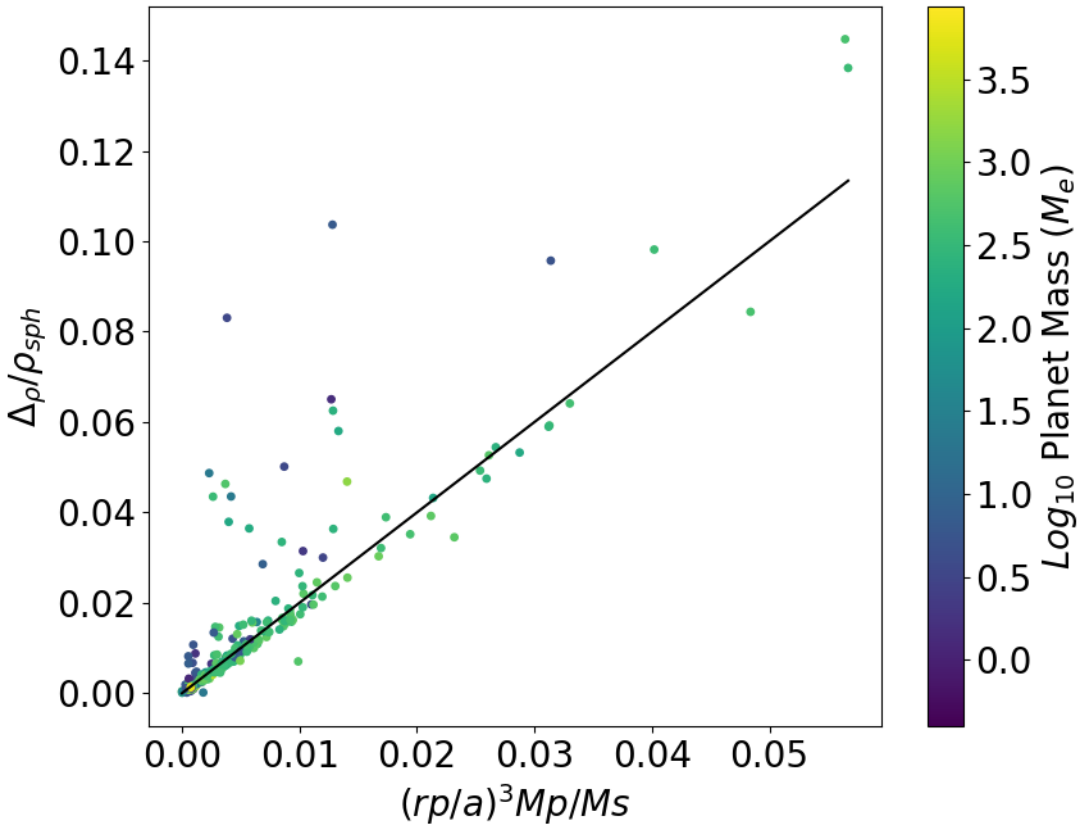


Figure 6-4: We show here agreement between the functional form the of the density perturbation we derive in section 6.4.2.2 (x-axis) against the values calculated in section 6.4.2.1 (y-axis). The black line a linear relationship with a slope of 2 passing through the origin. The coloring represents the mass of each planet on a log scale.

result they obtain is similar in that it is proportional to the ratio of planet to stellar mass, as well to the third power of planet size to orbital semi-major axis. While we find a constant scaling factor of two, they obtain a scaling factor of $7h_f/4$, where $h_f$ is the fluid second Love number. Estimating $h_f$ using the Darwin-Radau relation [Bourda and Capitaine, 2004] and a value of $\sim 0.27$ for the moment of inertia of Jupiter [Ni, 2018] gives a prefactor of 2.5. This difference of 25% in estimated tidal density is well below the measurement uncertainty on planet density, and using either equation would indicate weather or not the planet of density may be significantly different from that of a spherical planet.

An additional consideration of Correia [2014] is the effect of inclination on the

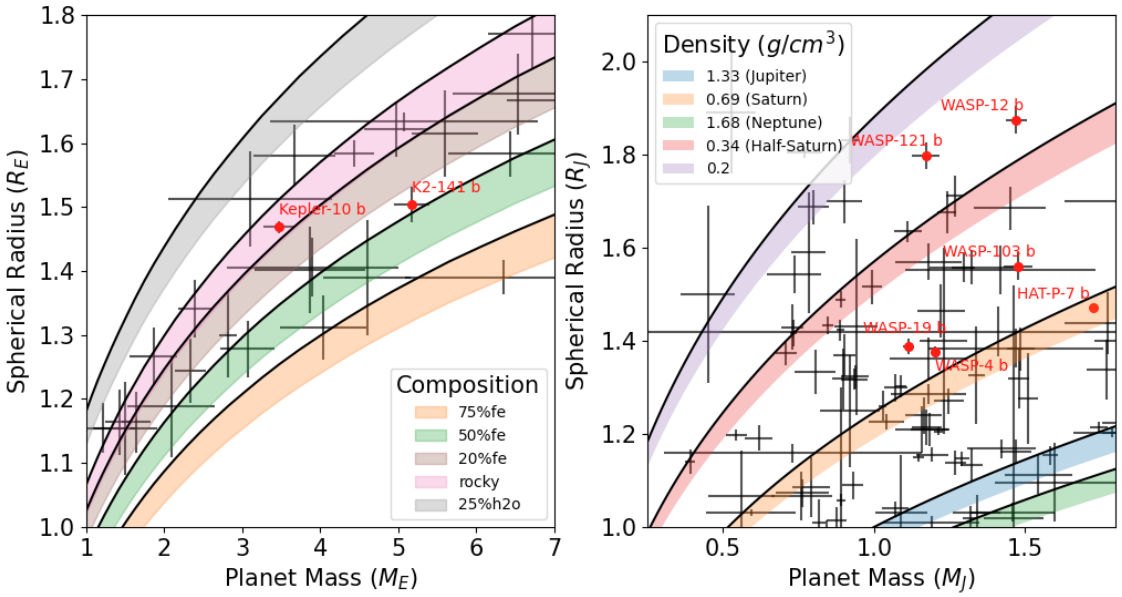


Figure 6-5: Mass-Radius relationships along with data points (and error-bars) for the sample of planets considered in this work. The left and right panels refer to low and high mass planets respectively. Black curves in the left figure are taken from Zeng et al. [2019]. Colored bands represent variations of these curves by up to 4.7% in radius, corresponding to density variations of up to 15%. The right hand panel shows a similar phenomenon for high mass planets, where we show constant-density relations corresponding to solar system gas giants giant densities, as well as a planet with half the density of Saturn and a planet with a density of $0.2 g/cm^3$ representative of 'super puffs'. The planets highlighted in red are those mentioned in Table 6.2 whose density uncertainty is less than the deviations caused by tides.

derived density, which introduces a correction term in their equation 27 proportional to $cos^2 i$. We find that for the planets in our sample, the effect of this correction term is at most 2% for a handful of planets, and more typically well below a 1% correction. Thus in our analysis we have chosen to neglect the effects of inclination, in order to provide a simple framework which still captures the bulk of the deviations. Even when considering the maximum inclination that would allow for a transit to occur, the correction term is at most 2% for the shortest period planets in our sample, and for most planets is much less than 1%.

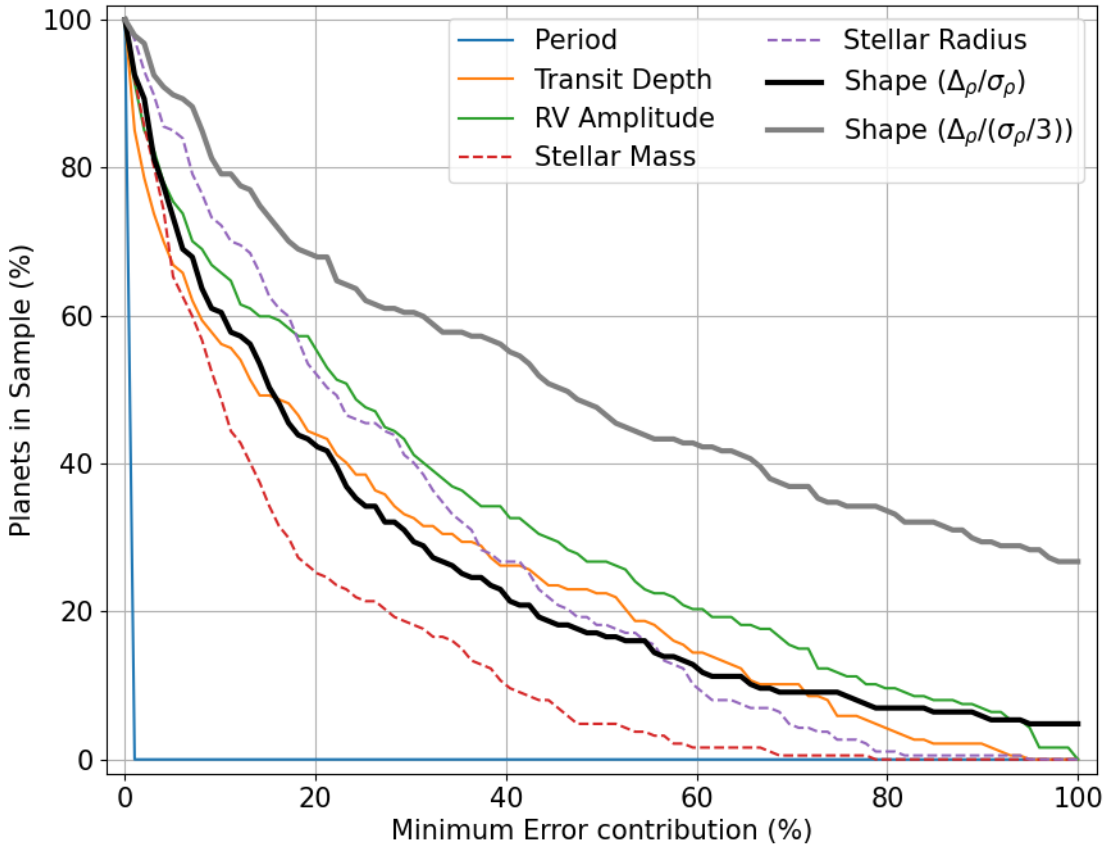


Figure 6-6: This figure illustrates the relative contribution of five underlying factors to the derived measurement error of a planets density. The x-axis represents a minimum amount that a given parameter contributes to the overall uncertainty on density. Solid colored lines represent directly observable quantities (period, transit depth and RV amplitude), while dashed colored lines refer to model-dependant quantities (stellar mass and radius). The black line ('shape') shows the ratio of tidally-induced variation to measurement error ($\Delta_\rho/\sigma_\rho$). The grey line shows a similar value, after having artificially reduced the overall uncertainty on density by a factor of three to highlight the effect of future measurement improvements.

## 6.5 Discussion

In the previous section we considered the absolute changes in density a planet may experience under the effects of tidal forces. We now focus on contextualizing these results with regards to measurement accuracy, and biases that may be introduced in measuring planet compositions to high precision.

### 6.5.1 Uncertainty in Mass-Radius Relations

During transit a tidally distorted planet will still have a nearly circular projection while having a larger than expected volume as shown in figure 6-2. The implication of this is that a spherical transiting planet could have the same density as a deformed planet with a smaller projected area, due to the 'hidden' extra volume. Thus when considering mass-radius composition curves, there is in-fact a degeneracy wherein a single curve could actually correspond to a range of projected radii, which we show in figure 6-5. The implication of this is that even if a planet had no error whatsoever on its transit depth, there would still remain uncertainty on its composition due to a lack of knowledge of its shape, becoming a bottleneck when attempting to measure planetary compositions to high precision.

We separate our sample of planets into low mass (Earth-sized) and high mass (Jupiter-size) planets, and for each we show a selection of various composition curves. For the low mass planets we show curves taken from Zeng et al. [2019], for a range of iron fractions as well as an Earth-like composition and a planet with a 25% water composition. For gas giant planets, we show a range of densities corresponding to the solar system gas giants, as well as a lower density of $0.2 g/cm^3$ as a representative value of large planets with low densities, so called 'super-puffs'[Masuda, 2014, Lopez and Fortney, 2014]. For each curve, we a plot a range of values (the colored regions) corresponding to a radius difference of $\sim 5\%$, which corresponds to a maximal density variation of $\sim 15\%$. This represents the range of projected radii which could all correspond to the same density.

The effect of these considerations is that, for example, a composition of 20% iron and one of pure-rock become a near continuous region of parameter space, and a planet such as Kepler-10 b, which we note in the next section has a relatively low measurement error, could now be equally described by either model. We additionally see planets which fall between models of 25% water and one of pure rock. While their own uncertainties make the distinction clear, with one model being two or three standard deviations away, it becomes much less obvious which model is correct once

the additional uncertainty from shape variations (colored bands) is considered.

### 6.5.2 Uncertainty of Density Measurements

In the previous section we considered the limiting case of perfect transit depth and mass radius knowledge and their effect on compositional analysis. We now focus on current measurement errors, how they compare to changes induced by tidal variations, and how upcoming improvement in precision of the quantities used to calculate density, namely transit depth, stellar radius, and planet mass (which itself depends on the stellar mass, RV semi-major amplitude, and orbital period) will in turn affect the uncertainty on density.

For a function $f$ which depends on independent variables $x_i$, we can write the uncertainty of $f$ (denoted $\sigma_f$) as:

$$\sigma_f^2 = \sum_i \left( \frac{\partial f}{\partial x} \sigma_{x_i} \right)^2 \tag{6.9}$$

which for a density calculated using planet mass ($M_p$), transit depth ($\delta$) and stellar radius ($R_s$) becomes

$$\sigma_\rho = \sqrt{\left( \frac{\rho}{M_p} \sigma_{M_p} \right)^2 + \left( \frac{3}{2} \frac{\rho}{\delta} \sigma_\delta \right)^2 + \left( 3 \frac{\rho}{R_s} \sigma_{R_s} \right)^2} \tag{6.10}$$

We note that most of the planets in our sample have reported values for their density along with an error-bar in their entries in the exoplanet archive. We additionally calculate the uncertainty by ourselves using equation 6.10 and the reported uncertainties for the involved quantities, and find a good agreement between the two values. An additional consideration is that the planet mass itself is dependant on the radial velocity semi-major amplitude (K), stellar mass ($M_s$), and orbital period (p), which allows us to write the uncertainty on the planet mass as:

$$\sigma_{M_p} = \sqrt{\left( \frac{M_p}{K} \sigma_K \right)^2 + \left( \frac{3}{2} \frac{M_p}{M_s} \sigma_{M_s} \right)^2 + \left( \frac{1}{3} \frac{M_p}{P} \sigma_P \right)^2} \tag{6.11}$$

The benefit of calculating the uncertainty directly in this way is that we are then

| Error Contributor | Min % | Max % | Median % |
|---|---|---|---|
| 1 | 31 | 100 | 59 |
| 2 | 0 | 45 | 25 |
| 3 | 0 | 28 | 9 |
| 4 | 0 | 18 | 3 |

Table 6.1: Summary of the ranked contributions to density error across all planets where 1 = largest contributing factor and 4 = smallest. We find that the largest source of error (regardless of which underlying parameter it comes from) comprises anywhere from 31%-100% of the uncertainty on a planets density, with a median value of 59%.

able to compare the relative contribution of each term to the overall uncertainty. We quantify the relative contribution of a variable $x_i$ as:

$$\left(\frac{\partial \rho}{\partial x_i}\sigma_{x_i}\right)^2 / \sigma_\rho^2 \tag{6.12}$$

such that the sum of the contributions of each variable is 100%. The results of this breakdown are shown in figure 6-6, where we illustrate how often a given parameter contributes a minimum amount to the uncertainty. We find for example that in our sample of planets the orbital period never contributes more than 0.0001% relative to the other parameters, which is unsurprising given that the orbital period of a transiting planet is typically measured to extremely high precision.

For the remaining four parameters we can categorise them as being either measurement dependant (transit depth and RV amplitude) or model dependant (stellar mass and stellar radius). We find that it is the measurement parameters which more often contribute the largest amount of uncertainty, with the RV amplitude alone contributing at least 60% of the relative uncertainty for ∼20% of the planets in our sample, and in some case it even contributes almost the entirety of the uncertainty. Transit depth similarly can contribute as much as 90% in some cases, whereas the model dependant parameters never contribute more than 80% of the relative uncertainty. In table 6.1 we show the ranked breakdown of error contributions, in order of largest to smallest contributor (regardless of which parameter it comes from). We find for example that for a given planet the largest source of uncertainty always contributes at least 31% of the error and potentially the entire uncertainty, with a median contribution of 59%.

This indicates that for most planets there is a single parameter which contributes more than half of the density uncertainty.

When we consider the overall uncertainty on the spherical density, we find that for most planets the calculated difference between the spherical and tidal density ($\Delta_\rho$) is smaller than the uncertainty ($\sigma_\rho$), illustrated by the black line in figure 6-6 which shows the ratio between the two. This implies that with current data precision assuming a planet to be spherical in most cases does not introduce a significant statistical bias, but may be causing density error uncertainties to be underestimated.

Given this result, we can then ask by how much the error on planet density needs to be reduced before we have $\sigma_\rho = \rho_{sphere} - \rho_{tidal}$, which we show in figure 6-7. We see that the peak lies around an improvement of roughly 3-10x, although for many planets the required improvement is much smaller. For planets where the radial velocity amplitude or transit depth are the largest contributing factor, this implies that at a reduction in their uncertainties by 3-10x, tidal effects on density will begin to become relevant and the planet can no longer safely assume to be spherical. This is shown by the grey curve in figure 6-6, where we reduce the density error by a factor of three and show the relative value of tidal effects, which is comparable to $\sim 50\%$ of the measurement error on density for $> 35\%$ of planets.

We note that there is a small sample of planets for which current measurement errors are in fact less than the calculated deviation on their densities due to tidal effects (the highlighted orange part of Figure 6-7). We report these planets in Table 6.2, sorted by the multiplicative factor by which tidal deviations outweigh measurement uncertainties. In the worst case, we find that for WASP-19 b this is almost a factor of four, implying that the reported precision on its density is significantly underestimated. Again we note that grey curve of figure 6-6 shows that after reducing the total error on density by a factor of three, we find $\sim 20\%$ of our sample or almost 40 planets for which tidal variations on density would become larger than measurement errors.

| Planet Name | Period (days) | $\Delta_\rho/\sigma_\rho$ | Reference |
|---|---|---|---|
| WASP-19 b | 0.8 | 3.8 | Hebb et al. [2009] |
| HAT-P-7 b | 2.2 | 3.6 | Pál et al. [2008] |
| WASP-12 b | 1.1 | 3.0 | Hebb et al. [2009] |
| WASP-121 b | 1.3 | 1.9 | Bourrier et al. [2020] |
| WASP-4 b | 1.3 | 1.4 | Bouma et al. [2019] |
| WASP-103 b | 0.9 | 1.4 | Gillon et al. [2014] |
| Kepler-10 b | 0.8 | 1.4 | Esteves et al. [2015] |
| K2-141 b | 0.3 | 1.1 | Malavolta et al. [2018] |

Table 6.2: List of planets with density uncertainties less than the potential deviation due to tidal effects.

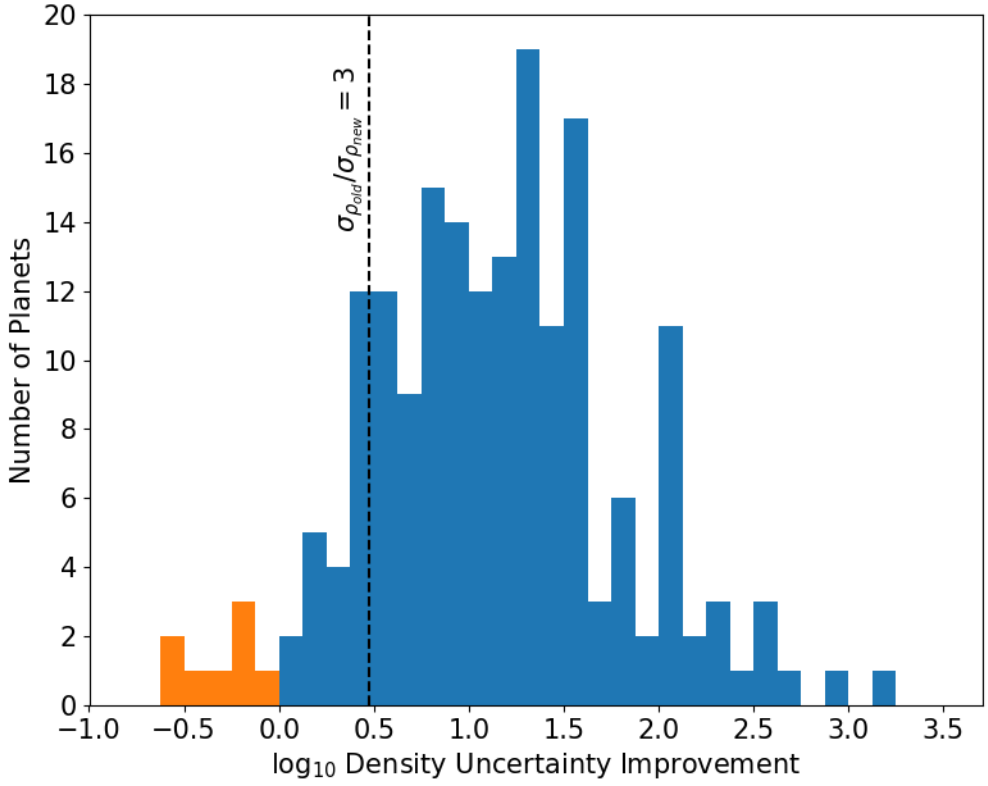


Figure 6-7: The factor by which the uncertainty on a planets density needs to be improved such that it is equal to the change in density due to tidal deformations. The black dotted line highlights a decrease by a factor of 3 in the uncertainty on spherical planet density. The orange region highlights planets whose density uncertainty is currently less than the difference between the spherical and tidal density values.

## 6.6 Conclusions

Using a gravitational potential framework to determine the shape of a planet under the influence of tidal distortions, we have expanded on the work of Burton et al. [2014] and calculated the amount by which such effects may bias the estimated density of an exoplanet with orbital periods of less than three days. In comparison to an assumption of being perfectly spherical, tidal effects serve to increase the perceived volume of an exoplanet (and thus decrease its density) by an amount of up to 15% for the shortest period planets, which agrees with the values reported in Burton et al. [2014] and Leconte et al. [2011], which reported their results as a change in effective planet radius. Similarly, Akinsanmi et al. [2019] considered a framework of a planet with ellipsoidal variations how that would affect their lightcurves and identified many of the same planets as we do in table 6.2 as being those which would exhibit the strongest signal of shape deformation.

We quantify this change more precisely in terms of the semi-major axis, planet to star mass radio, and planet radius for which we are able to derive a robust relationship (eq. 6.8). This allows for a rapid estimate of the magnitude of such variations, and whether or not an analysis of a planets density (and thus its internal composition) will be significantly biased by assuming the planet to be perfectly spherical. In Correia [2014] a similar expression was derived through an alternate analytic consideration, including the effect of inclination as well as the fluid Love number of the planet. We find the inclination effect to alter the density perturbation by at most 2% for the planets in our sample, although in most cases the effect is much less than 1%. The additional consideration of the fluid response of the planet implies potential variations of $\sim$ 20% between our results (i.e. a 15% density perturbation could change by a factor of 0.8-1.2), however this is strongly affected by uncertainty in the Love number. A more detailed analysis of the fluid response of planets in Wahl et al. [2021] identified WASP-12 b, WASP-103 b, and WASP-121b as those with the potential for the greatest variation in tidal response, which we also found to be among planets with the highest deviation in derived densities.

For planets with orbital periods beyond 2.5 days we measured variations of no more than 2%, well below current measurement errors ($\sigma_\rho/\rho > 2.7\%$ for $p > 2.5$ days). We find also that for most planets, even those with shorter orbital periods, measured uncertainties are currently too large to be affected by such deviations, however we identify a sample of planets whose uncertainties may be as much as four times smaller than the potential change caused by shape distortions. One such planet, WASP-103 b, was recently found to show tentative tidal deformations using multiple transit observations [Barros et al., 2022], where it is reported that the volumetric radius of a fit derived using an ellipsoidal planet model is 5-6% larger than the radius derived from a spherical planet model. This further strengthens the notion that for such planets susceptible to tidal deformation, any attempts to characterise their interior composition based on their density derived using spherical planet models are likely to be under-estimating their errors, and that there is a wall of accuracy which is limited by a lack of knowledge of their true shape. For other short period planets however we calculate that an overall improvement by a factor of three in density error would cause $\sim$ 25 planets to have density errors comparable to tidal distortions, and for $\sim$ 50 planets tidal distortions would compare to at least 50% of the measured density uncertainty.

With this in mind, we find that radius values in a range of up to a 5% deviation could in fact correspond to planets with the same density. This implies that composition curves are not just one-to-one functions but rather correspond to a family of mass-radius relationships, where there is a degeneracy induced by a lack of knowledge of the shape of a planet. This highlights a fundamental limit in the precision of characterising the composition of an exoplanet when disregarding tidal variations, which will become more severe as measurement errors decrease.

Finally, we break down the uncertainty on a planets density further as a contribution of five underlying factors, three of which are directly observable and two which are model-derived. This breakdown highlights the fact that it is the directly observable quantities (specifically RV amplitude and transit depth) which are in most cases responsible for the bulk of the error in a planets density (in some cases contributing

almost the entirety of the error budget). We also find that the median contribution of the largest piece of the uncertainty budget is 59%, implying that for most planets there is a single key parameter contributing the bulk of the uncertainty. Thus upcoming extreme precision RV measurements as well as high SNR transit observations such as those from JWST and PLATO imply that biases due to tidally-induced shape deformations will become a significant and unavoidable bottleneck when attempting to measure the density of planet to a high level of accuracy as the error in these key contributing factors is reduced.

# Chapter 7

# Searching for Exospheres Around Planets in the TRAPPIST-1 System

*The contents of the following chapter represent work intended for submission*

## 7.1 Introduction

The following chapter presents an analysis of data that was obtained as a result of Hubble Space Telescope (HST) proposal 15304 (PI: Julien de Wit), entitled "Collecting the Puzzle Pieces: Completing HST's UV+NIR Survey of the TRAPPIST-1 System ahead of JWST". The proposal consisted of 114 HST orbits with the goal of characterising the TRAPPIST system in preparation for upcoming observations with the James Webb Space Telescope. Previous observations with the Wide Field Camera 3 (WFC3) instrument on HST have ruled out the presence of $H_2$ atmospheres around the 5 innermost planets b-f [de Wit et al., 2016, De Wit et al., 2018]. It was found in [Wakeford et al., 2019] that for TRAPPIST-1g, an $H_2$/He-dominated atmosphere is ruled out at greater than $3\sigma$ significance. For TRAPPIST-1h, [Garcia, L. J. et al., 2022] reported that is unlikely to host an aerosol-free H/He-dominated atmosphere, with a transmission spectrum consistent with having no features due to a high mean molecular weight ($\geq$1000$\times$ solar).

Of the 114 requested orbits, 16 were observed with WFC3 in order to complete

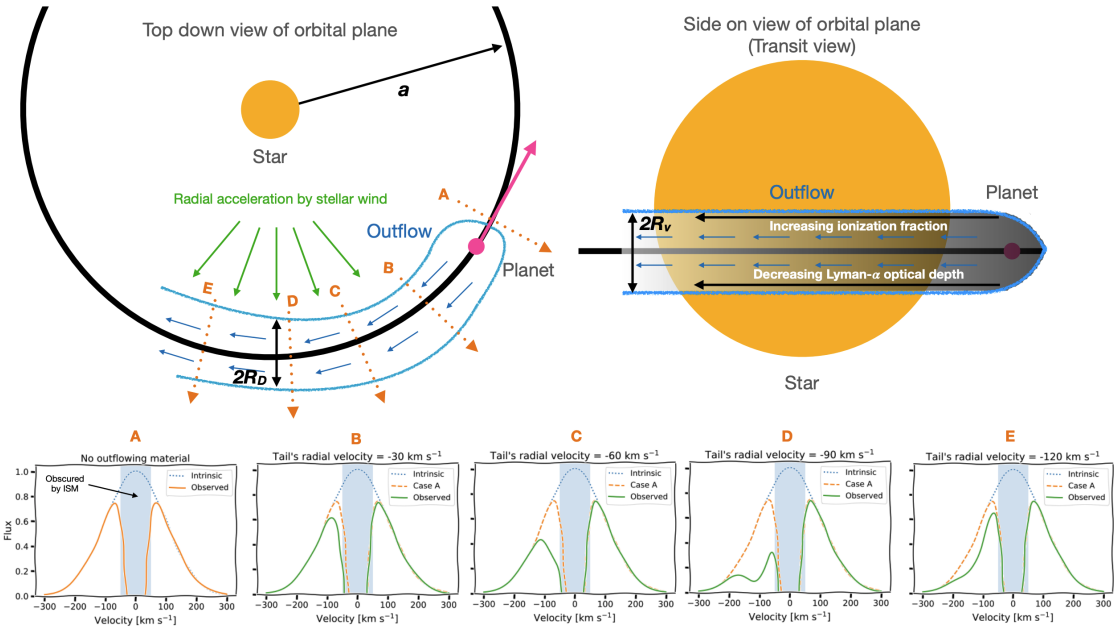


Figure 7-1: A schematic showing the motion of a transiting planet along with an extended exosphere (blue outline). The bottom plots show the effect of the exteneded exosphere on the observed Lyman-$\alpha$ signal from the host star, as a function of time. Figure taken from Owen et al. [2023]

the near infra-red reconnaissance survey of the system. The remaining 98 orbits were taken with the STIS instrument on HST, with the goal of searching for extended Hydrogen exospheres around the planets in the TRAPPIST-1 system, which would be the result of intense stellar irradiation causing the atmospheres of the planets to evaporate [Burrows and Lunine, 1995, Guillot et al., 1996]. H-exospheres provide the most accessible observables for volatile reservoirs, which have yet to be ruled out by the previously mentioned WFC3 observations. They have been previously observed to cause dips of up to 56% in the blue wing of stellar Lyman-$\alpha$ emission, as in the case of GJ 436 b[Lavie et al., 2017].

The goal of this work is to search for these H-exospheres around the planets in the TRAPPIST-1 system by observing the Lyman-$\alpha$ emission of the host star [Owen et al., 2023]. Planets which orbit sufficiently close to their host star suffer the risk of significant atmospheric escape due to high levels of stellar irradiation [Lammer et al., 2003, Yelle, 2004, García Muñoz, 2007, Murray-Clay et al., 2009, Owen and

Jackson, 2012], causing an extended tail of this evaporated material to trail behind the planet. In figure 7-1 we show a schematic of how this extended exosphere would transit the star, in particular long after the primary transit due to the planet has occurred. It is in this context that the full 3D nature of a planet must be considered [Bourrier and Lecavelier des Etangs, 2013], requiring 3D dynamical simulations of an evaporating exosphere to properly model the observed signals (eg Bisikalo et al. [2013], Carroll-Nellenback et al. [2017] and others).

## 7.2 Description of the data set

The observations are broken up into individual visits, each of which contain anywhere from 2-7 orbits of HST, taken with the STIS instrument using the G140M grating, which has a spectral range of 1140-1740Å[1]. The observations were taken with a central wavelength setting of 1222Å, spanning 1194-1249Å with a resolution of $\sim$20kms$^{-1}$ ensuring adequate coverage of the 1216Å Lyman-$\alpha$ emission line. The observations were taken periodically from September 2017 to July 2022, each coinciding with a transit of one or more of a planet in the TRAPPIST-1 system. In table 7.1 we outline in detail the individual visits taken, the number of orbits per visit, and which of the TRAPPIST-1 planets are seen to transit (taking into account transit timing variations of the individual planets which can be up to nearly an hour [Agol et al., 2021]). In total the observations overlap with 3 transits of planet g, 4 transits of planets e & h, 5 transits of planets b, d and f, and 6 transits of planet c. Each visit typically contains at least one orbit before and after the transit of one or more planets. The individual orbits have a typical integration time of $\sim$2000 seconds.

We show in figure 7-2 a sample exposure for one particular orbit of HST/STIS. The dominant feature in the image is geocoronal Hydorgen emission from the Earth's atmosphere [Meier and Mange, 1970], along with the faint signal due to Lyman-$\alpha$ emission from TRAPPIST-1 just to its left.

[1]https://hst-docs.stsci.edu/stisihb/chapter-13-spectroscopic-reference-material/13-3-gratings/first-order-grating-g140m

| Visit Id | orbits | Start (MJD) | End (MJD) | Transiting Planets |
|---|---|---|---|---|
| odhs07 | 6 | 57999.80554628 | 58000.13234036 | h |
| odhs29 | 6 | 58010.53201628 | 58010.8597711 | g |
| odhs30 | 6 | 58013.51192369 | 58013.83968999 | c,e |
| odhs32 | 7 | 58024.3072022 | 58024.70121849 | b |
| odhs16 | 4 | 58043.97447072 | 58044.16982961 | e |
| odhs05 | 4 | 58066.49076783 | 58066.68606894 | d |
| odhs08 | 4 | 58070.46400857 | 58070.65934413 | d |
| odhsd1 | 4 | 58244.62177988 | 58244.8160301 | d |
| odhsb1 | 4 | 58269.25489373 | 58269.44886373 | b,f |
| odhsb2 | 4 | 58335.73444453 | 58335.92925934 | b,c |
| odhsc1 | 4 | 58371.95377446 | 58372.14935298 | b,c |
| odhsf1 | 4 | 58453.33295479 | 58453.52589479 | f |
| odhsc2 | 4 | 58459.22383442 | 58459.4193785 | c,d |
| odhsg1 | 4 | 58616.00951054 | 58616.2045798 | g |
| odhsf2 | 4 | 58637.46029758 | 58637.65537832 | d,f |
| odhse1 | 4 | 59135.84576521 | 59136.03995521 | e |
| odhsg2 | 4 | 59159.54331234 | 59159.73883345 | g |
| odhsh1 | 4 | 59163.38209716 | 59163.57863642 | h |
| odhsc3 | 4 | 59166.36554642 | 59166.55782642 | c,e |
| odhsf3 | 4 | 59438.47639171 | 59438.67289652 | f |
| odhsh2 | 4 | 59501.15662499 | 59501.35231943 | h |
| odhse3 | 4 | 59782.3657781 | 59782.56156514 | e |
| odhs33 | 5 | 58039.00752627 | 58039.26906553 | f |
| odhs31 | 7 | 58018.41267591 | 58018.80671554 | b,c,h |

Table 7.1: Description of the observations taken as part of the observing program. Times listed are start of the first orbit and end of the last orbit with a visit, comprising anywhere from 4 - 7 individual orbits/integrations. The rightmost column lists which of the TRAPPIST-1 planets transits during the visit (typically during the central orbit).

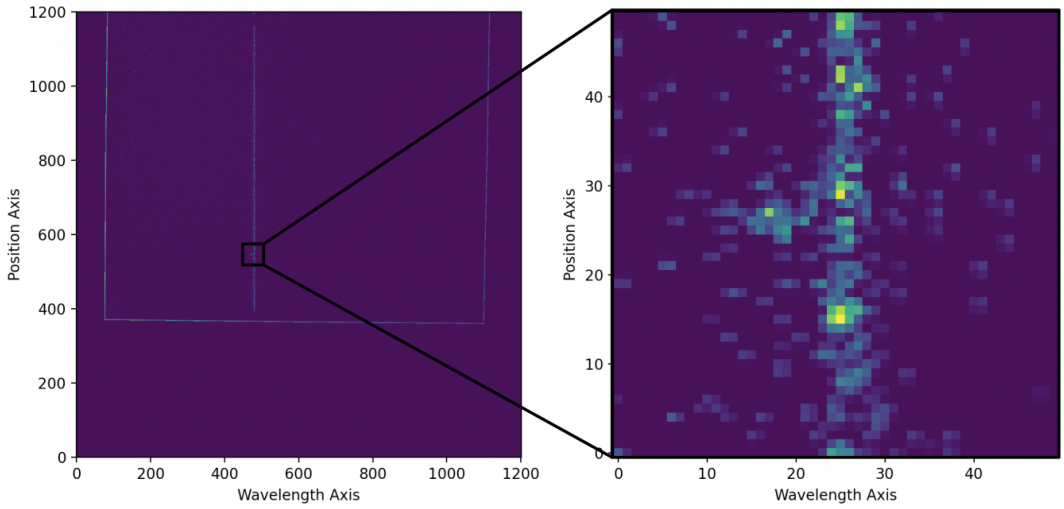


Figure 7-2: A raw CCD image of the observation obtained with each image. The left panel shows the full exposure, including the shift along the spatial direction. The right panel shows a zoomed in view, which highlights not only the strong airglow signal, but additionally a secondary signal due to Lyman-$\alpha$ emission just to its left.

## 7.3 Description of Observational Model

Each individual observation can be modeled as the sum of several components: a background signal, an airglow contamination signal due to the Earth's atmosphere, and finally the emission signal from TRAPPIST-1, which has been attenuated due to absorption from the interstellar-medium (ISM) [Landsman and Simon, 1993, Wood et al., 2005]. We describe here the mathematical formulation of each of these components, and how they are used to ultimately retrieve a Lyman-$\alpha$ lightcurve of TRAPPIST-1.

### 7.3.1 Airglow Model

The dominant signal observed is from geocoronal Hydrogen emitting Lyman-$\alpha$ photons around the Earth (which extends well past the orbit of the moon [Baliukin et al., 2019]), which we model with a Voigt profile [Sim, 2001] across the wavelength axis (the x-axis in figure 7-2):

$$V(x;\sigma,\gamma) = \int_{-\infty}^{\infty} G(x';\sigma)L(x-x';\gamma)dx' \tag{7.1}$$

where $G(x;\sigma)$ is a zero mean gaussian

$$G(x;\sigma) = \frac{e^{-x^2/2\sigma^2}}{\sqrt{2\pi\sigma^2}} \tag{7.2}$$

and $L(x;\sigma,\gamma)$ is a Lorentzian profile

$$L(x;\sigma,\gamma) = \frac{\gamma}{\pi(x^2+\sigma^2)} \tag{7.3}$$

which we implement using the astropy package [Astropy Collaboration et al., 2013, 2018, 2022]. In this framework, the Voigt profile is defined using a positional offset $x_{airglow}$, an amplitude $A_{airglow}$, and the full-width half-maximum (FWHM) of both the Gaussian and Lorentzian profiles, $\text{fwhm}_G$ and $\text{fwhm}_L$ respectively. These fwhm values are taken to be constant across all observations, and are thus fixed during fitting, having been measured during preliminary fitting to be 1.83458 for the Lorentzian width and 2.08911 for the Gaussian width. The position is taken to be a 'visit' parameter (i.e. it is calculated once for each set of orbits corresponding to a visit), and the amplitude is taken to be an orbit parameter and is kept as a free parameter for each observation.

### 7.3.2 Background Model

The background flux is modeled using a linear model on the spatial axis (the y-axis in figure 7-2), which accounts for a ramp effect across the image. The offset and slope of the ramp are found to change between each orbit, and so are parameters which must be varied in each fit:

$$\text{background} = \text{offset}_{orbit} + Y * slope_{orbit} \tag{7.4}$$

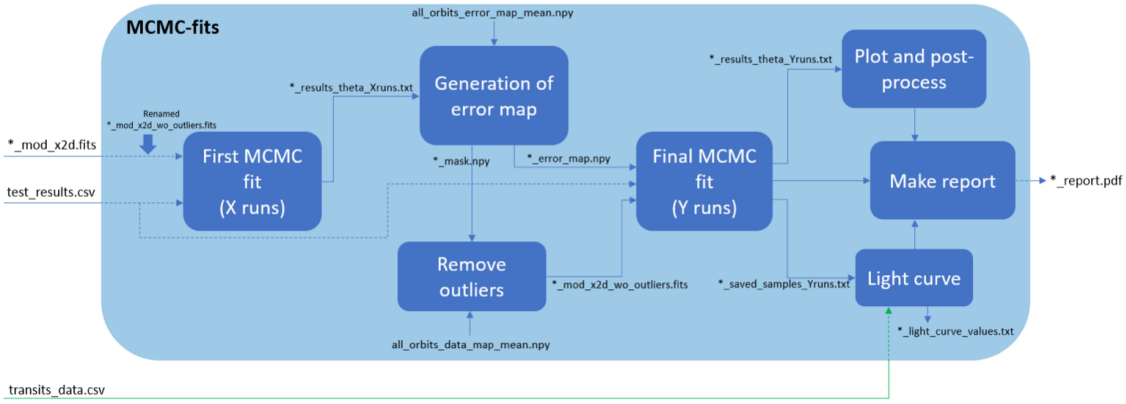


Figure 7-3: A flowchart diagram of the MCMC fitting pipeline used to analyse the images obtained from STIS

.

### 7.3.3 Signal Model

The final components to describe are the emission signal coming from TRAPPIST-1, as well the attenuation due to absorption by the interstellar medium (ISM) along the observer line-of-sight. The Lyman-$\alpha$ emission is modeled with a Voigt profile in the wavelength (X) axis (as was done for the Earth's airglow) and with a Gaussian profile in the spatial (Y) axis:

$$Signal(X,Y) = V_{sig}(X) * G_{sig}(Y) * (fL_{sig}/fG_{sig}) \tag{7.5}$$

where V is the Voigt profile defined in equation 7.1 and G is a normalized Gaussian profile with amplitude one. The overall profile is then multiplied by a scaling factor $fL_{sig}/fG_{sig}$ in order to decorrelate the widths from the amplitude in the Voigt profile. This allows for greater precision when fitting, since in general modifying the width of a Voigt profile will adjust its amplitude, which may not always be intended or necessary.

Finally, the absorption due to the interstellar medium is modeled as the negative exponential of a gaussian along the wavelength axis:

$$\text{Absorption} = e^{-G(x)} \tag{7.6}$$

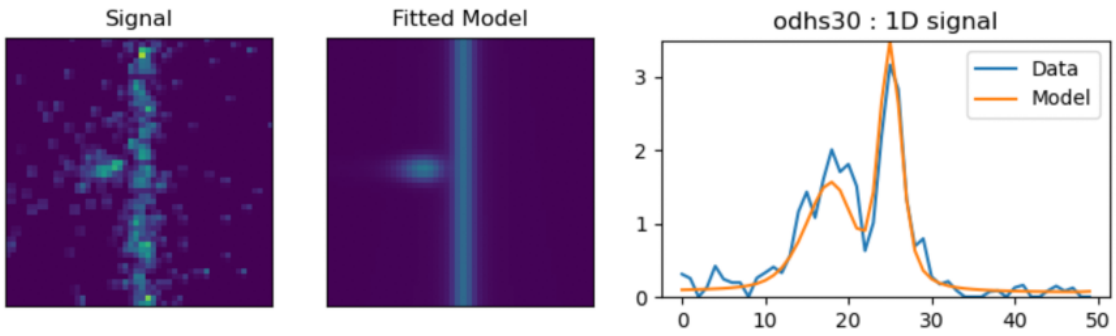


Figure 7-4: Sample MCMC fit output. The leftmost panel indicates the systematic-corrected signal image, for which a model fit is retrieved, which is shown in the central panel. The rightmost panel shows the spatially-flattened spectral profile of the image, indicating the strong airglow peak and blue shifted emission signal from TRAPPIST-1, along with the best fit model in orange.

Thus the overall model for the observed data, as a function of both spatial position and wavelength (the two axis in the detector image), can be described as a combination of three described components:

$$\text{Model}_{\text{total}} = \text{Background} + \text{Signal} \times \text{Absorption} + \text{Airglow}$$

## 7.4 Description of Analysis Routine

The analysis pipeline is broken down into a series of steps, which is shown as a flowchart diagram in figure 7-3. The analysis for each visit starts with a file with the *raw* tag, which contains an un-calibrated image. This image must first be adjusted for rotation, which in turn requires padding along the edges to ensure the image remains rectangular. Additionally, sigma clipping is used to highlight outlier pixels and replace them with the mean of their surrounding pixels. This process generates files with the $mod_{raw}$ tag.

Once this initial calibration has been done, we use the `calstis` module which is part of the `stistools`[2] suite of analysis functions, designed for the STIS instrument. This converts the $mod_{raw}$ tagged files to $mod_{x2d}$ files, which are finally ready for

[2]https://stistools.readthedocs.io/en/latest/calstis.html

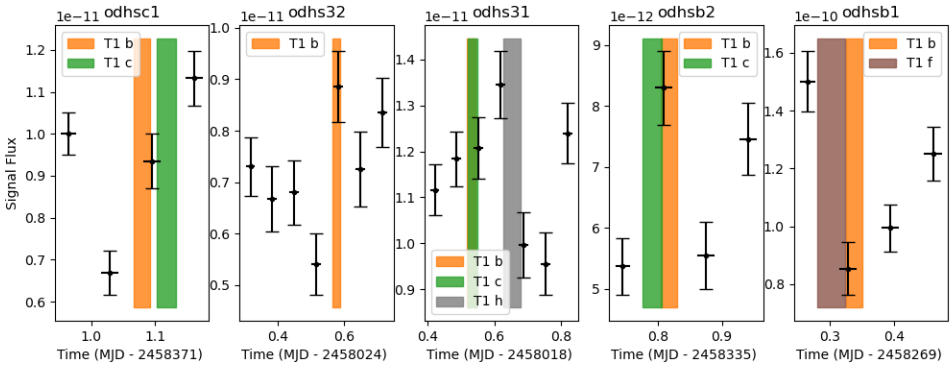


Figure 7-5: All visits which contained a transit of TRAPPIST-1 b, shown in orange indicating the duration of its transit. Other planets which happened to be transiting during these windows are also shown. The signal flux is the retrieved amplitude of the signal component of the observational model.

model fitting (i.e. the input on the left side of figure 7-3). The effect of the `calstis` function is to perform standard data reduction tasks, including flat-fielding, subtracting the dark image, rejecting cosmic rays, as well as perform wavelength calibration. Wavelength calibration is done using calibration files and the `wavecal` component of `calstis` to assign a wavelength value to each pixel.

Once the files have been calibrated, the first step is to fit for the Voigt profile of the airglow signal. For each orbit, the position, amplitude, and widths of the airglow signal are extracted, providing prior values for the airglow signal in the following steps. This is done at this stage independently of other fits since the signal due to Earth's glow is much stronger than any other signal present in the observations.

A first round of MCMC fitting is done using the full model description, including background, airglow, and emissions contributions. The output of this fitting is used to create an error map, i.e. a residual map to which sigma clipping can then be applied in order to remove noise pixels $>4\sigma$ away from the mean. Following the removal of these outliers, a final run of MCMC fitting is performed, providing the final posterior distributions for the individual model components. These outputs are then used to generate various diagnostic and summary information described in the next section.

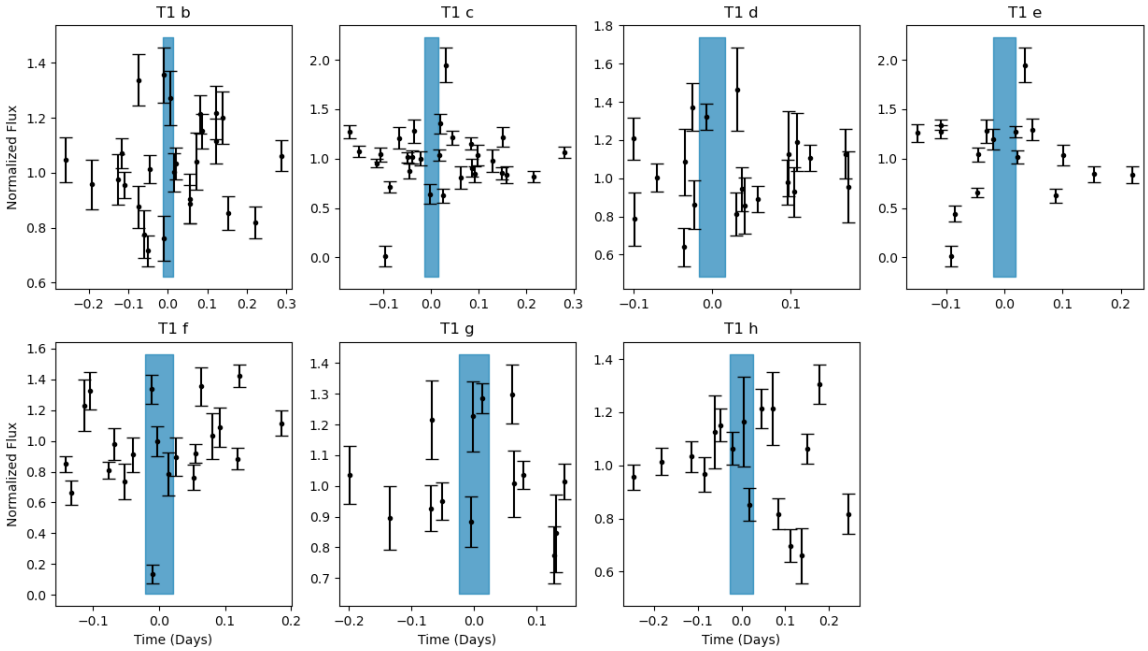


Figure 7-6: Normalized flux values of Lyman-$\alpha$ emission phases folded to the orbital periods of each of the seven transiting planets in the system. The blue bands highlight the duration during which each planet is transiting.

## 7.5 Fitting Results

Once MCMC analysis have been run for each orbit, within each visit, from each fit we extract the median and posterior values of the signal amplitude, i.e. the amplitude of the Voigt profile component of equation 7.5, which is used to construct a lightcurve of Lyman-$\alpha$ emission for each visit.

We first show an example fit in figure 7-4, which demonstrates a modified signal image, the combined signal, background, and airglow model, and finally the spatially flattened wavelength profile of the signal and best fit model. The larger peak is due to the airglow signal, while the smaller, Doppler shifted peak is due to emission from TRAPPIST-1. We then show in figure 7-5, a sample report for planet b. The five panels each represent lightcurves for a visit during which planet b happened to transit, indicated by the green bands. We additionally show any other planets which happened to be transiting during the same visit.

The lightcurves are normalized by considering only orbits which do not coincide

Table 7.2: Lyman $\alpha$ transit depths of TRAPPIST-1 planets

| Planet | Depth (%) | Depth Uncertainty (%) | OOT Baseline Scatter(%) |
|---|---|---|---|
| T1 b | -8.5 | 7.6 | 6.62 |
| T1 c | 1.1 | 15.0 | 14.54 |
| T1 d | -13.3 | 8.5 | 5.84 |
| T1 e | -19.2 | 24.5 | 24.04 |
| T1 f | 16.9 | 10.2 | 9.0 |
| T1 g | -13.1 | 9.9 | 8.57 |
| T1 h | -2.7 | 13.3 | 11.76 |

with the transit of any of the planets. For each visit, we then calculate the scatter of these background points, along with the difference between in-transit points and the background signal. We also add the scatter of the in-transit and out of transit points in quadrature, to obtain an estimate for the Lyman-$\alpha$ transit depth. For each planet, we compute this depth across all visits where it is seen to transit, and then calculate their mean value and uncertainty (again by adding the individual uncertainties in quadrature). We report these final transit depths, as well as background scatter, in table 7.2. We additionally show in figure 7-6 the flux values across all relevant orbits, phase folded to the periods of each individual planet. This was carefully done by the subtracting the transit center during each visit, using the predicted TTV variations provided by Agol et al. [2021] to account for any offsets in the transit centers. We similarly observe no correlated drop in flux either during or after a transit (during which the tail of an extended exosphere would continue to transit the host star).

### 7.5.1 Measuring the Rotation Period of TRAPPIST-1

In addition to the phase folded lightcurves shown in figure 7-6, we also examined the variability of the flux across all observations and looked for trends or periodic signals, in particular those which would be tied to the rotation period of TRAPPIST-1 itself. We first show the full extent of the observations across the total time they were observed in figure 7-7, where there is no immediate trend visible. Additionally, we show the same lightcurve folded to the current best guess for the rotation period,

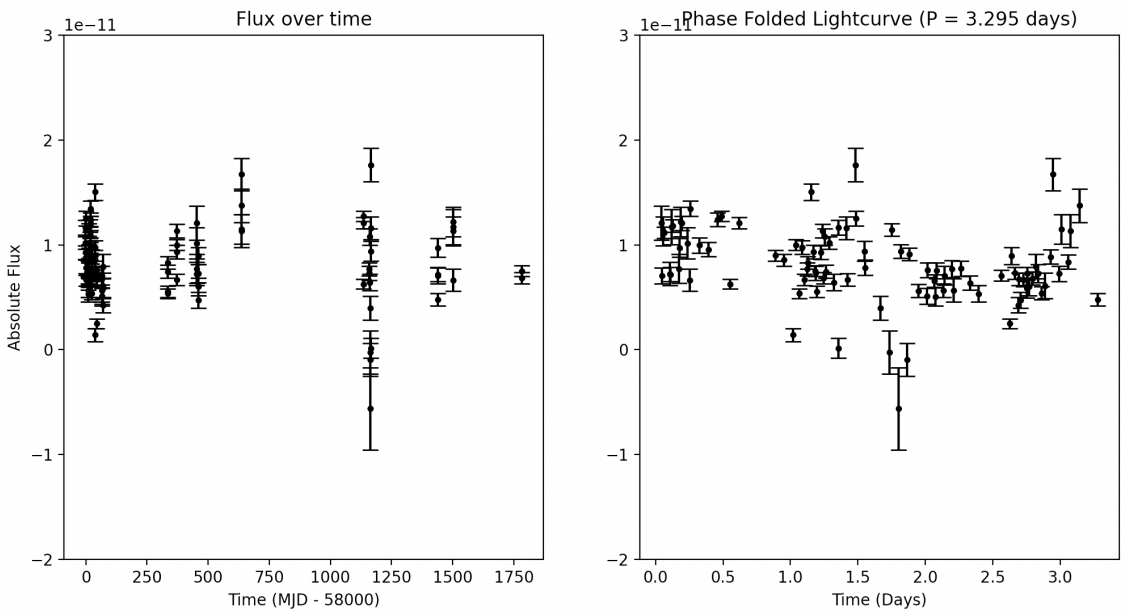


Figure 7-7: Left: Absolute emission flux from TRAPPIST-1, across all visits and orbits of STIS. Right: Absolute emission flux phase folded to the rotational period of TRAPPIST-1 (3.295 days).

P = 3.295 days, where again there is no discernible trend. We note however that due to the long baseline of the observations (just under five years), even miniscule changes to the folding period would cause a dramatic change in the folded lightcurve.

We normalized the flux within each visit as before, and in the left panel of figure 7-8 we show the stellar flux folded to a range of period values. These particular values were found to be global peaks in the Lomb-Scargle periodogram [Lomb, 1976, Scargle, 1982] of the time series Lyman-$\alpha$ emission of TRAPPIST-1. Several period values were found to have comparable signal power when phase folded, included the highest peak at an orbital period of P = 3.274 days, which closely matches the current estimate of the rotation of 3.295 days [Vida et al., 2017]. We find that even a minor adjustment of 0.021 days, or about 30 minutes, is enough for a coherent signal to emerge in the folded lightcurve. Thus despite the high amount of scatter and uncertainty in the data, we are still able to tentatively retrieve the rotational period of TRAPPIST-1 with a high degree of confidence.

## 7.6 Discussion

This work has focused on the analysis of nearly 100 HST/STIS orbits, grouped into 24 visits, in order to search for decreases in Lyman-$\alpha$ emissions from TRAPPIST-1 which would be indicative of extended neutral Hydrogen exospheres. The results compiled in table 7.2 indicate that there is no significant decrease in Lyman-$\alpha$ flux emitted from TRAPPIST-1 which can be associated with any of its seven known transiting planets. For each planet, the variation between in and out of transit observations is consistent with no decrease in flux, to within one standard deviation. In addition to measuring lightcurves occurring around transits of individual planets, we also show in figure 7-7 the absolute flux across all orbits, as well the flux phase folded to the rotational period of TRAPPIST-1 (p = 3.295 days [Vida et al., 2017]). This is done to monitor the time variability of the emission from the star. While an orbital period of 3.295 days not show a significant trend, when we analyze the power of the Lomb-Scargle periodogram of the full signal, we find that a nearby value of P = 3.274 days exhibits a noticeable sinusoidal variation in the Lyman-$\alpha$ emission of TRAPPIST-1 (shown in figure 7-8, although still at a low level of significance. Contemporaneous infrared observations with the *Spitzer* Space Telescope have found similarly low levels of variability over time [Delrez et al., 2018].

In Owen et al. [2023], a detailed description of the physical processes behind extended atmospheres is provided, in the context of absorbing stellar emission. In particular, they outline a sweet spot necessary to observe such transits, dependant on the stellar emission properties. If the amount of irradiation being absorbed by the planet is too low, then there won't be an active enough outflow generated, however if the amount of irradiation is too large, then the gas will become ionized more quickly and thus be incapable of absorbing Lyman-$\alpha$ photons. These arguments have previously been used as potential explanations for other non-detections, particular in cases of planets which are expected to be receiving significant amounts of radiation from their host star, such as HD 97658 b [Bourrier et al., 2017].

Finally, it is worth noting that non-detections stemming from HST/STIS observa-

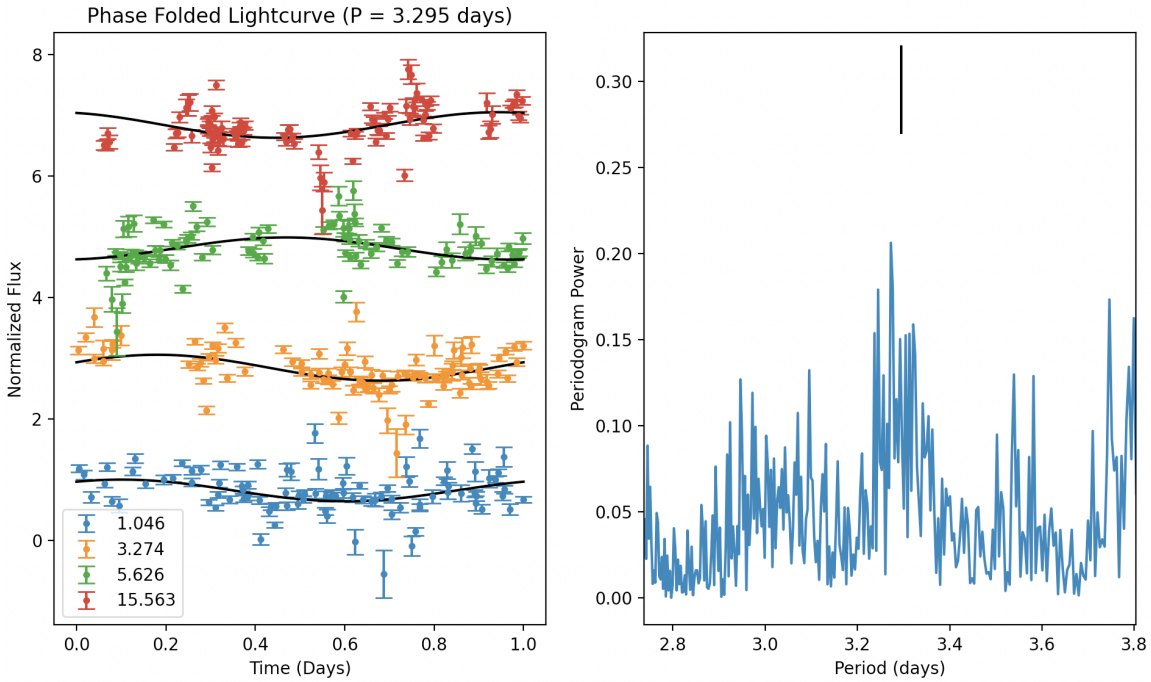


Figure 7-8: Left: Absolute emission flux from TRAPPIST-1, folded to various periods. Right: Lomb-Scargle periodogram power, centered on the current best estimate for the rotation period of TRAPPIST-1 of 3.295 days.

tions vary significantly in their ability to constrain the presence of extended neutral Hydrogen exospheres. In the case of HD 63433b, in Zhang et al. [2022] a $2\sigma$ upper limit of $\sim 3\%$ was able to be achieved. However in the case of K2-25b, only a $2\sigma$ of 30% was achievable [Rockcliffe et al., 2021]. Thus it remains possible that transit depths of a few percent could be attributed to the planets in the TRAPPIST-1 system, however HST's limited sensitivity prohibits them from being observed.

# Part IV

# Stellar Surfaces

# Chapter 8

# Simulating Lightcurves of Complex, Periodic Signals Observed in a sample of TESS M-dwarfs

*The work presented in this chapter originally appeared as a contributed section in the literature as*

Maximilian N. Gunther, David A. Berardo, Elsa Ducrot, et. al., *The Astronomical Journal, 163,144, (2022).*

In this chapter, I focus on the analysis of a set of rapidly rotating M-dwarfs first described in Zhan et al. [2019] which exhibit complex and periodic lightcurve modulations. In particular, I describe a robust and flexible star spot model I developed, which is capable of accounting for occultations from a range of sources including transiting planets, opaque clouds of dust, and an opaque torus of dust. The results of this work are a proof of concept that (1) the model I developed is capable of simulating the complex modulations observed and (2) that in the absence of a disk, it is difficult to recreate the sharp features seen in the lightcurves.

## 8.1 Introduction

Young M-dwarfs (20-150 Myr) have been observed to have rapid rotation rates ($\lesssim$ 2 days) [Rappaport et al., 2014]. Furthermore, their lightcurves are often found to display a range of anomalous features, including flares [Davenport et al., 2019, Mondrik et al., 2018, Günther et al., 2020] and large amplitude periodic modulations [Vida et al., 2010, Barnes et al., 2017]. These modulations are typical easily described by either a simple flaring model, or by a handful of spot features on the stellar surface described by just a few Fourier components. Some such stars exhibiting rotationally modulated signals do exhibit more complex features which are not as easily described by a simple spot model, such as KIC 7740983 [Rappaport et al., 2014] and HSS 348 [Strassmeier et al., 2017], however even these more complex lightcurve can be still be described with a more careful configuration of surface spots.

In Zhan et al. [2019], a new model was proposed to explain a new set of lightcurves which could not be explained by existing models, the so called 'dusty-torus' scenario in which an opaque, inclined disk which is mis-aligned with the stellar rotation axis accounts for the multitude of observed features. They also outlined counterarguments explaining why more simplistic models are incapable of re-creating the observed signals. Models with spots alone, even many spots, lead to smooth variations which can describe all the peaks in the frequency spectrum of the signals [Kővári and Bartus, 1997, Stauffer et al., 2017]. An accreting disk, on the other hand, would lead to too stochastic and aperiodic of a model compared the stable periodicity observed in the new complex rotator signals [Stauffer et al., 2017].

## 8.2 Observations

The original sample of ten *complex rotators* were discovered in TESS short-cadence photometry from Sector 1 (2018-07-25 to 2018-08-22) and Sector 2 (2018-08-22) obtained as part of the cool dwarf catalog [Stassun et al., 2018, Muirhead et al., 2018]. We present the set of lightcurves relevant to this work in figure 8-1. These represent

the pre-search data conditioned simple aperture (PDC_SAP) light curves, which have been detrended for instrumental systematics and which were prepared with the Science Processing Operations Center (SPOC) pipeline Jenkins et al. [2016].

## 8.3 Description of the Model

In order to generate the various models proposed to explain the observed lightcurves, it was necessary to consider either adapting currently existing transit generation codes, or to create a custom forward model which was capable of generating the necessary lightcurves.

### 8.3.1 Existing Lightcurve Simulation Codes

One of the most ubiquitous codes to generate transit lightcurves is `BATMAN`, written by Laura Kreidberg [Kreidberg et al., 2014], however this would have been insufficient for our purposes. The `BATMAN` code operates by solving the equations of [Mandel and Agol, 2002], which are applicable planets transiting the surface of a star with a radially symmetric limb darkening law. This code is highly optimized, producing accurate lightcurves very quickly. However, the cases we consider in this work are highly non-symmetric with regards to the kinds of occultations we consider, and in addition while spots can be considered in some context as disks transiting across the surface of a star, their geometric projection changes over time, altering their light curve signature.

A potentially more applicable code is the `STARRY` package, written by Rodrigo Luger [Luger et al., 2017]. This code is capable of producing more lightcurves of more complicated situations, including in particular stellar surface with star spots, and their interaction with planets. However, again the discrepency with our models proved to be insurmountable with the codebase of `STARRY`. The representation of spots in `STARRY` is through spherical harmonics, which allows for rapid surface brightness calculations give that the surface can be described completely analytically. This again results in accurate, rapidly generated lightcurves. However, our model requires the

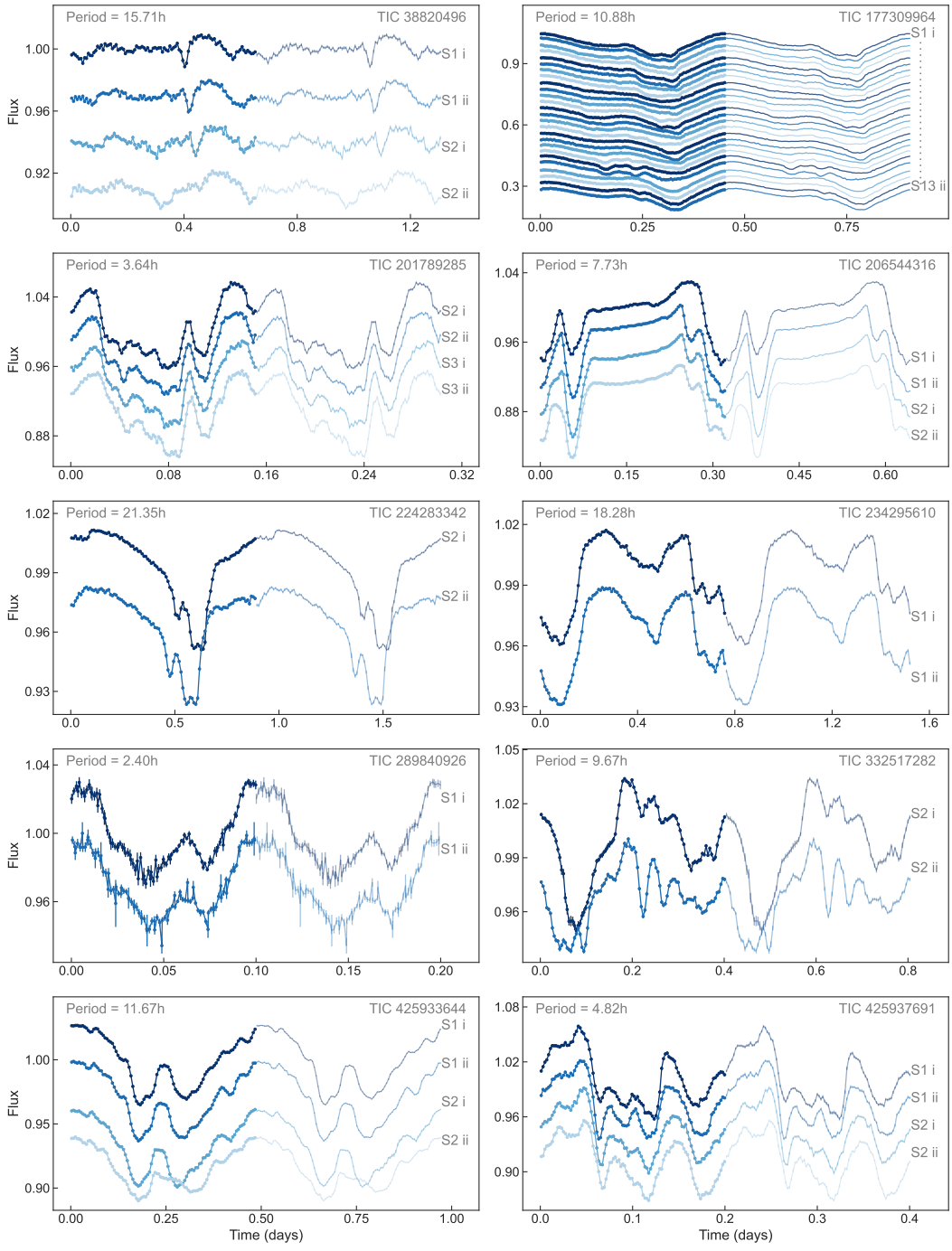


Figure 8-1: All available TESS light curves of young M dwarfs with complex photometric variability, spanning multiple Sectors of TESS observations. Each light curve shows the data of one TESS orbit (14 days of observations) phase-folded onto the rotational period of each star, with, e.g., "S1 i" denoting the first orbit of Sector 1 and "S13 ii" denoting the second orbit of Sector 13. Flares have been removed prior to phase-folding and plotting. All complex rotators' features show remarkable stability and longevity over many weeks to a year (at least). Figure taken from Günther et al. [2022]

interaction of a spotted stellar surface with an 'external' source, namely co-rotating clouds or an opaque disk. While clouds could in principle be modelled as transiting planets, the geometry of a disk proved to be too difficult to include the framework of `STARRY`.

### 8.3.2 The Spot Disk Model

Given the scale of the variations in the observed signals (∼5-10% for most of the lightcurves shown in figure 8-1), it was determined that the resolution of the models need not be sufficiently high as to exclude the use of non-analytic models. As such, I opted to develop a grid based model, where different effects could be simulated as different 'layers', and then composited together to create the final observed surface. A schematic of the model features is shown in Figure 8-2, and I describe the model in further detail here.

The surface of the host star is represented as two dimensional grid, with axis running across the latitudinal and longitudinal directions, having twice as many resolution elements running along the latitudinal direction (perpendicular to the rotation axis of the star). For each grid point, we calculate the projected area as $d\phi \sin\theta d\theta$, where $\theta$ and $\phi$ refer to the latitudinal and longitudinal directions respectively. We store this information as an area map, along with a map of the normal vector of each cell. This facilitates both rotating the grid (corresponding to an offset stellar rotation axis relative to the observer), as well as rapidly determining the contribution of each cell to the observed flux. We then generate three separate maps to describe the effect of spots, limb darkening, and a transiting opaque disk.

### 8.3.3 The Spot Layer

The spot layer is shown in the top left panel of figure 8-2. Each spot is described by four parameters: two coordinates $\theta$ and $\phi$, a size parameter r, and a temperature T. These spots then need to be 'painted' onto the surface of the star. One approach would be to calculate the distance between each cell and the center of the spot, and

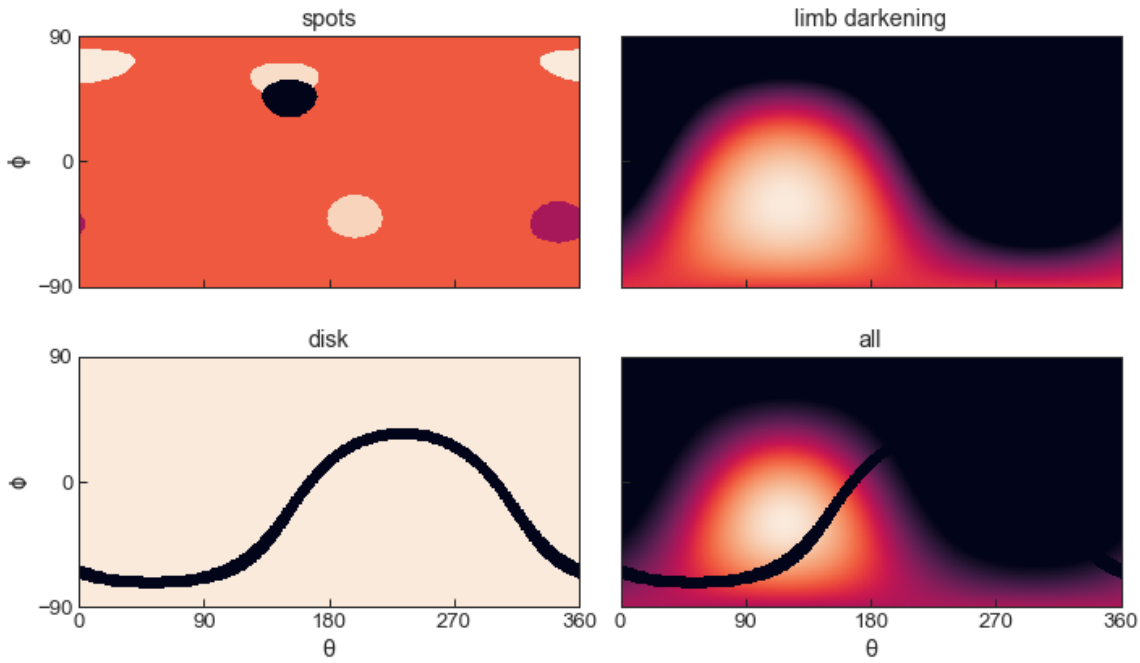


Figure 8-2: A breakdown of the individual components of the forward model used to simulate lightcurves, shown as un-wrapped projections of the stellar surface. In the top left panel we show a sample distribution of spots, with darker / brighter spots representing hot / cold surface regions (warping is an affect of the projection onto a rectangular grid). Similarly, the top right panel illustrates the unwrapped photosphere, accounting for a quadratic limb darkening law. The bottom left panel shows the projection of a disk on the stellar surface, and finally the bottom right panel shows the total map, where the three effect maps have been multiplied together.

use that as a determination of whether or not the cell is inside or outside the spot. In this case however care would need to be taken to ensure that the distance used accounts for the curvature of the stellar surface. In order to circumvent this, I consider a plane intersecting the stellar surface. I then need only to consider whether a spot on the stellar surface is above or below the intersecting plane. I then employ a 'flood-fill' algorithm, where I check this condition for each cell relative to each spot, and record the temperature of any spot which intersects with it. It should be noted that in this model, we don't account for any interactions between the spots, and allow spots of different temperatures to intersect.

For each cell which is found to belong to a particular spot, we attribute to it a flux value associated with a blackbody at the temperature of the spot, integrated across

the TESS bandpass ($\sim 600 - 1000$)nm[1]. In this spot layer we record only this total flux, and account for the size of the cell and the viewing angle through a series of geometry maps, which are used in the final flux calculation.

### 8.3.4 The Limb Darkening Layer

The top right panel of figure 8-2 shows the effects of a quadratic limb darkening law, parameterized by two parameters u1 and u2 as:

$$I(\mu)/I_0 = 1 - u_1(1-\mu) - u_2(1-\mu)^2 \tag{8.1}$$

where $I_0$ is the intensity at the center of the disk and $mu$ is the angle between the normal vector at the stellar surface and the observer line of sight. In principle, any limb darkening law which depends on the position along the stellar disk may be used, since this is used as a multiplicative factor to scale the flux of the stellar surface, regardless of whether it is from the photosphere or spots. An assumption being made with this model however is that both the spots and photosphere adhere to the same limb darkening law. This assumption is further assessed in the following chapter.

### 8.3.5 The disk layer

The final component of the model is the occultation due to an external object. In a standard exoplanet model, this might be surface occultation due to a transiting planet. In our case, we consider a thin, opaque disk which may be tilted relative to observers line of sight. This is the 'dusty torus' model considered in section 7 of Zhan et al. [2019]. The inclination of the disk is what provides the thickness to the projection of the disk onto the stellar surface, which is shown in the lower left panel of figure 8-2.

The disk position on the stellar surface is calculated by considering a straight line in 3-dimensional space, and then projecting that line along the line of sight and calculating the intersection with a spherical surface. In addition to a disk, this layer

[1]Values taken from: https://heasarc.gsfc.nasa.gov/docs/tess/the-tess-space-telescope.html

can also be used to simulate other features, such as co-rotating clouds, and in those cases a similar projection is done to calculate the surface occultation. The disk map is taken to be 1 everywhere the disk doesn't intersect with the surface, and where it does, a value from 0 to 1 is chosen representing the opacity of the disk, with a value of 1 indicating a completely opaque disk which blocks all emitted stellar light.

### 8.3.6 Simulating Observed Lightcurves

The final model is represented as a multiplication of the spot, limb darkening, and disk occultation map, and is shown in the bottom right panel of figure 8-2. Since each map is stored separately, we are able to apply arbitrary transformations in order to simulate rotation. Based on the orientation of the stellar rotation axis, a global rotation matrix is calculated, which is used to orient the normal vectors of the stellar surface. Thus for a given cell $i, j$, it's final contribution to the observed lightcurve can be expressed as

$$\text{Flux}_{ij}(t) = \text{Spot}_{ij} \times \text{Limb}_{ij} \times \text{Disk}_{ij} * \Delta\phi\Delta\theta\sin\theta * \mu_x(t) \tag{8.2}$$

where the factor $\mu_x(t)$ represents the dot product of the normal vector with the observers line of sight as a function of time. Given that the observer vector is parallel to the x-axis, this simply picks out the x-value of the normal vector of each cell. We note also that through this formalism, we have confined all aspects of time-variability into rotations of the normal vectors of the stellar surface, in addition to determining if a cell is visible at all (based on the sign of the x-component normal vector).

## 8.4 Comparing The Spot-Model to Observations

We took the TESS light curve of TIC 201789285 as an example, and tried to imitate its morphology as closely as possible while keeping the models simple, using a hybrid of statistical inference and manual parameter selection. The rotation axis of the star is left as a free parameter, and a quadratic limb darkening effect is applied to each

cell based on its orientation relative to the observer.

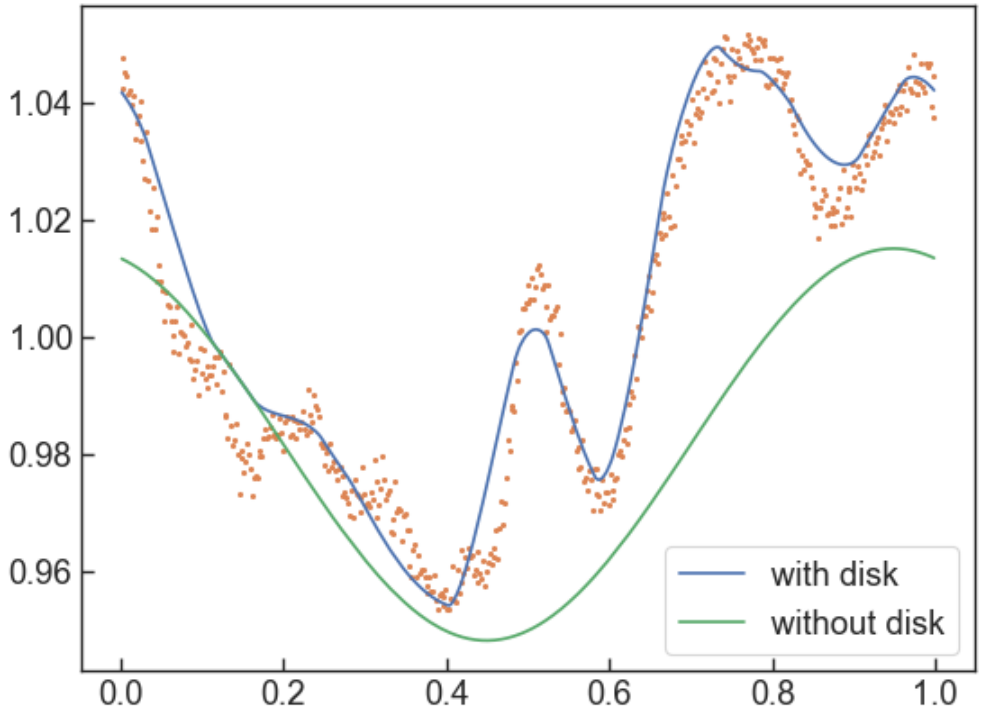


Figure 8-3: We show here the best fit posterior models for two scenarios. In both cases, we allow the model to vary the position, size, and temperature of two spot features. The blue curve represents the fit from a model which additionally contains an inclined, opaque disk.

For the spots and misaligned disk hypothesis, we fit spots with four parameters: two angles describing the location on the star, its size, and its temperature. The disk is parameterized by its inner and outer radius, inclination, and opacity. With this model setup, we then calculate the flux for each cell as described in the previous section. We then try to mimic the TESS light curve of TIC 201789285 by choosing a simple model with three cold spots and a fully opaque disk, optimizing their parameters using nested sampling via `Dynesty` (Speagle 2020). The results of fitting these two models are shown in 8-3, where we find that the spot model alone is incapable of recreating the sharp features seen in the lightcurve. This is due to the fact the regardless of how many spot components are added, the rotation period of the star

dictates the duration that they're visible, making it difficult to simulate sharp features which appear and disappear on different timescales. The disk model however allows precisely for this kind of behavior, given that some spots will briefly be occulted by the disk, while others may never intersect it all while they're visible. We note that while a significant improvement over the non-disk model, the fit (i.e. the blue line in figure 8-3) still struggles to re-create the lightcurve perfectly, however this may be due to requiring additional spot features to introduce higher order modulations to the signal.

In total (including the intersecting disk) we developed three simplified forward models for the three most promising ideas to explain the complex modulation signal of the TESS M-Dwarf sample:

- (i) co-rotating clouds
- (ii) spots and misaligned disk
- (iii) spots and co-rotating clouds

We run a similar analysis for the co-rotating clouds and spots and co-rotating clouds hypotheses, replacing the disk map with the relevant projection maps for these two new models. For the model with co-rotating clouds, we have as variables the size of the clouds, as well as their clustering.

We find that all three toy models can replicate the typical morphology of complex rotators (Fig. 8-4). Additionally, spots as drivers for an underlying large- amplitude modulation can explain a large portion of the signal, easing the constraints on circumstellar material.

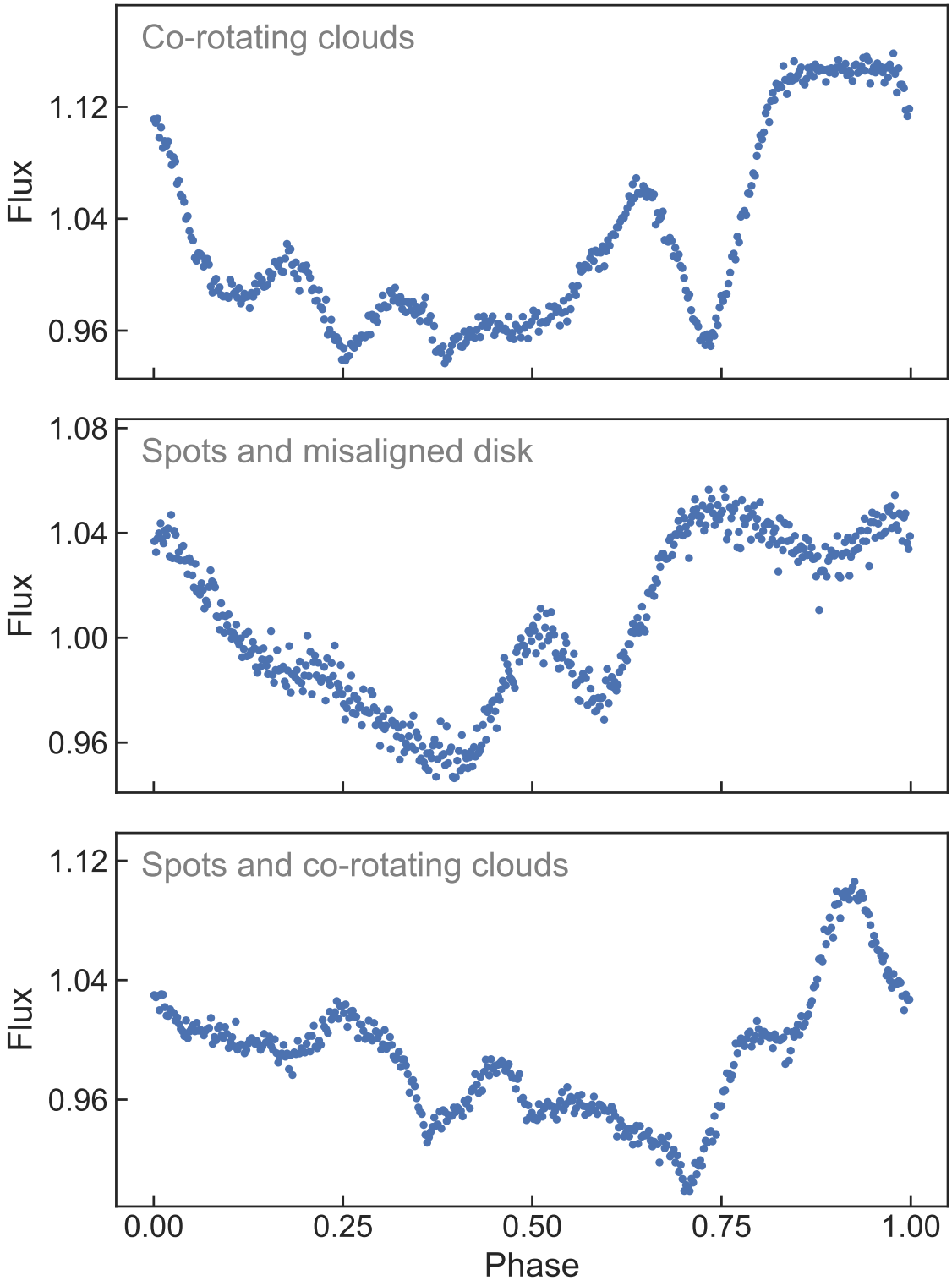


Figure 8-4: Three lightcurves representing simulations of a model with co-rotating clouds (top), spots and a misaligned opaque disk (middle) and stellar spots and co-rotating clouds (bottom).

# Chapter 9

# Empirically Retrieving Stellar Spectra

*The contents of the following chapter represent work in progress intended for publication*

## 9.1 Introduction

Transmission spectroscopy remains one of the best tools at our disposal when attempting to study and characterise the atmosphere of an exoplanet [Seager and Sasselov, 2000, Brown et al., 2001]. Typically, however, the light emitted from a planets host star will dominate any spectral observation of the system, and so it must be subtracted in order for the planetary spectra to be accurately measured. In the case of a perfectly homogeneous photosphere (taking into account limb-darkening), this could be done by obtaining an out-of-transit (OOT) stellar spectrum and subtracting that from an in-transit spectrum [Sing, 2018]. However if the surface of a star contains spots, faculae, or any other non-uniform features then this can introduce degeneracies and biases when attempting to measure the spectrum of a transiting planet. The features may be varying in time, either due to intrinsic changes in the properties such as intensity and size, or simply due to the rotation of the star altering their geometric contribution to the total flux, and these variations can imprint themselves as features

in a transmission spectrum of a planet [Sing et al., 2011, McCullough et al., 2014].

Much work has been done towards retrieving features on the stellar surface, typically through fitting lightcurves of spotted surfaces and using template spectra generated by physical simulations in order to remove the signal due to these non-uniform components [Zhang et al., 2018, Wakeford et al., 2019, Garcia, L. J. et al., 2022]. However as the precision of data afforded by space-based missions continues to improve, lack in fidelity of stellar spectral models can introduce uncertainty in the retrieved spectra which can be higher than the noise floor of the observations themselves [Rackham and de Wit, 2023]. Additionally, models which consider disk-averaged spectra, characterising star spots as just covering some fraction of the stellar surface, lose resolution and information content that could be use to reduce the uncertainty of retrieved spectra. This is especially true for late-M dwarfs such as TRAPPIST-1 [Gillon et al., 2016], as well as for active FGK stars which are expected to produce significant stellar contamination, such as the 'Transit Light Source' effect described in Rackham et al. [2018]. Thus, improvements in both theoretical and empirical spectral models are required in order to move towards measuring planetary spectra in a photon-dominated dominated regime, the latter of which is explored here.

The focus of this work is particularly on stars with properties similar to that of the M-dwarf TRAPPIST-1, which offers a wide range of opportunities to characterise its seven transiting planets. Additionally, I consider observations made with the NIRISS single object slitless spectroscopy (SOSS) instrument on JWST, which has spectral resolution of R$\approx$700 at 0.6-2.8 $\mu$m[1], providing an adequate compromise between resolving power and spectral coverage for such work considering the spectral energy distribution (SED) of stars (including M-dwarfs) [Allard et al., 2003].

In this chapter I first describe a model I developed to generate synthetic spectroscopic observations of spotted stellar surfaces, based off the framework described in Günther et al. [2022] (chapter 8 of this thesis) used to model interactions between a non-uniform stellar surface and arbitrarily shaped transiting objects. I then describe

[1]https://jwst-docs.stsci.edu/jwst-near-infrared-imager-and-slitless-spectrograph/niriss-observing-strategies/niriss-soss-recommended-strategies

a framework for extracting the spectra of individual spots, by considering the total observed spectrum as a linear combination of a constant photospheric component and a set of 'basis' lightcurves derived from the geometric projection of time varying spot feature. I then run a series of injection-retrieval tests on a suite of test stars with various spot configurations, using no prior knowledge about the truth spectra used to generate the data in order to assess the accuracy which which spectra can be retrieved. Finally, I consider the effects on the performance of a retrieval when varying both the duration of an observation (as a fraction of the stellar rotation period) as well as the phase of the stellar rotation cycle during which an observation begins.

## 9.2 Description of Synthetic Observations

Synthetic observations are generated using a stellar surface grid-model similar to the one described in the previous chapter, although in this work I omit the opaque disk and cloud features which were present in the model. As before, I define a list of spot objects, which are each described by a latitude, longitude, and radius. A critical difference here is the way in which surface flux is considered. In the previous chapter, the model was used to re-create broadband lightcurves, particularly those observed in the TESS band-pass of 600-1000nm[2], and so the temperature of a cell on the stellar surface was converted to a flux measurement by integrating a blackbody spectrum across this relevant wavelength range.

In this work the focus is specifically on retrieving the spectral contribution of each component of the stellar surface. Thus, when generating synthetic observations I generate a range of lightcurves for wavelengths that span the entire NIRISS bandpass. In order to model the emission of a spot object, I utilize models from the PHOENIX stellar spectral model grid [Husser, T.-O. et al., 2013]. I note that although I use simulated models to generate the data, this does not invalidate the premise of this study to empirically retrieve stellar spectra. This is because when I fit for these spectra, no information about the input spectra whatsoever is used, and thus the

[2]Values taken from: https://heasarc.gsfc.nasa.gov/docs/tess/the-tess-space-telescope.html

retrieval is not biased based on prior knowledge.

These grids provide adequate coverage to describe the photospheric background of an M-dwarf, as well as spots which vary by several hundred degrees in either direction. For the constant photosphere I use a spectral model with a temperature of 2500K, a logg of 5.0, and an [Fe/H] metallicity of zero (compared with TRAPPIST-1 which has a surface temperature of 2566±26, a logg of 5.2396±0.006 [Agol et al., 2021] and an [Fe/H] metallicity of 0.05±0.08 [Ducrot et al., 2020]). For spot features, I alter only the temperature of the model spectrum used, since the surface gravity and metallicity are typically expected to remain constant across a stellar surface [Freeman and Bland-Hawthorn, 2002]. The spectral resolution of the PHOENIX grids is much higher than can be observed with JWST, and so I first down-sample them to a resolution of R = 700 to match the expected signal from NIRISS. After adjusting the resolution, I also bin the spectra down a wavelength spacing of 8.8 $\mu$m. These are appropriate transformation in this case given that the forward model is linear, and thus high resolution is not needed (see Niraula et al. [2022] for further discussion on the effects of binning and down-sampling spectra).

The phoenix grid come in two 'flavors', one which is presented as a disk-averaged spectrum, and specific intensity spectra which provide spectral information as a function of viewing angle $\mu$[3]. When sampling from these specific intensity spectra, I take the value corresponding to $\mu = 0$ (i.e the center of the star, normal to the observers line of sight). I then calculate a quadratic limb darkening profile for the stellar surface, and scale this central intensity across the stellar surface, allowing me to have control over the generated signal.

Once a flux value is assigned to each grid on the stellar surface, the code described in the previous chapter is used to generate lightcurves for the star across a full rotation period, and for a wavelength range and spacing consistent with what would be observed by NIRISS. As before, we chose a rotation period of P = 3.295 days in order to match that of TRAPPIST-1 [Vida et al., 2017], and sample lightcurves with

[3]All spectral models referenced in this chapter were taken from: https://phoenix.astro.physik.uni-goettingen.de/

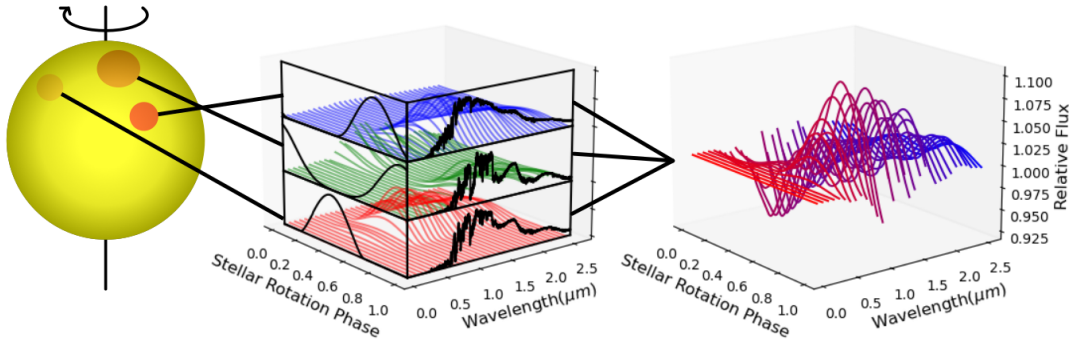


Figure 9-1: A schematic illustrating the way in which spot features on the surface of a star are modulated in both time and wavelength, and then combined to produce a final observed signal. The aim of this work is to demonstrate the ability to follow this diagram in reverse, going from multi-wavelength observations to individual component spectra, without the use of template spectra or any prior knowledge.

an integration time of two minutes.

## 9.3 Fitting for Spectral Components

In order to empirically retrieve the signatures due to individual spot features, I consider a framework in which the total observed spectra is taken to be a linear combination of the geometric signals of spots and photospeheres, modulated by the spectral signal of each components, which can be written as:

$$\text{Flux}(\lambda, t) = 4\pi\Lambda_{\text{phot}}(\lambda) + \sum_i \left[\Lambda_i(\lambda) - \Lambda_{\text{phot}}(\lambda)\right] \times S_i(t) \tag{9.1}$$

where Flux($\lambda$,t) is the observed flux at a given wavelength $\lambda$ and time t, $\Lambda_{\text{phot}}$ is the constant in time, spectral signal of the photosphere, $\Lambda_s(\lambda)$ is the spectrum of the $i^{th}$ spot, and $S_i(t)$ is the time varying geometric projection of a spot, which is a function of its size and position on the stellar surface, as well as any limb darkening effects. The sum runs over the number of individual spot features. A graphical depiction of this decomposition is show in figure 9-1

The contribution of spot components is written as a deviation from the photo-

sphere, so that the geometric projection of the photosphere can just be taken to be the disk-averaged integration $4\pi$.

### 9.3.1 SVD Decomposition of Observation

Given both a method of generating synthetic spectra, as well as a description for describing an observed spectral data-set as a linear combination of base components, I now describe our process for fitting our model to observations and retrieving the individual spectra of each basis component.

The data being considered are time series spectral observations of a rotating star, consisting of a $\lambda \times t$ array where $t$ is the number of time samples, and $\lambda$ are the number of wavelength bins. By treating the photosphere as a spot component with constant projection, and considering a model with N feautres (N-1 spots + 1 photosphere), I can condense equation 9.1 in the following form:

$$(F)_{\lambda \times t} = (\Lambda)_{\lambda \times N}(S)_{N \times t} \tag{9.2}$$

where the quantities are now being treated as matrices:

$$\begin{bmatrix} F_{11} & \dots & F_{1t} \\ \vdots & \ddots & \vdots \\ F_{\lambda 1} & \dots & F_{\lambda t} \end{bmatrix} = \begin{bmatrix} \Lambda_{11} & \dots & \Lambda_{1N} \\ \vdots & \ddots & \vdots \\ \Lambda_{\lambda 1} & \dots & \Lambda_{\lambda N} \end{bmatrix} \begin{bmatrix} S_{11} & \dots & S_{1t} \\ \vdots & \ddots & \vdots \\ S_{N1} & \dots & S_{Nt} \end{bmatrix} \tag{9.3}$$

When attempting to retrieve the component spectra, we seek to estimate the matrix $\Lambda$, based on a series of flux measurements (F) and spot signatures (S) generated by our model. In order to do this, we employ the use of Singular Value Decomposition (SVD)[4], which allows us to easily invert our (generally non-square) spot matrix S and use the standard solution for the matrix formulation of least-squares regression. The SVD algorithm works by decomposing a matrix, in this case our spot matrix S, into three matrices:

[4] https://en.wikipedia.org/wiki/Singular_value_decomposition

$$S^T_{t\times N} = U_{t\times N}\Sigma_{N\times N}V_{N\times N} \tag{9.4}$$

where U is an $t \times N$ unitary matrix, $\Sigma$ is a t by N rectangular matrix (where only the first N rows are kept), and V is an N by N unitary matrix. As indicated by the superscript T, in practice we decompose the transpose of the spot matrix S. In addition, I can calculate the ancillary matrix d which is comprised of the diagonal entries of $\Sigma$, which are known as the singular values of the original matrix.

The general ordinary least squares estimator for a linear equation $\mathbf{X}\beta = \mathbf{Y}$ can be written as

$$\tilde{\beta} = \left(X^T X\right)^{-1} X^T Y \tag{9.5}$$

and using the SVD decomposition of S given by equation 9.4, I can easily calculate the transposes and inverses needed to estimate $\Lambda$ in equation 9.2 as

$$\tilde{\Lambda}^T_{N\times\lambda} = V^T d^{-1}\left(U^T F_{\lambda t}\right) \tag{9.6}$$

where the matrix $F_{\lambda t}$ is the original matrix of observations. Inverting the matrix $\tilde{\Lambda}^T$ one last time gives the estimated matrix $\tilde{\Lambda}$, containing the ordinary least squares best fit values for the spectra of each component of the stellar surface. From the $\lambda \times N$ matrix $\tilde{\Lambda}$, the fitted spectrum of the photosphere is simply read off from the first row of the matrix. For the individual spot spectra, they are calculated as the sum of the remaining rows of $\tilde{\Lambda}$ and its first row, representing that was fit for was the difference between the spot and photosphere spectra, as per equation 9.1

### 9.3.2 A Note on Limb Darkening

The geometric signal of the a spot in the previous equations (i.e. the quantity $S_i(t)$) requires the choice of limb darkening coefficients for the stellar surface, since it is calculated the combination of the size of a cell, as well as its projected area towards the observer, multiplied finally by a limb darkening factor. However in general limb-

darkening is an effect which depends on the temperature of the stellar surface, which is the quantity we are attempting to fit for. Thus we find ourselves in a catch-22 where the stellar spectrum is required in order to know the appropriate value of the limb darkening coefficients, which is required in order to fit for the stellar spectrum. The result of fitting in this way is that I am assuming that limb-darkening is independent of wavelength or temperature, which is known in general to be an incorrect assumption [Claret and Bloemen, 2011].

One approach to mitigate this would be to retrieve the spectra through an iterative process, where in the first iteration all features are generated using the same limb darkening law. Once a spectrum is extracted for each feature, the geometric lightcurves can be re-calculated using previously estimated limb-darkening coefficient tables. The spectral fit can then be re-done, and this process continued until the models converge, which comes at the cost of time when fitting the models with say an MCMC. An alternate consideration would be to precisely quantify the effect this has on the final retrieval, which would depend on the rate of the change of limb darkening coefficients across the relevant temperature range.

## 9.4 Injection Retrieval Tests

In order to test the effectiveness of the model in retrieving spectral features of a star, I describe a series of injection retrieval tests in an idealized scenario in which I assume to know the number of spot features, as well as their positions and sizes. Thus I am attempting to retrieve only the spectral features of the spots and photosphere, and this represents a best case scenario, effectively acting as an upper limit on the strength of the current framework. Ongoing and future developments, described later in this chapter, will also implement a full MCMC retrieval in which the positions, sizes, and limb darkening effects will all be simultaneously fit for.

The model was tested on a suite of stellar surfaces, including ones with spots hotter than the photosphere, colder than the photosphere, both hot and cold spots, as well as anywhere from one to four individual spot features. Additionally, I tested

a series of single spot models with all but one parameter being held constant, varying either the size of a spot or its latitudinal position. I list the full sample of surfaces considered in table 9.1, along with the deviation from the true spectra used to simulate the observations. I show in figure 9-2 the breakdown of the SVD retrieval described in the previous section for each individual spot component. In addition, residual signal is also shown below the fits, in terms of % deviations from the injected truth spectra.

In figure 9-3, the time-series lightcurve is shown, as well the total fitted flux and the flux broken down by individual component. This figure highlights a potential weakness in the model, in the scenario where two spots (in this case spots 2 & 3), occur at the same longitude/phase along the stellar rotation (for this model the values of the longitudinal component were $\theta$ = VALUES respectively). This introduced a potential degeneracy, since a spot is identified solely by its geometric signal, and may be an explanation for why the retrieval of spot 1 shown in figure 9-2 is significantly worse than the other components.

It is found that in all cases the model is able to accurately retrieve the photospheric spectrum, often to a precision of well below 1%. Regarding the retrieval of the spot components, the precision is much more dependant on the specific details of the model, depending heavily in particular on the size of a spot, as well as its latitudinal position.

Future work will seek to expand on both the range of models considered and more critically on testing the feasibility of the model to retrieve the positional information of the spot in addition to the spectral information. Preliminary MCMC retrievals, fitting for all components of spots as well as for a quadratic limb darkening effect, have shown promising results and suggest that the model will be able to accurately retrieve stellar spectra with no prior assumptions on stellar spectra.

## 9.5 Varying Observation Baseline

In this section I focus on the biases and retrieval capabilities of an observation which encompasses only a fraction of the total rotational period of a star. Given the time-

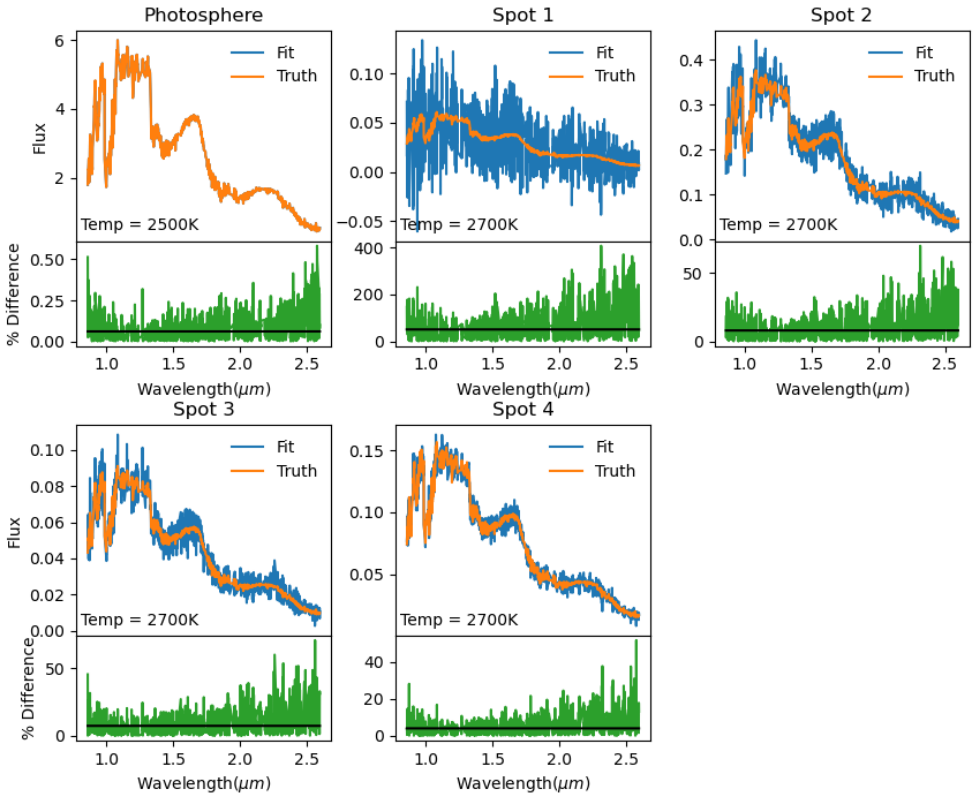


Figure 9-2: The results of fitting a model consisting of four spot features, plus a constant photosphere, to a set of lightcurves across a range of wavelength bins.

variability of a spot signal, there exists a strong correlation between the duration of an observation, the phase offset relative to a spots longitude, and the retrieved uncertainty on the stellar photosphere.

In order to test these biases, I first simulate a spotted stellar surface as in this previous section, with anywhere from 1-4 spot features which may be colder or hotter than the background photosphere. From this model, I then generate a set of synthetic observations again as described in the previous sections. In the previous section I considered observations which spanned the entire rotation phase of the star. I now seek to study the ability for our model to retrieve spectra signals when only a fraction of the total rotational cycle of a star is observed (although I still consider to be observing the full range of wavelengths as in the previous section).

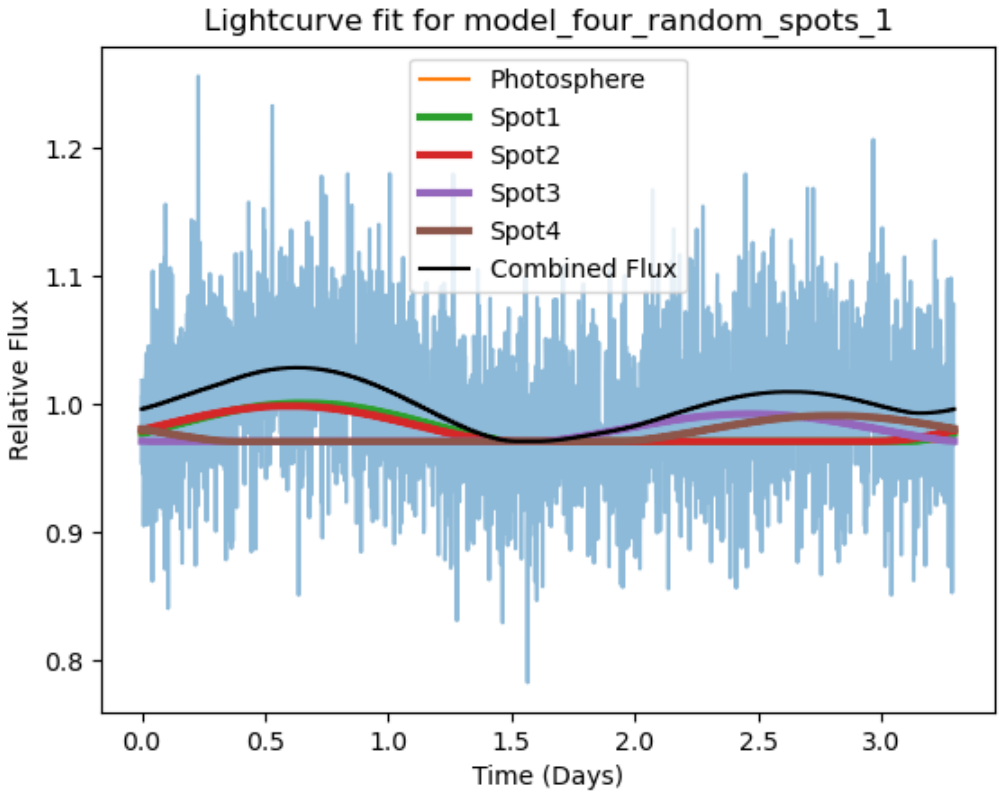


Figure 9-3: The results of fitting a model consisting of four spot features, plus a constant photosphere, to a set of lightcurves across a range of wavelength bins.

For each observation, I chose two parameters: (1) an offset for the longitudinal rotation of the star relative to the observer, and (2) a viewing window, defined as a fraction from 0-1 of the stellar rotation period. Selecting a value of 1 represents the analysis done in the previous section, for which the entire stellar rotation was supplied to the fitting routine. These two values then defined a time series, for which I generate the base-vector signals attributed to each spot feature on the stellar surface. I then use SVG decomposition to run a least-squares regression analysis and fit for the contribution function of each spot. As in the previous section, I can then compare the retrieved spectrum to the injected spectrum for each component (photosphere + spots), the results of which are shown in figure 9-4.

The various curves represent different observing covering fractions. The variation

Table 9.1: Test Model Details

| $\theta_1$ | $\phi_1$ | $r_1$ | $T_1$ | $\theta_2$ | $\phi_2$ | $r_2$ | $T_2$ | $\theta_3$ | $\phi_1$ | $r_3$ | $T_3$ | $\theta_4$ | $\phi_4$ | $r_4$ | $T_4$ | $\sigma_p$ | $\sigma_1$ | $\sigma_2$ | $\sigma_3$ | $\sigma_4$ |
|---|---|---|---|---|---|---|---|---|---|---|---|---|---|---|---|---|---|---|---|---|
| 2.26 | -1.34 | 0.31 | 2700.0 | 1.01 | -1.01 | 0.11 | 2700.0 | 1.27 | -0.26 | 0.09 | 2300.0 | -1.68 | 0.66 | 0.2 | 2700.0 | 0.19 | 11.89 | 80.08 | 106.87 | 4.6 |
| -1.25 | -0.01 | 0.08 | 2700.0 | -1.14 | -0.56 | 0.24 | 2700.0 | 1.58 | -0.57 | 0.12 | 2700.0 | 0.95 | 0.3 | 0.14 | 2700.0 | 0.06 | 49.94 | 8.23 | 7.49 | 4.09 |
| -2.32 | 1.12 | 0.13 | 2300.0 | 2.84 | 1.28 | 0.09 | 2700.0 | 3.04 | 0.32 | 0.15 | 2300.0 | -2.36 | 0.66 | 0.08 | 2700.0 | 0.05 | 357.09 | 167.68 | 31.97 | 254.66 |
| 2.65 | 0.91 | 0.09 | 2700.0 | 0.48 | -1.33 | 0.19 | 2700.0 | -1.02 | -0.45 | 0.22 | 2700.0 | 1.19 | 1.12 | 0.11 | 2300.0 | 0.11 | 23.92 | 16.43 | 2.12 | 40.85 |
| -1.51 | -0.57 | 0.34 | 2300.0 | 3.11 | 1.43 | 0.11 | 2700.0 | 0.07 | -0.06 | 0.06 | 2300.0 | 2.06 | -0.25 | 0.2 | 2300.0 | 0.24 | 2.45 | 118.47 | 82.94 | 5.77 |
| -1.72 | -1.36 | 0.08 | 2700.0 | 0.19 | -1.03 | 0.12 | 2700.0 | 2.97 | -1.22 | 0.2 | 2300.0 | | | | | 0.11 | 70.83 | 14.42 | 16.5 | |
| -0.31 | 0.89 | 0.3 | 2700.0 | -0.98 | -0.45 | 0.24 | 2300.0 | 1.16 | -1.23 | 0.12 | 2300.0 | | | | | 0.05 | 1.59 | 3.23 | 35.74 | |
| 0.6 | -0.58 | 0.27 | 2300.0 | 1.47 | 0.59 | 0.11 | 2700.0 | -1.41 | 0.03 | 0.22 | 2700.0 | | | | | 0.06 | 1.8 | 6.94 | 1.29 | |
| -2.71 | -0.25 | 0.2 | 2700.0 | 0.72 | -1.19 | 0.17 | 2700.0 | 1.34 | 1.49 | 0.11 | 2700.0 | | | | | 0.07 | 1.87 | 11.7 | 140.47 | |
| -1.87 | -0.86 | 0.24 | 2700.0 | -1.14 | 1.11 | 0.23 | 2700.0 | -1.47 | -0.13 | 0.27 | 2300.0 | | | | | 0.05 | 6.63 | 14.95 | 11.11 | |
| -1.0 | 1.36 | 0.16 | 2300.0 | -1.91 | 0.55 | 0.13 | 2700.0 | | | | | | | | | 0.04 | 31.72 | 4.23 | | |
| 2.75 | 0.82 | 0.08 | 2300.0 | -1.43 | -0.41 | 0.18 | 2700.0 | | | | | | | | | 0.05 | 28.56 | 2.05 | | |
| -1.62 | 1.19 | 0.3 | 2300.0 | -2.32 | -0.95 | 0.32 | 2700.0 | | | | | | | | | 0.04 | 5.69 | 1.37 | | |
| -2.78 | -0.36 | 0.34 | 2300.0 | -0.2 | 1.48 | 0.25 | 2700.0 | | | | | | | | | 0.11 | 1.24 | 22.2 | | |
| 0.79 | 1.19 | 0.24 | 2300.0 | -0.6 | 0.21 | 0.09 | 2700.0 | | | | | | | | | 0.04 | 5.91 | 5.98 | | |
| 0.0 | 0.0 | 0.1 | 2700.0 | | | | | | | | | | | | | 0.04 | 4.43 | | | |
| 0.0 | 0.39 | 0.1 | 2700.0 | | | | | | | | | | | | | 0.04 | 4.92 | | | |
| 0.0 | 0.79 | 0.1 | 2700.0 | | | | | | | | | | | | | 0.04 | 7.93 | | | |
| 0.0 | 1.18 | 0.1 | 2700.0 | | | | | | | | | | | | | 0.04 | 20.51 | | | |
| 0.0 | 0.0 | 0.2 | 2700.0 | | | | | | | | | | | | | 0.04 | 1.14 | | | |
| 0.0 | 0.39 | 0.2 | 2700.0 | | | | | | | | | | | | | 0.04 | 1.48 | | | |
| 0.0 | 0.79 | 0.2 | 2700.0 | | | | | | | | | | | | | 0.04 | 1.92 | | | |
| 0.0 | 1.18 | 0.2 | 2700.0 | | | | | | | | | | | | | 0.04 | 4.83 | | | |
| 0.0 | 0.0 | 0.05 | 2700.0 | | | | | | | | | | | | | 0.04 | 17.85 | | | |
| 0.0 | 0.0 | 0.11 | 2700.0 | | | | | | | | | | | | | 0.04 | 4.55 | | | |
| 0.0 | 0.0 | 0.17 | 2700.0 | | | | | | | | | | | | | 0.04 | 1.62 | | | |
| 0.0 | 0.0 | 0.24 | 2700.0 | | | | | | | | | | | | | 0.04 | 0.9 | | | |
| 0.0 | 0.79 | 0.05 | 2700.0 | | | | | | | | | | | | | 0.04 | 33.53 | | | |
| 0.0 | 0.79 | 0.11 | 2700.0 | | | | | | | | | | | | | 0.04 | 6.35 | | | |
| 0.0 | 0.79 | 0.17 | 2700.0 | | | | | | | | | | | | | 0.04 | 2.72 | | | |
| 0.0 | 0.79 | 0.24 | 2700.0 | | | | | | | | | | | | | 0.04 | 1.47 | | | |

Table 9.2: Parameters for the different stellar surfaces used to test the retrieval framework. The horizontal solid lines separate families of models. The first three are a random sampling of models with 4, 3 and 2 spot features, with maximal spot sizes of $r = 0.3$ and temperatures of either 2300K or 2700K. The fourth and fifth group show models with a single spot of varying latitudes, for two fixed sizes. The last two groups are for a series of models with spots of varying sizes, at two fixed latitudes. The $\sigma$ value show the % difference between the retrieved spectra and the injected truth spectra for each component (including the photosphere $\sigma_p$)

as the offset shifts can be attributed to spots coming into and out of view. For this particular example, it is seen that only for a covering fraction of $> 80\%$ can the stellar photosphere be reliably and consistently constrained to within 1%, regardless of where a spot is positioned along the stellar surface. Recall that this is a best-case scenario, where I assume to know the true position and size of the spot features. Thus for a real observation, it is likely that well above half of a stellar-rotation period is required to be observed in ordered to obtain 1% precision on the spectrum of the stellar photosphere.

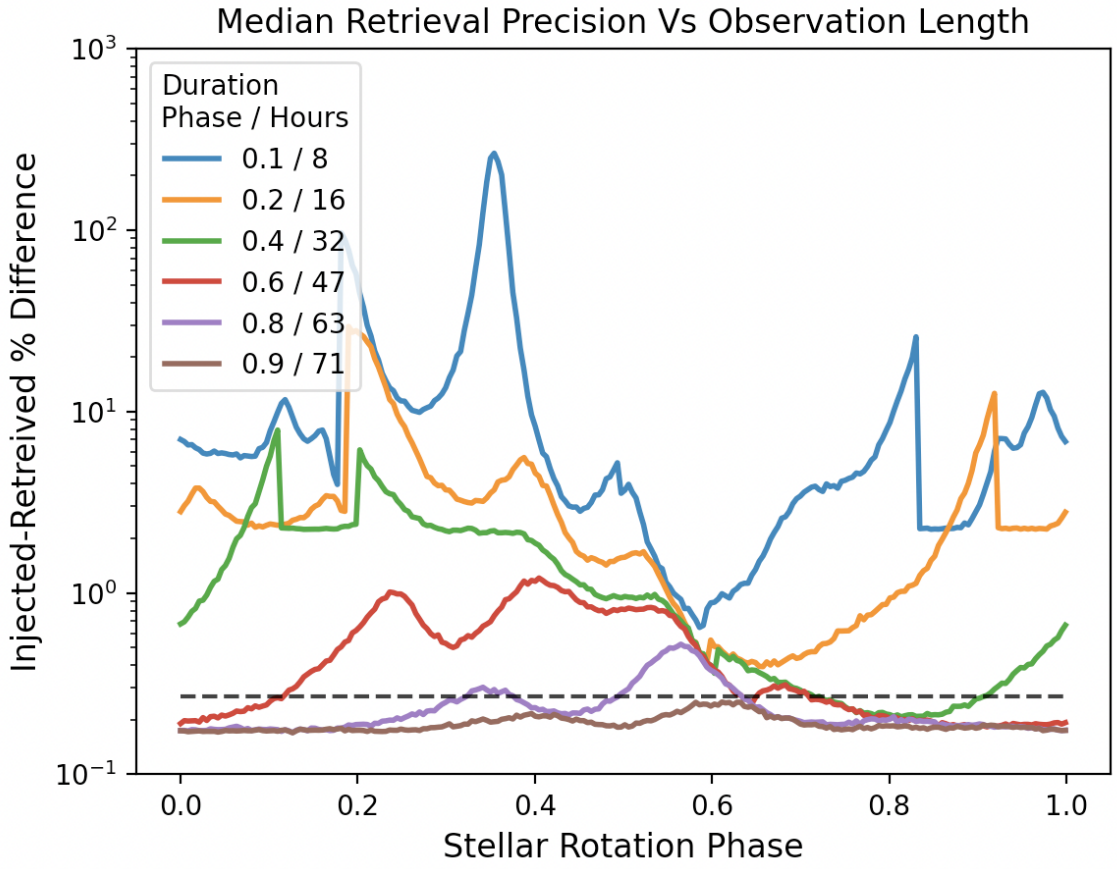


Figure 9-4: The median stellar photospheric spectral precision retrieved as the duration of an observation is varied from just a tenth of the stellar rotation period to a full rotational cycle (colored curves). The model analysed here contains four spot features. Additionally, I show the effect of varying the offset during the rotational cycle, indicated by the x-axis. The dashed line represents the out of transit uncertainty of a previous NIRISS observation of the TRAPPIST-1 system.

## 9.6 Discussion & Future Steps

I have described here a framework which can be used to generate synthetic time and wavelength observations of a stellar surface with an arbitrary disposition of inhomogeneities, focusing specifically on spot features. In addition to generating synthetic NIRISS data for a TRAPPIST-1 like planet, I have also described a framework for using Singular Value Decomposition (SVD) to quickly retrieve an Ordinary Least Squares estimate for the spectra used to generate the signal, without using any prior information about the spectra themselves. Within this framework I am able to em-

pirically estimate the spectra of a spotted photosphere to well below 1% accuracy, and the spectra of individual spot features to as low as just a few percent in ideal scenarios.

An additional benefit of this framework is the ability to consider interactions between a transiting planet and spot features. Since the model provides spectral fits for each component, they can be weighted appropriately during a transit in order to accurately calculate the total amount of flux observed from the stellar surface.

This work represents the first steps towards building a completely empirical library of spotted stellar surfaces (similar in scope to the work of Kesseli et al. [2017] which compiled a library of empirical spectra for various stellar types). An important distinction here is that the spectra being measured are not for disk-integrated features, but rather for 'pure' basis components which may be combined with rotational geometry in order to produce accurate spectra for stars with arbitrarily complex surface features.

The next steps for this study will involve first and foremost relaxing the constraints on prior knowledge, particularly on assumed positions and sized of spots, however a blind fit MCMC fit of all parameters would be too unconstrained. For example, the model might attempt to place two spot features near each other and attribute to each of them half the total flux emerging from a single spot. In order to mitigate this, it would be necessary to run a pre-fit analysis of any features in the lightcurves which would allow priors to be placed on spot features. Following this, an MCMC can then be run with a fixed number of spots, each confined to their own regions on the stellar surface. Statistics of fit metrics such as the Bayesian and Aikaike Information Criteria (BIC & AIC respectively) could then be used in order to determine how many spot features best describes the stellar surface. Additional improvements would also seek to incorporate knowledge from spectra models, in a way that would not bias the final results. This might consist of using models such as gaussian processes in order to constrain the correlations between spectral features as a function of wavelength.

The work presented thus far represents the initial steps and proof of concept that under ideal conditions we are able to accurately retrieve the individual spectra of

spot features, at the level of uncertainty that is provided by instruments such as NIRISS on the James Webb Space Telescope. It has also been shown however that even under such ideal conditions, a significant baseline of observation with regards to stellar rotation period is required in order to retrieve such an accurate measurement.

# Part V

# Summary

# Chapter 10

# Summary

The scope of topics in this thesis has been wide, illustrating the multitude of opportunities for characterising exoplanets that have resulted from both an explosive growth in the number of known exoplanets, as well as an increase in the quality of their observations. When considering the tools at our disposal for characterizing exoplanets in this and future decades, it is astounding to consider how far this fledgling field has advanced in a short 30 year time span. The focus of my work over these past years has been to ensure that we are able to extract the greatest amount of information from these rich data sets, as we continue towards the goals of finding new worlds, both like and unlike any we have previously found, and ultimately one day potentially finding life elsewhere in the universe.

In part two of this thesis (chapter 2 - 4), I first presented an in-depth analysis of the HIP41387 system. This is among a handful of exoplanet systems with five or more planets, and the brightness of the host star implies that the outer gas giants will provide excellent opportunities for atmospheric characterization [Alam et al., 2022]. My first contribution towards characterising this system was a combined analysis of several years and instruments worth of data, providing refined orbital parameters, as well as narrowing down the potential orbital periods for the two outer planets, which at the time of my analysis remained completely unknown. I used the known value of the stellar density to constrain the shape of the orbits of the two outer planets, based on the photoeccentric effect Dawson and Johnson [2012]. Using arguments pertaining

to orbital stability, which disallow intersecting orbits, I was able to predict the most likely specific values for the orbital periods of planets d and f, which in the interim have been shown to be their true values [Grouffal et al., 2022, Santerne et al., 2019].

Following these observations, as described in chapter 3 through a successful *Spitzer* DDT proposal I was able to obtain two additional transit times for HIP41378 c, which across all observations now spanned a 4 year baseline. Using dynamical TTV models, I found that perturbations from the five known planets in the system were not able to recreate the shifts in transit centers observed for planet c. It was only once I included an as yet-undetected sixth planet with an orbital period of 62 days (which is nearly a 2:1 resonance with the period of planet c), was I able to reproduce the observed TTV signal. Furthermore, in chapter 4 I highlighted contributions I made towards the refinement of the ephemerides of planets in two multi-planet systems, ensuring the ability to detect future transits for characterisation. The culmination of this work is the characterization of a series of multi-planet systems, which are ripe for the high signal-to-noise atmospheric characterization which will be afforded missions such as JWST, as well as future ground based ELTs (Extremely Large Telescopes) and next generation space based missions.

In part three of this thesis comprising chapters 5 - 7, I consider planets as proper three dimensional objects, and in particular focus on how deformations in their structure affect the analysis of their lightcurves. The aim of this work was to bring to light effects, which while previously considered in the literature, had yet to be properly contextualized in the regime of high precision photometry, while also including a larger sample of planets in my analysis than had previously been considered. In particular, I focused on the precision required for these effects to present themselves robustly in observations of transiting exoplanet lightcurves. Instruments such as JWST allow us to obtain high SNR transits of exoplanets with just a handful of observations, whereas with previous instruments it was often necessary to stack several observations in order to achieve a similar level of precision. The implication of this is that effects which were too small to be detectable with previous observations may begin to appear in more and more lightcurves, and that ignoring them could lead to biases

in the characterisation of an exoplanet.

Indeed, such a bias was found to occur in the case of planets experiencing tidally induced oblateness. If the degree of oblateness was low enough, then it was seen that a spherical transit model could seemingly fit the data to a high degree of statistical accuracy, while in fact retrieving the incorrect truth value. This is due to the flexibility of transit models, and degeneracy between certain parameters which allow them to adjust for variations during ingress and egress.

In addition to oblateness, in chapter 6 I also considered close in planets undergoing tidal deformation, which would imply an incorrect assessment of a planets density if it were assumed to be spherical. This effect was framed in the context of the uncertainty of the parameters that are used to calculate the density of an exoplanet. It was found that with current measurements, for many planets the observational impact of tidal distortions is below the uncertainty limit provided by measured parameters. However for a large number of planets, a reduction in the uncertainty on their density by just a factor of three is enough to causes these distortions to dominate their error budget. I conducted this analysis on the largest number of planets to date, focusing on nearly 200 planets with orbital periods less than 3 days, which is often taken to be a boundary for when planets will begin to experience tidal deformation.

As a final consideration of planets as proper 3-d objects, in chapter 7 I present an analysis of over 100 Hubble STIS observations of the TRAPPIST-1 system. The goal of these observations was to measure Lyman-$\alpha$ emission from the star, and to determine if its orbiting planets hosted exospheres which would cause transit like signals to appear. It was found the for most planets in the system, there is not a statistically significant associated reduction in flux from the host star, indicating the lack of an extended neutral Hydrogen exosphere. By looking at the nearly five year baseline of observations, it was however found to be possible to retrieve the current best estimate rotation period of TRAPPIST-1 (P = 3.295), indicating that the Lyman-$\alpha$ emission of the star is modulated by its rotation. This additionally confirms that an accurate retrieval of the Lyman-$\alpha$ lightcurve of the star is being obtained, since it is expected to exhibit variations correlated to the overall flux of the

star as it rotated.

In the last part of this thesis, comprising chapter 8 & 9, I turned my attention to stellar surfaces, and the way in which surface features and inhomogeneities can manifest themselves in both time series and spectral observations. In chapter 8 I first describe a model I created which is capable of calculating the lightcurve of a stellar surface which has hot and cold spots, which is also being eclipsed by an arbitrarily shaped object. The context for this study was a series of M-dwarfs, observed by TESS, which were found to have complex, periodic signals with high amplitudes which could not be explained by typical scenarios of M-dwarf variability. The model I created was used to show that interactions between start spots on the photosphere and a thin, opaque, misaligned disk of orbiting debris could properly recreate the sharp features observed in many of the observed lightcurves.

In the final chapter I adapt the model described in chapter 8 in order to generate simulated stellar spectral observations of TRAPPIST-1, using NIRISS observations of the system to calibrate the noise levels of the simulated spectra data. Using the same model of a spotted stellar surface, I generated 'base-vectors' representing the time-varying geometric projection of a star spot, which varied based on the latitude and size of the spot. Using these base curves, I then used SVD to empirically calculate the best fit spectral signature of each spot, which were retrieved using no prior information about the input spectra. This represents the first steps towards a framework of empirically measuring the spectra of stellar surfaces, without relying on simulated models which have been shown to be potential bottlenecks in reaching the highest levels of precision possible for space-based observatories [Rackham and de Wit, 2023].

Each of these individual components represent steps towards characterising exoplanets in greater detail than has ever been possible before. Upcoming ground based instruments such as the TMT [Skidmore et al., 2018], as well future space based missions such as *LUVOIR* [The LUVOIR Team, 2019] and the Vera C. Rubin observatory [Ivezić et al., 2019] will provide unprecedented opportunities to study exoplanets. However these advancements would be for nought if the methods used to analyze them do not account for details and features which were previously unde-

tectable. This would open the door to a host of degeneracies and biases which would limit us from realizing the full potential these instruments can provide. Indeed, we continuously strive towards a future in which we are able to describe exoplanets with a level of detail similar to what is capable for the planets in our own solar system, including precise descriptions of their orbits, shapes, surfaces features, atmospheres, internal structure, and more.

# Bibliography


E. Agol and D. C. Fabrycky. Transit-Timing and Duration Variations for the Discovery and Characterization of Exoplanets. In H. J. Deeg and J. A. Belmonte, editors, *Handbook of Exoplanets*, page 7. 2018. doi: 10.1007/978-3-319-55333-7_7.

E. Agol, C. Dorn, S. L. Grimm, M. Turbet, E. Ducrot, L. Delrez, M. Gillon, B.-O. Demory, A. Burdanov, K. Barkaoui, Z. Benkhaldoun, E. Bolmont, A. Burgasser, S. Carey, J. de Wit, D. Fabrycky, D. Foreman-Mackey, J. Haldemann, D. M. Hernandez, J. Ingalls, E. Jehin, Z. Langford, J. Leconte, S. M. Lederer, R. Luger, R. Malhotra, V. S. Meadows, B. M. Morris, F. J. Pozuelos, D. Queloz, S. N. Raymond, F. Selsis, M. Sestovic, A. H. M. J. Triaud, and V. Van Grootel. Refining the Transit-timing and Photometric Analysis of TRAPPIST-1: Masses, Radii, Densities, Dynamics, and Ephemerides. , 2(1):1, Feb. 2021. doi: 10.3847/PSJ/abd022.

B. Akinsanmi , S. C. C. Barros, N. C. Santos, M. Oshagh, and L. M. Serrano. Constraining the oblateness of transiting planets with photometry and spectroscopy. , 497(3):3484–3492, Sept. 2020. doi: 10.1093/mnras/staa2164.

B. Akinsanmi, S. C. C. Barros, N. C. Santos, A. C. M. Correia, P. F. L. Maxted, G. Boué, and J. Laskar. Detectability of shape deformation in short-period exoplanets. , 621:A117, Jan. 2019. doi: 10.1051/0004-6361/201834215.

M. K. Alam, J. Kirk, C. D. Dressing, M. López-Morales, K. Ohno, P. Gao, B. Akinsanmi, A. Santerne, S. Grouffal, V. Adibekyan, S. C. C. Barros, L. A. Buchhave, I. J. M. Crossfield, F. Dai, M. Deleuil, S. Giacalone, J. Lillo-Box, M. Marley, A. W. Mayo, A. Mortier, N. C. Santos, S. G. Sousa, E. V. Turtelboom, P. J. Wheatley, and A. M. Vanderburg. The first near-infrared transmission spectrum of hip 41378 f, a low-mass temperate jovian world in a multiplanet system. *The Astrophysical Journal Letters*, 927(1):L5, mar 2022. doi: 10.3847/2041-8213/ac559d. URL https://dx.doi.org/10.3847/2041-8213/ac559d.

C. Alcock, C. W. Akerlof, R. Allsman, T. Axelrod, D. Bennett, S. Chan, K. Cook, K. C. Freeman, K. Griest, S. L. Marshall, et al. Possible gravitational microlensing of a star in the large magellanic cloud. *nature*, 365(6447):621–623, 1993.

F. Allard, T. Guillot, H.-G. Ludwig, P. H. Hauschildt, A. Schweitzer, D. R. Alexander, and J. W. Ferguson. Model Atmospheres and Spectra: The Role of Dust. In E. Martín, editor, *Brown Dwarfs*, volume 211 of *IAU Symposium*, page 325, June 2003.

Astropy Collaboration, T. P. Robitaille, E. J. Tollerud, P. Greenfield, M. Droettboom, E. Bray, T. Aldcroft, M. Davis, A. Ginsburg, A. M. Price-Whelan, W. E. Kerzendorf, A. Conley, N. Crighton, K. Barbary, D. Muna, H. Ferguson, F. Grollier, M. M. Parikh, P. H. Nair, H. M. Unther, C. Deil, J. Woillez, S. Conseil, R. Kramer, J. E. H. Turner, L. Singer, R. Fox, B. A. Weaver, V. Zabalza, Z. I. Edwards, K. Azalee Bostroem, D. J. Burke, A. R. Casey, S. M. Crawford, N. Dencheva, J. Ely, T. Jenness, K. Labrie, P. L. Lim, F. Pierfederici, A. Pontzen, A. Ptak, B. Refsdal, M. Servillat, and O. Streicher. Astropy: A community Python package for astronomy. , 558:A33, Oct. 2013. doi: 10.1051/0004-6361/201322068.

Astropy Collaboration, A. M. Price-Whelan, B. M. Sipőcz, H. M. Günther, P. L. Lim, S. M. Crawford, S. Conseil, D. L. Shupe, M. W. Craig, N. Dencheva, A. Ginsburg, J. T. Vand erPlas, L. D. Bradley, D. Pérez-Suárez, M. de Val-Borro, T. L. Aldcroft, K. L. Cruz, T. P. Robitaille, E. J. Tollerud, C. Ardelean, T. Babej, Y. P. Bach, M. Bachetti, A. V. Bakanov, S. P. Bamford, G. Barentsen, P. Barmby, A. Baumbach, K. L. Berry, F. Biscani, M. Boquien, K. A. Bostroem, L. G. Bouma, G. B. Brammer, E. M. Bray, H. Breytenbach, H. Buddelmeijer, D. J. Burke, G. Calderone, J. L. Cano Rodríguez, M. Cara, J. V. M. Cardoso, S. Cheedella, Y. Copin, L. Corrales, D. Crichton, D. D'Avella, C. Deil, É. Depagne, J. P. Dietrich, A. Donath, M. Droettboom, N. Earl, T. Erben, S. Fabbro, L. A. Ferreira, T. Finethy, R. T. Fox, L. H. Garrison, S. L. J. Gibbons, D. A. Goldstein, R. Gommers, J. P. Greco, P. Greenfield, A. M. Groener, F. Grollier, A. Hagen, P. Hirst, D. Homeier, A. J. Horton, G. Hosseinzadeh, L. Hu, J. S. Hunkeler, Ž. Ivezić, A. Jain, T. Jenness, G. Kanarek, S. Kendrew, N. S. Kern, W. E. Kerzendorf, A. Khvalko, J. King, D. Kirkby, A. M. Kulkarni, A. Kumar, A. Lee, D. Lenz, S. P. Littlefair, Z. Ma, D. M. Macleod, M. Mastropietro, C. McCully, S. Montagnac, B. M. Morris, M. Mueller, S. J. Mumford, D. Muna, N. A. Murphy, S. Nelson, G. H. Nguyen, J. P. Ninan, M. Nöthe, S. Ogaz, S. Oh, J. K. Parejko, N. Parley, S. Pascual, R. Patil, A. A. Patil, A. L. Plunkett, J. X. Prochaska, T. Rastogi, V. Reddy Janga, J. Sabater, P. Sakurikar, M. Seifert, L. E. Sherbert, H. Sherwood-Taylor, A. Y. Shih, J. Sick, M. T. Silbiger, S. Singanamalla, L. P. Singer, P. H. Sladen, K. A. Sooley, S. Sornarajah, O. Streicher, P. Teuben, S. W. Thomas, G. R. Tremblay, J. E. H. Turner, V. Terrón, M. H. van Kerkwijk, A. de la Vega, L. L. Watkins, B. A. Weaver, J. B. Whitmore, J. Woillez, V. Zabalza, and Astropy Contributors. The Astropy Project: Building an Open-science Project and Status of the v2.0 Core Package. , 156(3):123, Sept. 2018. doi: 10.3847/1538-3881/aabc4f.

Astropy Collaboration, A. M. Price-Whelan, P. L. Lim, N. Earl, N. Starkman, L. Bradley, D. L. Shupe, A. A. Patil, L. Corrales, C. E. Brasseur, M. N"othe, A. Donath, E. Tollerud, B. M. Morris, A. Ginsburg, E. Vaher, B. A. Weaver, J. Tocknell, W. Jamieson, M. H. van Kerkwijk, T. P. Robitaille, B. Merry, M. Bachetti, H. M. G"unther, T. L. Aldcroft, J. A. Alvarado-Montes, A. M. Archibald, A. B'odi, S. Bapat, G. Barentsen, J. Baz'an, M. Biswas, M. Boquien, D. J. Burke, D. Cara, M. Cara, K. E. Conroy, S. Conseil, M. W. Craig, R. M. Cross, K. L. Cruz, F. D'Eugenio, N. Dencheva, H. A. R. Devillepoix, J. P. Dietrich, A. D.

Eigenbrot, T. Erben, L. Ferreira, D. Foreman-Mackey, R. Fox, N. Freij, S. Garg, R. Geda, L. Glattly, Y. Gondhalekar, K. D. Gordon, D. Grant, P. Greenfield, A. M. Groener, S. Guest, S. Gurovich, R. Handberg, A. Hart, Z. Hatfield-Dodds, D. Homeier, G. Hosseinzadeh, T. Jenness, C. K. Jones, P. Joseph, J. B. Kalmbach, E. Karamehmetoglu, M. Kaluszy'nski, M. S. P. Kelley, N. Kern, W. E. Kerzendorf, E. W. Koch, S. Kulumani, A. Lee, C. Ly, Z. Ma, C. MacBride, J. M. Maljaars, D. Muna, N. A. Murphy, H. Norman, R. O'Steen, K. A. Oman, C. Pacifici, S. Pascual, J. Pascual-Granado, R. R. Patil, G. I. Perren, T. E. Pickering, T. Rastogi, B. R. Roulston, D. F. Ryan, E. S. Rykoff, J. Sabater, P. Sakurikar, J. Salgado, A. Sanghi, N. Saunders, V. Savchenko, L. Schwardt, M. Seifert-Eckert, A. Y. Shih, A. S. Jain, G. Shukla, J. Sick, C. Simpson, S. Singanamalla, L. P. Singer, J. Singhal, M. Sinha, B. M. SipHocz, L. R. Spitler, D. Stansby, O. Streicher, J. Sumak, J. D. Swinbank, D. S. Taranu, N. Tewary, G. R. Tremblay, M. d. Val-Borro, S. J. Van Kooten, Z. Vasovi'c, S. Verma, J. V. de Miranda Cardoso, P. K. G. Williams, T. J. Wilson, B. Winkel, W. M. Wood-Vasey, R. Xue, P. Yoachim, C. Zhang, A. Zonca, and Astropy Project Contributors. The Astropy Project: Sustaining and Growing a Community-oriented Open-source Project and the Latest Major Release (v5.0) of the Core Package. *apj*, 935(2):167, Aug. 2022. doi: 10.3847/1538-4357/ac7c74.

I. I. Baliukin, J.-L. Bertaux, E. Quémerais, V. V. Izmodenov, and W. Schmidt. Swan/soho lyman- mapping: The hydrogen geocorona extends well beyond the moon. *Journal of Geophysical Research: Space Physics*, 124(2):861–885, 2019. doi: https://doi.org/10.1029/2018JA026136. URL https://agupubs.onlinelibrary.wiley.com/doi/abs/10.1029/2018JA026136.

I. Baraffe, G. Chabrier, T. S. Barman, F. Allard, and P. H. Hauschildt. Evolutionary models for cool brown dwarfs and extrasolar giant planets. The case of HD 209458. , 402:701–712, May 2003. doi: 10.1051/0004-6361:20030252.

J. R. Barnes, C. J. Leigh, H. R. A. Jones, T. S. Barman, D. J. Pinfield, A. Collier Cameron, and J. S. Jenkins. Near-infrared spectroscopic search for the close orbiting planet HD 75289b. , 379:1097–1107, Aug. 2007. doi: 10.1111/j.1365-2966.2007.11990.x.

J. R. Barnes, S. V. Jeffers, C. A. Haswell, H. R. A. Jones, D. Shulyak, Y. V. Pavlenko, and J. S. Jenkins. Surprisingly different star-spot distributions on the near equal-mass equal-rotation-rate stars in the M dwarf binary GJ 65 AB. *Monthly Notices of the Royal Astronomical Society*, 471(1):811–823, 06 2017. ISSN 0035-8711. doi: 10.1093/mnras/stx1482. URL https://doi.org/10.1093/mnras/stx1482.

J. W. Barnes and J. J. Fortney. Measuring the Oblateness and Rotation of Transiting Extrasolar Giant Planets. , 588(1):545–556, May 2003. doi: 10.1086/373893.

J. W. Barnes, C. S. Cooper, A. P. Showman, and W. B. Hubbard. Detecting the Wind-Driven Shapes of Extrasolar Giant Planets from Transit Photometry. , 706 (1):877–884, Nov. 2009. doi: 10.1088/0004-637X/706/1/877.

R. Barnes. Tidal locking of habitable exoplanets. *Celestial Mechanics and Dynamical Astronomy*, 129(4):509–536, Dec. 2017. doi: 10.1007/s10569-017-9783-7.

S. C. C. Barros, H. Gosselin, J. Lillo-Box, D. Bayliss, E. Delgado Mena, B. Brugger, A. Santerne, D. J. Armstrong, V. Adibekyan, J. D. Armstrong, D. Barrado, J. Bento, I. Boisse, A. S. Bonomo, F. Bouchy, D. J. A. Brown, W. D. Cochran, A. Collier Cameron, M. Deleuil, O. Demangeon, R. F. Díaz, A. Doyle, X. Dumusque, D. Ehrenreich, N. Espinoza, F. Faedi, J. P. Faria, P. Figueira, E. Foxell, G. Hébrard, S. Hojjatpanah, J. Jackman, M. Lendl, R. Ligi, C. Lovis, C. Melo, O. Mousis, J. J. Neal, H. P. Osborn, D. Pollacco, N. C. Santos, R. Sefako, A. Shporer, S. G. Sousa, A. H. M. J. Triaud, S. Udry, A. Vigan, and A. Wyttenbach. Precise masses for the transiting planetary system HD 106315 with HARPS. , 608: A25, Dec. 2017. doi: 10.1051/0004-6361/201731276.

S. C. C. Barros, B. Akinsanmi, G. Boué, A. M. S. Smith, J. Laskar, S. Ulmer-Moll, J. Lillo-Box, D. Queloz, A. C. Cameron, S. G. Sousa, D. Ehrenreich, M. J. Hooton, G. Bruno, B. O. Demory, A. C. M. Correia, O. D. S. Demangeon, T. G. Wilson, A. Bonfanti, S. Hoyer, Y. Alibert, R. Alonso, G. A. Escudé, D. Barbato, T. Bárczy, D. Barrado, W. Baumjohann, M. Beck, T. Beck, W. Benz, M. Bergomi, N. Billot, X. Bonfils, F. Bouchy, A. Brandeker, C. Broeg, J. Cabrera, V. Cessa, S. Charnoz, C. C. V. Damme, M. B. Davies, M. Deleuil, A. Deline, L. Delrez, A. Erikson, A. Fortier, L. Fossati, M. Fridlund, D. Gandolfi, A. G. Muñoz, M. Gillon, M. Güdel, K. G. Isaak, K. Heng, L. Kiss, A. L. des Etangs, M. Lendl, C. Lovis, D. Magrin, V. Nascimbeni, P. F. L. Maxted, G. Olofsson, R. Ottensamer, I. Pagano, E. Pallé, H. Parviainen, G. Peter, G. Piotto, D. Pollacco, R. Ragazzoni, N. Rando, H. Rauer, I. Ribas, N. C. Santos, G. Scandariato, D. Ségransan, A. E. Simon, M. Steller, G. M. Szabó, N. Thomas, S. Udry, B. Ulmer, V. Van Grootel, and N. A. Walton. Detection of the tidal deformation of WASP-103b at 3 $\sigma$ with CHEOPS. , 657:A52, Jan. 2022. doi: 10.1051/0004-6361/202142196.

J. C. Becker, A. Vanderburg, F. C. Adams, S. A. Rappaport, and H. M. Schwengeler. WASP-47: A Hot Jupiter System with Two Additional Planets Discovered by K2. , 812:L18, Oct. 2015. doi: 10.1088/2041-8205/812/2/L18.

C. A. Beichman, H. A. C. Giles, R. Akeson, D. Ciardi, J. Christiansen, H. Isaacson, G. M. Marcy, E. Sinukoff, T. Greene, J. J. Fortney, I. Crossfield, R. Hu, A. W. Howard, E. A. Petigura, and H. A. Knutson. Validation and Initial Characterization of the Long Period Planet Kepler-1654 b. *ArXiv e-prints*, Feb. 2018.

D. Berardo and J. de Wit. On the Effects of Planetary Oblateness on Exoplanet Studies. *Arxiv e-prints*, July 2022.

D. Berardo, A. Cumming, and G.-D. Marleau. The evolution of gas giant entropy during formation by runaway accretion. *The Astrophysical Journal*, 834(2):149, jan 2017. doi: 10.3847/1538-4357/834/2/149. URL https://dx.doi.org/10.3847/1538-4357/834/2/149.

D. Berardo, I. J. M. Crossfield, M. Werner, E. Petigura, J. Christiansen, D. R. Ciardi, C. Dressing, B. J. Fulton, V. Gorjian, T. P. Greene, K. Hardegree-Ullman, S. R. Kane, J. Livingston, F. Morales, and J. E. Schlieder. Revisiting the HIP 41378 System with K2 and Spitzer. , 157(5):185, May 2019. doi: 10.3847/1538-3881/ab100c.

J.-L. Beuzit, M. Feldt, K. Dohlen, D. Mouillet, P. Puget, J. Antichi, A. Baruffolo, P. Baudoz, A. Berton, A. Boccaletti, M. Carbillet, J. Charton, R. Claudi, M. Downing, P. Feautrier, E. Fedrigo, T. Fusco, R. Gratton, N. Hubin, M. Kasper, M. Langlois, C. Moutou, L. Mugnier, J. Pragt, P. Rabou, M. Saisse, H. M. Schmid, E. Stadler, M. Turrato, S. Udry, R. Waters, and F. Wildi. SPHERE: A 'Planet Finder' Instrument for the VLT. *The Messenger*, 125:29, Sept. 2006.

J. Biersteker and H. Schlichting. Determining Exoplanetary Oblateness Using Transit Depth Variations. , 154(4):164, Oct. 2017. doi: 10.3847/1538-3881/aa88c2.

D. Bisikalo, P. Kaygorodov, D. Ionov, V. Shematovich, H. Lammer, and L. Fossati. Three-dimensional Gas Dynamic Simulation of the Interaction between the Exoplanet WASP-12b and its Host Star. , 764:19, Feb. 2013. doi: 10.1088/0004-637X/764/1/19.

W. J. Borucki, D. Koch, G. Basri, N. Batalha, T. Brown, D. Caldwell, J. Caldwell, J. Christensen-Dalsgaard, W. D. Cochran, E. DeVore, E. W. Dunham, A. K. Dupree, T. N. Gautier, J. C. Geary, R. Gilliland, A. Gould, S. B. Howell, J. M. Jenkins, Y. Kondo, D. W. Latham, G. W. Marcy, S. Meibom, H. Kjeldsen, J. J. Lissauer, D. G. Monet, D. Morrison, D. Sasselov, J. Tarter, A. Boss, D. Brownlee, T. Owen, D. Buzasi, D. Charbonneau, L. Doyle, J. Fortney, E. B. Ford, M. J. Holman, S. Seager, J. H. Steffen, W. F. Welsh, J. Rowe, H. Anderson, L. Buchhave, D. Ciardi, L. Walkowicz, W. Sherry, E. Horch, H. Isaacson, M. E. Everett, D. Fischer, G. Torres, J. A. Johnson, M. Endl, P. MacQueen, S. T. Bryson, J. Dotson, M. Haas, J. Kolodziejczak, J. Van Cleve, H. Chandrasekaran, J. D. Twicken, E. V. Quintana, B. D. Clarke, C. Allen, J. Li, H. Wu, P. Tenenbaum, E. Verner, F. Bruhweiler, J. Barnes, and A. Prsa. Kepler Planet-Detection Mission: Introduction and First Results. *Science*, 327:977, Feb. 2010. doi: 10.1126/science.1185402.

L. G. Bouma, J. N. Winn, C. Baxter, W. Bhatti, F. Dai, T. Daylan, J. M. Désert, M. L. Hill, S. R. Kane, K. G. Stassun, J. Villasenor, G. R. Ricker, R. Vanderspek, D. W. Latham, S. Seager, J. M. Jenkins, Z. Berta-Thompson, K. Colón, M. Fausnaugh, A. Glidden, N. Guerrero, J. E. Rodriguez, J. D. Twicken, and B. Wohler. WASP-4b Arrived Early for the TESS Mission. , 157(6):217, June 2019. doi: 10.3847/1538-3881/ab189f.

G. Bourda and N. Capitaine. Precession, nutation, and space geodetic determination of the Earth's variable gravity field. , 428:691–702, Dec. 2004. doi: 10.1051/0004-6361:20041533.

V. Bourrier and A. Lecavelier des Etangs. 3D model of hydrogen atmospheric escape from HD 209458b and HD 189733b: radiative blow-out and stellar wind interactions. , 557:A124, Sept. 2013. doi: 10.1051/0004-6361/201321551.

V. Bourrier, D. Ehrenreich, G. King, A. Lecavelier des Etangs, P. J. Wheatley, A. Vidal-Madjar, F. Pepe, and S. Udry. No hydrogen exosphere detected around the super-Earth HD 97658 b. , 597:A26, Jan. 2017. doi: 10.1051/0004-6361/201629253.

V. Bourrier, D. Ehrenreich, M. Lendl, M. Cretignier, R. Allart, X. Dumusque, H. M. Cegla, A. Suárez-Mascareño, A. Wyttenbach, H. J. Hoeijmakers, C. Melo, T. Kuntzer, N. Astudillo-Defru, H. Giles, K. Heng, D. Kitzmann, B. Lavie, C. Lovis, F. Murgas, V. Nascimbeni, F. Pepe, L. Pino, D. Segransan, and S. Udry. Hot Exoplanet Atmospheres Resolved with Transit Spectroscopy (HEARTS). III. Atmospheric structure of the misaligned ultra-hot Jupiter WASP-121b. , 635:A205, Mar. 2020. doi: 10.1051/0004-6361/201936640.

B. P. Bowler. Imaging Extrasolar Giant Planets. , 128(968):102001, Oct. 2016. doi: 10.1088/1538-3873/128/968/102001.

L. Bradley, B. Sipocz, T. Robitaille, Z?Vin?ius, E. Tollerud, C. Deil, K. Barbary, H. M. G?nther, M. Cara, I. Busko, S. Conseil, M. Droettboom, A. Bostroem, E. M. Bray, L. A. Bratholm, M. Craig, G. Barentsen, S. Pascual, A. Donath, J. Greco, G. Perren, W. Kerzendorf, M. de Val-Borro, StuartLittlefair, S. Ogaz, P. L. Lim, L. Ferreira, F. D'Eugenio, and B. A. Weaver. astropy/photutils: v0.5, Aug. 2018. URL https://doi.org/10.5281/zenodo.1340699.

T. M. Brown, D. Charbonneau, R. L. Gilliland, R. W. Noyes, and A. Burrows. Hubble Space Telescope Time-Series Photometry of the Transiting Planet of HD 209458. , 552:699–709, May 2001. doi: 10.1086/320580.

A. Burrows and J. Lunine. Astronomical questions of origin and survival. , 378(6555): 333, Nov. 1995. doi: 10.1038/378333a0.

J. R. Burton, C. A. Watson, A. Fitzsimmons, D. Pollacco, V. Moulds, S. P. Littlefair, and P. J. Wheatley. Tidally Distorted Exoplanets: Density Corrections for Short-period Hot-Jupiters Based Solely on Observable Parameters. , 789(2):113, July 2014. doi: 10.1088/0004-637X/789/2/113.

J. Carroll-Nellenback, A. Frank, B. Liu, A. C. Quillen, E. G. Blackman, and I. Dobbs-Dixon. Hot planetary winds near a star: dynamics, wind-wind interactions, and observational signatures. , 466(2):2458–2473, Apr. 2017. doi: 10.1093/mnras/stw3307.

J. A. Carter and J. N. Winn. Parameter Estimation from Time-series Data with Correlated Errors: A Wavelet-based Method and its Application to Transit Light Curves. , 704:51–67, Oct. 2009. doi: 10.1088/0004-637X/704/1/51.

J. A. Carter and J. N. Winn. Empirical Constraints on the Oblateness of an Exoplanet. , 709(2):1219–1229, Feb. 2010a. doi: 10.1088/0004-637X/709/2/1219.

J. A. Carter and J. N. Winn. The Detectability of Transit Depth Variations Due to Exoplanetary Oblateness and Spin Precession. , 716(1):850–856, June 2010b. doi: 10.1088/0004-637X/716/1/850.

S. Chandrasekhar. *Ellipsoidal figures of equilibrium*. 1987.

D. Charbonneau, T. M. Brown, D. W. Latham, and M. Mayor. Detection of Planetary Transits Across a Sun-like Star. , 529:L45–L48, Jan. 2000. doi: 10.1086/312457.

J. Chen and D. Kipping. Probabilistic Forecasting of the Masses and Radii of Other Worlds. , 834:17, Jan. 2017. doi: 10.3847/1538-4357/834/1/17.

J. Choi, A. Dotter, C. Conroy, M. Cantiello, B. Paxton, and B. D. Johnson. Mesa Isochrones and Stellar Tracks (MIST). I. Solar-scaled Models. , 823:102, June 2016. doi: 10.3847/0004-637X/823/2/102.

A. Claret. A new non-linear limb-darkening law for LTE stellar atmosphere models. Calculations for -5.0 <= log[M/H] <= +1, 2000 K <= $T_{eff}$ <= 50000 K at several surface gravities. , 363:1081–1190, Nov. 2000.

A. Claret and S. Bloemen. Gravity and limb-darkening coefficients for the Kepler, CoRoT, Spitzer, uvby, UBVRIJHK, and Sloan photometric systems. , 529:A75, May 2011. doi: 10.1051/0004-6361/201116451.

A. C. M. Correia. Transit light curve and inner structure of close-in planets. , 570: L5, Oct. 2014. doi: 10.1051/0004-6361/201424733.

J. Crass, B. S. Gaudi, S. Leifer, C. Beichman, C. Bender, G. Blackwood, J. A. Burt, J. L. Callas, H. M. Cegla, S. A. Diddams, X. Dumusque, J. D. Eastman, E. B. Ford, B. Fulton, R. Gibson, S. Halverson, R. D. Haywood, F. Hearty, A. W. Howard, D. W. Latham, J. Löhner-Böttcher, E. E. Mamajek, A. Mortier, P. Newman, P. Plavchan, A. Quirrenbach, A. Reiners, P. Robertson, A. Roy, C. Schwab, A. Seifahrt, A. Szentgyorgyi, R. Terrien, J. K. Teske, S. Thompson, and G. Vasisht. Extreme precision radial velocity working group final report, 2021. URL https://arxiv.org/abs/2107.14291.

I. J. M. Crossfield. Exoplanet Atmospheres and Giant Ground-Based Telescopes. *ArXiv e-prints*, Apr. 2016.

I. J. M. Crossfield, D. R. Ciardi, H. Isaacson, A. W. Howard, E. A. Petigura, L. M. Weiss, B. J. Fulton, E. Sinukoff, J. E. Schlieder, D. Mawet, G. Ruane, I. de Pater, K. de Kleer, A. G. Davies, J. L. Christiansen, C. D. Dressing, L. Hirsch, B. Benneke, J. R. Crepp, M. Kosiarek, J. Livingston, E. Gonzales, C. A. Beichman, and H. A. Knutson. Two Small Transiting Planets and a Possible Third Body Orbiting HD 106315. , 153:255, June 2017. doi: 10.3847/1538-3881/aa6e01.

J. R. A. Davenport, K. R. Covey, R. W. Clarke, A. C. Boeck, J. Cornet, and S. L. Hawley. The Evolution of Flare Activity with Stellar Age. , 871(2):241, Feb. 2019. doi: 10.3847/1538-4357/aafb76.

R. I. Dawson and J. A. Johnson. The Photoeccentric Effect and Proto-hot Jupiters. I. Measuring Photometric Eccentricities of Individual Transiting Planets. , 756:122, Sept. 2012. doi: 10.1088/0004-637X/756/2/122.

R. I. Dawson, E. J. Lee, and E. Chiang. Correlations between Compositions and Orbits Established by the Giant Impact Era of Planet Formation. , 822:54, May 2016. doi: 10.3847/0004-637X/822/1/54.

J. de Wit, M. Gillon, B.-O. Demory, and S. Seager. Towards consistent mapping of distant worlds: secondary-eclipse scanning of the exoplanet HD 189733b. , 548: A128, Dec. 2012. doi: 10.1051/0004-6361/201219060.

J. de Wit, H. R. Wakeford, M. Gillon, N. K. Lewis, J. A. Valenti, B.-O. Demory, A. J. Burgasser, A. Burdanov, L. Delrez, E. Jehin, S. M. Lederer, D. Queloz, A. H. M. J. Triaud, and V. Van Grootel. A combined transmission spectrum of the Earth-sized exoplanets TRAPPIST-1 b and c. , 537(7618):69–72, Sept. 2016. doi: 10.1038/nature18641.

J. De Wit, H. Wakeford, N. Lewis, L. Delrez, M. Gillon, F. Selsis, J. Leconte, B.-O. Demory, E. Bolmont, V. Bourrier, A. Burgasser, S. Grimm, E. Jehin, S. Lederer, J. Owen, V. Stamenkovic, and A. Triaud. Atmospheric reconnaissance of the habitable-zone earth-sized planets orbiting trappist-1. *Nature Astronomy*, 2, 03 2018. doi: 10.1038/s41550-017-0374-z.

K. M. Deck, E. Agol, M. J. Holman, and D. Nesvorný. Ttvfast: An efficient and accurate code for transit timing inversion problems. *The Astrophysical Journal*, 787(2):132, may 2014. doi: 10.1088/0004-637X/787/2/132. URL https://dx.doi.org/10.1088/0004-637X/787/2/132.

L. Delrez, M. Gillon, A. H. M. J. Triaud, B.-O. Demory, J. de Wit, J. G. Ingalls, E. Agol, E. Bolmont, A. Burdanov, A. J. Burgasser, S. J. Carey, E. Jehin, J. Leconte, S. Lederer, D. Queloz, F. Selsis, and V. Van Grootel. Early 2017 observations of TRAPPIST-1 with Spitzer. *Monthly Notices of the Royal Astronomical Society*, 475(3):3577–3597, 01 2018. ISSN 0035-8711. doi: 10.1093/mnras/sty051. URL https://doi.org/10.1093/mnras/sty051.

D. Deming, H. Knutson, J. Kammer, B. J. Fulton, J. Ingalls, S. Carey, A. Burrows, J. J. Fortney, K. Todorov, E. Agol, N. Cowan, J.-M. Desert, J. Fraine, J. Langton, C. Morley, and A. P. Showman. Spitzer Secondary Eclipses of the Dense, Modestly-irradiated, Giant Exoplanet HAT-P-20b Using Pixel-level Decorrelation. , 805:132, June 2015. doi: 10.1088/0004-637X/805/2/132.

J. A. Dittmann, L. M. Close, E. M. Green, and M. Fenwick. A Tentative Detection of a Starspot During Consecutive Transits of an Extrasolar Planet from the Ground:

No Evidence of a Double Transiting Planet System Around TrES-1. , 701(1):756–763, Aug. 2009. doi: 10.1088/0004-637X/701/1/756.

D. Dragomir, M. Harris, J. Pepper, T. Barclay, J. Villanueva, Steven, G. R. Ricker, R. Vanderspek, D. W. Latham, S. Seager, J. N. Winn, J. M. Jenkins, D. R. Ciardi, G. Furesz, C. E. Henze, I. Mireles, E. H. Morgan, E. V. Quintana, E. B. Ting, and D. Yahalomi. Securing the Legacy of TESS through the Care and Maintenance of TESS Planet Ephemerides. , 159(5):219, May 2020. doi: 10.3847/1538-3881/ab845d.

E. Ducrot, M. Gillon, L. Delrez, E. Agol, P. Rimmer, M. Turbet, M. N. Günther, B. O. Demory, A. H. M. J. Triaud, E. Bolmont, A. Burgasser, S. J. Carey, J. G. Ingalls, E. Jehin, J. Leconte, S. M. Lederer, D. Queloz, S. N. Raymond, F. Selsis, V. Van Grootel, and J. de Wit. TRAPPIST-1: Global results of the Spitzer Exploration Science Program Red Worlds. , 640:A112, Aug. 2020. doi: 10.1051/0004-6361/201937392.

L. J. Esteves, E. J. W. De Mooij, and R. Jayawardhana. Changing Phases of Alien Worlds: Probing Atmospheres of Kepler Planets with High-precision Photometry. , 804:150, May 2015. doi: 10.1088/0004-637X/804/2/150.

G. G. Fazio, J. L. Hora, L. E. Allen, M. L. N. Ashby, P. Barmby, L. K. Deutsch, J.-S. Huang, S. Kleiner, M. Marengo, S. T. Megeath, G. J. Melnick, M. A. Pahre, B. M. Patten, J. Polizotti, H. A. Smith, R. S. Taylor, Z. Wang, S. P. Willner, W. F. Hoffmann, J. L. Pipher, W. J. Forrest, C. W. McMurty, C. R. McCreight, M. E. McKelvey, R. E. McMurray, D. G. Koch, S. H. Moseley, R. G. Arendt, J. E. Mentzell, C. T. Marx, P. Losch, P. Mayman, W. Eichhorn, D. Krebs, M. Jhabvala, D. Y. Gezari, D. J. Fixsen, J. Flores, K. Shakoorzadeh, R. Jungo, C. Hakun, L. Workman, G. Karpati, R. Kichak, R. Whitley, S. Mann, E. V. Tollestrup, P. Eisenhardt, D. Stern, V. Gorjian, B. Bhattacharya, S. Carey, B. O. Nelson, W. J. Glaccum, M. Lacy, P. J. Lowrance, S. Laine, W. T. Reach, J. A. Stauffer, J. A. Surace, G. Wilson, E. L. Wright, A. Hoffman, G. Domingo, and M. Cohen. The Infrared Array Camera (IRAC) for the Spitzer Space Telescope. , 154:10–17, Sept. 2004. doi: 10.1086/422843.

P. Figueira, F. Pont, C. Mordasini, Y. Alibert, C. Georgy, and W. Benz. Bulk composition of the transiting hot Neptune around GJ 436. , 493:671–676, Jan. 2009. doi: 10.1051/0004-6361:20078951.

D. A. Fischer, G. W. Marcy, R. P. Butler, S. S. Vogt, G. Laughlin, G. W. Henry, D. Abouav, K. M. G. Peek, J. T. Wright, J. A. Johnson, C. McCarthy, and H. Isaacson. Five Planets Orbiting 55 Cancri. , 675:790–801, Mar. 2008. doi: 10.1086/525512.

D. Foreman-Mackey, D. W. Hogg, D. Lang, and J. Goodman. emcee: The MCMC Hammer. *ArXiv e-prints*, Feb. 2012.

S. Frandsen and B. Lindberg. FIES: A high resolution FIber fed Echelle Spectrograph for the NOT (poster). In H. Karttunen and V. Piirola, editors, *Astrophysics with the NOT*, page 71, Jan. 1999.

K. Freeman and J. Bland-Hawthorn. The New Galaxy: Signatures of Its Formation. , 40:487–537, Jan. 2002. doi: 10.1146/annurev.astro.40.060401.093840.

B. J. Fulton and E. A. Petigura. The California Kepler Survey VII. Precise Planet Radii Leveraging Gaia DR2 Reveal the Stellar Mass Dependence of the Planet Radius Gap. *ArXiv e-prints*, May 2018.

B. J. Fulton, E. A. Petigura, A. W. Howard, H. Isaacson, G. W. Marcy, P. A. Cargile, L. Hebb, L. M. Weiss, J. A. Johnson, T. D. Morton, E. Sinukoff, I. J. M. Crossfield, and L. A. Hirsch. The California-Kepler Survey. III. A Gap in the Radius Distribution of Small Planets. , 154:109, Sept. 2017. doi: 10.3847/1538-3881/aa80eb.

Gaia Collaboration, T. Prusti, J. H. J. de Bruijne, A. G. A. Brown, A. Vallenari, C. Babusiaux, C. A. L. Bailer-Jones, U. Bastian, M. Biermann, D. W. Evans, and et al. The Gaia mission. , 595:A1, Nov. 2016. doi: 10.1051/0004-6361/201629272.

Gaia Collaboration, A. G. A. Brown, A. Vallenari, T. Prusti, J. H. J. de Bruijne, C. Babusiaux, and C. A. L. Bailer-Jones. Gaia Data Release 2. Summary of the contents and survey properties. *ArXiv e-prints*, Apr. 2018.

Garcia, L. J., Moran, S. E., Rackham, B. V., Wakeford, H. R., Gillon, M., de Wit, J., and Lewis, N. K. Hst/wfc3 transmission spectroscopy of the cold rocky planet trappist-1h. *A&A*, 665:A19, 2022. doi: 10.1051/0004-6361/202142603. URL https://doi.org/10.1051/0004-6361/202142603.

A. García Muñoz. Physical and chemical aeronomy of hd 209458b. *Planetary and Space Science*, 55(10):1426–1455, 2007. ISSN 0032-0633. doi: https://doi.org/10.1016/j.pss.2007.03.007. URL https://www.sciencedirect.com/science/article/pii/S0032063307000852.

J. P. Gardner, J. C. Mather, M. Clampin, R. Doyon, M. A. Greenhouse, H. B. Hammel, J. B. Hutchings, P. Jakobsen, S. J. Lilly, K. S. Long, J. I. Lunine, M. J. McCaughrean, M. Mountain, J. Nella, G. H. Rieke, M. J. Rieke, H.-W. Rix, E. P. Smith, G. Sonneborn, M. Stiavelli, H. S. Stockman, R. A. Windhorst, and G. S. Wright. The James Webb Space Telescope. , 123(4):485–606, Apr. 2006. doi: 10.1007/s11214-006-8315-7.

M. Gillon, D. R. Anderson, A. Collier-Cameron, L. Delrez, C. Hellier, E. Jehin, M. Lendl, P. F. L. Maxted, F. Pepe, D. Pollacco, D. Queloz, D. Ségransan, A. M. S. Smith, B. Smalley, J. Southworth, A. H. M. J. Triaud, S. Udry, V. Van Grootel, and R. G. West. WASP-103 b: a new planet at the edge of tidal disruption. , 562: L3, Feb. 2014. doi: 10.1051/0004-6361/201323014.

M. Gillon, E. Jehin, S. M. Lederer, L. Delrez, J. de Wit, A. Burdanov, V. Van Grootel, A. J. Burgasser, A. H. M. J. Triaud, C. Opitom, B.-O. Demory, D. K. Sahu, D. Bardalez Gagliuffi, P. Magain, and D. Queloz. Temperate Earth-sized planets transiting a nearby ultracool dwarf star. , 533(7602):221–224, May 2016. doi: 10.1038/nature17448.

P. Goldreich and S. Soter. Q in the Solar System. , 5(1):375–389, Jan. 1966. doi: 10.1016/0019-1035(66)90051-0.

S. Grouffal, A. Santerne, V. Bourrier, X. Dumusque, A. H. M. J. Triaud, L. Malavolta, V. Kunovac, D. J. Armstrong, O. Attia, S. C. C. Barros, I. Boisse, M. Deleuil, O. D. S. Demangeon, C. D. Dressing, P. Figueira, J. Lillo-Box, A. Mortier, D. Nardiello, N. C. Santos, and S. G. Sousa. Rossiter-McLaughlin detection of the 9-month period transiting exoplanet HIP41378 d. , 668:A172, Dec. 2022. doi: 10.1051/0004-6361/202244182.

T. Guillot, A. Burrows, W. B. Hubbard, J. I. Lunine, and D. Saumon. Giant Planets at Small Orbital Distances. , 459:L35, Mar. 1996. doi: 10.1086/309935.

M. N. Günther and T. Daylan. Allesfitter: Flexible Star and Exoplanet Inference From Photometry and Radial Velocity. Astrophysics Source Code Library, Mar. 2019.

M. N. Günther and T. Daylan. Allesfitter: Flexible Star and Exoplanet Inference from Photometry and Radial Velocity. , 254(1):13, May 2021. doi: 10.3847/1538-4365/abe70e.

M. N. Günther, D. A. Berardo, E. Ducrot, C. A. Murray, K. G. Stassun, K. Olah, L. G. Bouma, S. Rappaport, J. N. Winn, A. D. Feinstein, E. C. Matthews, D. Sebastian, B. V. Rackham, B. Seli, A. H. M. J. Triaud, E. Gillen, A. M. Levine, B.-O. Demory, M. Gillon, D. Queloz, G. R. Ricker, R. K. Vanderspek, S. Seager, D. W. Latham, J. M. Jenkins, C. E. Brasseur, K. D. Colón, T. Daylan, L. Delrez, M. Fausnaugh, L. J. Garcia, R. Jayaraman, E. Jehin, M. H. Kristiansen, J. M. D. Kruijssen, P. P. Pedersen, F. J. Pozuelos, J. E. Rodriguez, B. Wohler, and Z. Zhan. Complex Modulation of Rapidly Rotating Young M Dwarfs: Adding Pieces to the Puzzle. , 163(4):144, Apr. 2022. doi: 10.3847/1538-3881/ac503c.

M. N. Günther, Z. Zhan, S. Seager, P. B. Rimmer, S. Ranjan, K. G. Stassun, R. J. Oelkers, T. Daylan, E. Newton, M. H. Kristiansen, K. Olah, E. Gillen, S. Rappaport, G. R. Ricker, R. K. Vanderspek, D. W. Latham, J. N. Winn, J. M. Jenkins, A. Glidden, M. Fausnaugh, A. M. Levine, J. A. Dittmann, S. N. Quinn, A. Krishnamurthy, and E. B. Ting. Stellar flares from the first tess data release: Exploring a new sample of m dwarfs. *The Astronomical Journal*, 159(2): 60, jan 2020. doi: 10.3847/1538-3881/ab5d3a. URL https://dx.doi.org/10.3847/1538-3881/ab5d3a.

L. Hebb, A. Collier-Cameron, B. Loeillet, D. Pollacco, G. Hébrard, R. A. Street, F. Bouchy, H. C. Stempels, C. Moutou, E. Simpson, S. Udry, Y. C. Joshi, R. G.

West, I. Skillen, D. M. Wilson, I. McDonald, N. P. Gibson, S. Aigrain, D. R. Anderson, C. R. Benn, D. J. Christian, B. Enoch, C. A. Haswell, C. Hellier, K. Horne, J. Irwin, T. A. Lister, P. Maxted, M. Mayor, A. J. Norton, N. Parley, F. Pont, D. Queloz, B. Smalley, and P. J. Wheatley. WASP-12b: The Hottest Transiting Extrasolar Planet Yet Discovered. , 693:1920–1928, Mar. 2009. doi: 10.1088/0004-637X/693/2/1920.

A. M. Heras, H. Rauer, C. Aerts, M. Deleuil, L. Gizon, M.-J. Goupil, M. Mas-Hesse, G. Piotto, D. Pollacco, R. Ragazzoni, G. Ramsay, and S. Udry. The PLATO mission: Studying the diversity of exoplanets orbiting up to the habitable zone of Sun-like stars. In *European Planetary Science Congress*, pages EPSC2020–396, Sept. 2020. doi: 10.5194/epsc2020-396.

J. Holt. Spectroscopic determination of stellar rotation. *Astronomy and Astro-Physics (formerly The Sidereal Messenger)*, 12:646, 1893.

A. W. Howard, G. W. Marcy, J. A. Johnson, D. A. Fischer, J. T. Wright, H. Isaacson, J. A. Valenti, J. Anderson, D. N. C. Lin, and S. Ida. The Occurrence and Mass Distribution of Close-in Super-Earths, Neptunes, and Jupiters. *Science*, 330:653–, Oct. 2010. doi: 10.1126/science.1194854.

S. B. Howell, C. Sobeck, M. Haas, M. Still, T. Barclay, F. Mullally, J. Troeltzsch, S. Aigrain, S. T. Bryson, D. Caldwell, W. J. Chaplin, W. D. Cochran, D. Huber, G. W. Marcy, A. Miglio, J. R. Najita, M. Smith, J. D. Twicken, and J. J. Fortney. The K2 Mission: Characterization and Early Results. , 126:398–408, Apr. 2014. doi: 10.1086/676406.

W. B. Hubbard. *Planetary interiors*. 1984.

Husser, T.-O., Wende-von Berg, S., Dreizler, S., Homeier, D., Reiners, A., Barman, T., and Hauschildt, P. H. A new extensive library of phoenix stellar atmospheres and synthetic spectra. *A&A*, 553:A6, 2013. doi: 10.1051/0004-6361/201219058. URL https://doi.org/10.1051/0004-6361/201219058.

Ioannidis, P., Huber, K. F., and Schmitt, J. H. M. M. How do starspots influence the transit timing variations of exoplanets? simulations of individual and consecutive transits. *A&A*, 585:A72, 2016. doi: 10.1051/0004-6361/201527184. URL https://doi.org/10.1051/0004-6361/201527184.

Ž. Ivezić, S. M. Kahn, J. A. Tyson, B. Abel, E. Acosta, R. Allsman, D. Alonso, Y. AlSayyad, S. F. Anderson, J. Andrew, and et al. LSST: From Science Drivers to Reference Design and Anticipated Data Products. , 873:111, Mar. 2019. doi: 10.3847/1538-4357/ab042c.

J. M. Jenkins, J. D. Twicken, S. McCauliff, J. Campbell, D. Sanderfer, D. Lung, M. Mansouri-Samani, F. Girouard, P. Tenenbaum, T. Klaus, J. C. Smith, D. A. Caldwell, A. D. Chacon, C. Henze, C. Heiges, D. W. Latham, E. Morgan, D. Swade, S. Rinehart, and R. Vanderspek. The TESS science processing operations center.

In *Software and Cyberinfrastructure for Astronomy IV*, volume 9913 of *Proc. SPIE*, page 99133E, 8 2016. doi: 10.1117/12.2233418.

S. R. Kane, M. L. Hill, J. F. Kasting, R. K. Kopparapu, E. V. Quintana, T. Barclay, N. M. Batalha, W. J. Borucki, D. R. Ciardi, N. Haghighipour, N. R. Hinkel, L. Kaltenegger, F. Selsis, and G. Torres. A Catalog of Kepler Habitable Zone Exoplanet Candidates. , 830:1, Oct. 2016. doi: 10.3847/0004-637X/830/1/1.

E. M. R. Kempton, J. L. Bean, D. R. Louie, D. Deming, D. D. B. Koll, M. Mansfield, J. L. Christiansen, M. López-Morales, M. R. Swain, R. T. Zellem, S. Ballard, T. Barclay, J. K. Barstow, N. E. Batalha, T. G. Beatty, Z. Berta-Thompson, J. Birkby, L. A. Buchhave, D. Charbonneau, N. B. Cowan, I. Crossfield, M. de Val-Borro, R. Doyon, D. Dragomir, E. Gaidos, K. Heng, R. Hu, S. R. Kane, L. Kreidberg, M. Mallonn, C. V. Morley, N. Narita, V. Nascimbeni, E. Pallé, E. V. Quintana, E. Rauscher, S. Seager, E. L. Shkolnik, D. K. Sing, A. Sozzetti, K. G. Stassun, J. A. Valenti, and C. von Essen. A Framework for Prioritizing the TESS Planetary Candidates Most Amenable to Atmospheric Characterization. , 130(993):114401, Nov. 2018. doi: 10.1088/1538-3873/aadf6f.

A. Y. Kesseli, A. A. West, M. Veyette, B. Harrison, D. Feldman, and J. J. Bochanski. An empirical template library of stellar spectra for a wide range of spectral classes, luminosity classes, and metallicities using sdss boss spectra. *The Astrophysical Journal Supplement Series*, 230(2):16, jun 2017. doi: 10.3847/1538-4365/aa656d. URL https://dx.doi.org/10.3847/1538-4365/aa656d.

D. M. Kipping. Efficient, uninformative sampling of limb darkening coefficients for two-parameter laws. , 435:2152–2160, Nov. 2013. doi: 10.1093/mnras/stt1435.

D. G. Koch, W. J. Borucki, G. Basri, N. M. Batalha, T. M. Brown, D. Caldwell, J. Christensen-Dalsgaard, W. D. Cochran, E. DeVore, E. W. Dunham, I. Gautier, Thomas N., J. C. Geary, R. L. Gilliland, A. Gould, J. Jenkins, Y. Kondo, D. W. Latham, J. J. Lissauer, G. Marcy, D. Monet, D. Sasselov, A. Boss, D. Brownlee, J. Caldwell, A. K. Dupree, S. B. Howell, H. Kjeldsen, S. Meibom, D. Morrison, T. Owen, H. Reitsema, J. Tarter, S. T. Bryson, J. L. Dotson, P. Gazis, M. R. Haas, J. Kolodziejczak, J. F. Rowe, J. E. Van Cleve, C. Allen, H. Chandrasekaran, B. D. Clarke, J. Li, E. V. Quintana, P. Tenenbaum, J. D. Twicken, and H. Wu. Kepler Mission Design, Realized Photometric Performance, and Early Science. , 713(2): L79–L86, Apr. 2010. doi: 10.1088/2041-8205/713/2/L79.

Z. Kopal. Detailed effects of limb darkening upon light and velocity curves of close binary systems. *Harvard College Observatory Circular*, 454:1–12, Jan. 1950.

Z. Kővári and J. Bartus. Testing the stability and reliability of starspot modelling. *A&A*, 323:801–808, 1997. ISSN 0004-6361. URL https://ui.adsabs.harvard.edu/abs/1997A&A...323..801K/abstract.

L. Kreidberg. BATMAN: BAsic Transit Model cAlculatioN in Python. , 127:1161–1165, Dec. 2015. doi: 10.1086/683602.

L. Kreidberg, J. L. Bean, J.-M. Désert, B. Benneke, D. Deming, K. B. Stevenson, S. Seager, Z. Berta-Thompson, A. Seifahrt, and D. Homeier. Clouds in the atmosphere of the super-Earth exoplanet GJ1214b. , 505:69–72, Jan. 2014. doi: 10.1038/nature12888.

L. Kreidberg, M. R. Line, J. L. Bean, K. B. Stevenson, J.-M. Desert, N. Madhusudhan, J. J. Fortney, J. K. Barstow, G. W. Henry, M. Williamson, and A. P. Showman. A Detection of Water in the Transmission Spectrum of the Hot Jupiter WASP-12b and Implications for its Atmospheric Composition. *ArXiv e-prints*, Apr. 2015.

L. Kreidberg, M. R. Line, V. Parmentier, K. B. Stevenson, T. Louden, M. Bonnefoy, J. K. Faherty, G. W. Henry, M. H. Williamson, K. Stassun, J. L. Bean, J. J. Fortney, A. P. Showman, J.-M. Désert, and J. Arcangeli. Global Climate and Atmospheric Composition of the Ultra-Hot Jupiter WASP-103b from HST and Spitzer Phase Curve Observations. *ArXiv e-prints*, Apr. 2018.

H. Lammer, F. Selsis, I. Ribas, E. F. Guinan, S. J. Bauer, and W. W. Weiss. Atmospheric loss of exoplanets resulting from stellar x-ray and extreme-ultraviolet heating. *The Astrophysical Journal*, 598(2):L121, nov 2003. doi: 10.1086/380815. URL https://dx.doi.org/10.1086/380815.

W. Landsman and T. Simon. A Catalog of Stellar Lyman-Alpha Fluxes. , 408:305, May 1993. doi: 10.1086/172589.

B. Lavie, D. Ehrenreich, V. Bourrier, A. Lecavelier des Etangs, A. Vidal-Madjar, X. Delfosse, A. Gracia Berna, K. Heng, N. Thomas, S. Udry, and P. J. Wheatley. The long egress of GJ 436b's giant exosphere. , 605:L7, Sept. 2017. doi: 10.1051/0004-6361/201731340.

J. Leconte, D. Lai, and G. Chabrier. Distorted, nonspherical transiting planets: impact on the transit depth and on the radius determination. , 528:A41, Apr. 2011. doi: 10.1051/0004-6361/201015811.

M. Lendl, D. Ehrenreich, O. D. Turner, D. Bayliss, S. Blanco-Cuaresma, H. Giles, F. Bouchy, M. Marmier, and S. Udry. Ground-based photometry of the 21-day Neptune HD 106315c. , 603:L5, July 2017. doi: 10.1051/0004-6361/201731278.

Z. Li, S. R. Hildebrandt, S. R. Kane, N. T. Zimmerman, J. H. Girard, J. Gonzalez-Quiles, and M. C. Turnbull. Direct imaging of exoplanets beyond the radial velocity limit: Application to the hd 134987 system. *The Astronomical Journal*, 162(1):9, jun 2021. doi: 10.3847/1538-3881/abf831. URL https://dx.doi.org/10.3847/1538-3881/abf831.

Lightkurve Collaboration, J. V. d. M. Cardoso, C. Hedges, M. Gully-Santiago, N. Saunders, A. M. Cody, T. Barclay, O. Hall, S. Sagear, E. Turtelboom, J. Zhang, A. Tzanidakis, K. Mighell, J. Coughlin, K. Bell, Z. Berta-Thompson, P. Williams, J. Dotson, and G. Barentsen. Lightkurve: Kepler and TESS time series analysis in Python. Astrophysics Source Code Library, Dec. 2018.

J. J. Lissauer. Urey Prize Lecture: On the diversity of plausible planetary systems. , 114(2):217–236, Apr. 1995. doi: 10.1006/icar.1995.1057.

Y. Lithwick, J. Xie, and Y. Wu. Extracting Planet Mass and Eccentricity from TTV Data. , 761:122, Dec. 2012. doi: 10.1088/0004-637X/761/2/122.

N. R. Lomb. Least-Squares Frequency Analysis of Unequally Spaced Data. , 39(2): 447–462, Feb. 1976. doi: 10.1007/BF00648343.

E. D. Lopez and J. J. Fortney. Understanding the Mass-Radius Relation for Subneptunes: Radius as a Proxy for Composition. , 792:1, Sept. 2014. doi: 10.1088/0004-637X/792/1/1.

A. E. H. Love. *Some Problems of Geodynamics*. 1911.

R. Luger, M. Sestovic, E. Kruse, S. L. Grimm, B.-O. Demory, E. Agol, E. Bolmont, D. Fabrycky, C. S. Fernandes, V. Van Grootel, A. Burgasser, M. Gillon, J. G. Ingalls, E. Jehin, S. N. Raymond, F. Selsis, A. H. M. J. Triaud, T. Barclay, G. Barentsen, S. B. Howell, L. Delrez, J. de Wit, D. Foreman-Mackey, D. L. Holdsworth, J. Leconte, S. Lederer, M. Turbet, Y. Almleaky, Z. Benkhaldoun, P. Magain, B. M. Morris, K. Heng, and D. Queloz. A seven-planet resonant chain in TRAPPIST-1. *Nature Astronomy*, 1:0129, June 2017. doi: 10.1038/s41550-017-0129.

G. Maciejewski, D. Dimitrov, M. Fernández, A. Sota, G. Nowak, J. Ohlert, G. Nikolov, Ł. Bukowiecki, T. C. Hinse, E. Pallé, B. Tingley, D. Kjurkchieva, J. W. Lee, and C. U. Lee. Departure from the constant-period ephemeris for the transiting exoplanet WASP-12. , 588:L6, Apr. 2016. doi: 10.1051/0004-6361/201628312.

B. Macintosh, M. Troy, R. Doyon, J. Graham, K. Baker, B. Bauman, C. Marois, D. Palmer, D. Phillion, L. Poyneer, I. Crossfield, P. Dumont, B. M. Levine, M. Shao, G. Serabyn, C. Shelton, G. Vasisht, J. K. Wallace, J.-F. Lavigne, P. Valee, N. Rowlands, K. Tam, and D. Hackett. Extreme adaptive optics for the Thirty Meter Telescope. In *Society of Photo-Optical Instrumentation Engineers (SPIE) Conference Series*, volume 6272 of *Society of Photo-Optical Instrumentation Engineers (SPIE) Conference Series*, July 2006. doi: 10.1117/12.672032.

B. Macintosh, J. R. Graham, P. Ingraham, Q. Konopacky, C. Marois, M. Perrin, L. Poyneer, B. Bauman, T. Barman, A. S. Burrows, A. Cardwell, J. Chilcote, R. J. De Rosa, D. Dillon, R. Doyon, J. Dunn, D. Erikson, M. P. Fitzgerald, D. Gavel, S. Goodsell, M. Hartung, P. Hibon, P. Kalas, J. Larkin, J. Maire, F. Marchis, M. S. Marley, J. McBride, M. Millar-Blanchaer, K. Morzinski, A. Norton, B. R. Oppenheimer, D. Palmer, J. Patience, L. Pueyo, F. Rantakyro, N. Sadakuni, L. Saddlemyer, D. Savransky, A. Serio, R. Soummer, A. Sivaramakrishnan, I. Song, S. Thomas, J. K. Wallace, S. Wiktorowicz, and S. Wolff. First light of the Gemini Planet Imager. *Proceedings of the National Academy of Science*, 111:12661–12666, Sept. 2014. doi: 10.1073/pnas.1304215111.

L. Malavolta, A. W. Mayo, T. Louden, V. M. Rajpaul, A. S. Bonomo, L. A. Buchhave, L. Kreidberg, M. H. Kristiansen, M. Lopez-Morales, A. Mortier, A. Vanderburg, A. Coffinet, D. Ehrenreich, C. Lovis, F. Bouchy, D. Charbonneau, D. R. Ciardi, A. Collier Cameron, R. Cosentino, I. J. M. Crossfield, M. Damasso, C. D. Dressing, X. Dumusque, M. E. Everett, P. Figueira, A. F. M. Fiorenzano, E. J. Gonzales, R. D. Haywood, A. Harutyunyan, L. Hirsch, S. B. Howell, J. A. Johnson, D. W. Latham, E. Lopez, M. Mayor, G. Micela, E. Molinari, V. Nascimbeni, F. Pepe, D. F. Phillips, G. Piotto, K. Rice, D. Sasselov, D. Ségransan, A. Sozzetti, S. Udry, and C. Watson. An Ultra-short Period Rocky Super-Earth with a Secondary Eclipse and a Neptune-like Companion around K2-141. , 155(3):107, Mar. 2018. doi: 10.3847/1538-3881/aaa5b5.

K. Mandel and E. Agol. Analytic Light Curves for Planetary Transit Searches. , 580: L171–L175, Dec. 2002. doi: 10.1086/345520.

C. Marois, B. Macintosh, T. Barman, B. Zuckerman, I. Song, J. Patience, D. Lafrenière, and R. Doyon. Direct Imaging of Multiple Planets Orbiting the Star HR 8799. *Science*, 322:1348–, Nov. 2008. doi: 10.1126/science.1166585.

K. Masuda. Very Low Density Planets around Kepler-51 Revealed with Transit Timing Variations and an Anomaly Similar to a Planet-Planet Eclipse Event. , 783(1): 53, Mar. 2014. doi: 10.1088/0004-637X/783/1/53.

M. Mayor and D. Queloz. A Jupiter-mass companion to a solar-type star. , 378: 355–359, Nov. 1995. doi: 10.1038/378355a0.

Mazeh, T., Holczer, T., and Faigler, S. Dearth of short-period neptunian exoplanets: A desert in period-mass and period-radius planes. *A&A*, 589:A75, 2016. doi: 10.1051/0004-6361/201528065. URL https://doi.org/10.1051/0004-6361/201528065.

B. E. McArthur, M. Endl, W. D. Cochran, G. F. Benedict, D. A. Fischer, G. W. Marcy, R. P. Butler, D. Naef, M. Mayor, D. Queloz, S. Udry, and T. E. Harrison. Detection of a neptune-mass planet in the 1 cancri system using the hobby-eberly telescope. *The Astrophysical Journal*, 614(1):L81, sep 2004. doi: 10.1086/425561. URL https://dx.doi.org/10.1086/425561.

P. R. McCullough, N. Crouzet, D. Deming, and N. Madhusudhan. Water Vapor in the Spectrum of the Extrasolar Planet HD 189733b. I. The Transit. , 791:55, Aug. 2014. doi: 10.1088/0004-637X/791/1/55.

D. McLaughlin. Some results of a spectrographic study of the algol system. *The Astrophysical Journal*, 60, 1924.

R. Meier and P. Mange. Geocoronal hydrogen: An analysis of the lyman-alpha airglow observed from ogo-4. *Planetary and Space Science*, 18(6):803–821, 1970. ISSN 0032-0633. doi: https://doi.org/10.1016/0032-0633(70)90080-2. URL https://www.sciencedirect.com/science/article/pii/0032063370900802.

N. Mondrik, E. Newton, D. Charbonneau, and J. Irwin. An increased rate of large flares at intermediate rotation periods for mid-to-late m dwarfs. *The Astrophysical Journal*, 870(1):10, dec 2018. doi: 10.3847/1538-4357/aaee64. URL https://dx.doi.org/10.3847/1538-4357/aaee64.

T. D. Morton. isochrones: Stellar model grid package. Astrophysics Source Code Library, Mar. 2015.

P. S. Muirhead, C. D. Dressing, A. W. Mann, B. Rojas-Ayala, S. Lépine, M. Paegert, N. De Lee, and R. Oelkers. A Catalog of Cool Dwarf Targets for the Transiting Exoplanet Survey Satellite. *AJ*, 155:180, 4 2018. doi: 10.3847/1538-3881/aab710.

C. D. Murray and S. F. Dermott. *Solar system dynamics*. 1999.

R. A. Murray-Clay, E. I. Chiang, and N. Murray. Atmospheric Escape From Hot Jupiters. , 693:23–42, Mar. 2009. doi: 10.1088/0004-637X/693/1/23.

NASA Exoplanet Archive. Confirmed planets table, 2019. URL https://catcopy.ipac.caltech.edu/dois/doi.php?id=10.26133/NEA1.

D. Ni. Empirical models of Jupiter's interior from Juno data. Moment of inertia and tidal Love number $k_2$. , 613:A32, May 2018. doi: 10.1051/0004-6361/201732183.

P. Niraula, S. Redfield, F. Dai, O. Barragan, D. Gandolfi, P. W. Cauley, T. Hirano, J. Korth, A. M. S. Smith, J. Prieto-Arranz, S. Grziwa, M. Fridlund, C. M. Persson, A. B. Justesen, J. N. Winn, S. Albrecht, W. D. Cochran, S. Csizmadia, G. M. Duvvuri, M. Endl, A. P. Hatzes, J. H. Livingston, N. Narita, D. Nespral, G. Nowak, M. Patzold, E. Palle, and V. Van Eylen. Three Small Super-Earths Transiting the nearby star GJ 9827. *ArXiv e-prints*, Sept. 2017.

P. Niraula, J. de Wit, I. E. Gordon, R. J. Hargreaves, C. Sousa-Silva, and R. V. Kochanov. The impending opacity challenge in exoplanet atmospheric characterization. *Nature Astronomy*, 6:1287–1295, Nov. 2022. doi: 10.1038/s41550-022-01773-1.

J. E. Owen and A. P. Jackson. Planetary evaporation by UV  X-ray radiation: basic hydrodynamics. , 425:2931–2947, Oct. 2012. doi: 10.1111/j.1365-2966.2012.21481.x.

J. E. Owen, R. A. Murray-Clay, E. Schreyer, H. E. Schlichting, D. Ardila, A. Gupta, R. O. P. Loyd, E. L. Shkolnik, D. K. Sing, and M. R. Swain. The fundamentals of Lyman $\alpha$ exoplanet transits. , 518(3):4357–4371, Jan. 2023. doi: 10.1093/mnras/stac3414.

A. Pál, G. Á. Bakos, G. Torres, R. W. Noyes, D. W. Latham, G. Kovács, G. W. Marcy, D. A. Fischer, R. P. Butler, D. D. Sasselov, B. Sipőcz, G. A. Esquerdo, G. Kovács, R. Stefanik, J. Lázár, I. Papp, and P. Sári. HAT-P-7b: An Extremely Hot Massive Planet Transiting a Bright Star in the Kepler Field. , 680(2):1450–1456, June 2008. doi: 10.1086/588010.

M. J. Pecaut and E. E. Mamajek. Intrinsic Colors, Temperatures, and Bolometric Corrections of Pre-main-sequence Stars. , 208:9, Sept. 2013. doi: 10.1088/0067-0049/208/1/9.

F. Pepe, S. Cristiani, R. Rebolo, N. C. Santos, H. Dekker, A. Cabral, P. Di Marcantonio, P. Figueira, G. Lo Curto, C. Lovis, M. Mayor, D. Mégevand, P. Molaro, M. Riva, M. R. Zapatero Osorio, M. Amate, A. Manescau, L. Pasquini, F. M. Zerbi, V. Adibekyan, M. Abreu, M. Affolter, Y. Alibert, M. Aliverti, R. Allart, C. Allende Prieto, D. Álvarez, D. Alves, G. Avila, V. Baldini, T. Bandy, S. C. C. Barros, W. Benz, A. Bianco, F. Borsa, V. Bourrier, F. Bouchy, C. Broeg, G. Calderone, R. Cirami, J. Coelho, P. Conconi, I. Coretti, C. Cumani, G. Cupani, V. D'Odorico, M. Damasso, S. Deiries, B. Delabre, O. D. S. Demangeon, X. Dumusque, D. Ehrenreich, J. P. Faria, A. Fragoso, L. Genolet, M. Genoni, R. Génova Santos, J. I. González Hernández, I. Hughes, O. Iwert, F. Kerber, J. Knudstrup, M. Landoni, B. Lavie, J. Lillo-Box, J. L. Lizon, C. Maire, C. J. A. P. Martins, A. Mehner, G. Micela, A. Modigliani, M. A. Monteiro, M. J. P. F. G. Monteiro, M. Moschetti, M. T. Murphy, N. Nunes, L. Oggioni, A. Oliveira, M. Oshagh, E. Pallé, G. Pariani, E. Poretti, J. L. Rasilla, J. Rebordão, E. M. Redaelli, S. Santana Tschudi, P. Santin, P. Santos, D. Ségransan, T. M. Schmidt, A. Segovia, D. Sosnowska, A. Sozzetti, S. G. Sousa, P. Spanò, A. Suárez Mascareño, H. Tabernero, F. Tenegi, S. Udry, and A. Zanutta. ESPRESSO at VLT. On-sky performance and first results. , 645: A96, Jan. 2021. doi: 10.1051/0004-6361/202038306.

M. Perryman, J. Hartman, G. Á. Bakos, and L. Lindegren. Astrometric Exoplanet Detection with Gaia. , 797:14, Dec. 2014. doi: 10.1088/0004-637X/797/1/14.

B. V. Rackham and J. de Wit. Towards robust corrections for stellar contamination in JWST exoplanet transmission spectra. *arXiv e-prints*, art. arXiv:2303.15418, Mar. 2023. doi: 10.48550/arXiv.2303.15418.

B. V. Rackham, D. Apai, and M. S. Giampapa. The Transit Light Source Effect: False Spectral Features and Incorrect Densities for M-dwarf Transiting Planets. , 853(2):122, Feb. 2018. doi: 10.3847/1538-4357/aaa08c.

S. Rappaport, J. Swift, A. Levine, M. Joss, R. Sanchis-Ojeda, T. Barclay, M. Still, G. Handler, K. Oláh, P. S. Muirhead, D. Huber, and K. Vida. M-dwarf rapid rotators and the detection of relatively young multiple m-star systems. *The Astrophysical Journal*, 788(2):114, may 2014. doi: 10.1088/0004-637X/788/2/114. URL https://dx.doi.org/10.1088/0004-637X/788/2/114.

A. Reiners, M. Zechmeister, J. A. Caballero, I. Ribas, J. C. Morales, S. V. Jeffers, P. Schöfer, L. Tal-Or, A. Quirrenbach, P. J. Amado, A. Kaminski, W. Seifert, M. Abril, J. Aceituno, F. J. Alonso-Floriano, M. Ammler-von Eiff, R. Antona, G. Anglada-Escudé, H. Anwand-Heerwart, B. Arroyo-Torres, M. Azzaro, D. Baroch, D. Barrado, F. F. Bauer, S. Becerril, V. J. S. Béjar, D. Benítez, Z. M. Berdinas, G. Bergond, M. Blümcke, M. Brinkmöller, C. del Burgo, J. Cano,

M. C. Cárdenas Vázquez, E. Casal, C. Cifuentes, A. Claret, J. Colomé, M. Cortés-Contreras, S. Czesla, E. Díez-Alonso, S. Dreizler, C. Feiz, M. Fernández, I. M. Ferro, B. Fuhrmeister, D. Galadí-Enríquez, A. Garcia-Piquer, M. L. García Vargas, L. Gesa, V. Gómez Galera, J. I. González Hernández, R. González-Peinado, U. Grözinger, S. Grohnert, J. Guàrdia, E. W. Guenther, A. Guijarro, E. de Guindos, J. Gutiérrez-Soto, H. J. Hagen, A. P. Hatzes, P. H. Hauschildt, R. P. Hedrosa, J. Helmling, T. Henning, I. Hermelo, R. Hernández Arabí, L. Hernández Castaño, F. Hernández Hernando, E. Herrero, A. Huber, P. Huke, E. N. Johnson, E. de Juan, M. Kim, R. Klein, J. Klüter, A. Klutsch, M. Kürster, M. Lafarga, A. Lamert, M. Lampón, L. M. Lara, W. Laun, U. Lemke, R. Lenzen, R. Launhardt, M. López del Fresno, J. López-González, M. López-Puertas, J. F. López Salas, J. López-Santiago, R. Luque, H. Magán Madinabeitia, U. Mall, L. Mancini, H. Mandel, E. Marfil, J. A. Marín Molina, D. Maroto Fernández, E. L. Martín, S. Martín-Ruiz, C. J. Marvin, R. J. Mathar, E. Mirabet, D. Montes, M. E. Moreno-Raya, A. Moya, R. Mundt, E. Nagel, V. Naranjo, L. Nortmann, G. Nowak, A. Ofir, R. Oreiro, E. Pallé, J. Panduro, J. Pascual, V. M. Passegger, A. Pavlov, S. Pedraz, A. Pérez-Calpena, D. Pérez Medialdea, M. Perger, M. A. C. Perryman, M. Pluto, O. Rabaza, A. Ramón, R. Rebolo, P. Redondo, S. Reffert, S. Reinhart, P. Rhode, H. W. Rix, F. Rodler, E. Rodríguez, C. Rodríguez-López, A. Rodríguez Trinidad, R. R. Rohloff, A. Rosich, S. Sadegi, E. Sánchez-Blanco, M. A. Sánchez Carrasco, A. Sánchez-López, J. Sanz-Forcada, P. Sarkis, L. F. Sarmiento, S. Schäfer, J. H. M. M. Schmitt, J. Schiller, A. Schweitzer, E. Solano, O. Stahl, J. B. P. Strachan, J. Stürmer, J. C. Suárez, H. M. Tabernero, M. Tala, T. Trifonov, S. M. Tulloch, R. G. Ulbrich, G. Veredas, J. I. Vico Linares, F. Vilardell, K. Wagner, J. Winkler, V. Wolthoff, W. Xu, F. Yan, and M. R. Zapatero Osorio. The CARMENES search for exoplanets around M dwarfs. High-resolution optical and near-infrared spectroscopy of 324 survey stars. , 612:A49, Apr. 2018. doi: 10.1051/0004-6361/201732054.

K. Rice, L. Malavolta, A. Mayo, A. Mortier, L. A. Buchhave, L. Affer, A. Vanderburg, M. Lopez-Morales, E. Poretti, L. Zeng, A. Collier Cameron, M. Damasso, A. Coffinet, D. W. Latham, A. S. Bonomo, F. Bouchy, D. Charbonneau, X. Dumusque, P. Figueira, A. F. Martinez Fiorenzano, R. D. Haywood, J. A. Johnson, E. Lopez, C. Lovis, M. Mayor, G. Micela, E. Molinari, V. Nascimbeni, C. Nava, F. Pepe, D. F. Phillips, G. Piotto, D. Sasselov, D. Ségransan, A. Sozzetti, S. Udry, and C. Watson. Masses and radii for the three super-Earths orbiting GJ 9827, and implications for the composition of small exoplanets. , 484(3):3731–3745, Apr. 2019. doi: 10.1093/mnras/stz130.

G. R. Ricker, J. N. Winn, R. Vanderspek, D. W. Latham, G. Á. Bakos, J. L. Bean, Z. K. Berta-Thompson, T. M. Brown, L. Buchhave, N. R. Butler, R. P. Butler, W. J. Chaplin, D. Charbonneau, J. Christensen-Dalsgaard, M. Clampin, D. Deming, J. Doty, N. De Lee, C. Dressing, E. W. Dunham, M. Endl, F. Fressin, J. Ge, T. Henning, M. J. Holman, A. W. Howard, S. Ida, J. Jenkins, G. Jernigan, J. A. Johnson, L. Kaltenegger, N. Kawai, H. Kjeldsen, G. Laughlin, A. M. Levine, D. Lin,

J. J. Lissauer, P. MacQueen, G. Marcy, P. R. McCullough, T. D. Morton, N. Narita, M. Paegert, E. Palle, F. Pepe, J. Pepper, A. Quirrenbach, S. A. Rinehart, D. Sasselov, B. Sato, S. Seager, A. Sozzetti, K. G. Stassun, P. Sullivan, A. Szentgyorgyi, G. Torres, S. Udry, and J. Villasenor. Transiting Exoplanet Survey Satellite (TESS). In *Society of Photo-Optical Instrumentation Engineers (SPIE) Conference Series*, volume 9143 of *Society of Photo-Optical Instrumentation Engineers (SPIE) Conference Series*, page 20, Aug. 2014. doi: 10.1117/12.2063489.

K. E. Rockcliffe, E. R. Newton, A. Youngblood, V. Bourrier, A. W. Mann, Z. Berta-Thompson, M. A. Agüeros, A. Núñez, and D. Charbonneau. A ly transit left undetected: the environment and atmospheric behavior of k2-25b. *The Astronomical Journal*, 162(3):116, aug 2021. doi: 10.3847/1538-3881/ac126f. URL https://dx.doi.org/10.3847/1538-3881/ac126f.

J. E. Rodriguez, G. Zhou, A. Vanderburg, J. D. Eastman, L. Kreidberg, P. A. Cargile, A. Bieryla, D. W. Latham, J. Irwin, M. L. Calkins, G. A. Esquerdo, and J. Mink. A Multi-Planet System Transiting the $V = 9$ Rapidly Rotating F-Star HD 106315. *ArXiv e-prints*, Jan. 2017.

J. E. Rodriguez, A. Vanderburg, J. D. Eastman, A. W. Mann, I. J. M. Crossfield, D. R. Ciardi, D. W. Latham, and S. N. Quinn. A System of Three Super Earths Transiting the Late K-Dwarf GJ 9827 at 30 pc. , 155(2):72, Feb. 2018. doi: 10.3847/1538-3881/aaa292.

L. A. Rogers and S. Seager. Three Possible Origins for the Gas Layer on GJ 1214b. , 716:1208–1216, June 2010. doi: 10.1088/0004-637X/716/2/1208.

R. Rossiter. On the detection of an effect of rotation during eclipse in the velocity of the brigher component of beta lyrae, and on the constancy of velocity of this system. *The Astrophysical Journal*, 60, 1924.

M. Saillenfest, J. Laskar, and G. Boué. Secular spin-axis dynamics of exoplanets. , 623:A4, Mar. 2019. doi: 10.1051/0004-6361/201834344.

A. Santerne, L. Malavolta, M. R. Kosiarek, F. Dai, C. D. Dressing, X. Dumusque, N. C. Hara, T. A. Lopez, A. Mortier, A. Vanderburg, V. Adibekyan, D. J. Armstrong, D. Barrado, S. C. C. Barros, D. Bayliss, D. Berardo, I. Boisse, A. S. Bonomo, F. Bouchy, D. J. A. Brown, L. A. Buchhave, R. P. Butler, A. Collier Cameron, R. Cosentino, J. D. Crane, I. J. M. Crossfield, M. Damasso, M. R. Deleuil, E. Delgado Mena, O. Demangeon, R. F. Díaz, J. F. Donati, P. Figueira, B. J. Fulton, A. Ghedina, A. Harutyunyan, G. Hébrard, L. A. Hirsch, S. Hojjatpanah, A. W. Howard, H. Isaacson, D. W. Latham, J. Lillo-Box, M. López-Morales, C. Lovis, A. F. Martinez Fiorenzano, E. Molinari, O. Mousis, C. Moutou, C. Nava, L. D. Nielsen, H. P. Osborn, E. A. Petigura, D. F. Phillips, D. L. Pollacco, E. Poretti, K. Rice, N. C. Santos, D. Ségransan, S. A. Shectman, E. Sinukoff, S. G. Sousa, A. Sozzetti, J. K. Teske, S. Udry, A. Vigan, S. X. Wang, C. A. Watson, L. M.

Weiss, P. J. Wheatley, and J. N. Winn. An extremely low-density and temperate giant exoplanet. *arXiv e-prints*, art. arXiv:1911.07355, Nov. 2019. doi: 10.48550/arXiv.1911.07355.

J. D. Scargle. Studies in astronomical time series analysis. II. Statistical aspects of spectral analysis of unevenly spaced data. , 263:835–853, Dec. 1982. doi: 10.1086/160554.

J. E. Schlieder, I. J. M. Crossfield, E. A. Petigura, A. W. Howard, K. M. Aller, E. Sinukoff, H. T. Isaacson, B. J. Fulton, D. R. Ciardi, M. Bonnefoy, C. Ziegler, T. D. Morton, S. Lépine, C. Obermeier, M. C. Liu, V. P. Bailey, C. Baranec, C. A. Beichman, D. Defrère, T. Henning, P. Hinz, N. Law, R. Riddle, and A. Skemer. Two Small Temperate Planets Transiting Nearby M Dwarfs in K2 Campaigns 0 and 1. , 818:87, Feb. 2016. doi: 10.3847/0004-637X/818/1/87.

T. M. Schmidt, P. Molaro, M. T. Murphy, C. Lovis, G. Cupani, S. Cristiani, F. A. Pepe, R. Rebolo, N. C. Santos, M. Abreu, V. Adibekyan, Y. Alibert, M. Aliverti, R. Allart, C. Allende Prieto, D. Alves, V. Baldini, C. Broeg, A. Cabral, G. Calderone, R. Cirami, J. Coelho, I. Coretti, V. D'Odorico, P. Di Marcantonio, D. Ehrenreich, P. Figueira, M. Genoni, R. Génova Santos, J. I. González Hernández, F. Kerber, M. Landoni, A. C. O. Leite, J.-L. Lizon, G. Lo Curto, A. Manescau, C. J. A. P. Martins, D. Megévand, A. Mehner, G. Micela, A. Modigliani, M. Monteiro, M. J. P. F. G. Monteiro, E. Mueller, N. J. Nunes, L. Oggioni, A. Oliveira, G. Pariani, L. Pasquini, E. Redaelli, M. Riva, P. Santos, D. Sosnowska, S. G. Sousa, A. Sozzetti, A. Suárez Mascareño, S. Udry, M.-R. Zapatero Osorio, and F. Zerbi. Fundamental physics with ESPRESSO: Towards an accurate wavelength calibration for a precision test of the fine-structure constant. , 646:A144, Feb. 2021. doi: 10.1051/0004-6361/202039345.

S. Seager and L. Hui. Constraining the Rotation Rate of Transiting Extrasolar Planets by Oblateness Measurements. , 574(2):1004–1010, Aug. 2002. doi: 10.1086/340994.

S. Seager and G. Mallén-Ornelas. A Unique Solution of Planet and Star Parameters from an Extrasolar Planet Transit Light Curve. , 585:1038–1055, Mar. 2003. doi: 10.1086/346105.

S. Seager and D. D. Sasselov. Theoretical Transmission Spectra during Extrasolar Giant Planet Transits. , 537:916–921, July 2000. doi: 10.1086/309088.

S. Seager, M. Kuchner, C. A. Hier-Majumder, and B. Militzer. Mass-radius relationships for solid exoplanets. *The Astrophysical Journal*, 669(2):1279, nov 2007. doi: 10.1086/521346. URL https://dx.doi.org/10.1086/521346.

A. Shporer, J. N. Winn, S. Dreizler, K. D. Colón, W. M. Wood-Vasey, P. I. Choi, C. Morley, C. Moutou, W. F. Welsh, D. Pollaco, D. Starkey, E. Adams, S. C. C. Barros, F. Bouchy, A. Cabrera-Lavers, S. Cerutti, L. Coban, K. Costello, H. Deeg, R. F. Díaz, G. A. Esquerdo, J. Fernandez, S. W. Fleming, E. B. Ford, B. J. Fulton,

M. Good, G. Hébrard, M. J. Holman, M. Hunt, S. Kadakia, G. Lander, M. Lockhart, T. Mazeh, R. C. Morehead, B. E. Nelson, L. Nortmann, F. Reyes, E. Roebuck, A. R. Rudy, R. Ruth, E. Simpson, C. Vincent, G. Weaver, and J.-W. Xie. Groundbased Multisite Observations of Two Transits of HD 80606b. , 722:880–887, Oct. 2010. doi: 10.1088/0004-637X/722/1/880.

S. A. Sim. Modelling the H Lyman lines in evolved late-type stars. *Monthly Notices of the Royal Astronomical Society*, 326(2):821–832, 09 2001. ISSN 0035-8711. doi: 10.1046/j.1365-8711.2001.04632.x. URL https://doi.org/10.1046/j.1365-8711.2001.04632.x.

D. K. Sing. Observational Techniques With Transiting Exoplanetary Atmospheres. *arXiv e-prints*, art. arXiv:1804.07357, Apr. 2018. doi: 10.48550/arXiv.1804.07357.

D. K. Sing, F. Pont, S. Aigrain, D. Charbonneau, J.-M. Désert, N. Gibson, R. Gilliland, W. Hayek, G. Henry, H. Knutson, A. Lecavelier Des Etangs, T. Mazeh, and A. Shporer. Hubble Space Telescope transmission spectroscopy of the exoplanet HD 189733b: high-altitude atmospheric haze in the optical and near-ultraviolet with STIS. , 416:1443–1455, Sept. 2011. doi: 10.1111/j.1365-2966.2011.19142.x.

W. Skidmore, G. C. Anupama, and R. Srianand. The Thirty Meter Telescope International Observatory facilitating transformative astrophysical science. *arXiv e-prints*, art. arXiv:1806.02481, June 2018. doi: 10.48550/arXiv.1806.02481.

D. Spergel, N. Gehrels, C. Baltay, D. Bennett, J. Breckinridge, M. Donahue, A. Dressler, B. S. Gaudi, T. Greene, O. Guyon, C. Hirata, J. Kalirai, N. J. Kasdin, B. Macintosh, W. Moos, S. Perlmutter, M. Postman, B. Rauscher, J. Rhodes, Y. Wang, D. Weinberg, D. Benford, M. Hudson, W.-S. Jeong, Y. Mellier, W. Traub, T. Yamada, P. Capak, J. Colbert, D. Masters, M. Penny, D. Savransky, D. Stern, N. Zimmerman, R. Barry, L. Bartusek, K. Carpenter, E. Cheng, D. Content, F. Dekens, R. Demers, K. Grady, C. Jackson, G. Kuan, J. Kruk, M. Melton, B. Nemati, B. Parvin, I. Poberezhskiy, C. Peddie, J. Ruffa, J. K. Wallace, A. Whipple, E. Wollack, and F. Zhao. Wide-Field InfrarRed Survey Telescope-Astrophysics Focused Telescope Assets WFIRST-AFTA 2015 Report. *ArXiv e-prints*, Mar. 2015.

K. G. Stassun, E. Corsaro, J. A. Pepper, and B. S. Gaudi. Empirical Accurate Masses and Radii of Single Stars with TESS and Gaia. , 155:22, Jan. 2018. doi: 10.3847/1538-3881/aa998a.

K. G. Stassun, R. J. Oelkers, M. Paegert, G. Torres, J. Pepper, N. De Lee, K. Collins, D. W. Latham, P. S. Muirhead, J. Chittidi, B. Rojas-Ayala, S. W. Fleming, M. E. Rose, P. Tenenbaum, E. B. Ting, S. R. Kane, T. Barclay, J. L. Bean, C. E. Brassuer, D. Charbonneau, J. Ge, J. J. Lissauer, A. W. Mann, B. McLean, S. Mullally, N. Narita, P. Plavchan, G. R. Ricker, D. Sasselov, S. Seager, S. Sharma, B. Shiao, A. Sozzetti, D. Stello, R. Vanderspek, G. Wallace, and J. N. Winn. The Revised TESS Input Catalog and Candidate Target List. , 158(4):138, Oct. 2019. doi: 10.3847/1538-3881/ab3467.

J. Stauffer, A. C. Cameron, M. Jardine, T. J. David, L. Rebull, A. M. Cody, L. A. Hillenbrand, D. Barrado, S. Wolk, J. Davenport, and M. Pinsonneault. Orbiting Clouds of Material at the Keplerian Co-rotation Radius of Rapidly Rotating Low-mass WTTs in Upper Sco. *AJ*, 153(4):152, 4 2017. ISSN 0004-6256. doi: 10.3847/1538-3881/aa5eb9. URL https://doi.org/10.3847/1538-3881/aa5eb9.

N. I. Storch and D. Lai. Viscoelastic tidal dissipation in giant planets and formation of hot Jupiters through high-eccentricity migration. , 438(2):1526–1534, Feb. 2014. doi: 10.1093/mnras/stt2292.

K. G. Strassmeier, T. Granzer, M. Mallonn, M. Weber, and J. Weingrill. CoRoT photometry and STELLA spectroscopy of an eccentric, eclipsing, and spotted HgMn binary with sub-synchronized rotation. *A&A*, 597:A55, 1 2017. doi: 10.1051/0004-6361/201629150.

P. W. Sullivan, J. N. Winn, Z. K. Berta-Thompson, D. Charbonneau, D. Deming, C. D. Dressing, D. W. Latham, A. M. Levine, P. R. McCullough, T. Morton, G. R. Ricker, R. Vanderspek, and D. Woods. The Transiting Exoplanet Survey Satellite: Simulations of Planet Detections and Astrophysical False Positives. , 809:77, Aug. 2015. doi: 10.1088/0004-637X/809/1/77.

G. M. Szabó and L. L. Kiss. A Short-period Censor of Sub-Jupiter Mass Exoplanets with Low Density. , 727(2):L44, Feb. 2011. doi: 10.1088/2041-8205/727/2/L44.

J. H. Telting, G. Avila, L. Buchhave, S. Frandsen, D. Gandolfi, B. Lindberg, H. C. Stempels, S. Prins, and NOT staff. FIES: The high-resolution Fiber-fed Echelle Spectrograph at the Nordic Optical Telescope. *Astronomische Nachrichten*, 335 (1):41, Jan. 2014. doi: 10.1002/asna.201312007.

The LUVOIR Team. The LUVOIR Mission Concept Study Final Report. *arXiv e-prints*, art. arXiv:1912.06219, Dec. 2019. doi: 10.48550/arXiv.1912.06219.

G. Torres, J. Andersen, and A. Giménez. Accurate masses and radii of normal stars: modern results and applications. , 18:67–126, Feb. 2010. doi: 10.1007/s00159-009-0025-1.

A. Udalski, M. Szymanski, J. Kaluzny, M. Kubiak, W. Krzeminski, M. Mateo, G. Preston, and B. Paczynski. The optical gravitational lensing experiment. discovery of the first candidate microlensing event in the direction of the galactic bulge. *Acta astronomica*, 43:289–294, 1993.

V. Van Eylen and S. Albrecht. Eccentricity from Transit Photometry: Small Planets in Kepler Multi-planet Systems Have Low Eccentricities. , 808:126, Aug. 2015. doi: 10.1088/0004-637X/808/2/126.

A. Vanderburg and J. A. Johnson. A Technique for Extracting Highly Precise Photometry for the Two-Wheeled Kepler Mission. , 126:948–958, Dec. 2014. doi: 10.1086/678764.

A. Vanderburg, J. C. Becker, M. H. Kristiansen, A. Bieryla, D. A. Duev, R. Jensen-Clem, T. D. Morton, D. W. Latham, F. C. Adams, C. Baranec, P. Berlind, M. L. Calkins, G. A. Esquerdo, S. Kulkarni, N. M. Law, R. Riddle, M. Salama, and A. R. Schmitt. Five Planets Transiting a Ninth Magnitude Star. , 827:L10, Aug. 2016. doi: 10.3847/2041-8205/827/1/L10.

K. Vida, K. Oláh, Z. Kővári, J. Jurcsik, Sódor, M. Váradi, B. Belucz, I. Dékány, Z. Hurta, I. Nagy, and K. Posztobányi. Four-colour photometry of ey dra: A study of an ultra-fast rotating active dm1-2e star. *Astronomische Nachrichten*, 331(3):250–256, 2010. doi: https://doi.org/10.1002/asna.200911341. URL https://onlinelibrary.wiley.com/doi/abs/10.1002/asna.200911341.

K. Vida, Z. Kővári, A. Pál, K. Oláh, and L. Kriskovics. Frequent flaring in the trappist-1 system—unsuited for life? *The Astrophysical Journal*, 841(2):124, jun 2017. doi: 10.3847/1538-4357/aa6f05. URL https://dx.doi.org/10.3847/1538-4357/aa6f05.

S. Villanueva, Jr., B. S. Gaudi, R. W. Pogge, J. D. Eastman, K. G. Stassun, M. Trueblood, and P. Trueblood. DEdicated MONitor of EXotransits and Transients (DEMONEXT): System Overview and Year One Results from a Low-cost Robotic Telescope for Followup of Exoplanetary Transits and Transients. , 130(1):015001, Jan. 2018. doi: 10.1088/1538-3873/aa9603.

S. M. Wahl, D. Thorngren, T. Lu, and B. Militzer. Tidal Response and Shape of Hot Jupiters. , 921(2):105, Nov. 2021. doi: 10.3847/1538-4357/ac1a72.

H. R. Wakeford, N. K. Lewis, J. Fowler, G. Bruno, T. J. Wilson, S. E. Moran, J. Valenti, N. E. Batalha, J. Filippazzo, V. Bourrier, S. M. Hörst, S. M. Lederer, and J. de Wit. Disentangling the Planet from the Star in Late-Type M Dwarfs: A Case Study of TRAPPIST-1g. , 157(1):11, Jan. 2019. doi: 10.3847/1538-3881/aaf04d.

W. R. Ward. Past Orientation of the Lunar Spin Axis. *Science*, 189(4200):377–379, Aug. 1975. doi: 10.1126/science.189.4200.377.

W. R. Ward and D. P. Hamilton. Tilting Saturn. I. Analytic Model. , 128(5):2501–2509, Nov. 2004. doi: 10.1086/424533.

L. M. Weiss, G. W. Marcy, E. A. Petigura, B. J. Fulton, A. W. Howard, J. N. Winn, H. T. Isaacson, T. D. Morton, L. A. Hirsch, E. J. Sinukoff, A. Cumming, L. Hebb, and P. A. Cargile. The California-Kepler Survey. V. Peas in a Pod: Planets in a Kepler Multi-planet System Are Similar in Size and Regularly Spaced. , 155:48, Jan. 2018. doi: 10.3847/1538-3881/aa9ff6.

J. N. Winn. Transits and Occultations. *ArXiv e-prints*, Jan. 2010.

J. N. Winn, M. J. Holman, G. W. Henry, A. Roussanova, K. Enya, Y. Yoshii, A. Shporer, T. Mazeh, J. A. Johnson, N. Narita, and Y. Suto. The Transit Light Curve Project. V. System Parameters and Stellar Rotation Period of HD 189733. , 133 (4):1828–1835, Apr. 2007. doi: 10.1086/512159.

A. Wolszczan and D. A. Frail. A planetary system around the millisecond pulsar PSR1257 + 12. , 355(6356):145–147, Jan. 1992. doi: 10.1038/355145a0.

B. E. Wood, S. Redfield, J. L. Linsky, H.-R. Müller, and G. P. Zank. Stellar ly emission lines in the hubble space telescope archive: Intrinsic line fluxes and absorption from the heliosphere and astrospheres*. *The Astrophysical Journal Supplement Series*, 159(1):118, jul 2005. doi: 10.1086/430523. URL https://dx.doi.org/10.1086/430523.

R. V. Yelle. Aeronomy of extra-solar giant planets at small orbital distances. , 170: 167–179, July 2004. doi: 10.1016/j.icarus.2004.02.008.

L. Zeng, S. B. Jacobsen, D. D. Sasselov, M. I. Petaev, A. Vanderburg, M. Lopez-Morales, J. Perez-Mercader, T. R. Mattsson, G. Li, M. Z. Heising, A. S. Bonomo, M. Damasso, T. A. Berger, H. Cao, A. Levi, and R. D. Wordsworth. Growth model interpretation of planet size distribution. *Proceedings of the National Academy of Science*, 116(20):9723–9728, May 2019. doi: 10.1073/pnas.1812905116.

Z. Zhan, M. N. Günther, S. Rappaport, K. Oláh, A. Mann, A. M. Levine, J. Winn, F. Dai, G. Zhou, C. X. Huang, L. G. Bouma, M. J. Ireland, G. Ricker, R. Vanderspek, D. Latham, S. Seager, J. Jenkins, D. A. Caldwell, J. P. Doty, Z. Essack, G. Furesz, M. E. R. Leidos, P. Rowden, J. C. Smith, K. G. Stassun, and M. Vezie. Complex Rotational Modulation of Rapidly Rotating M Stars Observed with TESS. , 876(2):127, May 2019. doi: 10.3847/1538-4357/ab158c.

M. Zhang, H. A. Knutson, L. Wang, F. Dai, L. A. dos Santos, L. Fossati, G. W. Henry, D. Ehrenreich, Y. Alibert, S. Hoyer, T. G. Wilson, and A. Bonfanti. Detection of Ongoing Mass Loss from HD 63433c, a Young Mini-Neptune. , 163(2):68, Feb. 2022. doi: 10.3847/1538-3881/ac3f3b.

Z. Zhang, Y. Zhou, B. V. Rackham, and D. Apai. The near-infrared transmission spectra of trappist-1 planets b, c, d, e, f, and g and stellar contamination in multi-epoch transit spectra. *The Astronomical Journal*, 156(4):178, oct 2018. doi: 10.3847/1538-3881/aade4f. URL https://dx.doi.org/10.3847/1538-3881/aade4f.

W. Zhu, C. X. Huang, G. Zhou, and D. N. C. Lin. Constraining the Oblateness of Kepler Planets. , 796(1):67, Nov. 2014. doi: 10.1088/0004-637X/796/1/67.